A LABORATORY INVESTIGATION INTO THE BEHAVIOUR OF SAND AT LOW CONFINING STRESSES

By

Jonathan Robert Ford White

UNIVERSITY · OF · OXFORD

DPhil Thesis

Department of Engineering Science

St. Peter's College

Trinity Term 2020

DECLARATION

I declare that, except where specific reference is made to the works of others, the contents of this thesis are original and have never been submitted, in part or as a whole, to any other university for any degree, diploma or other qualifications.

Jonathan Robert Ford White

July 2020

ACKNOWLEDGEMENTS

For their guidance in my research, I would first like to thank my supervisors Professors Chris Martin and Guy Houlsby. I would also like to thank Professor Byron Byrne for both encouraging me to take up the studentship, and for his support during my time at Oxford.

Thanks must also go to Alison May for all your help procuring the new lab equipment, to Clive Baker for somehow managing to physically manoeuvre the apparatus into position, and to Dr Thomas Andolfsson for help with all things electro-mechanical, for teaching me to solder (I'm still rubbish), and for providing me with frequent and welcome distraction on those days when testing hadn't gone so well.

For providing me with training and loan of a cyclic triaxial apparatus, I would like to thank the team at Fugro, Wallingford, and specifically Dr Mike Rattley for his time and useful advice. Also to Sam Ingarfield at Fugro, Australia, thank you for going through and spotting some of the bugs in my NorSand code!

I consider myself very fortunate to have been offered this opportunity, and luckier still to have made such great friends along the way. In particular, thanks to Dr Russell Mayall and Dr Iona Richards for making those first few months at Cranfield so enjoyable, and to Toby Balaam for the various modelling discussions, and for sharing in my excitement over the purchase of a certain vintage calculator. Also to Dr Scott Whyte, Dr Peter Houlston, and Dr Trevon Joseph, thanks for all the nights out at our friendly local Wetherspoons, and the enthusiastic discussions had therein.

I would also thank Saeko and Jim for the numerous food deliveries, bottles of red wine, dinners out, and home-cooked Sunday lunches that helped remind me of life outside of my DPhil bubble. Special thanks must also go to Elsa for always keeping me company, no matter the hour, and to my parents, who ultimately made all of this possible.

Finally, to Jenny. Who has been by my side throughout. We got there in the end. Thank you so much for your patience, love, and unending support. I couldn't have done this without you.

ABSTRACT

A Laboratory Investigation into the Behaviour of Sand at Low Confining Stresses

Jonathan R.F. White
St. Peter's College, University of Oxford
A thesis submitted for the degree of Doctor of Philosophy
Trinity 2020

The mechanical behaviour of sands at low confining stresses may have important implications for the design of offshore wind turbine (OWT) foundations. However, previous research investigating this behaviour is limited and conflicting, and cyclic testing campaigns have historically adopted load characteristics that may be unrepresentative of those sustained by OWT foundations. This thesis endeavours to fill the gap in the literature through creation of a new experimental database of soil element tests, that explores the constitutive response of sand at low stress levels subjected to monotonic and cyclic loading.

Results of the monotonic experimental campaign indicate that while the shear strength properties (η_{max} and ϕ'_{max}) tend to increase with decreasing effective confining stress, $\sigma'_{c,0}$, this effect becomes increasingly minor for $\sigma'_{c,0} \leq$ 50 kN/m^2. Furthermore, tests undertaken at lower confining stresses exhibit a comparatively stiffer response than those tests sheared at higher pressures. Results of the cyclic triaxial testing campaign exemplify the complexities of the response of sands subjected to cyclic loading. However, clear and systematic trends are found that can be robustly captured by the new cyclic modelling framework adopted in this study.

Modern design methods for OWT foundations increasingly rely on finite element analysis (FEA); however, results depend critically on the constitutive models used, and the model parameters adopted in the numerical analyses. This thesis reviews the state-of-the-art with regard to constitutive modelling frameworks developed for predicting sand behaviour. Evaluation of four sophisticated constitutive models found that it was not possible to determine a single set of calibrated model parameters that yield satisfactory model simulations for both drained and undrained load cases. Furthermore, only the general trends could be predicted when simulating sustained undrained cyclic loading. Further model development is therefore required if such models are to be relied upon for predicting the long-term behaviour of OWT foundations.

TABLE OF CONTENTS

NOMENCLATURE

ROMAN SYMBOLS:

A	hardening modulus
A_0	bounding-surface model parameter used to control the rate of dilation
A_G	material constant used in empirical relationship to determine shear modulus
A_ψ	constant used in Bolton's (1986) flow rule
A_{corr}	area correction applied to triaxial test specimens
A_f	maximum stored energy
$A_{c,f}$	specimen cross sectional area at the end of the consolidation stage
A_{loop}	area of hysteresis loop
A_m	sample area covered by membrane
A_R	ratcheting area
$\boldsymbol{a}$	gradient vector to the yield function
$\boldsymbol{b}$	gradient vector to the plastic potential function
C_U	coefficient of uniformity
C_Z	coefficient of curvature
c'	effective cohesion
c	ratio of critical friction ratios in triaxial extension and compression
c_h	bounding-surface model parameter used to control the hardening modulus
c_z	bounding-surface model parameter
d_{20}	particle size of which 20 % of soil particles are smaller
d_{50}	median particle size
D	rate of dilation
D_{min}	maximum rate of dilation
D	sample diameter
$D_{1/3}$	corrected average diameter used in the calculation of deviator stress
$\boldsymbol{D^e}$	elastic stiffness matrix
$\boldsymbol{D^{ep}}$	elastoplastic stiffness matrix
D_{min}	peak measured dilatancy
D_r	relative density
E	Young's modulus
E_m	membrane stiffness
e	void ratio
e_g	reference void ratio for rounded and angular particle shapes
e_{cs}	critical state void ratio
$e_{cs(ref)}$	reference void ratio at zero mean effective stress
f	yield function
f	cycle frequency

G	shear stiffness
G_0	small-strain shear modulus
G_{ur}	shear stiffness measured from unload-reload loops
g	plastic potential function
$\boldsymbol{H}$	non-linear tensorial function used in hypoplasticity constitutive models
H	specimen height
H	horizontal load
H_0	plastic hardening parameter intercept used in NorSand
H_{tc}	plastic hardening parameter for triaxial compression conditions used in NorSand
H_ψ	plastic hardening parameter gradient used in NorSand
h_0	bounding-surface model parameter used to control the the hardening modulus
I_1, I_2, I_3	first, second, and third ‘fundamental’ stress invariants
I_r	relative density index
J_1, J_2, J_3	first second and third deviatoric stress invariants
J_1', J_2'	cross dependence parameters
K	bulk stiffness
K_0	coefficient of earth pressure at rest
k	empirical constant used in Bolton (1986) flow rule
k_f	central cyclic stiffness
k_l	loading stiffness
k_u	unloading stiffness
L_{tt}	‘tip to tip’ or wave path length
M	critical friction ratio
M	moment load
M_{AV}	average moment (in pile / model tests)
M_b	gradient of the bounding surface in bounding surface models
M_{CYC}	cyclic moment (in pile / model tests)
M_d	gradient of the dilatancy surface in bounding-surface models
M_i	image critical friction ratio
$M_{i,tc}$	image critical friction ratio at reference triaxial compression conditions
M_R	reference moment load (in pile / model tests)
M_{tc}	critical friction ratio in triaxial compression conditions
M_θ	Lode angle dependent critical friction ratio
m	yield surface parameter used in bounding surface models
m_{dry}	dry mass of sand used in sample preparation
n	cycle number
n	stress state coefficient used in CASM
n_b	model parameter controlling the position of the bounding surface from the CSL
n_d	model parameter controlling the position of the dilatancy surface from the CSL
N	total number of cycles

N	volumetric coupling coefficient
N_f	number of cycles to failure
N_L	number of cycles required to cause liquefaction
P	vertical force
p'	(Cambridge) mean effective stress invariant
p'_1, p'_2	net pressure acting across the membrane before and after the volume change
p'_c	hardening parameter used in CASM
p'_i	image mean effective stress used in NorSand
p'_{ref}	reference mean effective stress
q	(Cambridge) deviator stress invariant
q_{av}	average deviator stress (static bias used in cyclic triaxial tests)
q_{corr}	deviator stress corrected for membrane resistance and self-weight of the specimen
q_{cyc}	cyclic deviator stress
q_e	extreme deviator stress during a load cycle
q_{max}	maximum deviator stress
q_r	reversal deviator stress during a load cycle
q_{ref}	reference deviator stress
R_u	excess pore pressure ratio
$\boldsymbol{r}$	deviatoric stress ratio tensor used in some bounding surface plasticity models
r	spacing ratio
S	unit membrane penetration
$\hat{\boldsymbol{s}}$	deviatoric stress tensor in matrix form
s'	(MIT) mean effective stress invariant
T	cycle period
t	thickness
t_m	membrane thickness
u	pore pressure
V	sample volume
ΔV_m	sample volume change due to membrane penetration
v	specific volume (1 + e)
v_s	shear wave velocity
v_p	compression wave velocity
W	maximum stored energy
ΔW	energy loss per cycle
x	radial displacement from on-sample LVDTs
y	lateral displacement (in pile / model tests)
z	vertical displacement
z	bounding-surface fabric internal variable
z_{max}	bounding-surface model parameter

GREEK SYMBOLS:

α	direction of major principal stress
α	back stress used in the formulation of multi surface constitutive models
α	curve fitting parameter for estimating pore pressure development in cyclic tests
γ	engineering shear strain
γ'	effective unit weight
γ_{av}	average shear strain
γ_{sa}, γ_{da}	single, double amplitude shear strain
γ_{perm}	permanent shear strain
γ_{tl}	linear threshold shear strain
γ_{tv}	volumetric threshold shear strain
$\boldsymbol{\varepsilon}$	(total) strain tensor in Voigt/vector notation
$\boldsymbol{\varepsilon^e}$	elastic component of the strain tensor in Voigt/vector notation
$\boldsymbol{\varepsilon^p}$	plastic component of the strain tensor in Voigt/vector notation
$\boldsymbol{\varepsilon^p_p},$	plastic volumetric component of the strain tensor in Voigt/vector notation
$\boldsymbol{\varepsilon^p_q}$	plastic deviatoric component of the strain tensor in Voigt/vector notation
ε	strain
$\varepsilon_1, \varepsilon_2, \varepsilon_3$	major, intermediate, minor principal strain
ε_a	cyclic strain mobilised at σ_{av} on reloading during a load cycle
ε_b	cyclic strain mobilised at σ_{av} on unloading during a load cycle
ε_{acc}	accumulated residual strain
ε_{av}	average strain
ε_{cyc}	cyclic strain
ε_{da}	double amplitude strain
ε_e	cyclic strain mobilised at σ_e during a load cycle
ε_{sa}	single amplitude strain
ε_m	normalised membrane penetration
ε_N	average cyclic strain mobilised during a load cycle
ε_p	volumetric strain
ε_p	permanent cyclic strain mobilised during a load cycle
ε_q	deviatoric strain
ε_r	radial strain
ε_r	cyclic strain mobilised at σ_r during a load cycle
ε_{sa}	single amplitude cyclic strain
ε_z	axial strain
ζ	stress exponent used in CSL power law
ζ_b, ζ_c	dimensionless cyclic load characterisation parameters
η	dimensionless ratio of the triaxial stress invariants p' and q
η_{max}	peak stress ratio
θ	pile rotation (in pile / model tests)

θ	Lode angle
κ	generalised hardening parameter(s)
κ	slope of the swelling/recompression line in $e - \ln p'$ space
Λ	scalar plastic multiplier
λ	slope of the normal compression line in $e - \ln p'$ space
λ	power function constant used to plot curved critical state lines
λ	wavelength
μ	Poisson's ratio
μ'	drained Poisson's ratio
μ_u	undrained Poisson's ratio
ξ	energy loss factor
ξ	critical state line exponent used in power law
ρ	density
ρ_s	particle density
$\hat{\boldsymbol{\sigma}}$	(effective) stress tensor in matrix notation
$\boldsymbol{\sigma}$	(effective) stress tensor in Voigt/vector notation
σ	stress
σ_0	initial stress
σ_1, σ_1'	total, effective major principal stress
σ_2, σ_2'	total, effective intermediate principal stress
σ_3, σ_3'	total, effective minor principal stress
σ_a, σ_a'	total, effective axial principal stress
$\sigma_{av}, \sigma_{av}'$	average total, effective stress (static bias)
σ_c, σ_c'	total, effective confining stress
σ_{cell}'	effective cell pressure in triaxial tests
$\sigma_{c,0}'$	initial effective confining stress
$\sigma_{cyc}, \sigma_{cyc}'$	total, effective cyclic deviator stress
σ_e	extreme stress
$\sigma_{h,c}'$	effective horizontal consolidation stress
σ_n'	normal effective stress
σ_r	reversal stress
σ_r, σ_r'	total, effective radial principal stress
$\sigma_{r,m}$	membrane correction applied to the radial stress
$\sigma_{ref}, \sigma_{ref}'$	total, effective reference stress
σ_z, σ_z'	total, effective vertical stress
$\sigma_{z,c}'$	effective vertical consolidation stress
$\sigma_{z,m}$	membrane correction applied to the vertical stress
$\sigma_{z,sw}'$	effective vertical stress due to the self-weight of the triaxial test specimen
τ	shear stress
τ_f	shear stress at failure

ϕ'	effective angle of internal shearing resistance
ϕ'_{max}	peak or maximum effective angle of internal shearing resistance
ϕ'_{Ch}	characteristic effective angle of internal shearing resistance
ϕ'_{cv}	constant volume effective angle of internal shearing resistance
ϕ'_{f}	effective angle of internal shearing resistance at failure
ϕ'_{PT}	phase transformation effective angle of internal shearing resistance
ϕ'_{r}	residual effective angle of internal shearing resistance
χ_i	image state-dilation coefficient
χ_{tc}	state dilation coefficient derived from triaxial compression tests
ψ	state parameter
ψ_0	initial state parameter
ψ^D	angle of dilation
$\psi^D_{(1)}$	angle of dilation calculated according to Eqs. (6-16) and (6-17)
$\psi^D_{(2)}$	angle of dilation calculated according to Eqs. (6-19) and (6-20)
ψ_i	image state parameter
ψ_{ref}	reference state parameter

1. INTRODUCTION

1.1. BACKGROUND

The offshore wind energy industry is one of the UK and Europe's success stories, and has undergone rapid growth and development over the past 10 years. This is due to several factors, but is principally attributable to both the coordinated domestic policy (e.g. schemes such as the UK Carbon Trust's "Offshore Wind Accelerator"), and increased international pressure to reduce harmful emissions, and limit the rise in global temperatures (e.g. the Paris Agreement (United Nations, 2015)).

Over this time, the offshore wind technology has evolved and advanced to increase efficiency and lower costs. This has largely been achievable thanks to improvements in the European supply chain, and the continuing trend of building larger capacity (>14MW) turbines, thereby enabling economies of scale to be exploited. However, further reductions to the levelized cost of energy continue to be realised. For example, estimates suggest that adoption of the new PISA method (Byrne *et al.*, 2015) may have the potential to reduce steel requirements for foundations by up to 30 % in some design conditions, leading to significant cost savings.

This research project, which is part of the REMS CDT (Renewable Energy Marine Structures Centre for Doctoral Training), therefore aims to further contribute to the advancement of foundation design methods used in the offshore renewable energy industry by addressing some of the uncertainties associated with predicting the constitutive response of sand at low confining stresses.

1.2. PROBLEM DEFINITION

For certain design situations, such as the design of offshore wind turbine foundations, subsea pipelines, and slope stability analysis, the response of the shallow, near surface soil deposits often has a significant influence on the design. However, published data from experiments undertaken at low stresses representative of these design situations are both limited and conflicting.

Offshore wind turbine (OWT) foundations are also typically subjected to large numbers of low-amplitude load cycles over their operational lifetime. However, cyclic soil element testing investigations have historically been more focussed on earthquake-related phenomena, with test campaigns predominantly being performed on loose specimens subjected to relatively few, high-amplitude load cycles. The loading characteristics of these experimental programmes are therefore unlikely to be representative of the cyclic loads sustained by offshore marine wind energy structures.

Pertinent questions regarding the constitutive response of shallow soils in these low-stress, low cyclic stress amplitude design situations therefore remain unanswered. The aim of this thesis is therefore to address this evident gap in the literature, by obtaining high-quality experimental results investigating both the monotonic and cyclic behaviour of sand at low stress levels.

The use of finite element analysis (FEA) has become increasingly important in the design of OWT foundations in industry (Burd *et al*., 2019; Byrne *et al*., 2019). The results of such analyses depend critically on the constitutive models used, and the calibrated model parameters adopted in the numerical analyses. However, while there has been significant development in the capability of constitutive models over the past few decades, uptake of more sophisticated models in industry has been relatively limited. According to Grammatikopolou *et al*. (2017), this may due to both the limited availability of such models within commercial software packages, and difficulties associated with deriving model parameters from routine laboratory and field tests. Relatively simple, more robust models are therefore typically preferred in practice, though the predictive capabilities of such models may be limited for complex loading histories.

Furthermore, offshore wind farm sites tend to cover large areas, where soil conditions are often heterogeneous. As such, it is often necessary to tailor the choice of the constitutive model to best meet the requirements of a particular analysis. For example, separate models may be employed to model the small strain behavior (relevant for serviceability limit state considerations) and ultimate strength behaviour (relevant for ultimate limit state conditions). Similarly, while one model may be able to satisfactorily predict monotonic behaviour, the same model may be incapable of capturing cyclic loading behaviour. Results of the experimental campaign undertaken in this study will therefore provide a useful database that may be used to inform the choice, assessment, and development of constitutive models used in practice.

1.3. THESIS STRUCTURE

The structure of this thesis is briefly outlined below:

Chapter 1 provides some context and the motivation for researching the behaviour of cohesionless soils at low confining stresses, and why this may be relevant to the design of offshore renewable energy marine structures such as monopiles.

Chapter 2 presents a review of the literature associated with the behaviour of sands at low confining stresses. First, the monotonic, low stress behaviour, as investigated in soil laboratory element testing apparatus, is summarised, followed by a review of previous low stress amplitude, high cycle number experimental testing campaigns.

Chapter 3 summarises best practice associated with the laboratory element testing of sand. The influences of specimen size, end restraint, and sample reconstitution method on the results of triaxial tests are examined, and the various corrections applied to the measured data are discussed.

Chapter 4 provides a description of the triaxial testing apparatus (stress path and cyclic) and instrumentation used in this thesis. The classification and index properties of the test material (Leighton Buzzard sand) are then presented, and compared with values published in the literature. Testing methods, including sample preparation and testing procedures are then described. Finally, the methods used to calculate engineering parameters from the measured test data are summarised.

Chapter 5 reviews the concepts and terminologies required to describe the behaviour of cohesionless soils subjected to both monotonic and dynamic loading.

Chapter 6 presents the results of 23 drained monotonic stress path triaxial tests, performed to investigate the constitutive behaviour of a dense sand at low effective confining stresses. The results give additional experimental evidence to help clarify the conflicting behaviours reported in the literature, and provide a new database of tests that may be used to aid the development of advanced constitutive models, as described in Chapters 8 and 9.

Chapter 7 presents the results of 20 undrained cyclic triaxial tests, performed to explore the stress-strain behaviour and strength characteristics of a dense sand under cyclic loading. The effects of stress amplitude and effective confining stress on the development of excess pore water pressure, permanent strain and cyclic strain amplitude with number of cycles are investigated. The stiffness and damping characteristics are also examined.

Chapter 8 presents a review of constitutive models and frameworks developed for predicting the mechanical behaviour of sand. The current state-of-the-art is summarised, and four promising, state-dependent constitutive models are selected for the further evaluation presented in Chapter 9.

Chapter 9 provides an evaluation of four sophisticated constitutive models. The models are evaluated in terms of ease of calibration, numerical implementation, and predictive capability. Comparisons of single-element model simulations with both monotonic and cyclic experimental data are then presented, and their performance is critically assessed. Recommendations associated with scoping laboratory test schedules to enable calibration of such models are also provided.

Chapter 10 summarises the key contributions of this thesis, and provides suggestions for future work to refine and extend the research presented herein.

2. LITERATURE REVIEW

2.1. INTRODUCTION

The purpose of this chapter is to review the literature associated with element testing of sand undertaken at low effective stresses. The definition of what constitutes a 'low' effective stress is first discussed. Low-stress monotonic element testing publications are then reviewed, followed by an overview of published cyclic element tests undertaken at similarly low stress levels and their applicability to the design of offshore marine energy foundations.

2.2. BEHAVIOUR OF SANDS AT LOW STRESS LEVELS

In triaxial testing, the confining stress, σ_c, is typically associated with the applied radial pressure, σ_r, (also sometimes referred to as 'cell' pressure). The effective confining stress, σ_c', is therefore calculated as the difference between the cell pressure and pore pressure, u, such that:

$$\sigma_c = \sigma_r = \sigma_{cell}; \quad \sigma_c' = \sigma_r - u = \sigma_r' \tag{2-1}$$

In this work, triaxial tests undertaken at 'low' confining stresses are arbitrarily taken as tests in which the specimen is consolidated (isotropically or anisotropically) to an effective confining stress of 50 kN/m^2 or less prior to shearing, and corresponds to stress levels within approximately 10 m of the ground surface. The following sections present a review of previous experimental investigations undertaken at low confining stresses published in the literature.

2.3. PREVIOUS MONOTONIC TESTS AT LOW STRESS LEVELS

Stroud (1971) investigated the behaviour of Leighton Buzzard sand at low stress levels in the Cambridge simple shear device, and found some evidence to suggest that the failure envelope in $p' - q$ space (where p' and q are the triaxial stress invariants defined in Section 4.8.2) may be curved rather than straight, resulting in angles of shearing resistance, ϕ_{max}' and ϕ_{cv}', that vary with mean effective stress (see Section 5.1.1 for descriptions of ϕ_{max}' and ϕ_{cv}').

Ponce & Bell (1971) were some of the first investigators to attempt triaxial testing at low stresses, and reportedly achieved cell pressures as low as 1.38 kN/m^2. Tests were undertaken on 71 mm diameter, dry pluviated specimens of fairly uniform quartz sand, prepared to relative densities, D_r, of 5 % and 94 %. Enlarged, lubricated ends were not used, neither was local strain instrumentation. Figure 2.1a shows plots of ϕ'_{max} vs. σ'_c from results of drained triaxial compression tests undertaken by Ponce & Bell (1971), and shows that ϕ'_{max} increases rapidly once σ'_c decreases below 20 kN/m^2. They emphasised the need to re-evaluate several factors often neglected in conventional testing:

- the resistance contributed by the rubber membrane; and
- the self-weight of the specimen.

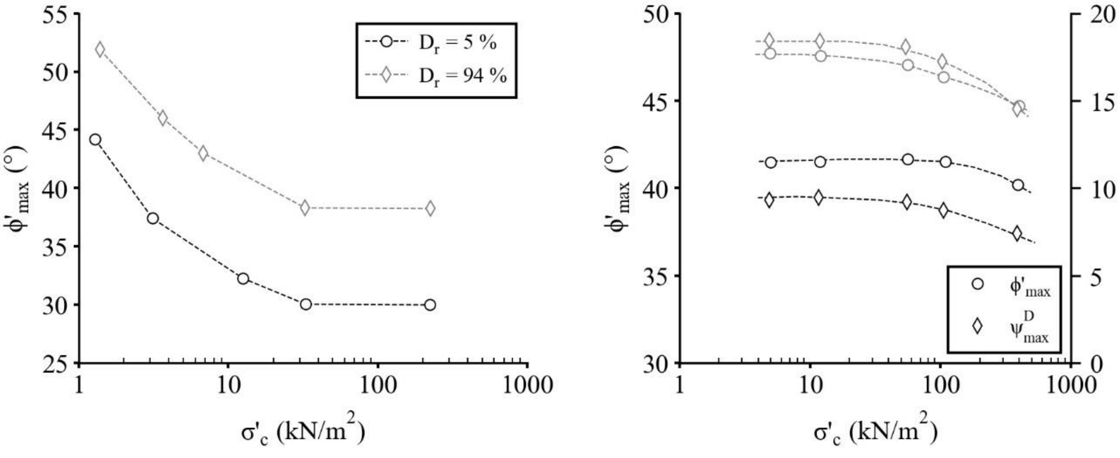

(a) *(b)*

Figure 2.1: Relationships between ϕ'_{max} & σ'_c found by (a) Ponce & Bell (1971) in triaxial compression tests; and (b) in plane strain (from Tatsuoka, 1987)

Fukushima & Tatsuoka (1984) also performed carefully controlled drained triaxial compression tests on Toyoura sand at low confining stresses (σ'_c = 2.0 to 392 kN/m^2). They also emphasized the importance of incorporating corrections for both membrane resistance and the self-weight of the sample. However, Fukushima & Tatsuoka (1984) observed that the dependency of ϕ'_{max} on σ'_c at low stresses was much smaller than that observed by Ponce & Bell (1971), with both ϕ'_{max} and the volumetric strain response (i.e. dilation) becoming largely independent of σ'_c below 50 kN/m^2.

Tatsuoka *et al*. (1986) performed additional drained plane strain tests on Toyoura sand at low confining stresses (σ'_c = 5.0 to 392 kN/m^2) and observed little variation in the peak friction angle or the maximum dilation angle for σ'_c below 50 kN/m^2, as shown in Figure 2.1b.

Fannin *et al*. (2005) investigated the shear strength of colluvium material by conducting a series of in situ and laboratory direct shear box tests, at vertical effective stresses between 5 to 20 kN/m^2.

They found ϕ'_{max} to range from 54 to 71°, and observed it to be inversely proportional to the logarithm of effective stress. Their data matched well with the general trend reported by Leps (1970) who undertook triaxial tests on rockfill at higher stresses (40 kN/m^2 to 3.5 MN/m^2) – see Figure 2.2. However, Tatsuoka (1987) cautioned that it may be misleading to assume that both ϕ'_{max} and the maximum angle of dilation, ψ^D_{max}, change in proportion to $\ln(p')$ in the low stress region, without reliable experimental results.

Sture *et al*. (1998) and Sture *et al*. (2004) undertook triaxial tests on reconstituted sand specimens (D_r = 35 to 85 %) aboard a NASA space shuttle, where they were able to achieve extremely low confining stresses in the range 0.05 to 0.5 kN/m^2. They observed peak friction angles as high as ϕ'_{max} = 72±2°; together with ψ^D_{max} = 30±1°, though it is not clear how ψ^D_{max} was calculated.

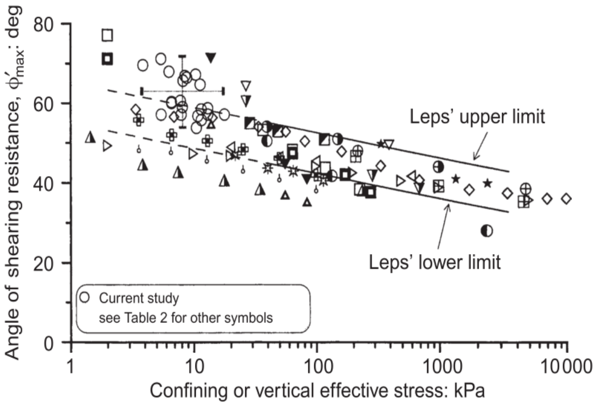

Figure 2.2: Comparison of ϕ'_{max} with σ'_c (from Fannin et al., 2005)

Lee (2000) undertook plane strain and triaxial compression tests on three sands and found even higher dilation angles. For the specimens prepared in loose and dense states, Lee observed ψ^D_{max} as high as 26° and 39°, respectively, when sheared under a confining stress of 25 kN/m^2. However, it is not clear how Lee (2000) calculated ψ^D_{max}, only stating that "the dilation angle is often obtained by measuring the slope angles of the linear portion of the volumetric strain versus axial strain curves of drained triaxial test data". This is inconsistent with conventional definitions typically used to determine ψ^D (see Section 6.5.3), and may explain the relatively high ψ^D_{max} values.

Figure 2.3 shows results of a study performed by Quinteros *et al*. (2017), who undertook drained triaxial tests on reconstituted specimens of a North Sea sand at low and high effective vertical consolidation stresses ($10 < \sigma'_{z,c} < 200$ kN/m^2). The aim was to investigate the effect of small-amplitude drained two-way cyclic loading stages, known as “pre-shearing”, prior to monotonic shearing, on the strength and stiffness response.

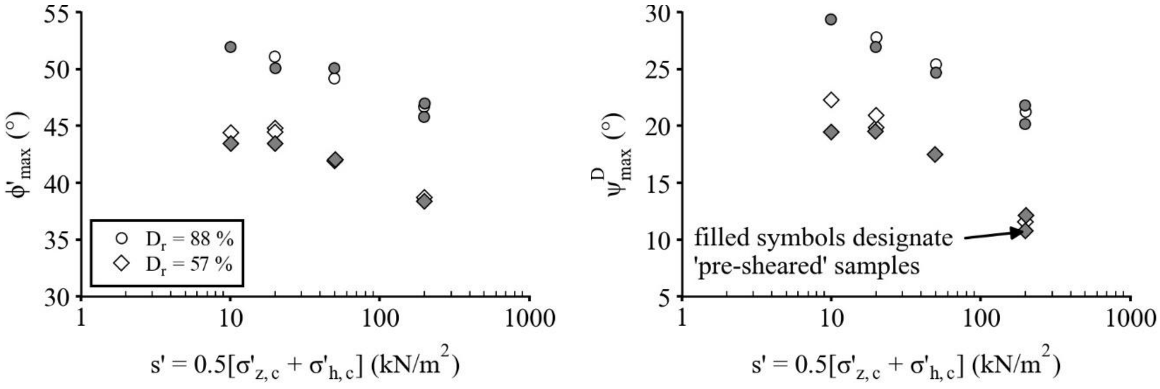

(a) *(b)*

Figure 2.3: Results of triaxial tests in terms of the influence of s' on (a) ϕ'_{max} and (b) ψ^D_{max} (modified from Quinteros et al., 2017)

Results indicated that pre-shearing did not significantly influence the drained strength or stiffness properties of the sand. However, for dense specimens reconstituted to a relative density, D_r, of 88 %, ϕ'_{max} and ψ^D_{max} were observed to increase from approximately ϕ'_{max} = 46°, ψ^D_{max} = 21° at s' = 200 kN/m^2, to ϕ'_{max} = 52°, ψ^D_{max} = 30° at s' = 10 kN/m^2, where $s' = 0.5(\sigma'_{z,c} + \sigma'_{h,c})$, and $\sigma'_{h,c}$ is the effective horizontal consolidation stress. Similar increases in ϕ'_{max} and $\psi_{D,max}$ were observed at lower stresses for the medium dense specimens (D_r = 57 %), as shown in Figure 2.3.

Previous research on monotonic element tests undertaken at low confining stresses has tended to focus on the influence of stress level on mobilised peak shear strengths and dilatory response. Investigations into the effect of low confining stresses on the initial stiffness and the shape of the whole stress-strain curve appear to be lacking.

2.4. PREVIOUS CYCLIC TESTING STUDIES

Historically, cyclic soil element testing has been concerned with earthquake-related phenomena (e.g. liquefaction susceptibility analyses). As such, cyclic element tests have typically been conducted undrained and on relatively loose specimens. Furthermore, tests tend to adopt large cyclic stress amplitudes which lead to failure in a relatively small number of cycles. These types of cyclic tests are termed ‘low-cycle’ tests in this thesis. However, offshore wind turbine (OWT) foundations (such as monopiles) are typically subjected to large numbers of low cyclic stress amplitude load cycles over their operational lifetime (as detailed in Section 5.2.1). As such, the loading characteristics of these ‘low-cycle’ experimental programmes prevalent in the literature are likely to be unrepresentative of the types of cyclic loads sustained by marine wind energy structures. The following sections therefore focus on published examples of ‘high-cycle’ test programmes undertaken on sand, using cyclic loads that are considered more representative of the types of cyclic loads experienced by offshore wind energy foundations.

2.4.1. REALISTIC STORM LOADING

Figure 2.4, from Richards *et al.* (2019), shows realistic storm loads sustained by an OWT foundation, presented within a normalised cyclic stress space framework, based on model pile experiments performed in a wave tank at the Danish Hydraulic Institute (Bredmose *et al.*, 2016). The loads are presented in terms of average and cyclic moment loads, M_{AV} and M_{CYC}, respectively, normalised by a reference moment load, M_R.

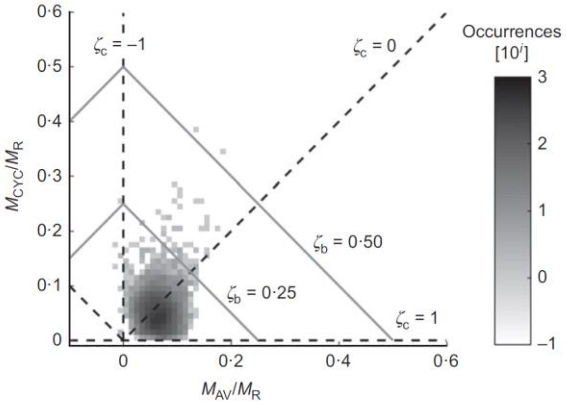

Figure 2.4: Typical moment loads sustained by an ofshore wind turbine foundation (from Richards et al., 2019)

The dimensionless cyclic loading characterisation parameters ζ_b and ζ_c , proposed by Leblanc *et al*. (2010) and detailed in Section 7.2.1, are also shown and provide a useful means of quantifying the magnitude and type of cyclic loads. Figure 2.4 shows that most of the loading occurs at $\zeta_b < 0.25$, and is either partial one-way ($0 < \zeta_c < 1$) or partial two-way ($-1 < \zeta_c < 0$), whereas the larger amplitude cycles tend to occur in partially two-way stress space. Although Figure 2.3 is formulated in terms of pile load test parameters, the framework may be extended to incorporate results of element tests (as described in Chapter 7).

2.4.2. PUBLISHED HIGH-CYCLE TEST RESULTS

Figure 2.5 shows locations in dimensionless cyclic stress space of selected testing programmes found in the literature. Results are presented in general stress terms, σ, which correspond to either moment, M, or horizontal, H, loads in pile load test studies, and deviator, q, or shear, τ, stresses in element test publications. It is readily evident from Figure 2.5 that many of the testing programmes occupy different spaces in terms of both the magnitude and type (e.g. one- or two-way) of cyclic loading. However, it must be noted that the locations of the test studies are strongly influenced by the reference stress used to normalise the results (as discussed in Section 7.2.1).

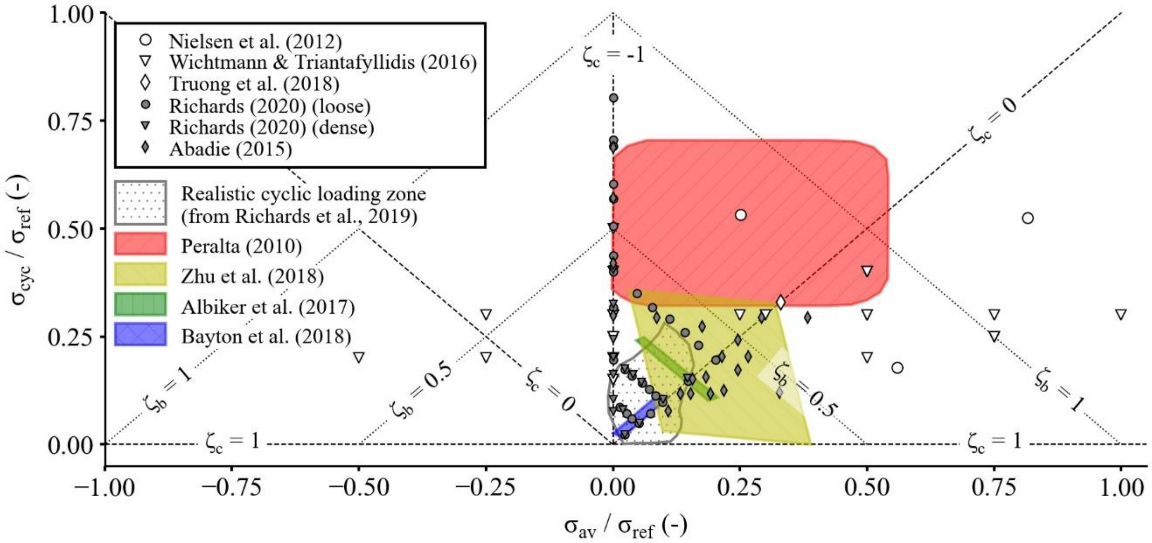

Figure 2.5 Location in cyclic stress space of selected cyclic model and element tests performed on sand

Albiker *et al*. (2017) and Bayton *et al*. (2018) undertook model pile tests at constant ζ_b and ζ_c values at low stress magnitudes which appear to sit within the realistic storm load stress space. Zhu *et al*. (2018) and Truong *et al*. (2019) modelled pile load tests in a centrifuge covering a wider range of stress magnitudes. Truong *et al*. (2019) also undertook three one-way loading cyclic triaxial tests to investigate the potential of using cyclic triaxial tests to estimate a so-called ‘accumulation coefficient’, used to predict the rotation of a pile subjected to long-term lateral cyclic loading.

Peralta (2010) and Peralta & Achmus (2010) undertook laboratory scale (1g) model pile load tests in dense to very dense dry sand, with variable load magnitudes, for 10 000 load cycles. The accumulated displacements were compared with power and logarithmic function predictions proposed by Long & Vanneste (1994) and Lin & Liao (1999), respectively. It was found that the results from flexible piles matched the logarithmic function best while the power function yielded closer agreement with the results of rigid pile tests.

Richards (2019) undertook 1g model pile tests on dry Leighton Buzzard sand (Fraction B), and observed that the rotational response for tests undertaken in very loose and dense sands were qualitatively similar. This indicated that theoretical models developed for very loose materials (e.g. Abadie, 2015) may be extended to the denser materials typically found offshore. Richards *et al*. (2019) also found pile capacities were either maintained or increased following cyclic loading, which is at odds with the idea that cyclic loading is always a damaging process.

However, Richards *et al*. (2019) note that while model test behaviour is broadly consistent with that observed under unidirectional cyclic loading at large field scale (Beuckelaers, 2017), the uncertainties associated with scaling 1g model tests means that results should not be applied directly to full scale design. Furthermore, the model pile load tests were performed in clean, dry sand and therefore behave fully drained. Peralta *et al*. (2017) showed that while this may be appropriate for modelling the response of smaller diameter piles, this may not be representative of full scale, large diameter piles which were found to exhibit partially drained to fully undrained behaviour, particularly where cohesive soil layers adjacent to sand layers were present.

Undrained cyclic element tests, undertaken with realistic cyclic load characteristics may therefore provide further insight into the behaviour of large diameter offshore wind turbine foundations subjected to long-term lateral loading. Results of such tests would also provide a more practical means of calibrating constitutive models used in routine design. However, while several high-cycle pile load test publications exist, similar high-cycle cyclic element test programmes are more limited.

Wichtmann & Triantafyllidis (2016) present results of 41 undrained cyclic triaxial tests undertaken on Karlsruhe fine sand. However, despite a variety of initial conditions and load characteristics being investigated, many of the test points shown in Figure 2.5 are located at relatively high ζ_b values that may be unrepresentative of realistic storm conditions. Nevertheless, the database of tests, that also includes oedometer, and monotonic triaxial tests, represents a valuable resource to aid the development, calibration, and verification of constitutive models capable of capturing the salient features of undrained cyclic loading. The study also highlights the inability of certain models to capture some of the features observed in the cyclic triaxial tests, e.g. no butterfly-shaped effective stress loops for isotropically consolidated tests.

The cyclic contour diagram framework (Andersen *et al*., 1988) is considered by some to represent a convenient means of predicting cyclic soil behaviour, and are often used in the front-end engineering design (FEED) stage of commercial offshore design projects. The diagrams also provide a means of estimating behaviour (for sites with similar soil conditions) when limited cyclic data are available, or in the planning stage of a cyclic laboratory test programme. However, published examples of cyclic contour diagrams developed for sand is limited (Andersen & Berre, 1999; Blaker & Andersen, 2019).

Nielsen *et al*. (2012) undertook a test programme of 17 undrained cyclic triaxial tests on dense Frederikshavn sand to simulate in situ conditions offshore, where relative densities are typically high. The aim was also to develop design (cyclic contour) diagrams, to estimate the undrained cyclic bearing capacity of Frederikshavn sand for arbitrary stress levels and cyclic loading conditions. Nielsen *et al*. (2012) found that the cyclic response was dependent on the stress path and in situ conditions; initial pore pressure, stress state and the combination of average and cyclic shear stresses. However, relatively high cyclic stress amplitudes were utilised, meaning that the tests are generally located outside the realistic storm loading zone in cyclic stress space shown in Figure 2.5.

2.5. SUMMARY AND CONCLUSIONS

Technical difficulties have long deterred investigators from attempting to capture the behavioural response of granular soils at low confining stresses. There are therefore relatively few examples of high-quality, experimental data available in the literature. Furthermore, there appear to be conflicting results with respect to the behaviour of granular media when sheared at low confining stresses. Furthermore, much of the research investigating the influence of low confining stresses has focused on the response in terms of mobilised peak shear strength and dilation angles. Investigations in to the effect of (low) stress level on the initial stiffness and the shape of the stress-strain curve also appear to be lacking.

Additional experimental testing utilising advanced, modern apparatus and techniques is therefore required to provide the experimental evidence to clarify the conflicting results published to date, and give further insight into the effect of low confining stress on the whole stress-strain response.

Cyclic element testing has historically been focussed on investigating the response of soil subjected to a relatively small number of high amplitude cyclic loads. Such tests are considered unrepresentative of the type and number of load cycles experienced by OWT foundations. While multiple laboratory scale tests investigating the performance of model piles subjected to long term cyclic loading at realistic stress magnitudes exist, examples of high-cycle, low stress amplitude cyclic element test databases are more limited.

A high-cycle cyclic element test database, undertaken with cyclic load characteristics comparable to realistic storm loads experienced by OWT foundations, is therefore required to enable more representative comparisons with 1g model pile test results. Furthermore, simulation of cyclic soil response at single element level is also an important component of constitutive model development. A new database of high-cycle cyclic element tests, undertaken at low stress amplitudes comparable to OWT loading conditions, will therefore also provide a useful tool for determining the ability of certain constitutive models to capture the important aspects of high-cycle, low amplitude loading.

3. LABORATORY TESTING OF SAND – BEST PRACTICE

3.1. INTRODUCTION

The purpose of this chapter is to review current best practices associated with the laboratory testing of sands, and also to investigate the factors most likely to influence the quality of results.

3.2. SPECIMEN SIZE

The sample size needs to be large enough to ensure that it contains a representative distribution of the particle sizes that are in the ground. To satisfy the concept of representative elementary volume, Holtz & Gibbs (1956) recommended that test specimens should be six to ten times larger than the size of the largest particle. Under this condition, it is assumed that the physical and mechanical properties of the element are essentially independent of the specimen size. However, larger samples are generally preferred when testing sand, as measurement inaccuracies (e.g. sample height, diameter) have less of an impact on the calculated initial voids ratio and density (Lade, 2016). Furthermore, when performing advanced triaxial tests with on-sample instrumentation, there is a lack of space available for attaching the instruments to specimens smaller than 70 mm diameter.

Figure 3.1 presents the influence of sample size on the results of experimental tests undertaken by several researchers, and shows that the relatively few published data tend to contradict each other. Scott (1987) performed drained triaxial compression tests on 38 mm and 100 mm diameter specimens of dense fine Leighton Buzzard sand. Results are presented in Figure 3.1a, and show the 100 mm specimens to develop higher peak strengths and initial shear stiffnesses. However, the 100 mm specimens mobilised lower post-peak shear strengths than the smaller specimens.

Figure 3.1b shows results of triaxial tests performed by Jefferies *et al*. (1990) on 36, 75, 154 and 289 mm diameter samples of Ticino sand. They noted three clear scale effects – initial modulus, volumetric strain at a given axial strain and post-peak brittleness. Unlike Scott's data which showed larger samples mobilising increased shear stiffnesses, Jefferies *et al*. (1990) observed the opposite effect, i.e. a reduction in stiffness with sample size.

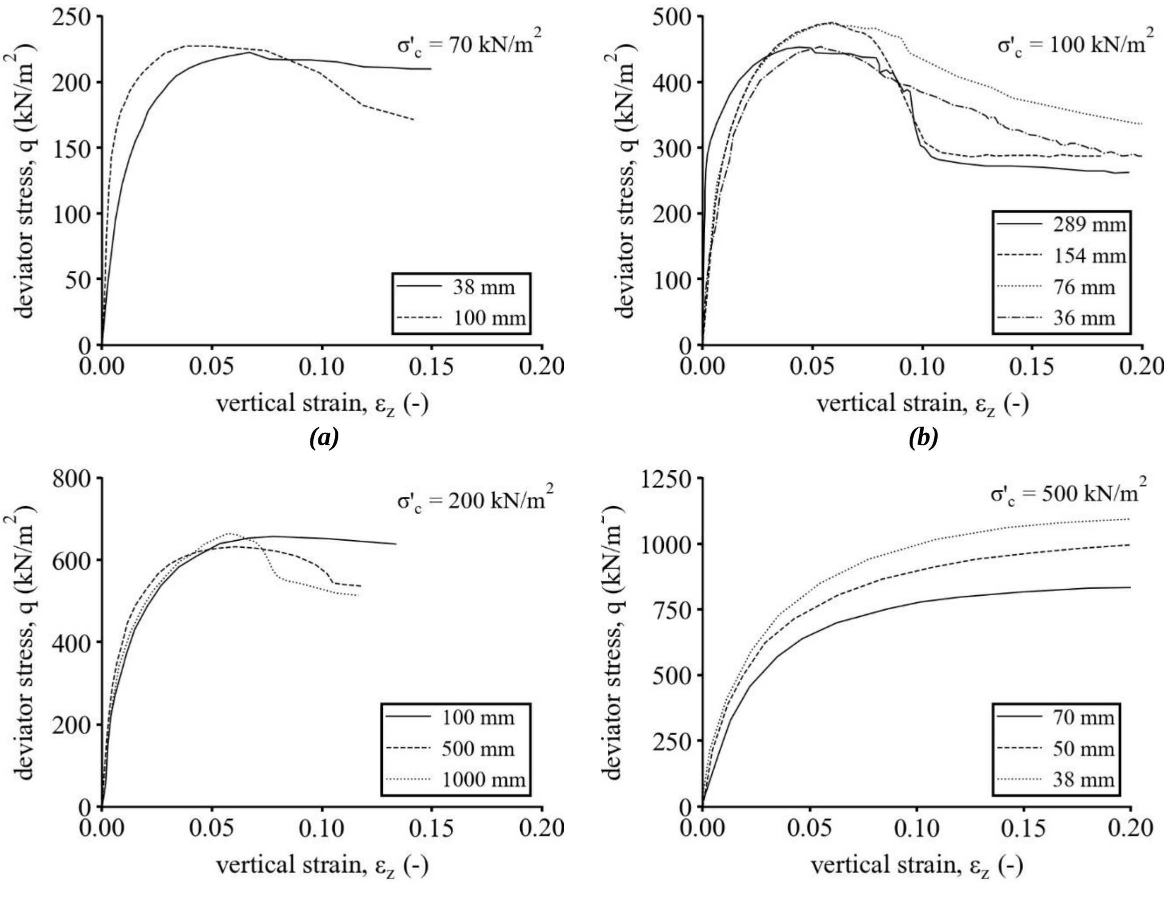

(a) (b)

(c) (d)

Figure 3.1: Influence of specimen size effects on the stress strain response of (a) fine Leighton Buzzard sand (Scott, 1987), (b) Ticino sand (Jefferies et al., 1990), (c) Loire River sand (Hu et al., 2011), and (d) Ottawa sand (Omar & Sadrekarimi, 2015)

Hu *et al*. (2011) performed a set of drained triaxial compression tests on 100, 500 and 1000 mm diameter specimens of Loire River sand (Figure 3.1c), and found that while the pre-peak behaviour was not affected, post-peak shearing mobilised smaller friction angles in the larger specimens.

Omar & Sadrekarimi (2015) undertook a comprehensive programme of isotropically consolidated triaxial compression tests on very loose 38, 50 and 70 mm diameter specimens of Ottawa sand. They observed that the larger specimens tended to be less compressible during isotropic consolidation than the smaller specimens. During shear, they found that the smaller specimens exhibited steeper critical state lines (indicative of their higher compressibility), and mobilised larger shear strengths, at both peak deviator stress and at large strains (Figure 3.1d). They concluded that the influence of sample size on the behavioural response of sands is therefore very important. To reduce specimen size effects, they recommended that the largest possible test specimens be used in triaxial testing.

Although there is little agreement in the test data of the above authors, most researchers tend to agree that it is generally better to test samples as large as is practicable. Large specimens tend to show less variability in terms of unit weights, modulus values, shear strength parameters and permeability (Lade, 2016). 100 mm diameter specimens are therefore preferred for the current study, as the larger apparatus required to perform tests on larger-diameter specimens becomes significantly more expensive. Such apparatus also require additional equipment for safe lifting of the triaxial cells.

3.3. INFLUENCE OF END RESTRAINT

For a laboratory test to be considered a true element test, the material properties measured must be virtually independent of both the dimensions of the test specimen and the test boundary conditions. Rough porous stones are often used in routine triaxial testing; however, it has long been recognised (Taylor, 1941) that such a boundary condition results in significant end restraint, leading to the formation of “dead zones” adjacent to the platens (Rowe & Barden, 1964), and the development of non-uniform stresses and strains in the sample. To minimise the effects of end restraint and stress non-uniformity, enlarged lubricated end platens should be used (Rowe & Barden, 1964).

3.3.1. ENLARGED LUBRICATED END PLATENS

The effects of end restraint can be considerably reduced by using enlarged lubricated end platens (Rowe & Barden, 1964; Bishop & Green, 1965). A typical lubricated end set-up is shown in Figure 3.2a, with systems typically involving an enlarged base pedestal and top cap with a small porous stone insert to allow drainage.

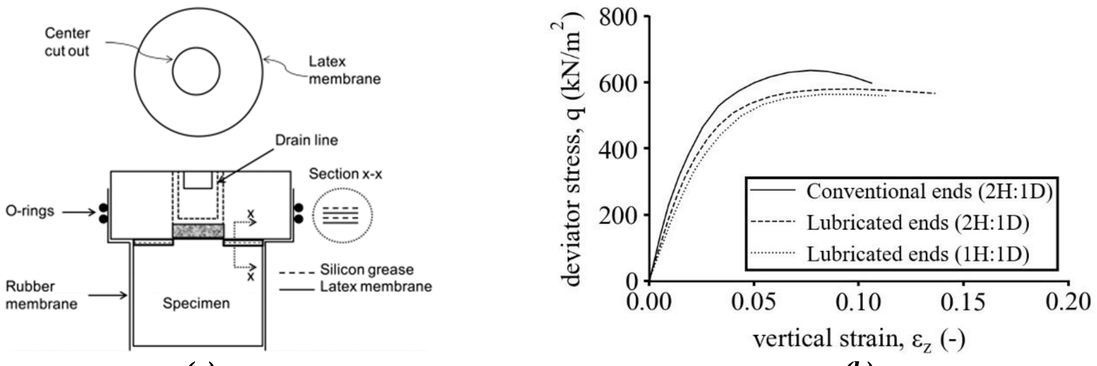

(a) *(b)*

Figure 3.2: (a) Typical enlarged lubricated end configuration (from Omar & Sadrekarimi, 2014), and (b) influence of end restraint on stress-strain response (from Raju et al., 1972)

Lubricated ends typically consist of one or two latex rubber discs, separated by a thin (c. 50 µm) layer of high-vacuum silicone grease. The latex discs are cut to the required specimen diameter with a hole cut to the size of the porous stone to allow drainage. An additional layer of high-vacuum silicone grease is also applied to the polished stainless steel end platens to provide a smooth and almost frictionless interface between the latex disc and the platen.

When subjected to compression, triaxial specimens with lubricated, or ‘free’ ends, have been shown to maintain an approximately cylindrical shape rather than barrelling, even at large strains, resulting in more uniform stress and strain distributions (Kirkpatrick *et al.*, 1974), enabling cross-sectional area corrections to be made with greater accuracy. Figure 3.2b shows results of triaxial tests undertaken by Raju *et al.* (1972) for triaxial specimens with lubricated and conventional ends, and with different H:D ratios, indicating the influence of lubricated ends on the stress-strain response.

Tatsuoka & Haibara (1985) investigated whether ‘frictionless’ ends could be obtained using just smooth end platens as opposed to a grease and latex disc configuration. The shear resistance between Toyoura sand and hard smooth surfaces of either Teflon, glass or polished stainless steel were tested and compared against a latex disc/grease setup. It was found that the smooth hard surfaces yielded similar results to each other; however, the lubrication method by means of a thin latex rubber membrane and a silicone grease layer was found to be much more effective in producing ‘frictionless’ ends. Furthermore, sand particles were found to indent themselves easily into the Teflon sheet under pressure, leading to an increase in shear resistance at the interface.

Rowe and others (Rowe & Barden, 1964; Bishop & Green, 1965; Roy & Lo, 1971) showed that a grease-coated rubber system could all but eliminate end restraint effects, thus making testing on shorter, 1:1 height to diameter ratios possible. Another advantage is that the likelihood of shear planes developing prematurely though weaker parts of the specimen is reduced.

Kuwano & Jardine (2002a) undertook a series of undrained triaxial compression tests on Ham River sand to ascertain the optimum lubricated end arrangement. They found that the best results were obtained using two membranes (each 0.3 mm thick) with high-vacuum silicone grease. Standard silicone grease was found to be insufficiently viscous and tended to ‘squeeze out’ during testing. A single 0.5 mm thick membrane was also found to provide similar results when used in some later tests. The thickness of the optimum end lubrication configuration was found to be 2.5 times the mean particle size, which was similar to the optimum arrangement suggested by Tatsuoka *et al*. (1984).

However, in addition to the extra difficulties associated with test set-up, several authors (Lee, 1978; Sarsby *et al*., 1980; Baldi *et al*., 1988; Kuwano & Jardine 2002a) have highlighted the fact that lubricated end platens introduce additional system compliance and bedding deformations, leading to errors in external measurements of volume change which must be accounted for.

3.4. LOCAL STRAIN INSTRUMENTATION

Conventional procedures for measuring sample deformations in routine triaxial testing are based on global measurements, made via transducers located external to the cell. However, it has been shown by several authors (Jardine *et al*., 1984; Tatsuoka, 1988) that this practice introduces significant errors (see Figure 3.3), and does not allow for sufficiently accurate determinations of sample deformation at small strains (i.e. at axial strains, $\varepsilon_z < 10^{-4}$). These inaccuracies can be mitigated by using local strain instrumentation.

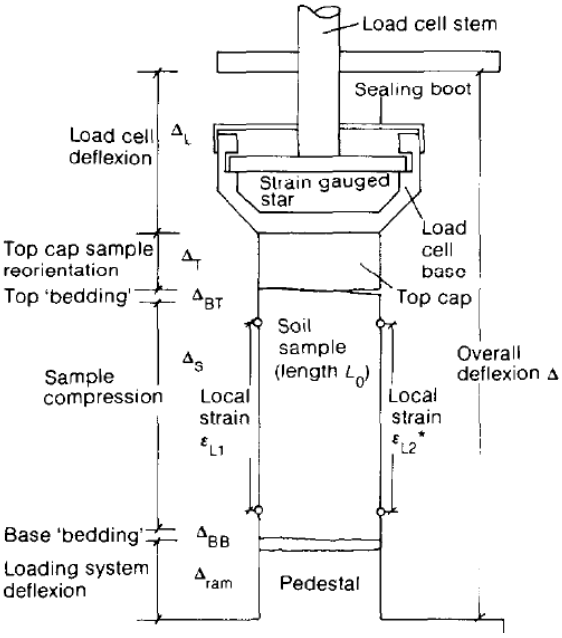

Figure 3.3: Sources of error in external strain measurements (from Jardine et al., 1984)

Several researchers have proposed devices for measuring local axial strains:

- Electrolytic liquid levels (Jardine *et al*., 1984; Ackerley *et al*., 1987);
- Hall effect strain transducers (Clayton & Khatrush, 1986; Clayton *et al*., 1989);
- Local deformation transducers, LDTs (Tatsuoka *et al*., 1990; Goto *et al*., 1991).

However, locally attached LVDTs (linear variable differential transformers), developed by Brown and his colleagues at the University of Nottingham (Brown & Snaith, 1974; Boyce & Brown, 1977;

Brown *et al*., 1980) have been found to offer a robust, reliable and highly accurate solution and are generally the preferred option in research and commercial soils testing laboratories in the UK today.

Similarly, local radial strains can be measured by placing displacement transducers into one or more horizontally-oriented callipers, secured to the specimen by two diametrically opposite mounting pads (Bishop & Henkel, 1962; El-Ruwayih, 1976). Alternative techniques such as proximity transducers (Hight *et al*., 1983; Hird & Yung, 1989) have also been developed. More recently, Ackerley *et al*. (2016) proposed a new LVDT system in which a calliper belt is no longer required, thereby overcoming many of the problems associated with such a device (i.e. weight, lack of range, etc.).

3.5. BENDER ELEMENTS

Schultheiss (1981) was the first to install bender elements in triaxial (and oedometer) cells, to estimate the small strain shear modulus, G_0. They consist of two piezoceramic plates, rigidly bonded together. The application of a voltage induces elongation in one of the plates, while the other is compressed (Ishihara, 1996). This results in a bending displacement that generates a shear wave that propagates through the sample.

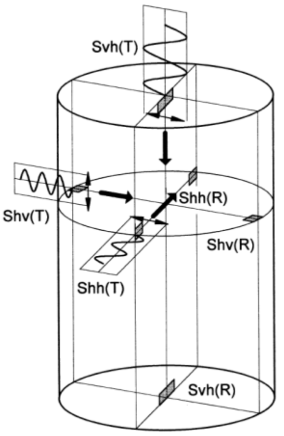

Figure 3.4: Multidirectional shear wave measurement (from Kuwano et al., 2000)

The elements are placed opposite each other, with one acting as a transmitter. When the shear wave reaches the opposite plate, it is deformed by soil movement, inducing a voltage. By measuring the time taken for the shear wave to traverse the distance between the two elements, it is possible to estimate the shear wave velocity and thus a value of the elastic shear modulus, G_0, from:

$$G_0 = \rho v_s^2 \tag{3-1}$$

where ρ is the material's bulk density, and v_s is the shear wave velocity.

Leong *et al*. (2005) and Clayton (2011) provide a good commentary on the state-of-the-art of using bender elements in geotechnical engineering, emphasising the following key factors:

- Bender element characteristics: y-poled, parallel-wired elements are more suited to transmitter elements, while x-poled, series-wired elements are more suited to receiver elements;
- Waveform: Sinusoidal waveforms are preferred as square waveforms may lead to greater ambiguity when attempting to determine arrival times;
- Applied voltage: The magnitude of the voltage applied to the transmitter element does not affect the shape or appearance of the receiver signal; however, it does increase the signal to noise ratio (SNR) of the receiver signal. The SNR may therefore be improved by increasing the voltage applied to the transmitter element with a power amplifier, and/or adopting parallel and series connections for the transmitter and receiver elements, respectively;
- Frequency: Near-field effects are quantified in terms of the ratio of the wave path length, L_{tt}, to the wavelength, λ, and affect the shape of the received signal, leading to uncertainty when determining the first arrival of the shear wave. High frequency, sinusoidal pulses are therefore recommended, such that $L_{tt}/\lambda \geq 3.33$, as this helps to ensure separation of near field coupled compression and shear waves.

The use of bender elements in a conventional triaxial test typically incorporates one pair of vertically aligned bender elements. However, granular soils have been shown to exhibit cross-anisotropic properties. Installing two additional pairs of horizontal bender elements (see Figure 3.4) enables estimates of the anisotropy of the material to be made (Kuwano & Jardine, 2002b). However, while bender element tests are generally quick and easy to perform, Alvarado & Coop (2011) caution that their interpretation is not straightforward, with several methods available.

3.6. CORRECTIONS

Triaxial testing involves procedures and measurements with many sources of error. It may therefore be necessary to apply corrections to all measured quantities, unless measures (such as the use of local strain instrumentation) are taken to avoid the experimental problems that require corrections. The following sections review the various corrections that have been proposed in the literature.

3.6.1. MEMBRANE RESISTANCE

Lade (2016) provides a comprehensive review of the various expressions proposed by researchers for corrections to the stresses acting on a triaxial specimen due to the rubber membrane (e.g. Duncan & Seed, 1967; Fukushima & Tatsuoka, 1984; Henkel & Gilbert, 1952). Ponce & Bell (1971) emphasised the importance of correcting for membrane resistance when testing at low stresses, and gave the following equations for the axial and radial membrane corrections:

$$\sigma_{z(corr)} = \sigma_z + \sigma_{z,m}; \text{ and } \sigma_{r(corr)} = \sigma_r + \sigma_{r,m} \tag{3-2}$$

$$\sigma_{z,m} = -\left[\frac{2}{3}E_m\left(1 + 2\varepsilon_z - \sqrt{\frac{1-\varepsilon_p}{1-\varepsilon_z}}\right) + \sigma_r\right]\frac{4t_{m,0}}{D_0(1-\varepsilon_p)} \tag{3-3}$$

$$\sigma_{r,m} = -\left[\frac{2}{3}E_m\left(2 + 2\varepsilon_z - 2\left(\sqrt{\frac{1-\varepsilon_p}{1-\varepsilon_z}}\right)\right) + \sigma_r\right]\frac{2t_{m,0}}{D_0(1-\varepsilon_p)} \tag{3-4}$$

where:

$\sigma_{z,m}$ = membrane correction to be applied to the vertical stress
$\sigma_{r,m}$ = membrane correction to be applied to the radial stress
ε_z = vertical strain
ε_p = volumetric strain
E_m = modulus of elasticity of the rubber membrane
$t_{m,0}$ = initial thickness of the rubber membrane
D_0 = initial diameter of the specimen

3.6.2. VOLUME CHANGE DUE TO MEMBRANE PENETRATION

Penetration of the rubber membrane enclosing the triaxial specimen into the voids between the particles in granular soils causes spurious volume changes in tests with changing effective confining stresses (Lade, 2016), as illustrated in Figure 3.5. Predicting the magnitude of membrane penetration and the factors that influence it has been extensively researched over the years.

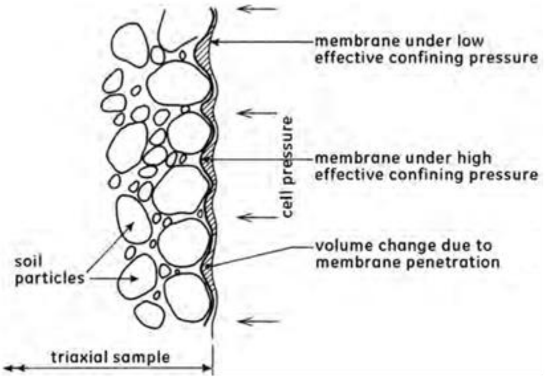

Figure 3.5: Membrane penetration effect in granular soils (from Head & Epps, 2014)

Nicholson *et al*. (1993) and Ali *et al*. (1995) provide reviews of previous membrane compliance evaluation methods. To summarise, membrane compliance evaluation methods have typically been investigated either experimentally (e.g. Frydman *et al*., 1973; Newland & Allely, 1957, 1959; Roscoe *et al*., 1963; Vaid & Negussey, 1984a), or theoretically (e.g. Baldi & Nova, 1984; Kramer *et al*., 1990; Molenkamp & Luger, 1981). The concepts of unit membrane compliance and normalised membrane penetration proposed by Frydman *et al*. (1973) represent an important contribution, and it is now well established that there is an essentially linear relationship between the membrane-induced volume change and applied effective stress when plotted on a semi-logarithmic scale.

Nicholson *et al*. (1993) also investigated the factors that influence membrane compliance effects during undrained triaxial tests. In agreement with previous investigations, they concluded that soil grain size, specimen geometry, specimen density and the range of applied effective confining stresses were the most significant contributing factors. They found that the following factors were observed to have only minor effects on membrane compliance:

- sample particle angularity;
- sample fabric or method of preparation;
- sample density;
- membrane thickness or stiffness (within reasonable limits depending on relative ratio of particle size to membrane thickness).

Regarding sample density, concurring with several other previous studies, they found only minor effects on membrane compliance; however, they cautioned that membrane penetration may become more significant for very loose or very dense soils. Regarding particle size, they found that membrane compliance effects may be negligible for fine sands and silts tested in conventional 71 mm diameter samples, as even when very thin membranes are used, they cannot penetrate significantly into the small surficial voids. However, medium to coarse sands and gravels are likely to have significant membrane compliance effects.

Contrary to the work of some researchers (e.g. Molenkamp & Luger, 1981; Baldi & Nova, 1984), who derived analytical formulas for unit membrane penetration as a function of both membrane thickness and stiffness, Nicholson *et al*. (1993) found that using different thicknesses and numbers of membranes had little or no influence on unit membrane compliance. They also found that while previous researchers had consistently correlated membrane compliance magnitudes with median particle size, d_{50}, their results showed that for non-uniformly graded soils, an improved correlation could be achieved if correlated against the smaller particle size, d_{20}.

However, according to Jefferies & Been (2015), for all practical purposes, the membrane penetration can be quantified in terms of the normalised membrane penetration, ε_m. Values of ε_m may be determined from Figure 3.6. The volume change associated with membrane penetration can then be calculated for a given sample area and change in net pressure from:

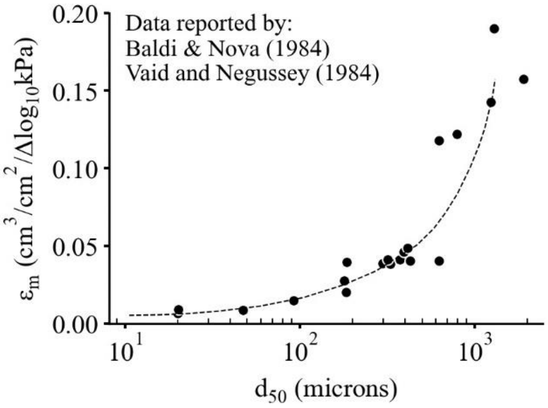

Figure 3.6: Normalized membrane penetration coefficient as a function of median grain size (from Jefferies & Been, 2015)

$$\varepsilon_m = \frac{\Delta V_m}{A_m \log(p_1'/p_2')} \tag{3-5}$$

where:

ΔV_m = sample volume change due to membrane penetration
A_m = sample area covered by the membrane
p_1', p_2' = net pressure acting across the membrane before and after the volume change

3.6.3. VOLUME CHANGE DUE TO BEDDING ERRORS

The externally measured vertical deformation is influenced by the bedding errors associated with lubricated ends (Sarsby *et al*., 1980). Vertical deformation may be measured error-free by using local strain measurement devices (see Section 3.4) However, the high resolution of these components means that they are only able to operate over a limited displacement range (±5 mm is common). Corrected global measurements are thus still important when considering behaviour at large strains. Molenkamp & Tatsuoka (1983) analysed the bedding errors in terms of dimensionless quantities, and divided them into reversible and irreversible components:

Reversible:
$$\frac{\Delta\alpha}{d_{50}} = \left(0.68 + 0.51\exp\left(-2\frac{t}{d_{50}}\right)\right)\left(\frac{\sigma_n}{E_m}\right)^{2/3} \tag{3-6}$$

Irreversible:
$$\frac{\Delta_{\mathrm{BE}}}{d_{50}} = \left(0.221\left(\frac{t}{d_{50}}\right)^{0.3} - 0.126\left(\frac{t}{d_{50}}\right)^{0.25}\right)\log\left(\frac{\sigma_n}{E_m}\right) + f\left(\frac{t}{d_{50}}\right) \tag{3-7}$$

where:

$\Delta\alpha$ = conventional membrane penetration
t/d_{50} = ratio of thickness of latex rubber disc, t, and mean grain size, d_{50}
σ_n/E_m = ratio of normal stress, σ_n, and Young's modulus of latex rubber, E_m
Δ_{BE}/d_{50} = ratio of bedding error, Δ_{BE}, and mean grain size, d_{50}

3.6.4. AREA CORRECTION FOR SPECIMEN DEFORMATION

The vertical stress in a triaxial specimen is computed by dividing the force measured in the load cell by the cross-sectional area at the mid-height of the specimen. It is conventionally assumed that a triaxial specimen deforms as a right cylinder during triaxial compression (La Rochelle *et al*., 1988), with constant diameter over its full height, where:

$$A_{corr} = A_{f,c}\frac{(1-\varepsilon_p)}{(1-\varepsilon_z)} \tag{3-8}$$

where:

A_{corr} = corrected cross-sectional area of the specimen
$A_{f,c}$ = cross-sectional area of the specimen at end of consolidation/creep stage

BS 1377-8 (BSI, 1990) and ASTM D4767 (ASTM, 2011) recommend this approach when analysing triaxial compression test data. However, end restraint at the platens can cause bulging, or barrelling at the mid-height of the specimen at large compressive axial strains, resulting in non-uniform vertical, lateral, and volumetric strain (and stress) distributions inside the sample. This bulging leads to errors when calculating the deviator stress, and subsequent estimates of the material’s shear strength parameters. The deformed shape may be better approximated as a parabola, where the cross sectional area at the mid-height of the specimen can be estimated from (Omar & Sadrekarimi, 2014):

$$A_{corr} = \left[-0.25 + \frac{\sqrt{(25-20\varepsilon_z-5\varepsilon_z^2)}}{4(1-\varepsilon_z)}\right]^2 \tag{3-9}$$

In this work, the area correction described by Zhang & Garga (1997) is adopted. They measured the deformation profile of sand specimens during triaxial compression tests utilising lubricated ends (section 3.3.1). They also assumed the soil specimen to deform as a parabola; however, their area correction is based on the average specimen diameter over the middle third, which may be measured with good accuracy from local radial strain instrumentation:

$$D_{max} = \frac{D_0}{4}\left[\left(\frac{30(1-\varepsilon_p)}{(1-\varepsilon_z)}-5\right)^{1/2}-1\right] \tag{3-10}$$

$$D_{1/3} = D_{max} - \frac{1}{12}(D_{max}-D_0) \tag{3-11}$$

where:

D_{max} = maximum diameter assumed to mobilise at the mid-height of the specimen
$D_{1/3}$ = corrected average diameter used in the calculation of deviator stress

3.6.5. SELF-WEIGHT OF THE SPECIMEN

The vertical stresses due to the weight of the specimen, $\sigma'_{z,sw}$, may be a significant contribution to the stresses inducing failure when testing at low confining stress (Ponce & Bell, 1971), where:

$$\sigma'_{z,sw} = z\gamma' \tag{3-12}$$

where:

z = the depth from the top of the specimen to a given level (i.e. mid-height)
γ' = effective unit weight of the specimen material

3.7. SAMPLE RECONSTITUTION TECHNIQUES

Due to the difficulty and relative expense associated with obtaining high-quality, 'undisturbed' samples of sand, performing laboratory tests on reconstituted specimens from disturbed samples has become standard practice. The effect of sample preparation on a material's fabric and stress-strain behaviour has been the subject of much research for many years (Been *et al*., 1991; Høeg *et al*., 2000; Ladd, 1977; Vaid *et al*., 1999).

The main aim in preparing test samples for laboratory testing is to produce a reconstituted specimen that reflects the in situ properties of the material (Rad & Tumay, 1987). According to Oda *et al*. (1978), the anisotropic orientation of particles in naturally deposited sands may be simulated by adopting a suitable method in the laboratory. However, some researchers (Jefferies & Been, 2015) question whether samples prepared in laboratories are able to accurately mimic the fabric and anisotropies developed in often turbulent depositional environments.

While there are several widely accepted sample preparation methods for sands, no industry standard method has been established to date. This has led to research and commercial testing laboratories developing their own methods, resulting in differences in preparation detail between institutions. This can lead to problems as different methods create different fabrics and anisotropies within the sample, influencing the mechanical response of the specimen under loading (Been *et al*., 1991).

3.7.1. MOIST TAMPING AND LADD'S UNDERCOMPACTION METHOD

The moist tamping method consists of measuring five or six equal portions of pre-weighed, oven-dried sand, that are then mixed with de-aired water to a target water content of approximately 5 %.

Each portion of the slightly moist sand is then deposited into a sample former and compacted, or 'tamped' to a predetermined height in five to six equal lifts.

Ladd (1978) modified this method, calling it the "undercompaction" technique, in an attempt to minimise the shortcomings associated with the traditional moist tamping technique and wet pluviation methods (i.e. segregation of fines and sample non-uniformities). Ladd's method differs in that each layer is typically compacted to a lower density than the final desired value; however, as each successive layer is deposited and compacted, additional densification occurs in the underlying sand, leading to better homogeneity across the sample. Table 3.1 summarises the key advantages and disadvantages associated with moist tamping methods.

Table 3.1: Advantages and disadvantages associated with moist tamping techniques

Moist tamping techniques	
Advantages	**Disadvantages**
• Able to produce specimens encompassing a wide range of relative densities (i.e. from very loose to very dense); • Quick and (relatively) easy to prepare a sample; • Capillary forces give the specimen strength, enabling it to stand unsupported on triaxial base pedestals (i.e. split mould sample formers and vacuum lines are not required).	• Compactive effort required to obtain very dense samples may crush sand particles; • Non-uniform density throughout specimen (lower layers become more densified than upper layers); - Ladd's undercompaction method largely rectifies this issue; • Unnatural soil fabric created; • Creates a 'honeycomb' type structure, susceptible to collapse. • Specimens are not fully saturated.

3.7.2. DRY PLUVIATION

The dry pluviation technique is a common and reliable technique used to obtain uniform specimens in clean sands. The technique may be considered analogous to the natural deposition of wind-blown Aeolian deposits, which generally consist of either well-sorted sand or silt (Kuerbis & Vaid, 1988). A wide range of relative densities can be achieved ($D_r \approx$ 30 to 70 %) by controlling the drop height and pouring rate; however, careful control of the drop height is required to obtain uniform samples.

Rad & Tumay (1987) give a detailed assessment of the technique and the factors which affect the final density. The technique requires more sophisticated equipment than the moist tamping or wet pluviation method, and thus a number variants of the method have been developed (e.g. Bishop & Henkel, 1962; Tatsuoka *et al*., 1986). Conflicting views on the effects of drop height on the relative density of samples prepared by air pluviation techniques have been proposed (Miura & Toki, 1982; Tatsuoka *et al*., 1982). Vaid & Negussey (1984) study the topic in detail, and provide theoretical and experimental evidence supporting the idea that the density of air pluviated samples is highly dependent on the drop height. Table 3.2 summarises the key advantages and disadvantages associated with dry pluviation method.

Table 3.2: Advantages and disadvantages associated with the dry pluviation technique

Dry pluviation techniques	
Advantages	**Disadvantages**
• Able to prepare uniform specimens in clean sands (if drop height is carefully controlled); • Sample preparation is very quick.	• Very loose and loose specimens difficult to achieve; • Sophisticated equipment is required to ensure constant drop height, volume flow rate etc. • Unsuitable for sand containing plastic fines • Oven drying process can coagulate the fines, leading to non-uniformities within the specimen; • Specimens require subsequent saturation.

3.7.3. WET PLUVIATION (WATER SEDIMENTATION)

The wet pluviation method is attractive, as the technique may be considered analogous to the underwater depositional processes that occur in natural seabed or river environments. Some researchers have therefore suggested that samples prepared using this technique may have similar fabrics and anisotropy to natural sands found in situ (Oda *et al*., 1978; Vaid *et al*., 1999). Ghionna & Porcino (2006) tested this theory, and found that wet pluviated samples were able to capture the behaviour exhibited by undisturbed frozen samples. They concluded that such samples closely replicate the in situ fabric of marine deposits, and allow the substitution of expensive undisturbed samples with their reconstituted counterparts.

There are several variations in the methodologies proposed by researchers and testing laboratories (e.g. Bishop & Henkel, 1962; Ishihara, 1993; Vaid & Negussey, 1988). The wet pluviation method may produce samples of relatively loose densities ($D_r \approx 30\ \%$). However, higher relative density specimens can also be achieved with additional vibratory effort.

Kuerbis & Vaid (1988) and Ladd (1978) suggest that the method is less suitable for well graded or silty sands, as segregation of particles can occur during pluviation which may lead to non-uniform specimens. Jefferies & Been (2015) also state that the wet pluviation technique often results in an approximate loss of fines of about 50 %. Accounting for this fines loss should therefore be considered when performing the target density and dry mass calculations. Table 3.3 summarises the key advantages and disadvantages associated with wet pluviation method.

Table 3.3: Advantages and disadvantages associated with the wet pluviation technique

Wet pluviation techniques	
Advantages	**Disadvantages**
• Able to prepare uniform specimens in clean sands; • Able to prepare specimens covering a wide spectrum of relative densities (D_r = 40 – 90 %); • May be considered analogous to underwater depositional process; • Specimens are prepared with a high initial degree of saturation.	• Very loose specimens (D_r < 40 %) difficult to achieve; • Longer preparation time than other methods; • Loss and segregation of fines can occur during pluviation; • Loose zone can develop at the top surface if left unconfined during densification.

3.7.4. SLURRY DEPOSITION

Kuerbis & Vaid (1988), and more recently Carraro & Prezzi (2008) proposed a new sample preparation technique in an attempt to overcome some of the problems associated with the methods described above – particularly the problem of particle segregation in poorly graded or silty sand samples. The method may be considered analogous to sands deposited in natural fluvial environments or as hydraulic fill. Wood *et al*. (2008) further modified the method to accommodate different sized specimens, as well as enlarged lubricated end platens. Advantages and disadvantages of the method are summarised in Table 3.4.

Table 3.4: Advantages and disadvantages associated with the slurry deposition technique

Slurry deposition techniques	
Advantages	**Disadvantages**
• Able to prepare homogenous specimens of sand containing fines; • Specimens are prepared with a high initial degree of saturation; • The typical stress-strain response of the specimens resembles that of natural underwater soil deposits.	• More sophisticated equipment is required; • Very loose specimens (D_r < 40 %) difficult to achieve.

3.7.5. REVIEW OF RECONSTITUTION TECHNIQUES

Several researchers have suggested that the moist tamping method is unrepresentative of natural sand deposition and results in non-uniform samples that have a fabric or structure dissimilar to that produced in nature (Castro, 1969; Castro *et al*., 1982). The wet pluviation method is the preferred technique of several researchers (Andersen, 2015; Vaid *et al*., 1999) and is capable of producing specimens to a wide spectrum of densities. However, the technique is less suitable for soils containing a significant percentage of fines, or when very low target densities are required.

The slurry deposition method provides a feasible solution to these shortcomings. The method is similar to wet pluviation in that the process may be considered analogous to some natural depositional environments, and may overcome the inherent problems associated with wet pluviation (and other techniques), in that homogenous samples can be obtained in silty or well-graded sand. Furthermore, the method recently proposed by Dominguez-Quintans *et al*. (2019) reports to overcome the potential shortcomings associated with preparation of very loose (D_r < 30 %) and very dense specimens (D_r > 80 %). However, the method fails to incorporate enlarged lubricated end platens which are considered critically important when testing sands in triaxial apparatus.

In this work, all tests were performed on a clean, uniform-graded, silica sand (described in Section 4.6). The wet pluviation technique was therefore considered suitable and used to prepare the very dense specimens ($D_r \approx$ 83 %) tested in Chapters 6 and 7. A full description of the modified wet pluviation technique developed as part of this study is given in Section 4.7. For tests requiring very loose specimens (i.e. the constitutive model calibration tests described in Chapter 8), a variant of Ladd’s undercompaction technique was used (as described by Jefferies & Been, 2015).

However, as shown by Jones *et al*. (2020) and Blaker & Andersen (2015), natural North Sea sands can contain a significant portion of fines. It is therefore recognised that wet pluviation methods are unlikely to be suitable for use in commercial laboratory testing projects. Further effort to reduce and/or replace commercial testing laboratory’s reliance on moist tamping techniques with the more versatile slurry deposition techniques is therefore recommended.

4. EQUIPMENT AND METHODOLOGY

4.1. INTRODUCTION

The purpose of this chapter is first to describe the testing apparatus (including ancillary equipment) and instrumentation used in this study, together with details of the adopted calibration procedures. Secondly, the test material is introduced along with results of index tests. Thirdly, the sample preparation techniques and test methodologies are described. Finally, data reduction procedures including adopted corrections are presented.

4.2. STRESS PATH TRIAXIAL APPARATUS

All of the monotonic triaxial tests presented in this thesis were undertaken using a TriScan-100 Pro stress path triaxial apparatus supplied and manufactured by VJ Tech, shown in Figure 4.1.

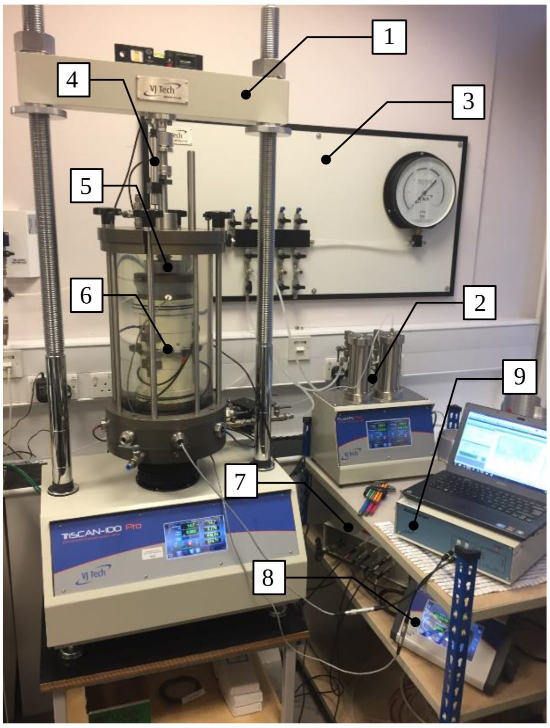

Key:
1. 100 kN load frame and base unit
2. Dual cell / back automatic pressure controller
3. De-aired water distribution panel
4. External 50mm LSCT
5. Internal submersible load cell
6. On-sample LVDTs
7. Local LVDT signal conditioning unit
8. Data acquisition unit (for local LVDTs)
9. Bender element apparatus

Figure 4.1: TriScan-100 Pro stress path triaxial apparatus

The apparatus, including all instrumentation, plumbing fittings and ancillary equipment, was specified, acquired, and commissioned specifically for this research project. The apparatus consists of the following elements:

4.2.1. LOADING SYSTEM

The TriScan-100 Pro's loading system consists of a 100 kN capacity load frame, and a stepper motor mounted within the base unit. The stepper motor provides computer-controlled, motorised actuation of load, has a stroke of approximately 100 mm, and is able to move at speeds up to 50.8 mm per minute. Axial load is applied to the test specimen via a load ram which, once connected to the specimen top cap, is carefully screwed into the upper horizontal cross beam.

4.2.2. DATA ACQUISITION AND CONTROL SYSTEM

The base unit of the TriScan-100 Pro contains five analogue and one digital channel inputs and uses high speed sensor data conversion (24 bit, up to 4000 samples per second). More channels were provided by a six channel (five analogue, one digital) data logger (MiniScanner Pro, supplied and manufactured by VJ Tech), with similar speed and sampling capabilities to the TriScan-100 Pro.

The load frame utilises a closed-loop control system, and is capable of both load and displacement control. Tests are automated and controlled using VJ Tech's proprietary modular software 'Clisp Studio'. However, during the commissioning process, it was found that the standard triaxial testing software modules (csTriax and csStressPath) were extremely restrictive in that they do not permit any deviation from the standard 'commercial' type triaxial test procedures, and thus leave little scope for the level of test customisation required for research testing. To overcome this issue, a bespoke test plan was created for use with the csHostAdvanced module, enabling complete control of the instruments, data collection, and parameter calculation, as well as the number and type of test stages, and associated automation start/stop triggers.

4.2.3. TRIAXIAL CELL

The triaxial cell is fabricated from hard anodised aluminium, with a transparent acrylic chamber. It measures approximately 410 x 230 mm, allows specimen sizes of up to 100 mm diameter by 200 mm high to be tested, and is rated up to a safe working pressure of 2000 kN/m^2. The top plate includes a sealed brass linear bushing through which runs a stainless steel low friction piston, an air-bleed screw for de-airing, and an additional exit port for use with suction-type top platens. To improve handling and manoeuvrability, the cell is split into three components (base, chamber and top plate), which are secured together and sealed using four external strain rods. The base unit incorporates an eight port ‘access ring’ through which instrumentation cabling may be passed.

4.2.4. FORCE TRANSDUCER

A 5 kN capacity internal submersible load cell (ISLC) was used in the majority of monotonic tests presented in this thesis. However, the large diameter (and associated area), and high relative densities adopted in this study, resulted in the 5 kN ISLC capacity being exceeded in drained tests undertaken even at relatively modest effective confining stresses (e.g. $\sigma_c' \geq$ 100 kN/m^2). 10 kN ISLCs were therefore also used when necessary. The ISLCs are manufactured by Applied Measurements Ltd, and are based on the design of Dr. A.E. Skinner at Imperial College (Bishop *et al.*, 1975). The ISLCs were calibrated against reference load cells (5 kN and 10 kN capacity), and were calibrated approximately every six months to an accuracy of $\pm$1 N.

4.2.5. AUTOMATIC PRESSURE CONTROLLER WITH VOLUME CHANGE MEASUREMENT

Cell and back pressures were measured and/or controlled via a dual cylinder Automatic Pressure Controller (APC), manufactured and supplied by VJ Tech. The unit provides two independent channels with pressure and volume feedback and control, and incorporates high speed sensor conversion (24 bit, 4000 samples per second). Cell and back pressure is applied via computer-controlled stepper motors. Pressures are measured via independent external 3500 kN/m^2 pressure transducers, with accuracies of 0.15 % FRO (full range output), and a resolution of 0.1 kN/m^2. Each cylinder has a volume capacity of 250 cm^3, an accuracy of 0.25 % FRO, and a 0.001 cm^3 resolution.

4.2.6. PRESSURE TRANSDUCERS

Specimen pore water pressures were measured via pressure transducers located immediately outside the triaxial cell, connected in series with the specimen top cap and base platen drainage lines. Low capacity (e.g. 1000 kN/m^2) transducers were adopted whenever possible so as to improve the reliability of measurements. High-accuracy transducers (<0.15 % FRO), supplied by VJ Tech, were used in all tests, and were periodically calibrated (every six months) and checked against a known reference device to an accuracy of ±1 kN/m^2.

4.2.7. DISPLACEMENT TRANSDUCERS

Large axial strains (e.g. $\varepsilon_z \geq 35$ %) were mobilised during the monotonic stress path tests. A 100 mm LVDT (linear variable differential transformer) was therefore used to measure displacements and ensure displacement travel capacities were not prematurely exceeded. The LVDT was sourced from departmental stock and exact specifications are unknown. The transducer was calibrated using a comparator stand and ceramic gauge blocks (Grade 0) manufactured by Mitutoyo, following the procedure described in Head & Epps (2011).

4.2.8. ON-SAMPLE SMALL-STRAIN SYSTEM

Up to four submersible LVDTs (two vertical and two radial) were used as part of the on-sample, small-strain measurement system. The LVDTs were manufactured by the RPD Group (Model no: D5/200WRA/429), and supplied by VJ Tech. All LVDTs have a travel capacity of ±5 mm, and an output resolution of ±0.001 mm. The LVDTs were powered and conditioned via a signal conditioning unit supplied by VJ Tech, and logged using the MiniScanner Pro data acquisition unit.

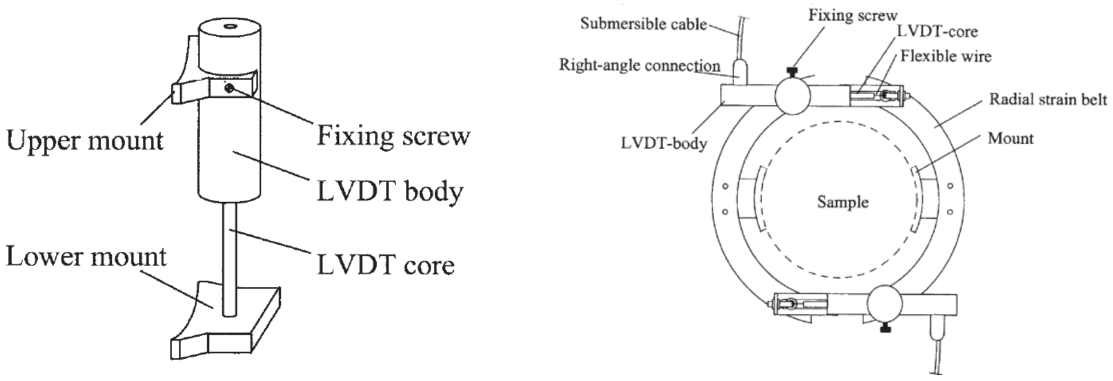

(a) *(b)*

Figure 4.2: (a) axial LVDT setup; and (b) radial LVDT calliper (from Klotz & Coop, 2002)

Axial LVDTs were affixed to the sample using brackets similar to those presented in Figure 4.2a, while radial LVDTs were mounted in a radial calliper. During commissioning tests, use of the radial calliper supplied by VJ Tech resulted in the radial LVDT’s displacement capacity being exceeded even after mobilisation of relatively small axial strains. To extend the range of local strains that could be measured, a prototype radial calliper utilising two radial LVDTs (similar to the design given by Klotz & Coop (2002), see Figure 4.2b) was developed.

4.3. CYCLIC TRIAXIAL APPARATUS

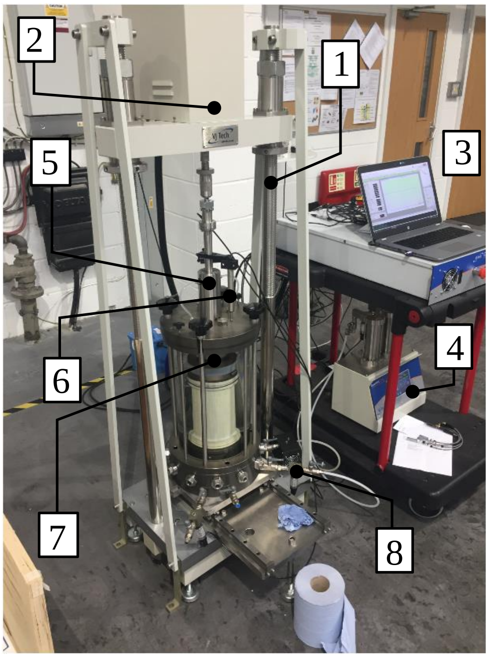

Key:

1. 100 kN load frame and base unit
2. Electro-mechanical dynamic actuator
3. Dynamic servo controller (DSC-3000)
4. Dual automatic pressure controllers
5. Balanced ram
6. External 50 mm LSCT
7. Internal submersible load cell
8. Pore pressure transducer

Figure 4.3: Cyclic triaxial apparatus

4.3.1. LOADING SYSTEM

The cyclic triaxial apparatus' loading system comprises a 100 kN capacity load frame, with a beam-mounted electro-mechanical screw drive dynamic actuator. The dynamic actuator provides computer-controlled, motorised actuation of load, has a stroke of approximately 100 mm, and may operate at frequencies of up to 10 Hz. Axial load is applied to the test specimen via a load ram which, once connected to the specimen top cap, is carefully screwed in to the actuator.

4.3.2. DATA ACQUISITION AND CONTROL SYSTEM

The dynamic servo controller (DSC-3000) provides PID (proportional-integral-derivative) closed loop control of the electro-mechanical screw drive dynamic actuator and incorporates adaptive peak and trough control. The 24 bit controller is able to apply both user-defined and typical cyclic load waveforms (e.g. square, sinusoidal, sawtooth etc.). Eight analogue input channels are available, with in-built signal amplification, conditioning and logging capabilities (up to 500 samples per second).

4.3.3. TRIAXIAL CELL

The triaxial cell used in the cyclic triaxial apparatus is similar to that used in the stress path apparatus. However, the cyclic cell differs in that it incorporates a 'balanced ram', specified such that the movement of the load ram into and out of the cell during cyclic shearing stages results in only minor cell pressure changes. The balanced ram therefore eliminates the need for additional (and expensive) pneumatic cell pressure controllers, and the hazardous air gaps that are typically required with cyclic triaxial systems. The performance of the balanced ram was assessed during commissioning tests, with typical cell pressure fluctuations of less than ±0.5 kN/m^2 being observed.

4.3.4. AUTOMATIC PRESSURE CONTROLLER WITH VOLUME CHANGE MEASUREMENT

A dual APC for cell and back pressure control and volume change measurement, similar to that described for the stress path triaxial apparatus (see Section 4.2), was used in all cyclic tests.

4.3.5. INSTRUMENTATION

Similar instrumentation (e.g. internal load cells, pressure and external/local displacement transducers) to that described for the stress path triaxial apparatus (see Section 4.2) was used with the cyclic triaxial apparatus and so the description is not repeated here.

4.4. BENDER ELEMENT APPARATUS

The bender element testing system was supplied by VJ Tech and comprises a single bender element interface unit, incorporating a function generator, oscilloscope and signal amplification and filtering. The system is controlled from a laptop with VJ Tech's software 'csBender', and allows for sinusoidal, square or triangular waveforms, pulse frequencies of 0.1 to 50 kHz, and amplitudes of 1 to 12 Volts. The bender elements (also supplied by VJ Tech) utilise both x- and y- polarised configurations, and were installed in the base (receiver) and top (transmitter) platens, respectively, following the recommendations of Leong *et al*. (2005).

4.5. ANCILLARY EQUIPMENT

4.5.1. PLUMBING CONNECTIONS AND TUBING

High quality, stainless steel twin ferrule compression fittings (e.g. Parker A-Lok fittings) were used for all critical external plumbing. 8 x 6 mm (outer x inner diameter) advanced polyamide semi-rigid nylon tubing (manufactured by Parker Legris) was used to connect the APC cell pressure cylinder to the triaxial cell. The tubing was selected due its durability and thermal/mechanical properties. Smaller, 3 x 1.8 mm diameter tubing was used for the back pressure drainage lines to reduce tube expansion, and improve the accuracy of volume change measurements.

4.5.2. DE-AIRED WATER SUPPLY

De-aired water was used as the cell fluid in all tests, and was produced in the laboratory using a de-aired water system supplied by Controls Group (previously Wykeham Farrance). The system consists of a 23 l water reservoir, a vacuum pump with air-drying unit, and a valve panel. De-aired water was obtained by filling the water reservoir with mains tap water, and subsequently applying a vacuum to the tank for at least 45 minutes. The water reservoir was installed close to ceiling height, allowing the triaxial cells to be supplied with de-aired water under gravity.

4.5.3. ENLARGED LUBRICATED END PLATENS

Enlarged lubricated end platens were designed and manufactured for use with the stress path and cyclic triaxial apparatus. Both platens incorporated a 38 mm OD annular sintered bronze (grade C) disc to allow drainage, and vertical bender elements. The lubricated ends were provided by two c. 0.35 mm thick latex discs, separated by a thin layer of Dow Corning high-vacuum silicone grease. The lower latex discs also included circumferential cuts to facilitate lateral expansion during shear.

Figure 4.4 shows a sketch of the enlarged lubricated top cap. To minimise the weight acting on the specimen, the top caps were fabricated from acrylic. The top platens were connected to the ISLC via an M10 threaded connection, tapped into a stainless steel plate secured to the top cap body via four allen-head bolts. A suction type connection similar to that developed by Skinner (Atkinson & Evans, 1985) is also possible and was adopted in early commissioning tests. However, the procedure for connecting the suction cap to the load cell was found to be extremely problematic. This connection method was therefore unfortunately abandoned in favour of a screwed connection. Further research into the use and in-house manufacture of vylastic sleeves is therefore recommended.

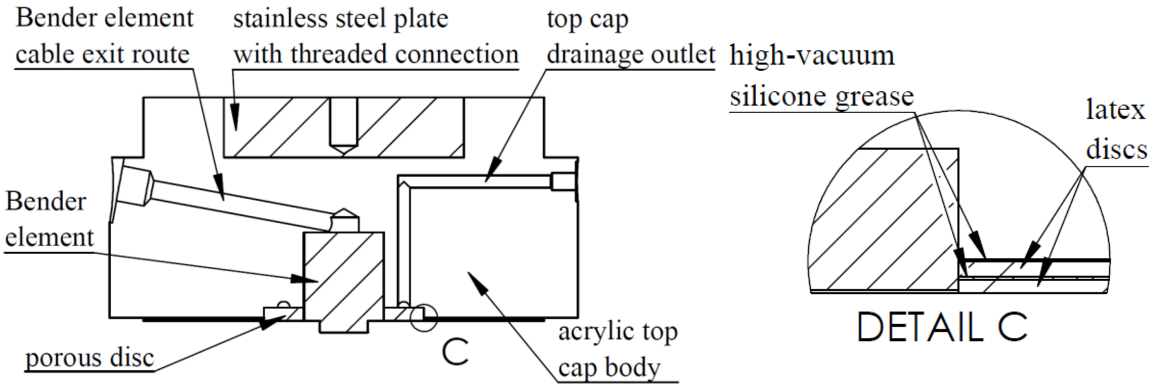

Figure 4.4: Sketch of enlarged lubricated top platen used with the triaxial apparatus

4.5.4. WET PLUVIATION APPARATUS

A new two-part split-mould sample former assembly was designed and manufactured to facilitate preparation of wet pluviated samples. It was necessary to design a new split-mould sample former, as 'off the shelf' split formers are typically incompatible with enlarged end platens. The various components making up the assembly are shown in Figure 4.5, and incorporate several additional features and components to aid in the sample preparation process, as described in Section 4.7.2.

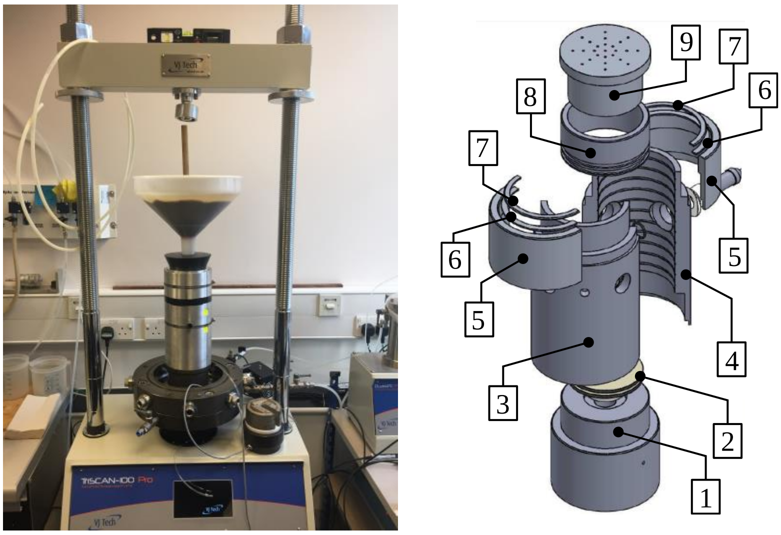

Key:

1. Enlarged base platen
2. Latex discs
3. Split mould (front)
4. Split mould (rear)
5. Outer collar
6. Lower split spacer
7. Upper split spacer
8. Inner collar
9. Mushroom compactor

(a) **(b)**

Figure 4.5: New two-part split mould assembly sample preparation equipment

4.6. LEIGHTON BUZZARD SAND

Leighton Buzzard sand (LBS) is a commercially available aggregate often used in the construction industry. The sand is sub-angular to rounded and consists of pure quartz with only a few traces of microcline. It is available in different gradings or 'fractions', as defined in BSI (1998), ranging from coarse (fraction A) to fine (fraction E). When comparing results with other published LBS data, it is therefore important to know the specific grading of the material if fair comparisons are to be made.

4.6.1. GEOLOGICAL ORIGIN

LBS is part of the Lower Greensand formation which stretches across most of southern England. It was deposited in a shallow marine environment during the early Cretaceous period approximately 100 to 140 million years ago. The material used in this study is sourced from the Leighton Buzzard Beds from a quarry in southwest Bedfordshire, where it is locally known as 'The Woburn Sands'. Leighton Buzzard is an unusual area, as the Woburn Sands can be divided into three distinct types:

- the Brown Sands: the oldest and thus located at the bottom of the formation;
- the Silver Sands: found in the middle of the formation and which may be many colours, including red-brown, sandy-tan, and silver-grey;
- the Red Sands: are the youngest and rarest of the deposits, and are unusual in that they contain tiny black balls of an iron mineral known as goethite.

4.6.2. LEIGHTON BUZZARD SAND – FRACTION B

LBS fraction B (LBS-B) has been used in this study as its index and mechanical properties are well-documented in the literature (e.g. Abate *et al*., 2010; Çabalar & Clayton, 2010; Dietz & Muir Wood, 2007; Penna *et al*., 2016; Stroud, 1971), and is readily available in the Oxford soils laboratory.

Researchers have traditionally designated the grading of LBS by specifying two bounding sieve sizes. For example, LBS-B has historically been known as LBS 14/25, and is graded such that 100 % of the material passes the no. 14 (1.18mm) sieve and is retained on the no. 25 (0.6mm) sieve. The '14/25' relates to the 'mesh number' (number of meshes per inch) which up until 1962, was the recognised standard designation used by sieve manufacturers for identifying sieve sizes (BSI, 2000). However, despite BS 410 (BSI, 2000) being withdrawn and replaced by BS ISO 3310 (BSI, 2016), the terminology continues to be used. Other classifications and descriptions based on colour (e.g. ‘silver Leighton Buzzard sand’) are also used in the literature; however, this is not recommended as the material can come in a range of colours and this offers no information on particle size distribution.

4.6.2.1. *Index and Classification Tests*

Leighton Buzzard sand in its various fractions has been the subject of many research investigations and its index properties are therefore well documented. The following sections present results of index tests undertaken as part of this study along with values found in the literature.

4.6.2.2. *Particle Size Distribution*

Figure 4.6 and Table 4.1 show the results of particle size distribution (PSD) tests performed during this study. As the behaviour of sands is grading dependent, a careful control of the initial grading is essential to obtain repeatable, high-quality test data. It was therefore decided to sieve the bulk LBS into its constituent fractions, and make up fresh batches of a controlled grading (LBS-B1). This is because the material has been in use for many years in the testing laboratories at Oxford, and results of PSD tests indicate that the grading curve no longer sits within the ‘fraction B’ range (LBS-B0).

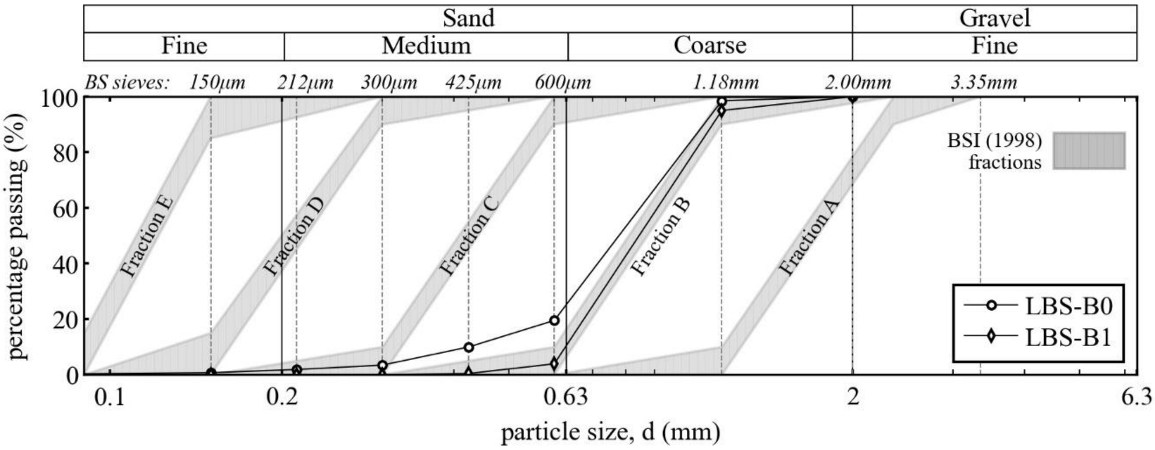

Figure 4.6: Particle size distribution curves used in this study, and grading fractions specified in BSI (1998)

The PSD of the controlled batch (LBS-B1) is presented in Figure 4.6, and is shown to lie within the middle of the fraction B range. The coefficient of uniformity, C_U, and the coefficient of curvature, C_Z, provide a means of describing the general slope and shape of the distribution curve. The low C_U and C_Z values (1.44 and 0.93, respectively) indicate that LBS-B may be classified as being poorly graded, consisting of relatively uniform sized particles.

Table 4.1: Summary of LBS-B particle size distribution test results

batch ID	**significant particle size**					**fines content**	**coefficient of uniformity**	**coefficient of curvature**
- (-)	d_{10} **(mm)**	d_{20} **(mm)**	d_{30} **(mm)**	d_{50} **(mm)**	d_{60} **(mm)**	FC **(%)**	C_U **(-)**	C_Z **(-)**
LBS-B0	0.50	0.60	0.66	0.78	0.85	0.04	1.70	1.02
LBS-B1	0.63	0.68	0.73	0.85	0.91	0.00	1.44	0.93

where: $$C_U = \frac{d_{60}}{d_{10}} \quad (4\text{-}1)$$ and $$C_Z = \frac{d_{30}^2}{d_{60}\ x\ d_{10}} \quad (4\text{-}2)$$

Table 4.2 shows index and classification test data for LBS 14/25 published in the literature, and shows C_U values to range from 1.16 (Stroud, 1971) to 2.13 (Abate *et al.*, 2010). This emphasises the issue associated with the use of ‘14/25’ nomenclature, in that studies using LBS 14/25 may have different grading characteristics; therefore, cross-study comparisons of the material behaviour of LBS 14/25 may be invalid given the influence of soil grading on the mechanical response.

Table 4.2: Index Properties for Leighton Buzzard 14/25 sand reported in the literature

median particle size	**coefficient of uniformity**	**maximum voids ratio**	**minimum voids ratio**	**fines content**	**particle density**	**Reference**
d_{50} **(mm)**	C_U **(-)**	e_{max} **(-)**	e_{min} **(-)**	FC **(%)**	ρ_s **(Mg/m^3)**	**-** **(-)**
-	1.24	0.790	0.530	0	-	Kolbuszewski (1965)
0.86	1.16	0.790	0.490	0	2.66	Stroud (1971)
0.80	1.30	0.774	0.479	-	-	Schnaid (1990)
0.93	-	0.760	0.490	0	2.62	Schupp (2009)
0.85	1.35	0.776	0.510	0	2.65	Çabalar & Clayton (2010)
0.94	2.13	0.745	0.465	0	2.68	Abate *et al.* (2010)

4.6.2.3. Particle shape and colour

Figure 4.7 shows a scanning electron microscope (SEM) image of LBS-B taken from Çabalar (2008). Based on the BS 5930 classification system (BSI, 1999) and a visual inspection of the material, the LBS-B used in this study can therefore be classified as a yellowish brown, sub-angular to rounded, uniformly-graded, coarse SAND (SPu).

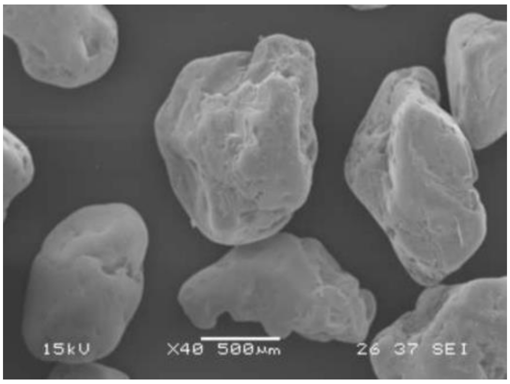

Figure 4.7: SEM image of LBS-B sand particles (from Çabalar, 2008)

4.6.2.4. *Particle density*

Klotz (2000) undertook 10 particle density tests on samples of LBS (fraction D), to verify the values reported in the literature. Particle density, ρ_s, values were found to range from 2.63 to 2.66 Mg/m^3, with an average of 2.65 Mg/m^3. These results agree well with commonly reported values given in the literature for LBS-B (see Table 4.2), and so further verification tests have not been undertaken. A particle density of ρ_s = 2.65 Mg/m^3 has therefore been adopted for LBS-B in this study.

4.6.2.5. *Limiting density tests*

Granular material has typically been characterised in terms of its relative density, D_r, defined as:

$$D_r = \frac{e_{max} - e}{e_{max} - e_{min}} \tag{4-3}$$

where:

e_{max}, e_{min} = maximum and minimum index void ratios
e = current void ratio

Limiting void ratio index tests were performed on samples of LBS-B, adopting the methods given in BS 1377 (BSI, 2002), yielding values of e_{max} = 0.815, and e_{min} = 0.533. Figure 4.8 presents the results of these tests (OxBS), along with additional test results for LBS-B reported by Lunne *et al*. (2019). Results show close agreement with the comparable "BS" method; however, Figure 4.8 shows that the magnitudes of e_{max} and e_{min} are greatly affected by the adopted test standard/method.

Tavenas & La Rochelle (1972) report similar findings, concluding that reliable comparisons of test results undertaken by different organisations may be invalid. Further research to satisfy this issue is therefore highly recommended. In the absence of a universally agreed method, the above values (OxBS) have been adopted for LBS-B in this study.

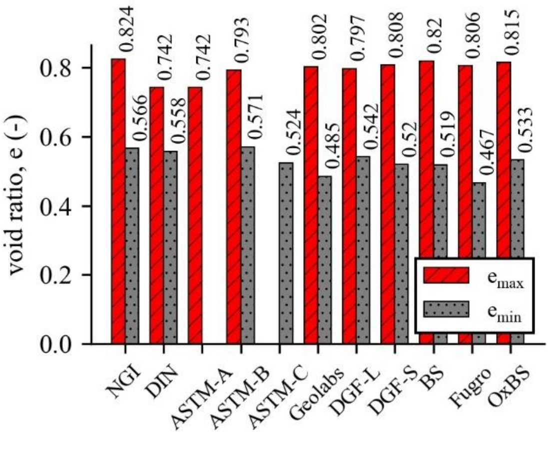

Figure 4.8: Method dependent variation of limiting densities (modified from Lunne et al., 2019)

4.7. TEST PROCEDURE

The following sections describe the procedures, sample reconstitution methods and typical test plans adopted in this study. The methodologies adopted in this study were devised based on a review of the literature, and from time spent at the advanced soil testing laboratory of Fugro Limited in Wallingford, UK.

4.7.1. PRELIMINARIES

Several tasks require completion prior to setting up a sample in the triaxial apparatus. These include preparation of the enlarged lubricated end platens, weighing out and saturating the required mass of dry sand, m_{dry}, for use in the test, and marking up membranes to aid fixing local instrumentation.

4.7.1.1. Preparing enlarged, lubricated end platens

The following describes the preparation process for enlarged, lubricated end platens:

- Clean/degrease the porous discs by placing in an ultrasonic cleaner filled with a degreasing agent for at least 6 minutes. After, flush discs with tap water for several minutes;
- Saturate the porous discs by placing them in a tub of de-aired water inside a vacuum desiccator for at least 45 minutes, and leave to ‘cure’ overnight;
- Cut four donut-shaped membranes to suit the required dimensions of the enlarged platens being used (batch cutting the membranes with a laser cutter yielded significant time savings);
- Measure and record the thickness of each membrane (membranes with thicknesses greater than 0.35 mm were not used to ensure the final height of the lubricated layers did not protrude above the top of the porous disc);
- Carefully spread a thin and even layer of high-vacuum grease over the face of the base and top platens, and then place the first membrane layer. Repeat for the second layer (Figure 4.9a);
- Place a mass on top of the lubricated platen assemblies and leave overnight to help squeeze out excess grease, and aid in the formation of uniform and repeatable assemblies (Figure 4.9b);
- The following morning, remove the mass and carefully clean any expelled grease from the sides of the membrane-grease layers, particularly around the porous disc recess (a cotton bud dipped in isopropyl alcohol has been found to work well for this task);
- Flush the base pedestal with de-aired water to remove any air bubbles in the drainage lines. Insert the porous disc immediately before commencing the chosen reconstitution process.

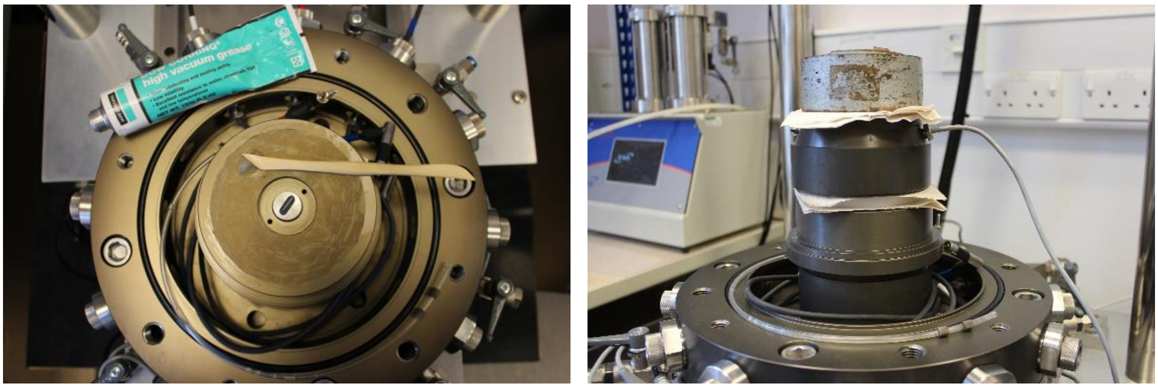
(a) (b)

Figure 4.9: Preparation of enlarged lubricated end platens

4.7.2. SAMPLE PREPARATION

Test specimens in this study have mainly been prepared using the wet pluviation technique, similar to that described by Bishop & Henkel (1962). However, it was found that this method was unable to produce specimens with relative densities less than approximately 40 %. A modified undercompaction technique was therefore also used in circumstances where loose specimens were required such as in tests aiming to determine critical state conditions (see Chapter 8).

4.7.2.1. Wet pluviation

The wet pluviation sample preparation equipment was specifically designed for this study. The following presents the methodology developed for preparing test specimens of reconstituted sand using the wet pluviation technique with this equipment:

- Note/mark the orientation of the bender element located in the base pedestal. This is important as the bender element located in the top platen must be orientated in a similar manner, and cannot be identified once the sand has been deposited in the mould;
- Place pre-measured and marked-up membrane over base pedestal and secure with two O-rings, ensuring not to entrap any air between the pedestal and the inside of the membrane;
    - To help make a good seal around the top and bottom platens, 3.5 mm thick nitrile (NBR) O-rings have been used, with an internal diameter equal to approximately 95 % of the platen diameter. The O-rings are stored in an air-tight container filled with distilled water;
- Place the two parts of the split-mould sample former over the base pedestal – taking care not to pinch the membrane between the two halves, and secure with two worm gear clamps;
- Place two O-rings around the upper portion of the split-mould in preparation for securing the membrane to the enlarged top platen;

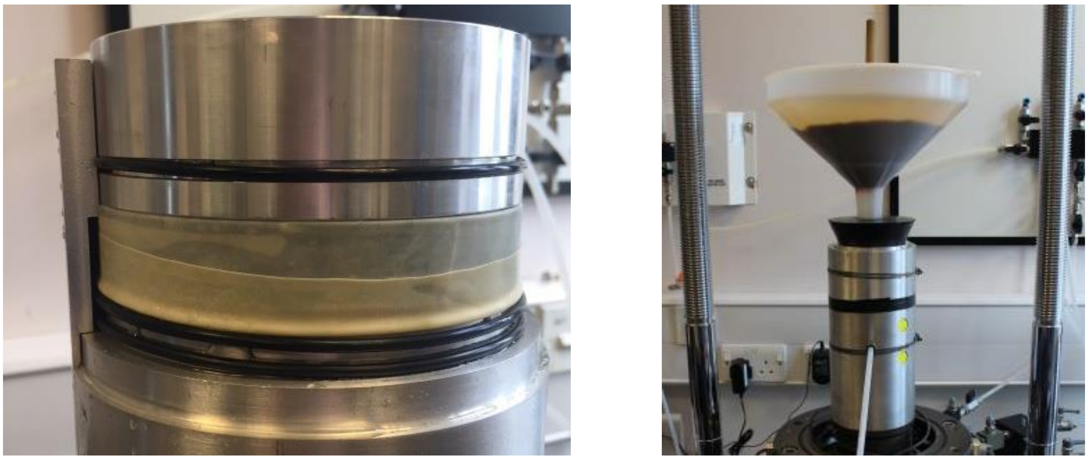

(a) (b)

Figure 4.10: Preparation of split mould assembly

- Place the upper and lower split spacers on the top rim of the split-mould, and secure with tape. Fold the membrane over the top (Figure 4.10a);
    - The purpose of the upper split-spacer is to provide a stable platform upon which the inner collar is seated, and allows the sand to be levelled and compacted to the approximate final height using the mushroom compactor;
    - The purpose of the lower split-spacer is to provide some clearance, which allows the sample to reduce in height unhindered upon removal of the vacuum;
- Apply a vacuum to the membrane via the push-in fitting located on the front half of the split-mould. This helps draw the membrane tightly against the internal face of the split-mould and ensure the maximum volume is available for the sand specimen;
- Fill mould with de-aired water;
    - Also flush the base drainage line with de-aired water from the APC;
- Insert the inner collar and seat on the top of the split-mould assembly;
    - The inner collar has spaces for two O-rings around its outside surface which help create a tight seal between the inner and outer collars;
- Place the outer split-collar around the split-mould, and tighten around the inner collar with a worm gear clamp;
    - To help prevent excessive leakage, the outside joint between the split-mould and outer collar is sealed with electrical insulation tape;
- Insert the bung-funnel assembly into the inner collar to create a water-tight seal;
- Fill the split-mould and bung-funnel assembly with de-aired water, leaving enough clearance such that no overspill occurs when the sand specimen is added to the funnel;
- Plug the funnel with a rod fitted with a rubber stopper;
- Deposit the required mass of sand (prepared the previous day) into the funnel (Figure 4.10b);
- Remove the stopper and allow the sand to pluviate freely into the sample former;

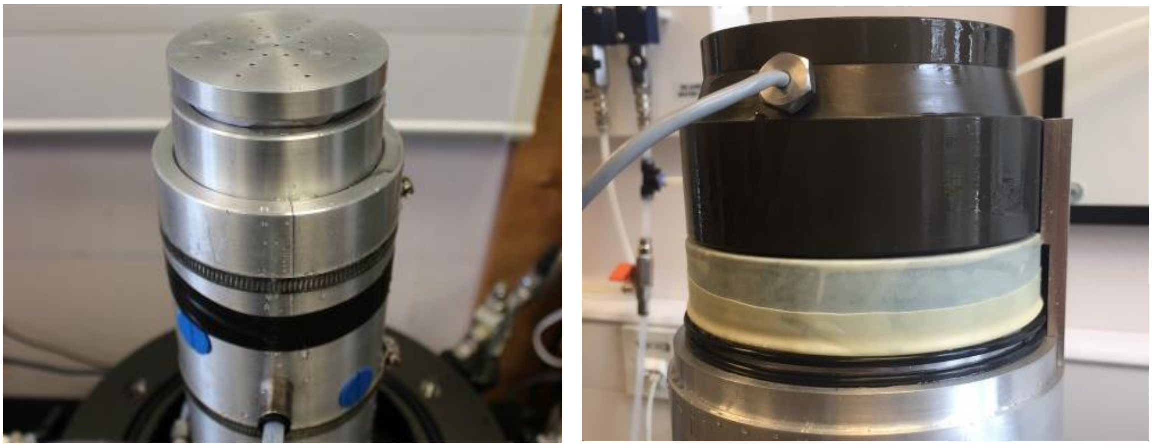

(a) insert mushroom compactor and densify ***(b) Remove inner collar and insert top platen***

(c) Roll up membrane and O-rings ***(d) Remove upper spacer***

(e) Densify until contact with lower spacer ***(f) Remove lower spacer, apply vacuum***

Figure 4.11: Preparation of wet pluviated samples

- Once all sand has been deposited, syphon excess water from the funnel and remove the bung-funnel assembly;
- Insert a circular disc of filter paper inside the inner collar, followed by the mushroom compactor, and compact until contact is made with the inner collar (Figure 4.11a);
    - The specimen is densified by tapping the outside of the split mould with a nylon hammer;
    - The purpose of the mushroom compactor is to provide a controlled means of densifying the sand specimen to the required height, and also minimise the likelihood of a loose layer forming at the top of the sample;

- Remove the mushroom compactor and filter paper, and then carefully extract excess water from inside the inner collar using a syringe;
- Remove the inner collar and then carefully insert the enlarged top platen, taking care to correctly align the bender element with the element located in the base pedestal (Figure 4.11b);
- Remove the outer split-collar, and then carefully roll the membrane up and on to the enlarged top platen, securing in place with two O-rings (Figure 4.11c);
    - The upper split-spacer means that downward pressure can be applied to the top platen during this procedure without disturbing/compressing the sample;
- Remove the upper spacer (Figure 4.11d), and tap the outside of the mould to further densify the specimen until it makes contact with the lower split-spacer (Figure 4.11e);
- The specimen should now be at the desired height and aspect ratio (2:1);
- Remove the lower split-spacer and apply a 10 kN/m^2 vacuum to the specimen via the back-pressure APC line connected to the base pedestal;
- Remove the split-mould sample former and monitor the back-pressure APC pressure and volume readings on the control panel (Figure 4.11e);
    - Failure of the pressure reading to stabilise indicates the presence of a leak. If such a leak cannot be located and repaired, the sample preparation must be abandoned and repeated;
- Using digital Vernier callipers, take two orthogonal diameter measurements at five positions along the height of the specimen, and three height measurements equally spaced about the perimeter of the sample;
    - Calculate the initial sample diameter, D_0, height, H_0, and volume, V_0, of the specimen from the average of the measurements, allowing for the membrane thickness;
- Assuming the specimen is fully saturated, then the initial void ratio (and relative density, Eq. (4-3)) may then be calculated from phase relationships: $e_0 = V_v/V_s = (V_0 - V_s)/V_s$, where V_v and V_s are the volume of voids and solids, respectively, and $V_s = m_{dry}/\rho_s$.

4.7.2.2. *Undercompaction*

For tests requiring loose specimens, a modified undercompaction technique was adopted. Full details can be found in Jefferies & Been (2015) and will not be repeated here. This method was adopted over Ladd's (1978) original method, as it deposits layers of uniform thickness, meaning that a jig could be used to help set the drop height of the tamper, resulting in reduced preparation times.

4.7.2.3. *Installation of on-sample displacement transducers*

The methodology for attaching the local displacement transducers to the sample was as follows:

- To help position the axial LVDT brackets at the correct height, the membrane is marked up using a fine-tipped permanent marker with vertical and horizontal centrelines, and two additional horizontal lines offset 28 mm from the centre;
    - The two offset horizontal lines indicate the required vertical locations of the upper and lower axial LVDT brackets, and ensure the displacement transducers are correctly positioned over the central third of the test specimen;
- Following application of the vacuum to the sample and removal of the split mould assembly, the radial belt is first positioned using the horizontal centreline as a guide, and loosely secured in place with an elastic tie (a strip of membrane works well for this purpose);
- Mark the location of the radial belt pads and the position of the axial LVDT brackets;
- Loosen the clamping bolt on the top bracket, and then apply a thin layer of glue to each bracket and attach to the sample/membrane. Leave to dry.
    - Loctite 4860 flexible, high viscosity, bendable instant adhesive has been found to work well for this purpose;
- Apply a thin layer of glue to the radial belt pads and adhere to the membrane. Leave to dry.
- Insert the axial LVDT transducers into the top brackets, then drop the armature through the top of LVDT so it rests on the bottom bracket's base pedestal.
- Adjust the position of the LVDT in the top bracket whilst monitoring the read-out display to maximise the available travel. Tighten the clamping bolt to secure.
    - For the ±5 mm LVDTs used in the experiments, the axial LVDTs were positioned such that approximately 8.5 mm of travel remained available, i.e. an initial reading of +3.5mm was targeted for compression tests; while -3.5mm was targeted for extension tests.
- Insert the radial LVDT(s) into the radial belt and adjust and secure accordingly to maximise the displacement range of the test.

4.7.3. TEST SET-UP

Tests typically consisted of five (for monotonic) or six (for cyclic) stages. The first stage, termed 'set up' involves flooding the cell with de-aired water and then docking the specimen's top cap to the ISLC. Great care was exercised during docking to minimise disturbance to the specimen:

- Manually suspend the load ram so that the base of the threaded connecting rod (screwed into the underside of the ISLC) is suspended marginally above the top cap. Record the (submerged) load cell reading;
    - It is not possible to 'zero' the ISLC using VJ Tech's proprietary "CLISP Studio" software. Therefore, this initial reading is required so that subsequent load measurements may be suitably offset;

- With extreme care, lower the threaded connecting rod into the tapped hole located in the centre of the top cap. Screw into the top cap by rotating the entire load ram assembly, making sure not to over-torque and twist/disturb the sample;
- For triaxial compression tests, raise pedestal using the triaxial frame's stepper motor to approximately 5 mm. This ensures sufficient vertical displacement to shear the sample to large axial strains (>30 %), and also provides a buffer to prevent premature test failure due to the mobilisation of negative axial strains that can occur during saturation and/or consolidation;
- Lower the triaxial frame's cross beam so that the threaded connection (to fix the cross beam to the load ram) is fractionally above the load ram.
- Using the stepper motor's displacement control, very slowly raise the pedestal until it comes into contact with the cross-beam connection and screw together with a quarter-turn;
- Using the stepper motor's load control, set the target load to the initial ISLC reading recorded in the first step, minus the buoyant weight of the top cap. The weight of the top cap is therefore fully compensated, meaning that subsequent load measurements require no further correction;
- Continue to (slowly) screw the cross-beam – load ram connection until the load ram is fully secured. It was found from monitoring the ISLC output during this process that loads could be controlled to within 20 N of the target value.

Once docked, the cell and back pressure are increased to 10 kN/m^2 and 0 kN/m^2 over a 5-minute period, respectively, whilst maintaining the aforementioned target load.

4.7.4. SATURATION

The second test stage comprises saturating the specimen. To aid this process, carbon dioxide (CO_2) was first flushed through the sample for at least 30 minutes, followed by flushing with de-aired water. Flushing was continued until a volume of de-aired water equal to at least three times the sample volume had passed through, by which time no bubbles should be seen to emerge from the exit drainage line. Longer CO_2 flushing times (one hour) and de-aired water volumes (five times sample volume) were used for specimens prepared using the undercompaction method, as their moisture contents and associated degree of saturation were initially much lower, thus requiring greater effort.

Conventional saturation procedures followed, in which cell and back pressures were typically ramped to 300 and 290 kN/m^2, respectively, at a rate of 60 kN/m^2 per hour. Preliminary tests found that for these cell and back pressures, Skempton B-values greater than 0.99 were repeatedly achieved for wet pluviated samples. To avoid disturbing the specimen, it was decided not to undertake B checks for tests undertaken at low confining stresses (Chapters 6 and 7). However, B checks were employed for specimens prepared using undercompaction, where a similar 10 kN/m^2 cell-back pressure offset was used. Pressures were increased until B-values greater than 0.98 were achieved.

4.7.5. CONSOLIDATION

The third stage typically consisted of an isotropic consolidation stage in which the cell pressure was increased to a target effective confining stress, σ_c', at a rate of 60 kN/m^2 per hour. To investigate the influence of anisotropic consolidation, 'K_0' consolidation paths were also adopted to better simulate in situ stress conditions prior to shearing, where K_0 is the coefficient of earth pressure at rest. K_0 consolidation paths may be achieved from closed-loop computer control of axial and radial stresses, such that the radial strain, ε_r, is maintained at zero – as measured from local strain instrumentation. However, preliminary tests indicated that K_0 consolidation paths based on feedback from local strain instrumentation were found to be unsatisfactory due to:

- The stress path in $p' - q$ space was seldom linear, and often exhibited large 'spikes';
- Although target σ_c' values were the same for each test, the final positions in $p' - q$ space were different as a result of variable stress paths taken during consolidation.

It was therefore decided to base anisotropic consolidation paths on explicit p' and q values. For normally consolidated conditions, K_0 can be estimated from: $K_0 = 1 - \sin(\phi_{max}')$, where ϕ_{max}' is the peak effective angle of internal shearing resistance, determined from isotropically consolidated, drained triaxial compression tests (CIDc) undertaken for a comparable soil state (Jaky, 1944).

Figure 4.12a shows a comparison of the K_0 consolidation stress paths obtained using the two methods described above, for two similar anisotropically consolidated, drained triaxial compression tests (CADc) with D_r = 80 %, and σ_c' = 50 kN/m^2. Figure 4.12b shows that when adopting the 'Stress path' approach (i.e. targeting explicit $p' - q$ values), the approximate 1:1 ratio of axial to volumetric strain indicates that mobilised values of ε_r remain very close to 0 %. This approach is therefore considered acceptable for approximating K_0 conditions.

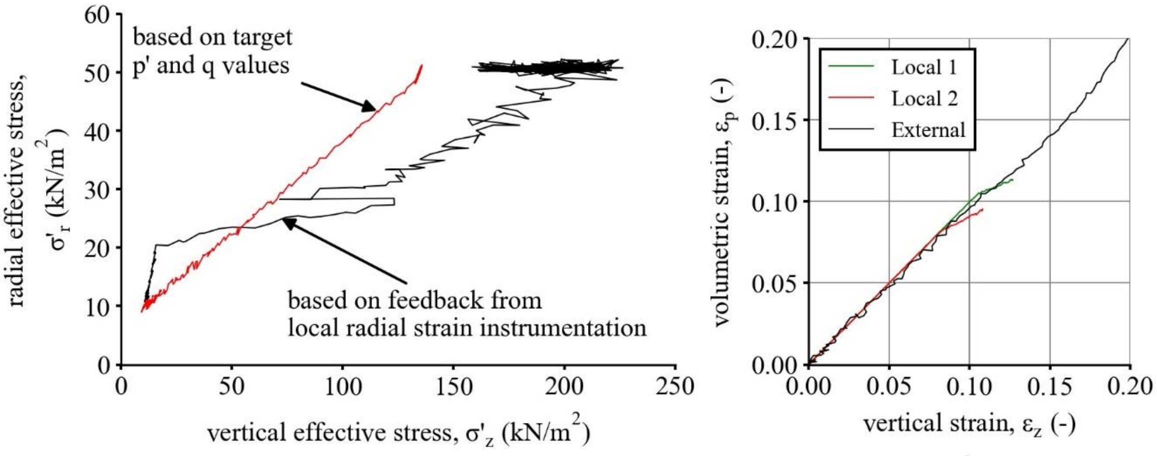

(a) *(b)*

Figure 4.12: (a) Comparison of anisotropic consolidation methods based on feedback from local radial strain instrumentation and target stress invariant values; (b) measured axial and volumetric strains.

4.7.6. CREEP

The stress-strain behaviour of sand is considered by many to be time-dependent (Aghakouchak *et al*., 2015; Kuwano, 1999). Tatsuoka (1988) found that the cyclic strength of a normally consolidated Toyoura Sand specimen, consolidated slowly over a period of 68 days, was approximately equal to that exhibited by a similar sample with an OCR of two. It is not the intention of this research to investigate the effects of ageing/consolidation time; however, following the recommendations of Aghakouchak *et al*. (2015), the fourth test stage consists of a 24 to 48 hour ‘creep’ period.

4.7.7. MONOTONIC SHEAR AND CYCLIC LOADING

For monotonic tests, the fifth stage consists of either drained or undrained shearing, in which the specimen is sheared along a defined stress path in $p' - q$ space. All monotonic tests adopted an axial strain rate of $\dot{\varepsilon_z}$ = 0.5 % per hour. Test-specific drainage conditions and stress paths are described in detail in Chapters 6 and 8.

For cyclic tests, the fifth stage consists of a conventional drained axial stress ramp (i.e. $dq\ /\ dp'$ = 3) to a pre-determined average deviator stress, q_{av}, followed by application of an undrained cyclic deviator stress, q_{cyc}, for a specified number of load cycles. Test-specific details of the cyclic loading characteristics are presented in Chapter 7.

4.8. COMPUTATION AND PRESENTATION OF TEST RESULTS

The purpose of this section is to outline how the raw variables measured in each triaxial apparatus were converted and reduced into the engineering parameters (e.g. stress and strain) used in subsequent interpretation and analyses. The stress path apparatus instrumentation enabled the following variables to be measured and logged:

- Force: via internal submersible load cells (5 kN or 10 kN capacities used);
- 'Global' displacement: via external LSCT (50 mm) or external LVDT (100 mm);
- Pore water pressure: via two pressure transducers installed along the back pressure (base pedestal and top cap) drainage lines, located immediately outside the triaxial cell;
- Cell pressure: via a pressure transducer installed along the cell pressure drainage line, located immediately outside the triaxial cell;
- Sample / cell volume change: via volume change measurement apparatus incorporated within the dual APCs (see Menzies (1988) for further details);
- Local displacement: via two 'axial' LVDTs and one/two 'radial' LVDTs

Values were logged from the various instruments at a frequency of 1 Hz for the first 20 seconds of each new test stage. Logging frequencies were gradually reduced over the first two minutes of each new test stage, and maintained at a final rate of 0.05 Hz. Similar instrumentation and logging rates were used with the cyclic triaxial apparatus, though significantly faster logging frequencies (50 to 100 Hz) were used in the cyclic loading stages.

4.8.1. SIGN CONVENTION

This thesis adopts the usual soil mechanics convention of taking compressive stresses and strains as positive. This is due to most soils typically exhibiting negligible tensile strength, and because volumetric deformations are most often the result of an applied compressive stress. Because of this sign convention, volumetric strains are positive for compression and negative for dilation.

4.8.2. TRIAXIAL STRESS AND STRAIN VARIABLES

All of the laboratory testing has been carried out in axially symmetric tests, the triaxial stress invariants, p' and q, and corresponding conjugate strain invariants, ε_p and ε_q, are used extensively in this thesis. For triaxial compression conditions, the mean effective stress, p', is calculated from:

$$p' = \frac{(\sigma_1' + 2\sigma_3')}{3} \tag{4-4}$$

where:

σ_1' = major principal effective stress (vertical effective stress, σ_z', in triaxial comp.)
σ_3' = minor principal effective stress (radial effective stress, σ_r', in triaxial comp.)

In triaxial testing, the deviator stress, is usually defined according to:

$$q = (\sigma_z' - \sigma_r') \tag{4-5}$$

In this study, the vertical and radial effective stresses were calculated using a similar method to that described by Fukushima & Tatsuoka (1984), where:

$$\sigma_r' = \sigma_{cell}' + \sigma_{r,m} \tag{4-6}$$

$$\sigma_z' = \frac{P}{A_{corr}} + \sigma_{cell}' + \sigma_{sw}' + \sigma_{z,m} \tag{4-7}$$

The axial and lateral membrane resistance ($\sigma_{z,m}$ and $\sigma_{r,m}$) is calculated according to Eqs. (3-3) and (3-4), respectively, and the self-weight of the specimen, σ_{sw}', is estimated at the specimen mid-height using Eq. (3-12). The measured vertical force, P, was zeroed once the cell had been filled with de-aired water, and corrected to account for the buoyant weight of the top platen. The area correction, A_{corr}, described by Zhang & Garga (1997) was used (Section 3.6.4).

Triaxial strain invariants are calculated from measured linear and volumetric deformations. It is assumed that deformations are distributed uniformly throughout the specimen, with strains calculated with reference to original specimen dimensions. In this thesis, all strains are expressed as pure numbers (i.e. mm/mm), 'global' vertical displacement changes, Δz, are positive in the downward direction, and strains are calculated and tracked from initial specimen height measurements at the start of the test. For the shearing stage, the vertical strain, ε_z, is calculated as:

$$\Delta z = z_i - z_{f,c} \tag{4-8}$$

$$\varepsilon_z = \frac{\Delta z}{H_{f,c} - (z_{f,c} - z_{0,shear})} \tag{4-9}$$

where:

z_i = current vertical displacement measurement
$z_{f,c}$ = final vertical displacement at the end of the consolidation/creep stage
$z_{0,shear}$ = initial vertical displacement measurement at the start of the shearing stage
$H_{f,c}$ = height of the specimen at the end of the consolidation/creep stage

Similar expressions are used to calculate ε_z from local axial strain instrumentation measurements, ε_z^{LA}, where the reference height is taken as the distance between the top of the LVDT mounting bracket and the underside of the core pedestal. The volumetric strain is estimated from initial specimen height and diameter measurements, and volume change measurements recorded by the back pressure APC. For the shearing stage, the volumetric strain, ε_p, is calculated from:

$$\Delta V = V_{f,c}^{BP} - V_i^{BP} \tag{4-10}$$

$$\varepsilon_p = \frac{\Delta V_m}{V_{f,c} + (V_{f,c}^{BP} - V_{0,shear}^{BP})} \tag{4-11}$$

where:

ΔV = measured change in sample volume
ΔV_m = volume change corrected for membrane penetration (see Section 3.6.2)
$V_{f,c}^{BP}$ = back pressure volume measurement at the end of the consolidation/creep stage
V_i^{BP} = current back pressure cylinder volume measurement
$V_{0,shear}^{BP}$ = back pressure volume measurement at the start of the shearing stage
$V_{f,c}$ = estimated specimen volume at the end of the consolidation/creep stage

Assuming uniform strain, the radial strain, ε_r, can then be estimated from Eq. (4-12), which allows the deviatoric strain, ε_q, to be calculated, where:

$$\varepsilon_r = 1 - \sqrt{\frac{1 - \varepsilon_p}{1 - \varepsilon_z}} \tag{4-12}$$

$$\varepsilon_q = \frac{2}{3}(\varepsilon_z - \varepsilon_r) = \varepsilon_z - \frac{\varepsilon_p}{3} \tag{4-13}$$

Alternatively, a more accurate estimate of radial strain can be obtained from local strain instrumentation. A single radial LVDT measures circumferential displacements, from which radial strains are calculated from:

$$\Delta c = x_{f,c}^{LR} - x_i^{LR} \tag{4-14}$$

$$\varepsilon_r^{LR} = \frac{\Delta c}{\pi\left(D_{f,c}^{LR} - \left(x_{f,c}^{LR} - x_{0,shear}^{LR}\right)\right)} \tag{4-15}$$

where:

Δc = change in radial caliper circumference
$x_{f,c}^{LR}$ = local radial disp. measurement at the end of the consolidation/creep stage
x_i^{LR} = current local radial dispalcement measurement
$x_{0,shear}^{LR}$ = initial local radial displacement measurement at the start of the shearing stage
$D_{f,c}^{LR}$ = radial caliper diameter at the end of consolidation/creep stage

Volumetric strains may thus be estimated directly from local instrumentation via Eq. (4-16). Note that Eq. (4-16) is preferred over the simpler form often used ($\varepsilon_p = \varepsilon_1 + 2\varepsilon_3$), which leads to the accumulation of significant errors when tests are sheared to $\varepsilon_z \geq 0.1$ (Lade, 2016).

$$\varepsilon_p = (\varepsilon_1 + \varepsilon_2 + \varepsilon_3) - (\varepsilon_1\varepsilon_2) - (\varepsilon_2\varepsilon_3) - (\varepsilon_3\varepsilon_1) + (\varepsilon_1\varepsilon_2\varepsilon_3) \tag{4-16}$$

where:

ε_1 = major principal strain (ε_z in triaxial compression; ε_r in triaxial extension)
ε_2 = intermediate principal strain (ε_r in triaxial compr.; ε_z in triaxial extension)
ε_3 = minor principal strain (ε_r in triaxial compression; ε_z in triaxial extension)

Calculating ε_p based on local strain instrumentation is particularly useful as reliable estimates of ε_p may be obtained throughout all test stages, including the sample flushing phase (see Section 4.7.4) when the back pressure APC is isolated from the sample. Furthermore, such calculations are not susceptible to membrane penetration, bedding errors, system compliance etc. and therefore further corrections to measured values are not required. This also enables the void ratio to be tracked throughout all test stages, which is critically important for reliable determinations of the CSL, where:

$$e = e_0 - (1 + e_0)\varepsilon_p \tag{4-17}$$

Cyclic triaxial test results are often presented in terms of the shear strain, γ, which may be calculated from undrained cyclic triaxial test results where the undrained Poisson's ratio, μ_u = 0.5, such that:

$$\gamma = (1 + \mu_u)\varepsilon_z \tag{4-18}$$

4.8.3. SHEAR STRENGTH PARAMETERS

4.8.3.1. Effective Stress Shear Strength Parameters

It is convenient to present triaxial test data in terms of the dimensionless ratio of stress invariants, η:

$$\eta = \frac{q}{p'} \tag{4-19}$$

However, much of the historical literature uses the 'friction angle' concept as a means of describing the shear strength of drained materials. This angle, termed the effective angle of internal shearing resistance, ϕ', may be determined from:

$$\sin\phi' = \frac{|(\sigma_1' - \sigma_3')|/2}{(\sigma_1' + \sigma_3')/2} = \frac{3|\eta|}{6 + \eta} \tag{4-20}$$

Alternatively, for triaxial compression and extension conditions, Eq. (4-20) can be inverted to give:

In triaxial compression: $$\eta_{tc} = \frac{6\sin\phi'_{tc}}{3-\sin\phi'_{tc}} \tag{4-21}$$

In triaxial extension: $$\eta_{te} = \frac{6\sin\phi'_{te}}{3+\sin\phi'_{te}} \tag{4-22}$$

where the subscripts tc and te denote triaxial compression and extension conditions, respectively.

4.8.3.2. *Total Stress Shear Strength Parameters*

In undrained cyclic triaxial tests, the maximum shear stress, τ, is induced on a 45 degree plane (Ishihara, 1996) and may therefore be determined from the following:

$$\Delta\tau = \frac{\Delta\sigma_{cyc}}{2} \tag{4-23}$$

where:

$\Delta\sigma_{cyc}$ = cyclic deviator stress (as defined in Chapter 7)

4.8.4. STIFFNESS PARAMETERS

Graham & Houlsby (1983) and Atkinson & Richardson (1985) present a set of constitutive equations relating p', q, ε_p, and ε_q, where:

$$\delta\varepsilon_q = \frac{\delta q}{3G} + \frac{\delta p'}{J'_1} \tag{4-24}$$

$$\delta\varepsilon_p = \frac{\delta q}{J'_2} + \frac{\delta p'}{K} \tag{4-25}$$

The parameters J'_1 and J'_2 express the cross dependence of ε_q on p', and ε_p on p', respectively. G is therefore strictly defined as the gradient of the stress-strain curve in $\varepsilon_q - q$ space for tests in which $\delta p' = 0$. Similarly, the (tangent) bulk stiffness, K, is the gradient of the $\varepsilon_p - p'$ curve for tests with $\delta q = 0$.

According to Smith (1992), for other stress paths the cross coupling conceals the true nature of G and K unless the magnitude of the J'_1 and J'_2 moduli are infinitely large. For the anisotropic, perfectly elasto-plastic materials described by Graham & Houlsby (1983), $J'_1 = J'_2$; whereas for an isotropic elastic soil, $J'_1 = J'_2 = \infty$. The shearing and volumetric components are then effectively decoupled in that increments of ε_q are related only to increments of q, and increments of ε_p are related only to increments of p'. Eq. (4-24) and (4-25) for an isotropic material may therefore be simplified to:

$$G = \frac{1}{3}\frac{\delta q}{\delta \varepsilon_q^e} \tag{4-26}$$

$$K = \frac{\delta p'}{\delta \varepsilon_p^e} \tag{4-27}$$

Stiffness values presented in this thesis are based on this assumption. Furthermore, as the increments of stress and strain in Eq. (4-26) and (4-27) tend towards zero, G and K become tangent stiffnesses, such that $G_{tan} = dq/3d\varepsilon_q$ and $K_{tan} = dp'/d\varepsilon_p$. Alternatively, secant stiffness values may be obtained if increments are taken from the origin: $G_{sec} = \Delta q/3\Delta\varepsilon_q$, and $K_{sec} = \Delta p'/\Delta\varepsilon_p$.

It should also be noted that for a perfectly elastic, isotropic material, G is unaffected by drainage conditions. Therefore, the Young's modulus, E, may be obtained from the shear stiffness, from:

$$\frac{E_u}{2(1+\mu_u)} = G_u = G' = \frac{E'}{2(1+\mu')} \tag{4-28}$$

where the subscript u denotes undrained conditions. For conditions of no volume change (i.e. undrained conditions), μ_u = 0.5, therefore Eq. (4-28) reduces to:

$$E_u = 3G_u = 3G' \tag{4-29}$$

A distinction is also made here between stiffness and modulus terminology, which are often used interchangeably in soil mechanics literature. However, in this thesis, the term modulus is considered a specific material property, determined exclusively at small strains (e.g. $\varepsilon_q < 10^{-6}$) where the stress-strain relationship is linear.

5. BEHAVIOUR OF COHESIONLESS SOILS

To adequately describe and evaluate the results of the experimental testing programme outlined in Chapters 6 and 7, the key concepts and terminologies used to describe the behaviour of cohesionless soils subjected to both monotonic and dynamic loads must first be reviewed.

In the first part of this chapter, the main concepts used to describe and quantify the monotonic behaviour of sand are examined. The critical state concept is first reviewed followed by the state parameter framework developed by Been & Jefferies (1985). The Characteristic and Phase Transformation States are then introduced, before investigating the existence of the quasi-steady state.

The second part of the chapter looks at some of the key definitions and behaviours associated with the dynamic behaviour of cohesionless soils, including threshold strains, and the various liquefaction-related phenomena commonly used to describe dynamic failure conditions. The various failure criteria adopted in the literature are also reviewed. The section concludes with looking at whether any connections exist that might link the monotonic and dynamic response.

The final section brings together all the concepts reviewed above by introducing some cyclic experimental data, and discusses some of the factors that influence the measured response.

5.1. MONOTONIC BEHAVIOUR

5.1.1. SHEAR STRENGTH AND DILATANCY PROPERTIES OF SAND

The shear strength of soils is largely determined by the frictional forces arising during slip at the contacts between soil particles. The shear strength of cohesionless soils is often expressed in terms of the Mohr-Coulomb failure criterion and effective stress parameters, where:

$$\tau_f = c' + \sigma_n' \tan(\phi_f') \tag{5-1}$$

where:

τ_f = shear stress at failure
c' = effective cohesion (= 0 for most uncemented, silica sands)
σ_n' = effective normal stress
ϕ_f' = effective angle of shearing resistance mobilised at failure

Figure 5.1 shows the various idealisations of ϕ' used in engineering design, and how the stress-strain response varies with density and strain level. The behaviour shown in Figure 5.1 can be explained using the flow rule proposed by Bolton (1986), who reviewed extensive plane strain and triaxial test data undertaken on predominantly silica sands.

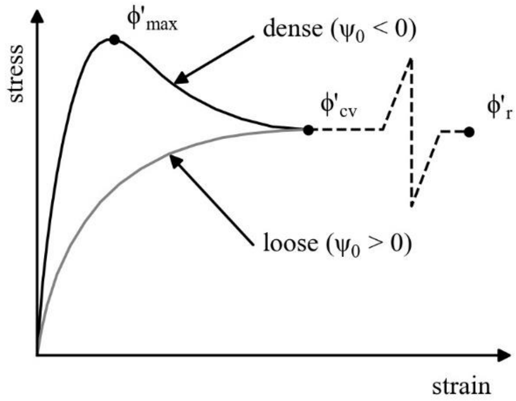

Figure 5.1: Idealisations of ϕ'_{max}, ϕ'_{cv} and ϕ'_r

Bolton (1986) found that ϕ' could be predicted with good accuracy (±1°) from:

$$\phi' = \phi'_{cv} + k\psi_D \tag{5-2}$$

where:

ϕ'_{cv} = critical state or 'constant volume' value of ϕ'
ψ_D = angle of dilation
k = empirical constant (0.8 for plane strain; 0.48 for triaxial conditions)

It is clear from Eq. (5-2) that ϕ' is a function of dilation rate. The peak of the shear stress-strain response occurs at the point where the rate of dilation is at a maximum. There is some debate as to how ψ^D, should be calculated from triaxial tests results (discussed in Section 6.5.3); however, its magnitude has been shown to depend on the characteristics of the sand grains (i.e. particle shape, roughness, grading). Beyond the peak, the rate of dilation (and ψ^D) decreases, 'strain-softening' occurs, and ϕ' tends towards the critical state or 'constant volume' value, ϕ'_{cv}, as the rate of dilation tends to zero (the critical state concept is described in Section 5.1.2). Loose sands tend to contract and thus exhibit no peak, and instead 'strain-harden' towards a maximum value which coincides with ϕ'_{cv}. For cohesionless soils with rounded or sub-rounded grains, the residual state angle, ϕ'_r is essentially equal to ϕ'_{cv} (Kulhawy & Mayne, 1990), though platy grains can yield lower ϕ'_r values.

It is also interesting to note that there is some evidence to suggest that the obtained value of ϕ'_{max} is influenced by the drainage conditions of the test. Georgiannou *et al.* (2008) undertook hollow cylinder tests on samples sheared from similar initial densities and stress conditions, and obtained peak angles of ϕ'_{max}= 41° and 38° from drained and undrained tests, respectively. Zhang *et al.* (1997)

also reported that on specimens of Toyoura sand, ϕ'_{max} was higher for the drained tests by 3°. Similarly, Blaker & Andersen (2015) found that for Dogger Bank sand reconstituted to D_r = 100 %, ϕ'_{max} reduced from 45.7° in drained tests to 43.4° in undrained tests, and from 43.6° (drained) to 39.7° (undrained) for D_r = 80 % samples. Georgiannou *et al*. (2008) attribute the relatively higher values to the work required to overcome physical dilation that occurs in drained tests.

5.1.2. STEADY STATE VS CRITICAL STATE

Casagrande (1936) was one of the first to investigate the behaviour of loose and dense sands sheared to large strains. Using shear box apparatus, Casagrande found that at large shear strains, dense sands would dilate and loose material would contract towards a similar void ratio, termed the 'critical void ratio'. Roscoe *et al*. (1958) further defined the concept of critical state as the state at which a soil continues to deform at constant stress and constant void ratio, which formed the basis of the Critical State Soil Mechanics (CSSM) theoretical framework (Schofield & Wroth, 1968).

However, in the mid-1960s, Castro (1969), a student of Casagrande's, undertook a series of stress controlled triaxial tests on loose samples of sand. These tests all resulted in liquefaction failures leading to a well-defined 'steady state' at large strains. This state was later formally defined by Poulos (1981) as the "state in which the mass is continuously deforming at constant volume, constant normal effective stress, constant shear stress and constant velocity."

There has been much debate on whether the critical and steady state are equivalent (Alarcon-Guzman *et al*., 1988; Casagrande, 1975; Sladen *et al*., 1985). Critical state supporters generally used drained, strain-controlled tests on dilatant samples to determine critical state conditions; while steady state researchers typically used undrained, load-controlled tests on loose, contractive samples. Been *et al*. (1991) and Chu (1995) examined the issue in detail and concluded that for all practical purposes, equivalence can be assumed.

5.1.3. SHAPE OF THE CRITICAL STATE LINE FOR SANDS

First attempts to apply CSSM modelling concepts to sands used a simple linear form in $e - \ln(p')$ space (Been & Jefferies, 1985). However, the occurrence of particle breakage at high stresses (i.e.

$p' > 1$ MN/m^2) resulted in a significant increase in the slope of the Critical State Line (CSL). To overcome this issue, Been *et al*. (1991) proposed a bi-linear form for the CSL, shown in Figure 5.2a.

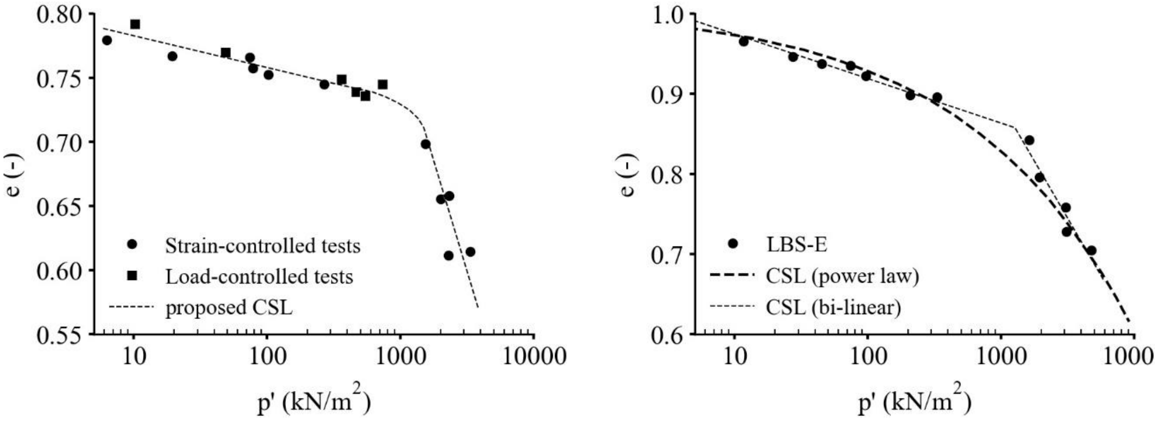

(a) *(b)*

Figure 5.2: (a) Bi-linear crticial state line for Ersak 330/0.7 sand (from Been et al., 1991); and (b) comparison between bi-linear and power law CSL approximations (from Taborda, 2011)

However, this approach led to the prediction of very high critical state void ratios at very low stress levels. Verdugo & Ishihara (1996) observed that the CSL tends to curve towards the horizontal at low stresses, and Klotz & Coop (2002) suggested that the CSL might intercept the axis of zero mean effective stress at a value close to the e_{max} at atmospheric pressure. To reproduce the required shape at both high and low mean effective stresses, Li *et al*. (1999) proposed a power law, where:

$$e_{cs} = e_{\Gamma} - \lambda \left(\frac{p'}{p'_{ref}} \right)^{\xi} \tag{5-3}$$

where:

e_{cs} = critical state void ratio
e_{Γ} = reference void ratio at $p' = 0$ kN/m^2
λ = power function constant
p'_{ref} = reference mean effective stress
ξ = stress exponent

Figure 5.2b shows a comparison between the bi-linear and power law approximations for the CSL, indicating the clear advantages of such approximations over the simple linear form (Taborda, 2011). Such approximations have therefore been regularly adopted in modern constitutive models for sand (e.g. Dafalias & Manzari, 2004; Loukidis & Salgado, 2009; Taborda, 2011).

5.1.4. UNIQUENESS OF THE CRITICAL STATE LINE

Uniqueness is defined here as the general requirement that the CSL may be calculated as a single-valued function of p' (and potentially the Lode angle, θ, defined in Appendix A). The uniqueness of the CSL is an important issue as it leads to physical simplicity and easily understandable idealisations of soil response, i.e. with a unique CSL, it is relatively straightforward to model the behaviour of a soil when sheared. However, published studies on the existence and uniqueness of the CSL are conflicting. Jefferies & Been (2015) summarise the various conclusions:

- There is a unique CSL, but care is required in both testing technique and interpretation to accurately establish the CSL (Been *et al*., 1991; Ishihara, 1993; Poulos *et al*, 1988).
- A band of states represents steady-state conditions, depending on the initial density and stress level, so that the CSL is actually a zone rather than a line (Konrad, 1993).
- Sample preparation methods result in different fabrics and anisotropies, giving different stress paths and critical states (Kuerbis & Vaid, 1988; Vaid *et al*., 1990).
- There is an ‘S-line’ from drained tests, and an ‘F-line’ from undrained tests that differ as a result of the collapse potential of the soil (Alarcon-Guzman *et al*., 1988).
- Strain rate affects the CSL (Hird & Hassona, 1990)

More recently, Li & Dafalias (2012) proposed the anisotropic critical state theory (ACST), which incorporates the role of fabric anisotropy by supplementing the stress ratio and void ratio conditions of the classical CSSM theory with a third fabric term. They claim to cpresent a thermodynamic proof of the uniqueness of the CSL on the basis of the well-known Gibbs condition of stability. 2D Discrete Element Modelling (DEM) simulations performed by Wang *et al*. (2017) further support this framework and the existence of a unique CSL.

5.1.5. STATE PARAMETER FRAMEWORK

The concept of a ‘state parameter’, originally suggested by Wroth & Bassett (1965), was developed into a powerful framework by Been & Jefferies (1985). It combines the influence of density and stress level with reference to critical state conditions, as shown in Figure 5.3, and is defined as:

$$\psi = e - e_{cs} \qquad (5\text{-}4)$$

Been & Jefferies (1985) showed that materials with similar values of ψ exhibited similar qualitative behaviour during shearing, despite having different densities and effective stress conditions.

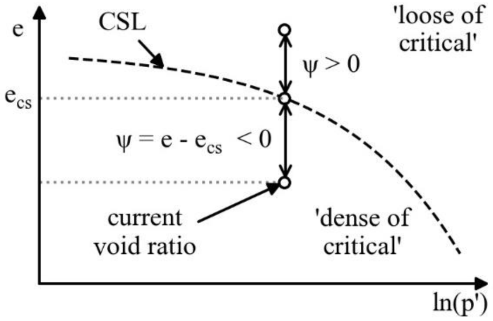

Figure 5.3: Definition of the state paramer, ψ

From Figure 5.3, it is clear that the sign of ψ distinguishes whether the sand is currently in a denser-than-critical ($\psi < 0$) or looser-than-critical ($\psi > 0$) state. This separation has been shown to capture important features of sand behaviour, such as the tendency to dilate or contract when sheared. The magnitude of $|\psi|$ has also been shown to influence behaviour, with larger values exhibiting greater dilative responses and peak strengths, as shown in Figure 5.4. The state parameter framework has therefore been widely adopted as a general framework for modern constitutive models for sands.

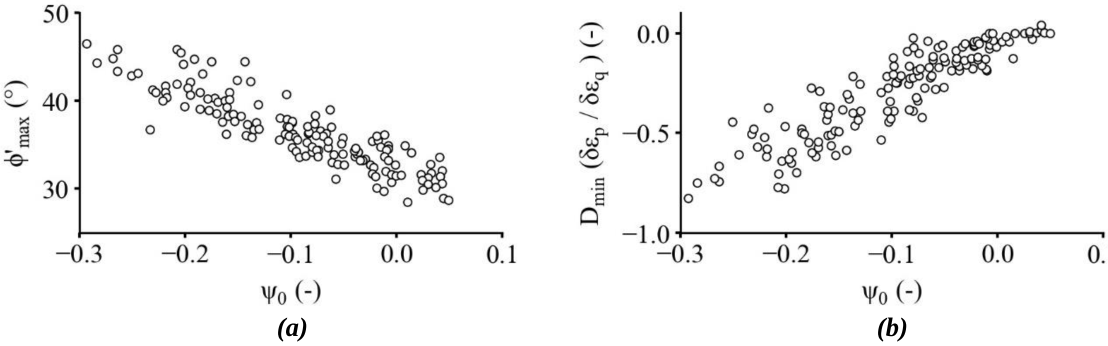

(a) ***(b)***

Figure 5.4: The influence of the initial state parameter, ψ_0, on (a) peak angle of internal shearing resistance; and (b) maximum dilatancy rate (from Jefferies & Been, 2015)

5.1.6. CHARACTERISTIC AND PHASE TRANSFORMATION STATES

Luong (1980) proposed the "Characteristic State" for describing the stress ratio corresponding to the separation point between volumetric compression and dilation in drained triaxial tests. It is obtained from graphs of deviatoric strain, ε_q, against volumetric strain, ε_p, as the point at which the ratio $\delta\varepsilon_p$ / $\delta\varepsilon_q$ tends towards zero. For an entirely contractive sand, the $\delta\varepsilon_p$ / $\delta\varepsilon_q = 0$ condition is reached at the critical state, and the two states may therefore be considered similar. However, for dilative sands, the characteristic state is a transition state reached at a relatively low strain level, while the critical state is an ultimate state that is not achieved until the soil is sheared to large shear strains (Chu, 1995).

The concept of 'Phase Transformation' was introduced by Ishihara *et al*. (1975) to describe the behaviour of sands in undrained triaxial tests, and is defined as the point at which the stress path is observed to change direction the $\delta p' \,/\, \delta q = 0$. Ishihara (1993) describes this point in $p' - q$ space as a transient state, separating contractive and dilative-like behaviours. For relatively loose materials which exhibit entirely contractive behaviour, the state of phase transformation coincides with the critical state.

Georgiannou *et al*. (2008), Chu (1995) and Lade & Ibsen (1997) studied the characteristic and phase transformation states based on drained and undrained shear tests on sands. For a given density and initial mean effective stress, p'_0, they concluded that the phase transformation and characteristic states were similar. Lade & Ibsen (1997) also found that relative density had no influence on the location of the two state lines; however, the gradient of the lines defined in $q - p'$ space was observed to increase with increasing confining pressure, as was also reported by Verdugo & Ishihara (1996).

5.1.7. PHASE TRANSFORMATION AND QUASI-STEADY STATE

Under undrained loading conditions, loose sands sheared at large initial effective confining pressures tend to exhibit a "quasi-steady state" (QSS) (Alarcon-Guzman *et al*., 1988; Been *et al*., 1991). This state is illustrated schematically in Figure 5.5, and is characterised by a peak strength at a low strain level followed by a limited period of strain-softening, followed by continuous dilation to a high strength at a large mean effective stress. The state of minimum strength defines the QSS, and coincides with the point of phase transformation (Ishihara, 1993). This was later confirmed experimentally by Uthayakumar & Vaid (1998).

The QSS shares many similar aspects associated with the definition of steady state given by Poulos (1981); however, for the QSS, the condition of no change in deviatoric stress is only temporary and care is therefore required in interpretation of test data to not mistake the QSS as the steady state.

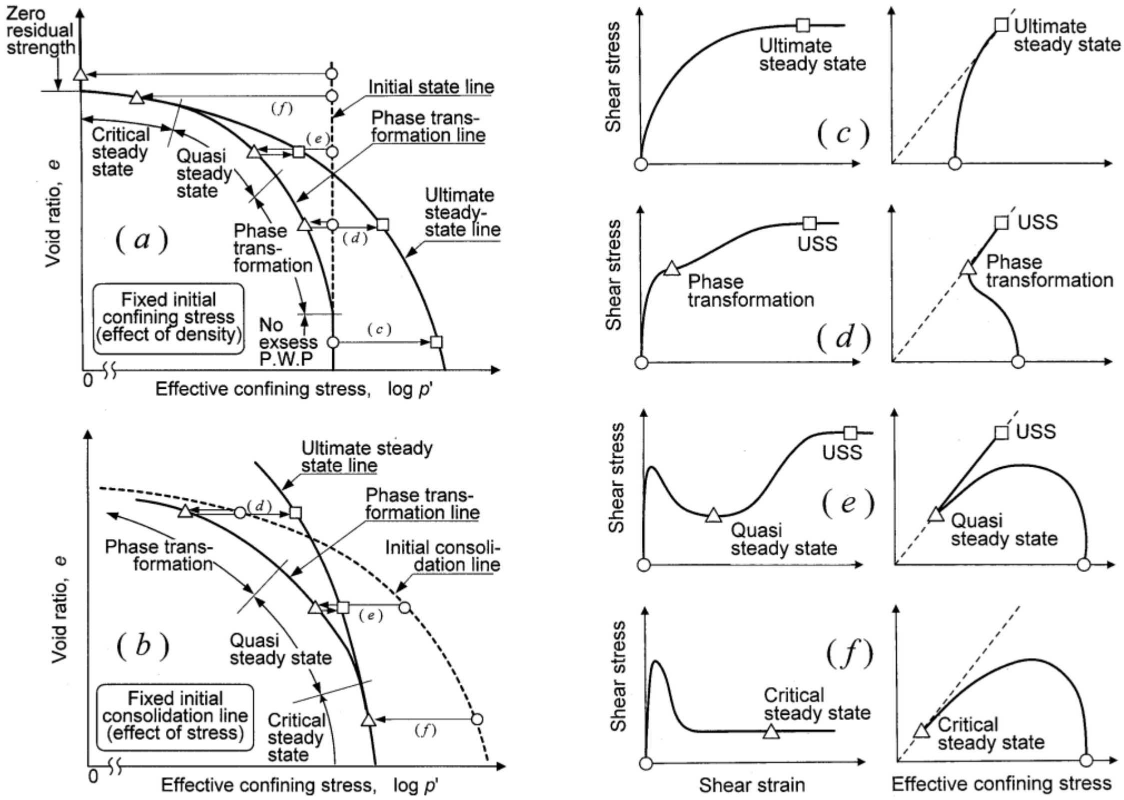

Figure 5.5: Undrained shear behaviour of sand under large deformations (Yoshimine & Ishihara, 1998)

The existence of the quasi-steady state has been the subject of some controversy. Questions have been raised as to the distinction between the quasi-steady and steady state, leading to some researchers (Jefferies & Been, 2015) arguing that erroneous, mis-interpretation of the QSS as the steady state (Konrad, 1993; Vaid *et al.*, 1990) resulted in resistance to the acceptance of state-parameter type approaches. Zhang & Garga (1997) also argued that the QSS is not a real material behaviour, but rather a test-induced phenomenon, mainly attributable to end restraint / friction, but also non-uniform deformation, membrane penetration and sample dimension correction.

However, Vaid *et al*. (1999) observed the QSS in their triaxial tests regardless of the use of lubricated (frictionless) end platens. Furthermore, Yang & Dai (2011) examined the existence of the QSS from a micromechanical perspective, concluding that it is a real soil behaviour rather than a testing phenomenon, and may be regarded as a transient state resulting from spatial rearrangement of discrete particles sheared under the constant volume condition.

5.2. CYCLIC BEHAVIOUR

Cyclic loading generally leads to a breakdown of the soil structure. For fully saturated, undrained conditions, volumetric changes due to dynamic loading are prevented due to the relative incompressibility of water, and instead manifest themselves as changes in the pore water pressure. The tendency for loose soils to contract results in an increase in pore pressure, and the effective stress in the soil decreases accordingly. Each additional stress cycle yields additional incremental pore pressure changes, until the stress path eventually reaches some failure envelope.

5.2.1. NATURE OF STATIC, CYCLIC AND DYNAMIC LOADING

Cyclic loads typically originate from environmental (e.g. waves, wind, earthquakes) or anthropogenic sources (e.g. traffic, machinery rotations, pile driving). The nature of loading in terms of both number of applied cycles and frequency content varies considerably between sources, as illustrated in Figure 5.6.

This means that the loading waveform may be relatively uniform and essentially consist of a single frequency (e.g. vibrating machinery), or somewhat random and contain a range of frequencies (e.g. earthquakes). Multi-directional, multi-amplitude loading can also occur, as is the case for wave and wind loads acting on offshore wind power structures.

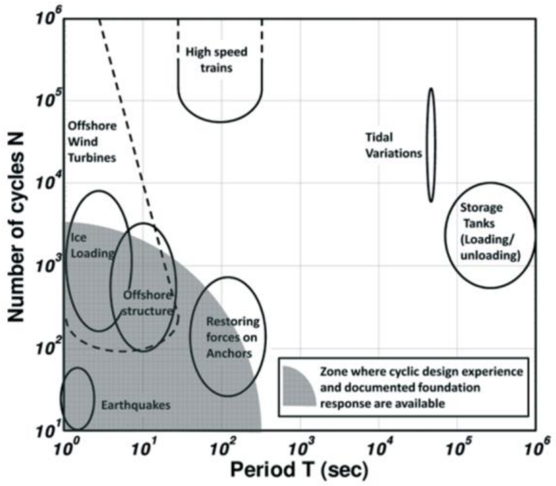

Figure 5.6: Periods and number of cycles charcterising typical cyclic loading events (from Andersen, 2013)

Table 5.1: Typical frequency ranges adopted in cyclic triaxial testing

Loading type	Typical test frequency (Hz)
Wave action	0.1
Wind action	0.1 – 1.0
Earthquake	1.0
Rail transit	>1.0
Vibrating machinery	>60

Static loads are those whose characteristics do not change with time. Conversely, cyclic loads are loads which vary in their magnitude, direction, or position with respect to time. Das & Ramana (2011) define cyclic loads as a particular type of dynamic load which tend to exhibit a degree of regularity both in their magnitude and frequency. For practical purposes, Ishihara (1996) suggests that the division between static and cyclic frequencies is generally in the order of 0.05 – 0.1 Hz. Typical test frequency ranges for various cyclic loading scenarios are presented in Table 5.1.

The duration of extreme cyclic loading events also varies, ranging from one to two days for an offshore storm to less than one minute for most earthquakes (Andersen, 2013). However, critical cases for design are not always governed by these extreme events. A very important feature for offshore monopile foundations, for example, is that they may be subjected to extremely large numbers ($>10^8$) of small-amplitude cycles (Houlsby, 2016). Despite the intensity of these individual loads being relatively trivial, their accumulated effect is likely to be of engineering significance.

5.2.1.1. Cyclic Loading for use in Element Test Programmes

Laboratory element tests are often used to explore the response of a soil subjected to cyclic loading. However, applying complex waveforms to a soil specimen in the laboratory requires sophisticated test systems, and is often impractical from a load control perspective. Therefore, tests are usually restricted to those which can be conducted within feasible timeframes, and at loading frequencies that allow suitable control, precision, and data acquisition rates (Andersen, 2013).

Complex load histories may be transformed into simplified parcels of constant cyclic loads using the ‘rain flow’ procedure (ASTM, 2017; Matsuishi & Endo, 1968), or alternative methods such as that proposed by Norén-Cosgriff *et al.* (2015). Such regular-cycle tests can therefore be defined in terms of the number of cycles, N, the cycle period, T, the average stress, q_{av}, and the cyclic stress amplitude, q_{cyc} (see Figure 5.7). Three types of cyclic loading must also be distinguished:

- Case 1: This case, usually referred to as ‘one way’ or ‘repeated’ loading, involves a fluctuating shear stress that oscillates in $p' - q$ space without ever crossing the p'-axis (i.e. $q_{av} - q_{cyc} \geq 0$). The direction of the major principal effective stress, σ_1', remains fixed throughout the test, and is therefore analogous to a triaxial compression test with variable deviator stress.

- Case 2: This case, usually referred to as ‘two way’ loading, is similar to case 1 in that the orientation of stresses remains fixed; however, the direction of σ_1' switches between the vertical and horizontal throughout the cycle (i.e. $q_{av} - q_{cyc} < 0$). Therefore, the magnitude of the principal stress direction, α (where α is the angle between the direction of the major principal stress and the direction of deposition of the soil), jumps instantaneously between 0° and 90° as the stress point crosses the p'-axis.
- Case 3: This case has both vertical and horizontal stress components, but also includes shear stresses. Because of the shear component, σ_1' is no longer oriented with the reference vertical direction and thus the directions of the principal effective stresses rotate with time as the magnitude of the shear stress varies. This case is analogous to the cyclic simple shear test.

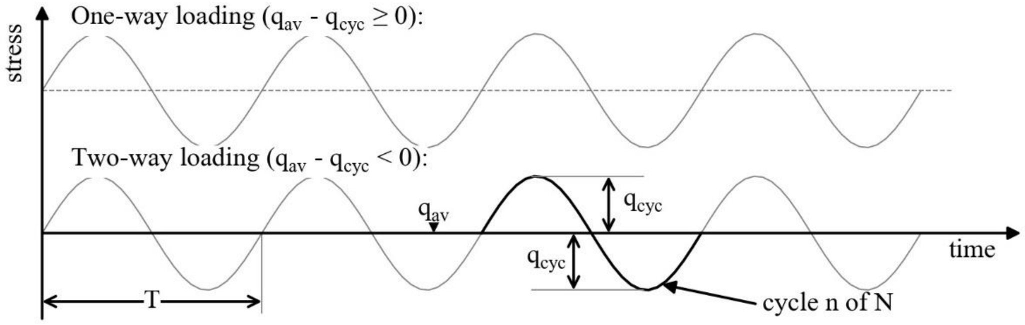

Figure 5.7: Conventional definitions of cyclic loading used in cyclic triaxial test programmes

5.2.2. QUALITATIVE CYCLIC BEHAVIOUR

Several concepts are often used to qualitatively describe the behaviour of soil under cyclic loading, particularly when considering relatively large numbers of cycles. These concepts are illustrated in Figure 5.8, and based on the definitions given by Rascol (2009):

- Adaptation: The cyclic stress-strain hysteresis loop converges to a new elastic state, such that further cycling involves no dissipation of energy. In soils this state is never reached practically, as a small amount of energy dissipation always occurs during cyclic loading.
- Accommodation: The cyclic stress-strain hysteresis loop evolves and accumulates permanent strains, before eventually stabilising and forming a closed hysteresis loop. Energy continues to be dissipated with each cycle; however, no further plastic strains are accumulated.
- Ratcheting: Plastic strain continuously accumulates with each new load cycle. Soil failure is eventually reached if loading continues.
- Cyclic softening: the secant stiffness of the soil decreases with the number of cycles.
- Cyclic hardening: the secant stiffness of the soil increases with the number of cycles.

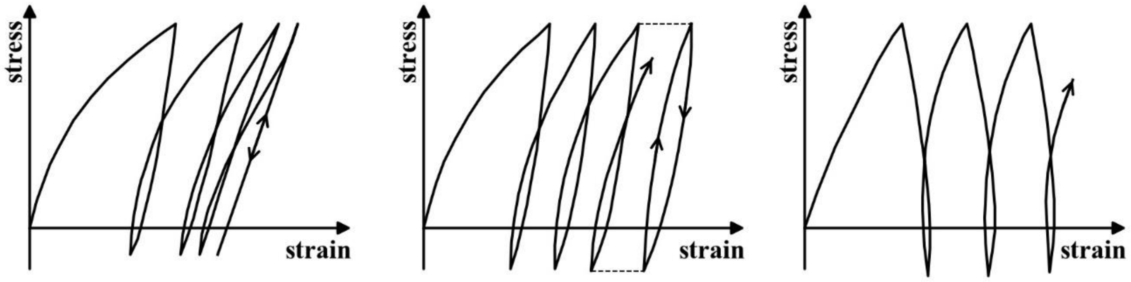

(a) Adaptation *(b) Accommodation* *(c) Ratcheting*

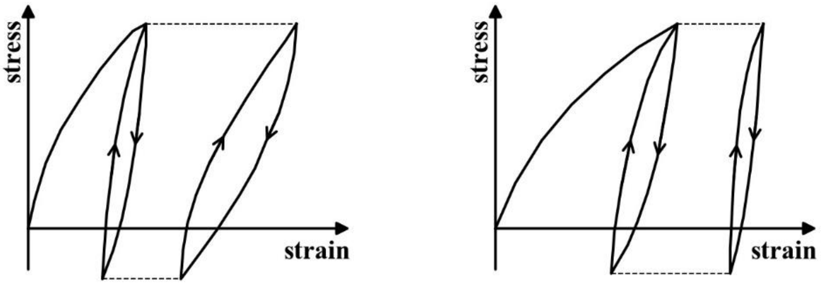

(e) Softening *(f) Hardening*

Figure 5.8: Summary of qualitative descriptions of soil behaviour under cyclic loading (Rascol, 2009)

5.2.3. THRESHOLD STRAINS AND STRAIN-LEVEL RESPONSE

Vucetic (1994) studied published cyclic laboratory test data and examined two types of cyclic threshold shear strains, which represent boundaries between fundamentally different categories of cyclic soil behaviour. These are illustrated graphically in Figure 5.9 and classified as follows:

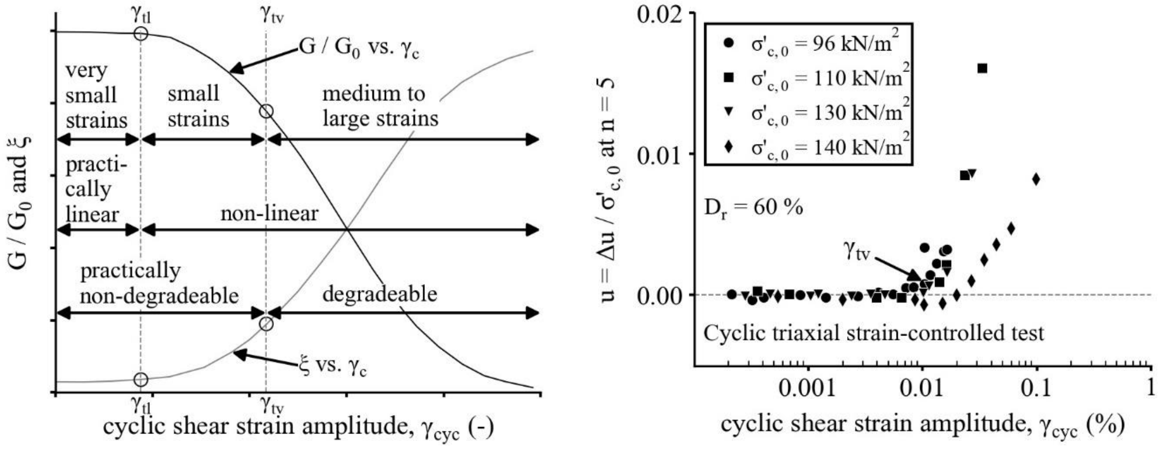

(a) *(b)*

Figure 5.9: (a) Secant shear stiffness degradation curve and damping curve with different zones of cyclic shear strain amplitude (Vucetic, 1994); and (b) effect of mean confining stress on γ_{tv} (Dyvik et al., 1984)

- The linear threshold shear strain, γ_{tl}: Below this strain level (typically $\gamma_{tl} < 10^{-5}$), material behaviour is essentially linear-elastic, and any deformations are recoverable. Theoretically no energy dissipation takes place below γ_{tl}; however, there is some experimental evidence to suggest that limited dissipation takes place even in this very small, pseudo-elastic strain range. For sands, γ_{tl} is usually taken as the shear strain mobilised at G / G_0 = 0.99.

- The volumetric threshold shear strain, γ_{tv}: Above this strain level, soil behaves in an increasingly non-linear and inelastic manner, with significant permanent microstructural changes taking place under cyclic loading.

Dobry, Ladd and co-workers (Dobry & Ladd, 1980; Dobry *et al*., 1982; Ladd *et al*., 1989) undertook the first comprehensive review of γ_{tv} and concluded that for many different types of sands, γ_{tv} is essentially 10^{-4}, regardless of confining stress, density and specimen fabric. However, additional studies have since shown that the magnitude of γ_{tv} in sand tends to increase with OCR, and p' (Dobry, 1991; Dyvik *et al*., 1984; Kim *et al*., 1992).

Between γ_{tl} and γ_{tv}, (i.e. $10^{-5} < \gamma < 10^{-4}$) the soil behaves in a markedly non-linear way, but remains largely elastic because permanent changes of its microstructure do not occur or are negligible. The soil shear stiffness, G and energy loss factor, ξ, therefore remain constant with increasing numbers of cycles. This kind of behaviour is known as 'non-degraded hysteresis' behaviour (Ishihara, 1996), and may be modelled with reasonable accuracy using linear-viscoelastic models.

However, once γ_{tv} is exceeded, (i.e. $10^{-4} < \gamma < 10^{-2}$) soil properties tend to change considerably with both γ and increasing numbers of cycles. Non-linear hysteresis loops are formed, their breadth depending on the magnitude of the induced shear strain. This type of response, known as 'degraded hysteresis' behaviour (Ishihara, 1996), is characterised by G and ξ evolving with the number of cycles due to either changes in the effective confining stress resulting from excess pore-water pressure development (for undrained cyclic loading), or permanent volume changes (for drained test conditions). The Masing law is typically used to describe the stress-strain relationship at each stage of loading (i.e. first loading, unloading and reloading).

5.2.4. PORE PRESSURE RESPONSE TO CYCLIC LOADING

Excess pore pressures tend to increase when soils are subjected to undrained cyclic loading in cyclic triaxial tests, eventually approaching a value equal to the initial effective cell pressure, $\sigma'_{c,0}$. Excess pore pressures are therefore typically expressed as the pore water pressure ratio, R_u, where:

$$R_u = \frac{\Delta u}{\sigma'_{c,0}} = \frac{\Delta p'}{p'_0} \tag{5-5}$$

where:

Δu = excess pore water pressure
$\sigma'_{c,0}$ = initial effective confining stress

For loose sands, the first instance of R_u = 1.0, termed ‘initial liquefaction’ by Lee & Seed (1967), is immediately followed by significant deformation and a sudden and complete loss of strength. Medium-dense to dense sands also undergo a state of softening on achieving 100 % pore water pressure build-up, but subsequent deformations do not grow indefinitely large and complete loss of strength does not occur (Ishihara, 1996). However, significant cyclic strains are mobilised following this condition, which is why the state of 100 % excess pore pressure build-up (i.e. R_u = 1.0) is often used as a measure of cyclic instability.

Dobry *et al*. (1982) investigated the build-up up of pore pressures and liquefaction susceptibility of sands and found that there is a predictable correlation between the cyclic shear strain amplitude and the excess pore water pressures developed. They also suggested that no excess pore pressures will develop if cyclic shear strains remain lower than the threshold strain (described in Section 5.2.3), due to no inter-particle sliding occurring at the particle contacts.

Erten & Maher (1995) investigated the influence of silt content on the development of pore pressures in sand. They found that there is a significant increase in the pore pressures developed at strain levels higher than the threshold strain in those soils with increased fines content. Ishihara (1996) also states that pore pressure build-up in sandy soils containing some amount of fines tends to stop increasing over a value of R_u = 0.9 to 0.95. However, as with medium-dense to dense clean sands, significant cyclic shear strains are mobilised. Furthermore, tests that involve no stress reversal may not necessarily reach 100 % pore pressure build-up, yet significant permanent plastic strains are accumulated. The failure of some soil types or test conditions to ever achieve R_u = 1.0 is one reason why limiting double amplitude strains (usually 5 %) are often preferred as the failure criterion over the onset of so-called ‘initial liquefaction’. Failure definitions are discussed in detail in Section 5.2.6.

5.2.5. LIQUEFACTION RELATED PHENOMENA

The development of excess pore pressures and the associated reduction of mean effective stress under undrained loading conditions is a hallmark of all liquefaction phenomena. Historically, liquefaction related phenomena have been classified as either ‘flow liquefaction’ or ‘cyclic mobility’. A proper understanding of the behaviours associated with these phenomena is therefore important if the response of saturated soils subjected to cyclic loading is to be evaluated.

5.2.5.1. *Flow Liquefaction*

The term ‘static’ or ‘flow’ liquefaction is often adopted to describe the phenomenon in which loose sands lose a large percentage of their shear resistance and flow in a liquid manner when subjected to undrained monotonic loading (Castro, 1969). This type of behaviour is illustrated in Figure 5.10 and is associated with relatively loose soils that lie above the CSL (i.e. $e_0 > e_{cs}$; $\psi_0 > 0$).

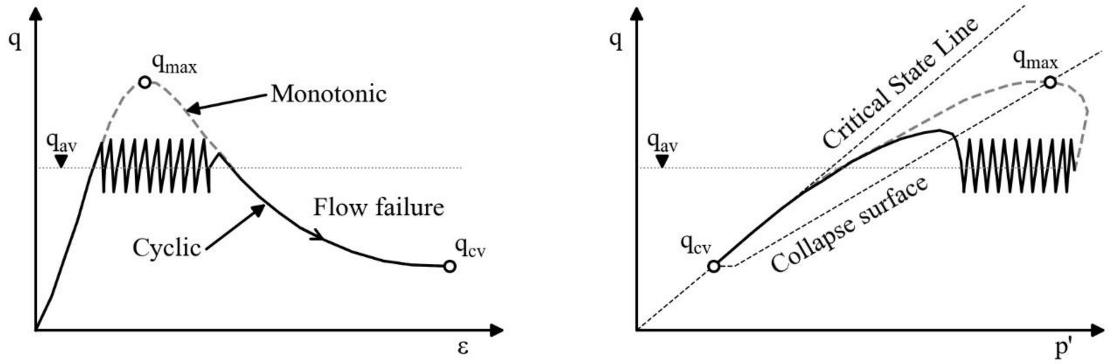

(a) ***(b)***

Figure 5.10: Flow liquefaction stress paths in monotonic and cyclic triaxial tests

When sheared, these soils exhibit an easily identifiable maximum shear strength, q_{max}, at relatively small strains, and then flow rapidly to large strains as at low mean effective stresses. According to Kramer (1996) axial strains in element tests may increase from less than 1 % to more than 20 % in a fraction of a second. This behaviour occurs because the mobilised shear stress required for the static equilibrium of the soil mass increases beyond the shear strength of the liquefied soil.

‘Flow with limited liquefaction’ may also occur. In this case, rather than contracting immediately to the critical state following mobilisation of q_{max}, the material softens to a minimum value coinciding with the QSS, before dilating towards the steady state. However, in practical terms the distinction between the two cases is unimportant as the strains generated during softening are likely to be above permissible thresholds for most geotechnical structures. It is also important to note that relatively dense soils (i.e. $e_0 < e_{cs}$; $\psi_0 < 0$) are not susceptible to flow liquefaction type behaviour (Kramer, 1996). After initially contracting, dense specimens tend to dilate towards critical state conditions at relatively large axial strains (e.g. $\varepsilon_z > 25$ %). The CSL therefore provides a useful tool in determining the susceptibility of a soil to flow liquefaction.

5.2.5.2. *Flow Liquefaction Surface*

Figure 5.11 shows a graphical representation of a ‘Flow Liquefaction Surface’ (FLS) (Kramer, 1996). This surface is similar to the ‘critical effective stress ratio’ proposed by Vaid & Chern (1983), and provides a useful framework for describing the conditions required to initiate flow liquefaction.

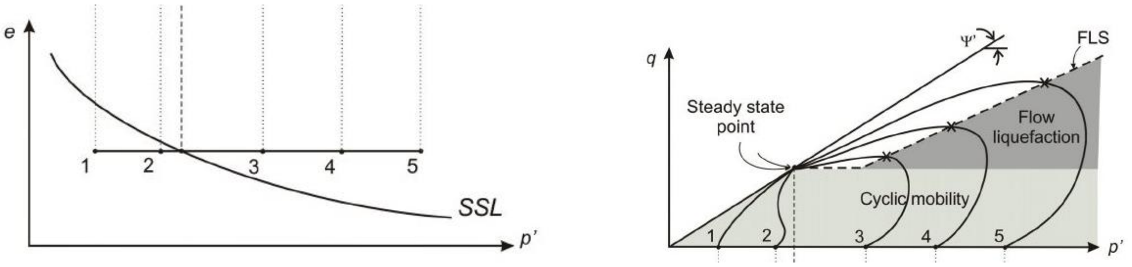

(a) ***(b)***

Figure 5.11: (a) Response of five specimens isotropically consolidated to the same void ratio and sheared from different initial effective stresses; and (b) orientation of the FLS in p'-q space (after Kramer, 1996)

Several researchers (Hanzawa *et al.*, 1979; Olson & Stark, 2003) suggested that a locus going through the effective stress conditions at the onset of flow liquefaction (i.e. q_{max}) is a straight line, that projects through the origin in $p' - q$ space. However, since flow liquefaction cannot occur for samples that are located below the CSL, the FLS is truncated at the deviatoric stress conditions at critical state. The FLS therefore marks the boundary between stable and unstable states in undrained shear. If the stress conditions in an element of soil reach the FLS under undrained conditions, whether by monotonic or cyclic loading, flow liquefaction will be triggered, and the strength of the soil will be reduced to the critical state strength.

5.2.5.3. *Cyclic Mobility*

Cyclic mobility is another liquefaction phenomenon that can lead to the accumulation of significant permanent deformations. However, unlike flow liquefaction, it is difficult to define the point at which cyclic mobility is initiated. Furthermore, both loose and dense soils are susceptible to cyclic mobility, which occurs when the static shear stress is less than the liquefied strength of the soil. Therefore, any stress state that plots below the upper shaded region of Figure 5.11b is susceptible to cyclic mobility.

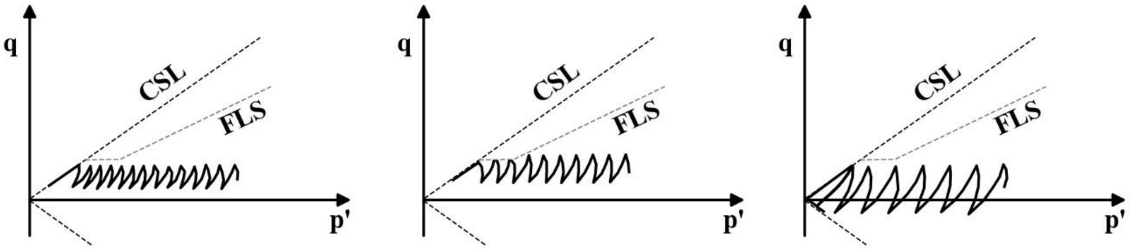

(a) *(b)* *(c)*

Figure 5.12: Three cases of cyclic mobility (from Kramer, 1996)

Figure 5.12 illustrates the three initial state and cyclic loading combinations generally required to produce cyclic mobility (Kramer, 1996):

a. No shear stress reversal and no exceedance of steady state strength: Development of excess pore water pressure causes the effective stress path to move to the left until it reaches the drained failure envelope. For any additional loading cycles, the stress path moves up and down along the envelope.
b. No shear stress reversal and momentary periods of ultimate state strength exceedance during cycling: Each time the stress path reaches the FLS, momentary periods of instability occur causing permanent significant straining.
c. Shear stress reversal and no exceedance of steady state strength: Once the stress path reaches the drained failure envelope, it oscillates along the compression and extension portions passing instantaneously through the origin ($p' = 0$). Significant permanent strains may accumulate, but flow failure cannot occur. The first instance of $p' = 0$ occurring may be referred to as ‘initial liquefaction’ (Lee & Seed, 1967); however, that is not to say that the soil has no shear strength – subsequent monotonic loading will show strain-hardening (dilative) behaviour until it reaches the steady point.

5.2.6. Failure Criteria under Cyclic Stress Conditions

Contrary to monotonic loading tests where failure conditions are relatively easy to identify, the definition of failure conditions in cyclic loading problems can be chosen in many different ways. Historically, failure criteria were developed in relation to liquefaction susceptibility research. These criteria were typically based on either the build-up of excess pore pressures or some double-amplitude strain within a sample. This has led to numerous definitions of ‘soil liquefaction’ and inevitable inconsistencies within the geotechnical community over the years.

5.2.6.1. Pore Water Pressure Based Criteria

Pore water pressure criteria capture some vital elements of the mechanism of liquefaction; and as a result, it is appealing to researchers who actually measure the change of pore pressure in the laboratory. When based on pore pressure related criteria, failure has often been defined as the state at which liquefaction initially occurs, i.e. the moment at which the excess pore water pressure ratio, $R_u = 1$. However, as discussed in Section 5.2.4, Ishihara (1993) found that R_u in silty sands may stop increasing beyond 90 to 95 % of the initial confining stress. Therefore, if failure was strictly defined as the occurrence of ‘initial liquefaction’ at R_u 1.0, these soils would never technically ‘liquefy’ despite behaving as liquefiable materials for all practical engineering purposes.

5.2.6.2. Strength Based Criteria

Changes in soil strength due to cyclic loading are often of great concern for the overall stability of structures. Strength-based criteria therefore also exist; however, given that soil strength is a function of the mean effective stress, this definition is essentially equivalent to the pore water pressure criteria definitions, and consequently suffers from the same previously discussed shortcomings.

5.2.6.3. Strain / Deformation Based Criteria

Cyclic shear strain and deformation serve as good criteria for dynamic performance assessment purposes. The response of most structures to cyclic loading is strongly linked to the performance of the soils on which they are built. Defining failure based on some limiting cyclic or permanent strain therefore serves as a good criterion for dynamic performance assessment purposes.

Yet according to Wu *et al*. (2004), this type of failure criterion was not initially as popular as pore pressure or shear strength criteria. This may in part be due to many researchers tending to regard shear strain/deformation in soils as a consequence of liquefaction. This misconception quickly became obsolete, as it is now accepted that shear deformations and pore pressure (and thus effective stress and strength) are all closely interrelated. However, while the shear strain/deformation failure criterion seems to be the preferred basis for performance-based engineering, it potentially suffers from some serious limitations.

One such limitation is the influence of the applied mode of deformation (i.e. triaxial or simple shear) on the type of mobilised strain. For example, while shear strain may be obtained from undrained cyclic triaxial tests (Eq. (4-18)), to allow comparisons with cyclic simple shear test data, drained cyclic triaxial test data is typically limited to measurement of axial strain. Different strain criteria have therefore developed for different deformation shear modes and test conditions. In cyclic triaxial testing, Ishihara (1993) suggests 5 % double-amplitude axial strain, ε_{da}, as a criterion to define the occurrence of liquefaction / cyclic softening for both clean sands and sands with fines. Whereas for cyclic simple shear tests, a value of 3 % single-amplitude shear strain, γ_{sa}, was proposed.

This has led to another potential limitation in that there is no consistent, recommended value associated with these limiting strains (values ranging between 2 and 10 % have been proposed in the literature). Furthermore, strain-based liquefaction criteria are also sometimes used interchangeably with strain-based failure criteria, such as the ε_{da} = 20 % value proposed by Lee & Seed (1967) and given in the ASTM cyclic triaxial standard (ASTM, 2015).

Furthermore, these values have largely been developed in relation to liquefaction susceptibility research, where the test material is subjected to relatively few high amplitude, two-way stress cycles. These failure criteria definitions may therefore be inappropriate when considering other design situations, such as an offshore wind structure, which is subjected to very different cyclic stress conditions. Nielsen *et al*. (2012) suggest that when analysing cyclic tests, failure modes may be separated into two main groups. Tests in which permanent, or residual shear strains, γ_p, dominate, were subjected to one-way loading and failed by incremental collapse. While the other group of tests, subjected to two-way loading, were dominated by cyclic strains, γ_{cyc}, and failed due to liquefaction.

Nielsen *et al*. (2012) defined failure as either the point at which γ_p = 15 % or γ_{cyc} = 15 %. This is similar to the failure criterion adopted by the Norwegian Geotechnical Institute (NGI) who define failure as the point where either the average strain, γ_{Av}, or γ_{cyc} reaches 15 % (Andersen, 2015). The difference between the use of γ_p and γ_{Av} (defined in Section 7.2.2) in the above-mentioned failure definitions is relatively minor for all practical purposes; however, it again illustrates the lack of a consistent and robust framework for defining failure criteria in cyclic element tests.

5.2.7. EVALUATION OF CYCLIC SHEAR STRENGTH

Cyclic strength is an important design consideration in the evaluation of a soil's dynamic performance. Although there is much detail in the cyclic stress–strain response, cyclic strength is commonly represented in terms of a fatigue model, in which the number of cycles to a particular failure criterion, N_f, is taken as the basic result of the cyclic triaxial test. Typically, results are presented in terms of the cyclic stress ratio, CSR, vs N_f, where CSR is the shear stress induced by the dynamic load as a fraction of the initial effective confining pressure, and is calculated from:

$$CSR = \frac{q_{cyc}}{2\sigma'_{c,0}} \tag{5-6}$$

It has been customary to select 10 or 20 cycles as N_f; however, in principle, this value is entirely arbitrary and was adopted due to it being similar to the typical number of significant cycles present in earthquake acceleration time-history records (Ishihara, 1996). Cyclic strength is then defined as the cyclic stress ratio required to cause 'failure' (i.e. ε_{da} =5 %) after e.g. 20 stress cycles.

5.2.8. CONNECTIONS BETWEEN MONOTONIC AND CYCLIC RESPONSE

Alarcon-Guzman *et al*. (1988) performed undrained monotonic and cyclic torsional shear tests on saturated sand samples, and found that the undrained monotonic stress path constituted a state boundary surface that controlled the initiation of strain softening under undrained cyclic loading. However, cyclic and monotonic triaxial tests undertaken by Vaid & Chern (1985) showed that flow liquefaction was initiated once the cyclic stress path intercepted the flow liquefaction surface (defined in Section 5.2.5.2).

Cyclic triaxial tests performed by Hyodo *et al*. (1994) to help clarify the issue remained inconclusive. More recently, Georgiannou *et al*. (2008) undertook a series of cyclic torsional shear tests using hollow cylinder apparatus, and found density to be an influencing factor, with looser material exhibiting flow liquefaction at the point of crossing the FLS, while denser materials showed instability as they approached the phase transformation line. Yang & Sze (2011) also found some difference in the points at which flow deformation was triggered in their cyclic and monotonic triaxial tests, and attributed the discrepancy to the use of stress-controlled loading in cyclic tests but of strain-controlled loading in monotonic tests.

5.3. INFLUENCE OF CYCLIC TEST VARIABLES

Figure 5.13 shows the stress-strain behaviour of a saturated medium-dense sand subjected to undrained cyclic loading. For sufficiently low cyclic stress amplitudes, the soil will exhibit only contractive tendencies, resulting in increases to excess pore pressures and decreases to the mean effective stress. The cyclic stress path will therefore migrate leftwards in $p' - q$ space until it intercepts the phase transformation line (PTL).

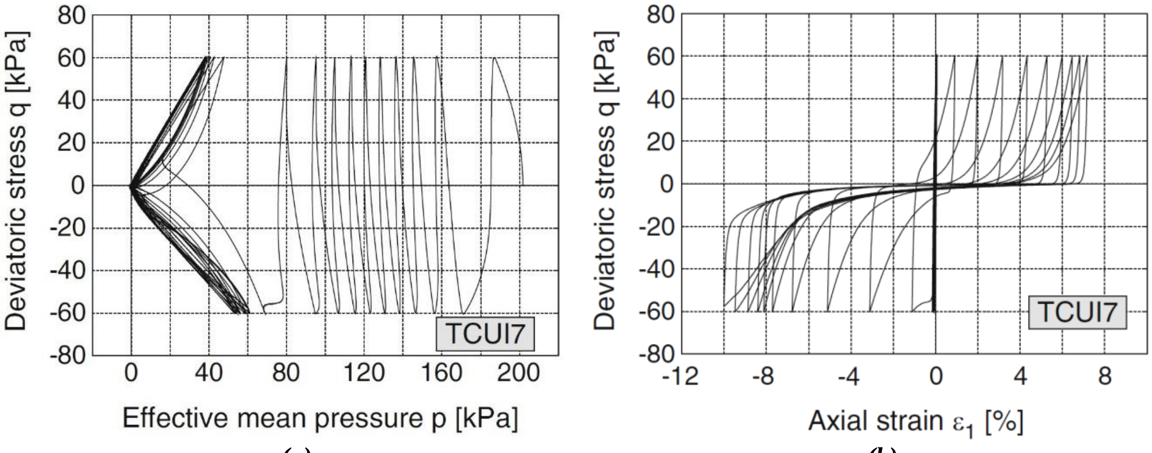

(a) *(b)*

Figure 5.13: Undrained cyclic behaviour of a medium-dense sand (Wichtmann & Triantafyllidis, 2016)

As defined in Section 5.1.7, the phase transformation state marks the boundary between contractive and dilative behaviour. Large strains are rapidly mobilised on approach and during transition;

however, once the PTL is crossed, the soil tends to dilate, excess pore pressures decrease, mean effective stresses increase and the cyclic stress path moves to the right. The shear strength and stiffness of the material rapidly increase with dilation, thereby limiting the mobilisation of further excessively large strains. Similar behaviour occurs on unloading, leading to the characteristic 'butterfly' profile arising from alternate phases of dilation (hardening) and densification (softening).

This type of behaviour, known as 'cyclic mobility' (see in Section 5.2.5.3), tends to be limited to clean sands and non-plastic silts with relative densities above 45 % (Seed, 1979). While large, liquefaction-induced cyclic shear strains continue to accumulate with stress cycles, complete loss of strength and subsequent flow-type failure – characteristic of relatively loose soils – does not occur.

Historically, investigation into the behaviour of sand subjected to cyclic loading was dominated in the literature by geotechnical earthquake engineering researchers, and the need to develop robust liquefaction-susceptibility design guidelines. The response of loose sand to relatively high stress amplitude, low-cycle number cyclic loading has therefore been extensively investigated using cyclic triaxial, cyclic simple shear, and cyclic torsional shear tests, as summarised in a series of comprehensive state-of-the-art reviews (Finn, 1981; Seed, 1979; Townsend, 1978; Yoshimi *et al*., 1977). These early studies showed that the liquefaction resistance of laboratory-reconstituted clean sand to cyclic loading is primarily influenced by the initial state, the intensity of shaking, and the number of cyclic stress applications.

However, as described in Section 5.2.1, the cyclic loads appropriate for the design of earthquake hazard resistant structures are very different to those used in the design of offshore wind energy structures. Such structures are typically subjected to millions of relatively low-stress amplitude cycles. Limiting the gradual accumulation of permanent deformation over the design life of the structure therefore becomes important if serviceability limit design criteria are to be satisfied.

Despite the large body of cyclic triaxial test data available, comparison of data between different soils and different testing laboratories can be confusing as there are numerous testing factors that influence the test results. The following sections therefore examine some of the factors found to influence sand response, with a particular emphasis on the accumulation of permanent strains following application of large numbers of cycles.

5.3.1. INFLUENCE OF THE NUMBER OF CYCLES

According to Jefferies & Been (2015), soil shows fatigue-like behaviour in that much the same result is obtained with many low amplitude cycles as a few large cycles. Frameworks that capture both high- and low-cycle response are therefore preferred over those requiring some artificial distinction. Figure 5.14 presents three idealised strain cases given in Wichtmann (2005) used to qualitatively describe the relationship between accumulated residual strains, ε_{acc}, and cycle number, n, where:

- Stepwise failure: residual strains are observed to increase linearly with cycle number.
- Shakedown: the magnitude of residual strain decreases with cycle number and eventually stabilises. Only elastic strains need to be considered in the following cycles. This is similar to the 'Accommodation' case defined in Section 5.2.2.
- Abation: the rate of residual strain accumulation decreases with each cycle, but never completely disappears (e.g. $\varepsilon_{acc} \sim \ln(N)$). This is equivalent to the 'Ratcheting' case defined in Section 5.2.2.

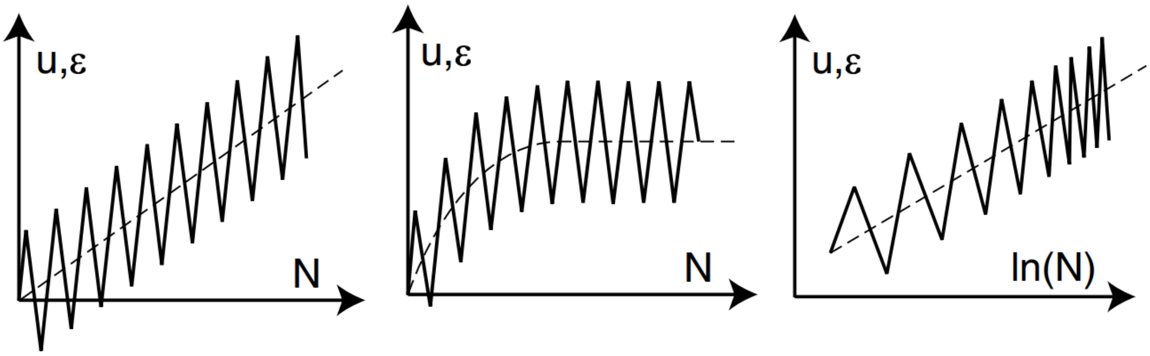

(a) *(b)* *(c)*

Figure 5.14: Distinction of the deformation behaviour of a foundation (dispalcement, u) or a soil specimen (strain, ε) under cyclic loading: (a) stepwise failure; (b) shakedown; (c) abation (from Wichtmann, 2005)

Figure 5.15 shows plots of accumulated strain with cycles found in the literature. Figure 5.15a shows drained cyclic triaxial test results from Lentz & Baladi (1980), who found the accumulated axial strain to increase linearly with the logarithm of the number of cycles. A similar relationship is shown in Figure 5.15b; however, Wichtmann (2005) suggests that the increase of the residual strain with the number of cycles is proportional to $\ln(N)$ only up to $N = 10^4$. Beyond this, over-logarithmical curves were obtained, which Wichtmann (2005) attributes to abrasion at the particle contacts.

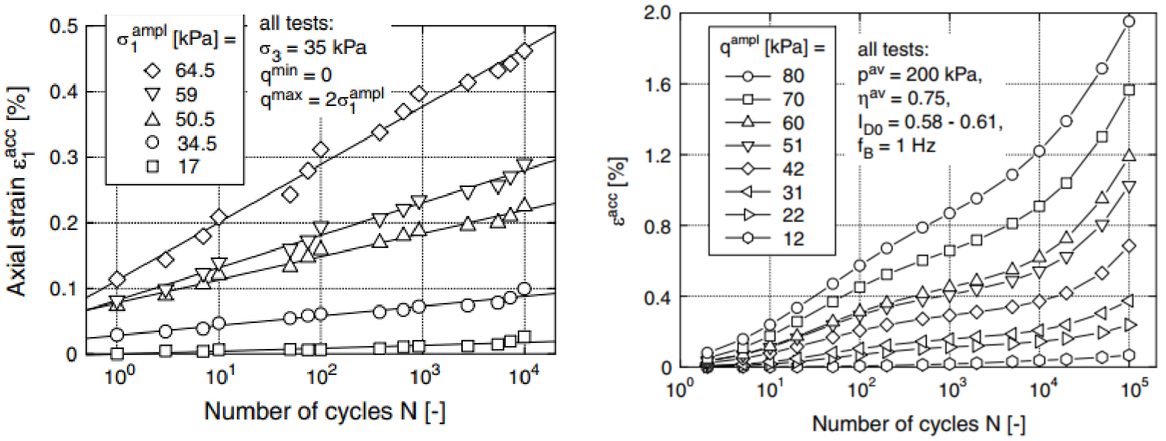

(a) (Lentz & Baladi, 1980) ***(b) (Wichtmann, 2005)***

Figure 5.15: Influence of the number of cycles on accumulated axial strain

5.3.2. INFLUENCE OF FREQUENCY

The influence of frequency, f, has been examined by many researchers (e.g. Hardin, 1965; Peacock & Seed, 1968; Tatsuoka *et al*., 1986; Wong *et al*., 1975), who found virtually no significant effect of loading rate on the dynamic properties of sands. Wichtmann (2005) examined the effect of frequency in relation to the accumulation rate of permanent residual strains, and concluded that for the tested range of $0.05 \le f \le 2$ Hz, f had no influence on the accumulation rate.

5.3.3. INFLUENCE OF FABRIC

Early studies (Ladd, 1974, 1977; Mulilis *et al*., 1977; Tatsuoka *et al*., 1986) also found the cyclic resistance of sand to vary depending on the fabric created by different sample reconstitution techniques, with air pluviation and moist tamping methods shown to produce the lowest and greatest resistance to liquefaction, respectively. Similar conclusions were reported more recently by Sze & Yang (2014). Ishihara (1996) therefore recommends that cyclic element tests be conducted on undisturbed samples if the dynamic response of in situ sand deposits is to be evaluated with any reasonable level of confidence.

5.3.4. INFLUENCE OF STATIC BIAS AND CYCLIC STRESS AMPLITUDE

Cyclic triaxial testing often includes anisotropic consolidation to give an initial average stress, or static bias. Historic research investigating the influence static bias on the occurrence of flow deformation (Castro, 1975; Hyodo *et al*., 1991; Lee & Seed, 1967; Mohamad & Dobry, 1986; Vaid & Chern, 1983) was conflicting, concluding that an initial static bias either improves or deteriorates the resistance to flow deformation.

As described in Section 5.2.8, the monotonic stress path defines a collapse boundary surface (Alarcon-Guzman *et al*., 1988; Georgiannou *et al*., 2008; Vaid & Chern, 1985). In symmetrical two-way loading (i.e. no static bias), the first indication of large strains occurs in extension since the critical friction ratio in extension, M_{te}, is less than in compression, M_{tc} (Jefferies & Been, 2015). With a constant cyclic deviator stress, a positive static bias therefore reduces the excursion into triaxial extension space during each stress cycle. The cyclic strength or resistance to liquefaction may therefore increase, as the cycle approaches the compression and extension instability surfaces at the same time. However, a larger static bias will decrease the cyclic strength by bringing in the compression failure mode more quickly. This is illustrated schematically in Figure 5.16.

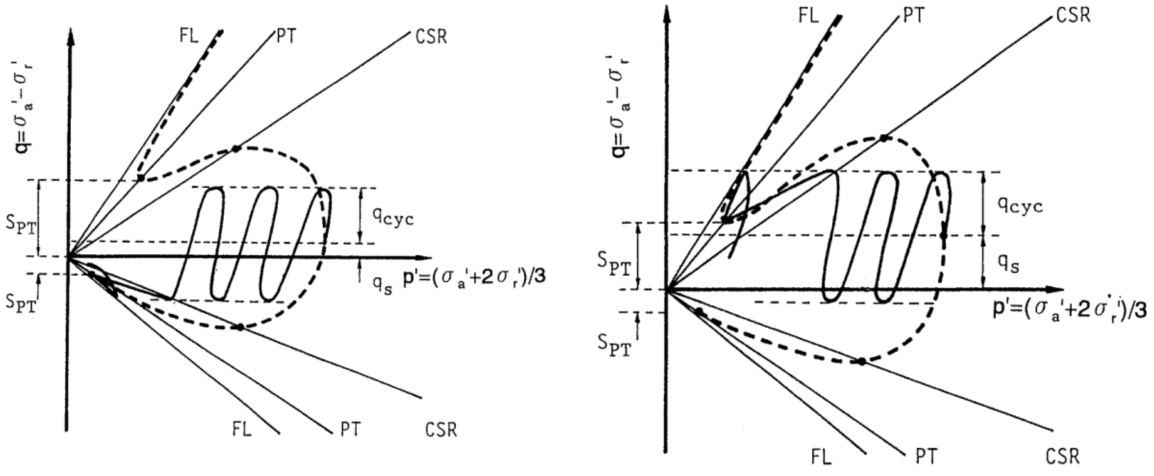

(a) *(b)*

Figure 5.16: Schematic diagram outlining the initiation of cyclic instability based on initial static bias (from Hyodo et al., 1994)

5.3.5. INFLUENCE OF STATE

As discussed in Section 5.1.5, the mechanical response of a sand is largely governed by its state (density and stress level). Vaid & Chern (1983) performed undrained cyclic triaxial tests on Ottawa sand, to investigate the influence of D_r on the CSR needed to cause specified levels of strain in 10 stress cycles. Results showed that resistance to liquefaction increases significantly for $D_r > 60$ %.

Wichtmann (2005) investigated the influence of void ratio and mean effective stress on the rate of strain accumulation in a series of high-cycle, drained cyclic triaxial tests. Figure 5.17a shows that the accumulation rate increases with increasing void ratio. Figure 5.17b shows that the influence of p' on the accumulated residual strain is negligible until $N > 10^4$, after which the curves diverge, with larger values of ε_{acc} mobilised at smaller effective stresses.

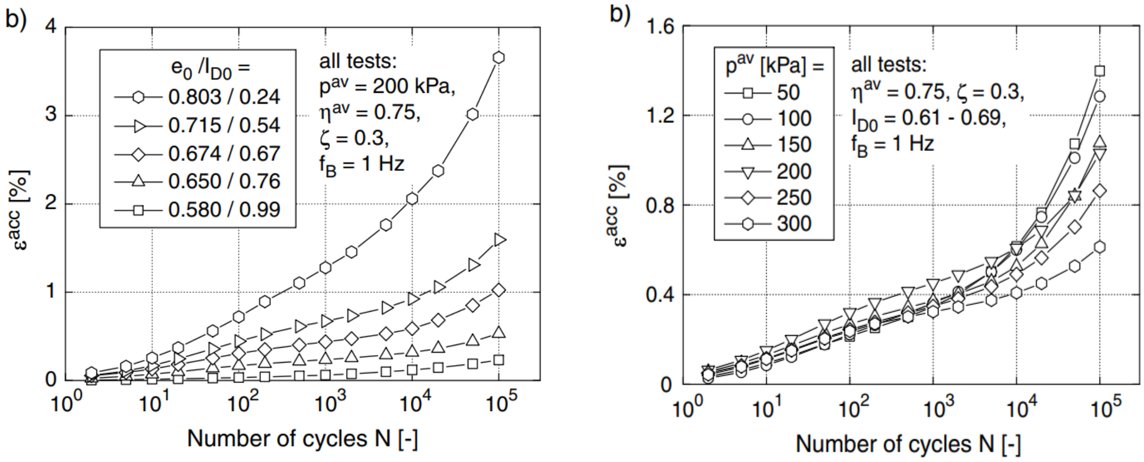

(a) *(b)*

Figure 5.17: Influence of sand state in terms of (a) relative density, and (b) mean effective stress, on the accumulation of residual strain (from Wichtmann, 2005)

According to Ishihara (1996), all cyclic shear tests ever performed on sands indicate a tendency for cyclic strength to decrease with increasing confining stress. This is evident from Figure 5.18, which shows a summary of cyclic triaxial test results from 13 sands compiled by Jefferies & Been (2015). The plot shows the cyclic stress ratio, CSR (defined in Section 5.2.7) vs the number of cycles required to reach a given failure criterion N_f. All tests were isotropically consolidated, with relative densities ranging from 30 to 80 %. Figure 5.18a shows significant scatter. This is expected as the data have not been normalised, and are therefore subject to the influences of the aforementioned factors.

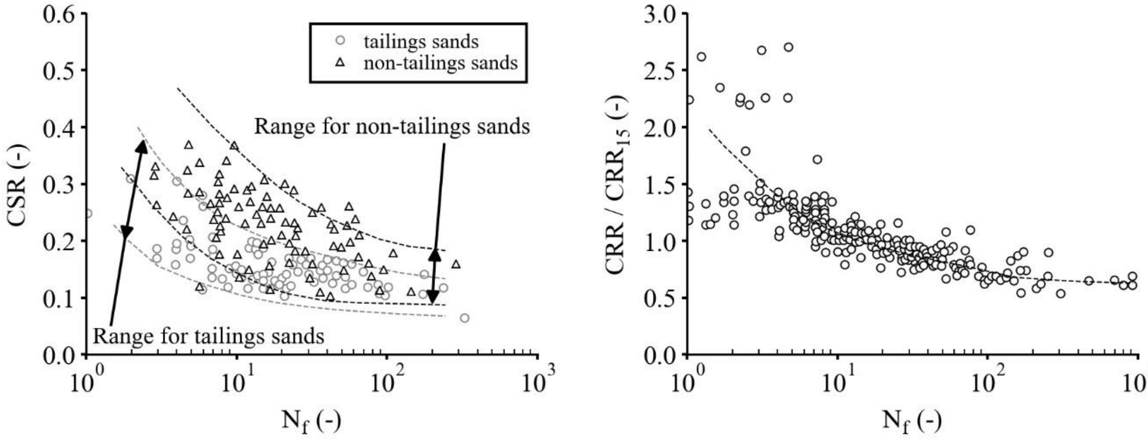

(a) *(b)*

Figure 5.18: (a) Cyclic triaxial test data on 13 sands for which the CSL is known; (b) results normalised by the CSR required to cause failure after 15 cycles, CRR$_{15}$ (from Jefferies & Been, 2015)

However, despite the large range in behaviour, Jefferies & Been (2015) suggest that there is actually a simple underlying behavioural trend. For any given sand, state parameter and sample preparation procedure, normalising the CSR by the CSR that results in liquefaction failure after 15 cycles, a relatively narrow band now fits the data (Figure 5.18b), and the trend smoothly extends from a few cycles to nearly a thousand cycles. Jefferies & Been (2015) call this normalised strength as the 'cyclic resistance ratio', CRR, which is the CSR that causes failure after a given number of cycles. Jefferies & Been (2015) therefore propose that the complex, multi-variable situation described above, has now been largely reduced to understanding how state and fabric control CRR_{15}.

Figure 5.19 shows a graph of CRR_{15} vs. the state parameter, ψ, and a reasonable trend is obtained. Jefferies & Been (2015) suggest that the scatter of results is likely to be due to the influence of fabric, which is not captured by ψ, and comment that the error band of CRR_{15} shown in Figure 5.19 (approximately ±0.1), is consistent with studies investigating the influence of sample preparation technique on cyclic stability (e.g. Ladd, 1977).

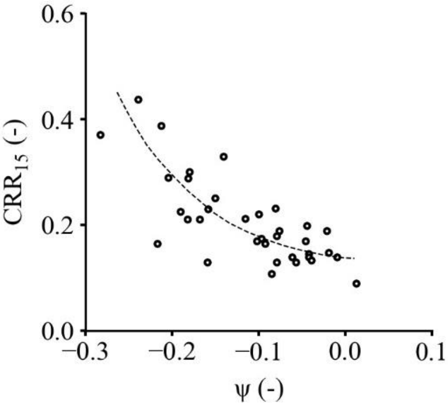

Figure 5.19: CRR$_{15}$ as a function of state parameter for sands (from Jefferies & Been, 2015)

6. MONOTONIC TRIAXIAL TESTS

6.1. INTRODUCTION

This chapter presents results of monotonic triaxial tests undertaken on 100 mm diameter samples of Leighton Buzzard (Fraction B) sand (LBS-B). As described in Chapter 2, there are conflicting views in the literature regarding the behaviour of sand at very low stress levels. The primary aim of this study was therefore to investigate the constitutive behaviour of sand at such low (less than 50 kN/m^2) effective confining stresses, and, with the aid of modern, commercially available triaxial testing apparatus, provide the additional experimental evidence needed to clarify the issue.

The secondary aim of the test programme was to produce a suite of tests that could be readily used to calibrate nested-surface, kinematic-hardening type constitutive models such as the Prévost model (Prévost, 1985) described in Chapter 8. Despite the large quantity of triaxial tests undertaken on sands published in the literature, freely available numerical data comprising both compression and extension test results are extremely limited. According to Cerfontaine (2014), the VELACS (Verification of Liquefaction Analyses by Centrifuge Studies) programme (Arulmoli *et al*., 1992), is the only freely available triaxial test database containing the necessary tests required to fully calibrate a nested-surface, kinematic-hardening type model.

As discussed in Chapter 8, nested surface, kinematic hardening models are identified as a potentially useful tool for modelling the long-term behaviour of offshore wind turbine (OWT) foundations installed in the North Sea and elsewhere. North Sea sand formations tend to be relatively uniform and have high (greater than 80 %) relative densities (Bjerrum, 1973); however, the majority of the VELACS test programme was undertaken on 63.5 mm diameter samples of Nevada Sand at relative densities of approximately 40 % and 60 %. Calibration and further development of such models for use in the design of North Sea OWT foundations would therefore benefit from a modern database of triaxial tests, undertaken on sand samples at densities more representative of in situ conditions.

6.2. TESTING SCHEDULE

The 23 monotonic triaxial tests performed as part of this programme included both conventional isotropically and anisotropically consolidated, drained compression and extension tests, as well as a number of constant mean effective stress compression and extension tests. The nomenclature used to identify the tests is described below and further explained in Table 6.1. A summary of all monotonic tests presented in this chapter is given in Table 6.2.

$$\underbrace{180916}_{\mathrm{a}}\text{-}\underbrace{\mathrm{VJ}}_{\mathrm{b}}\,\underbrace{\mathrm{LBS\text{-}B}}_{\mathrm{c}}\,\underbrace{\mathrm{CIDc}}_{\mathrm{d}}\,\underbrace{(+\mathrm{v}')}_{\mathrm{e}}\,\underbrace{80.}_{\mathrm{f}}\underbrace{50.}_{\mathrm{g}}\underbrace{8}_{\mathrm{h}}$$

Table 6.1: Nomenclature used to identify tests

Key	Description	Nomenclature
a	Date of test	yymmdd e.g. 180916
b	Triaxial test apparatus	VJ: Stress path apparatus
		VJX: Cyclic triaxial apparatus
c	Material tested	LBS-B: Leighton Buzzard Sand (Fraction B)
d	Test type	CIDc: Isotropically consolidated, drained compression test
		CIDe: Isotropically consolidated, drained extension test
		CIUc: Isotropically consolidated, undrained compression test
		CADc: Anisotropically consolidated, drained compression test
e	Stress path	See Figure 6.1 for details
f	Relative density	Numerical value (in percent)
g	Effective confining stress	Numerical value (in kN/m^2)
h	Overconsolidation Ratio	Numerical value (usually neglected as OCR typically = 1)

The bulk of the drained testing programme were undertaken on normally consolidated samples, prepared to an initial target relative density of 80 % using the wet pluviation technique described in Section 4.7.2. Table 6.2 shows that the prepared test specimens were slightly denser than anticipated, and were generally in the range D_r = 82 ±1 %.

The tests typically utilised a $\sigma'_{c,0}$ of 50, 25, 12 and 6 kN/m^2. To investigate the influence of overconsolidation ratio (OCR), one test was undertaken on a specimen with OCR = 8.0. This was considered necessary as the application of a -10 kN/m^2 vacuum pressure after sample deposition, placement of the top cap, and subsequent filling of the triaxial cell results in an effective confining pressure of approximately 16 kN/m^2 acting on the sample. The specimens sheared at initial effective confining pressures of 6 and 12 kN/m^2 are therefore overconsolidated.

Table 6.2: Summary of monotonic triaxial stress-path tests undertaken on Leighton Buzzard Sand (Fraction B)

Test ID (-)	p'_0 (kN/m^2)	**OCR** (-)	e_0 (-)	$D_{r,0}$ (%)	**Test type** (-)	**Stress path** (-)	**Filename** (-)
s01	50	1	0.584	81.9	CIDc	+v′	180509 - VJ LBS-B CIDc(+v) 80.50.s01
s02a	25	1	0.586	81.3	CIDc	+v′	181016 - VJ LBS-B CIDc(+v) 80.25.s02a
s03	12	1	0.587	81.0	CIDc	+v′	180718 - VJ LBS-B CIDc(+v) 80.12.s03
s04a	6	1	0.584	82.0	CIDc	+v′	181219 - VJ LBS-B CIDc(+v) 80.6.s04a
s05	80	1	0.586	81.3	CADc	+v′	180515 - VJ LBS-B CADc(+v) 80.50.s05
s06	40	1	0.587	80.9	CADc	+v′	180705 - VJ LBS-B CADc(+v) 80.25.s06
s07	20	1	0.588	80.3	CADc	+v′	180727 - VJ LBS-B CADc(+v) 80.12.s07
s08	-	-	-	-	-		-
s09a	50	1	0.585	81.5	CIDe	-v′	181106 - VJ-LBS-B CIDe(-v) 80.50.s09a
s10a	25	1	0.585	81.6	CIDe	-v′	181109 - VJ-LBS-B CIDe(-v) 80.25.s10a
s11	12	1	0.583	82.3	CIDe	-v′	181210 - VJ LBS-B CIDe(-v) 80.12.s11
s12	6	1	0.587	80.9	CIDe	-v′	181214 - VJ LBS-B CIDe(-v) 80.6.s12
s13a	50	1	0.582	82.8	CIDc	+q	181103 - VJ LBS-B CIDc(+q) 80.50.s13a
s14	25	1	0.588	80.5	CIDc	+q	181005 - VJ LBS-B CIDc(+q) 80.25.s14
s15	12	1	0.587	81.0	CIDc	+q	181009 - VJ LBS-B CID(+q) 80.12.s15
s16	6	1	0.586	81.3	CIDc	+q	181012 - VJ LBS-B CIDc(+q) 80.6.s16
s17a	50	1	0.586	81.3	CIDe	-q	181001 - VJ LBS-B CIDe(-q) 80.50.17a
s18	25	1	0.584	81.9	CIDe	-q	181023 - VJ LBS-B CIDe(-q) 80.25.s18
s19	12	1	0.586	81.4	CIDe	-q	181026 - VJ LBS-B CIDe(-q) 80.12.s19
s20	6	1	0.584	81.8	CIDe	-q	181029 - VJ LBS-B CIDe(-q) 80.6.s20
s21	50	8	0.585	81.5	CIDc	+v′	180821 - VJ LBS-B CIDc(+v) 80.50.8.s21
s22	100	1	0.591	79.6	CIDc	+v′	180611 - VJ LBS-B CIDc(+v) 80.100.s22
s23	200	1	0.585	81.5	CIDc	+v′	190205 - VJ LBS-B CIDc(+v) 80.200.s23
s24	-	-	-	-	-	-	-
s25	400	1	0.586	81.3	CIDc	+v′	190211 - VJ LBS-B CIDc(+v) 80.400.s25

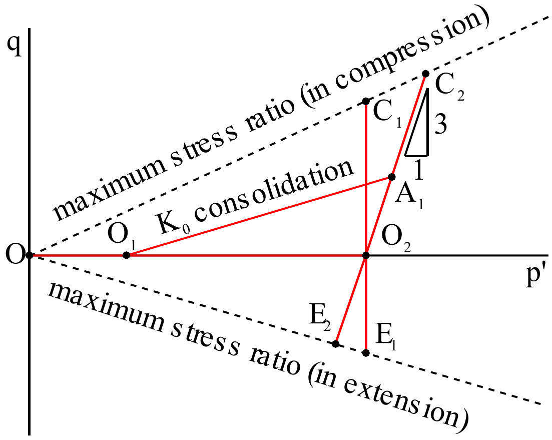

Test	Stress path
CIDc(+v′)	O-O1-O2-C2
CIDe(-v′)	O-O1-O2-E2
CIDc(+q)	O-O1-O2-C1
CIDe(-q)	O-O1-O2-E1
CADc(+v′)	O-O1-A1-C2

Figure 6.1: Typical stress paths for monotonic triaxial tests

To ensure fully drained conditions, all samples were sheared at an axial strain rate of $\dot{\varepsilon_z}$ = 0.5 % per hour, as recommended by Kuwano (1999). In an attempt to achieve critical state conditions, the CIDc(+v′) and CADc(+v′) tests were generally extended until the axial strain exceeded 35 %; while the remaining tests were terminated following observation of peak conditions, typically between $|\varepsilon_z|$ = 10 to 15 %. To investigate the effect that stress ratio and mobilised deviatoric strain have on the small-strain shear modulus, G_0, many tests also included several unloading-reloading cycles of varying magnitude.

6.3. TEST RESULTS

Test results are summarised in Figure 6.2 through Figure 6.7, and contain plots of deviatoric stress, q, vs mean effective stress, p'; q vs. deviatoric strain, ε_q; volumetric strain, ε_p, vs. ε_q, and void ratio, e, vs. p'. Normalised plots of stress ratio, $\eta = q\,/\,p'$ vs. ε_q based on local, small-strain instrumentation are also shown.

All of the tests performed on LBS-B were carried out on the monotonic stress path apparatus described in Chapter 4 (Section 4.2). The stress paths were followed by computer control of the cell pressure, and allowed continuous paths to be followed and all instrumentation to be logged automatically. All of the tests used local axial and radial strain instrumentation, which were used to determine the deformations at small strains (i.e. ε_q < 5 %). The stress-strain response at large strain magnitudes is calculated based on external instrumentation. Results are summarised in Table 6.3.

6.3.1. DRAINED ISOTROPIC COMPRESSION TESTS

6.3.1.1. CIDc(+v′) Tests ($\sigma'_{c,0} \leq 50$ kN/m^2)

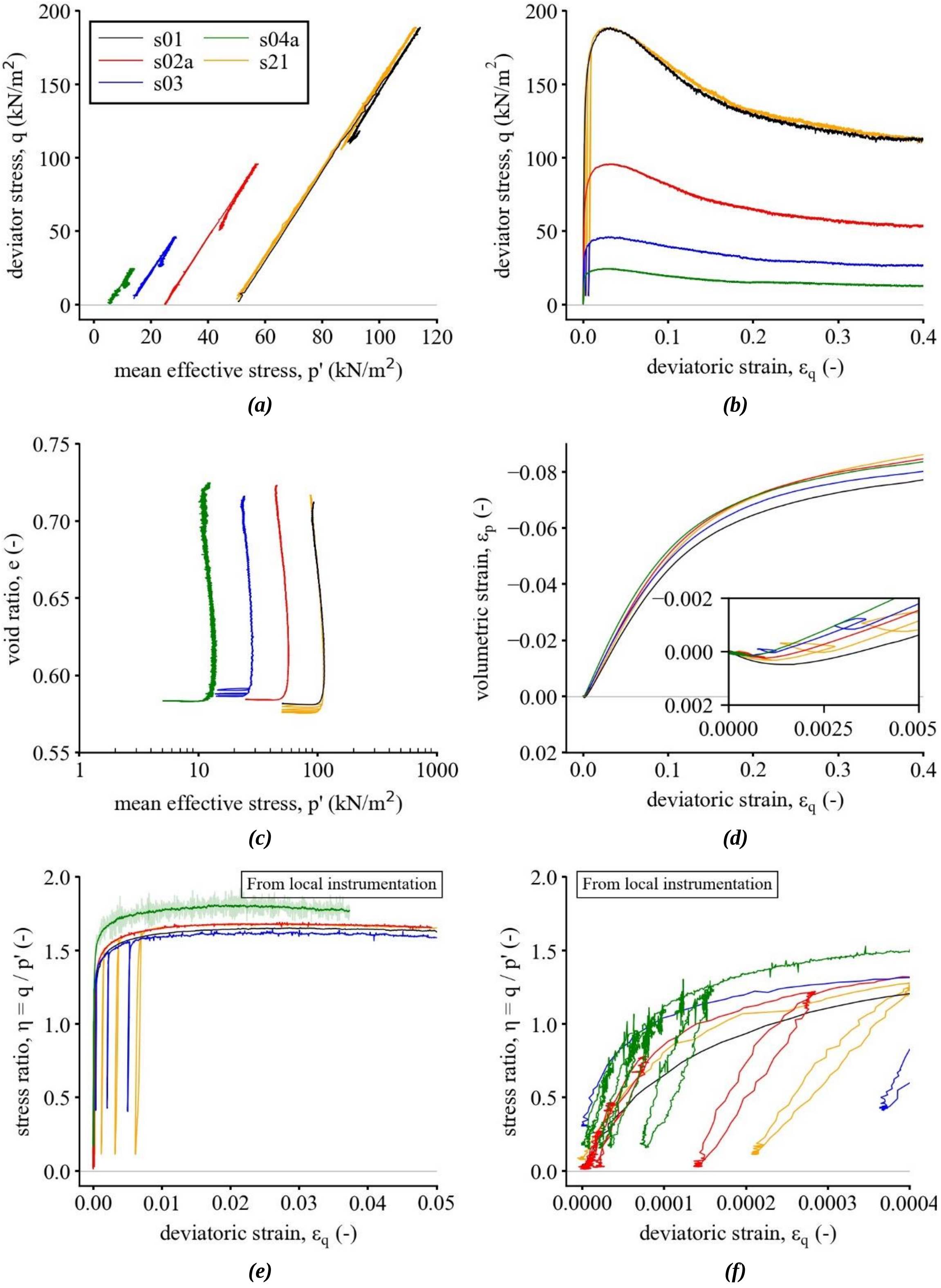

(a) *(b)*

(c) *(d)*

(e) *(f)*

Figure 6.2: Summary of CIDc(+v′) test results (for $\sigma'_{c,0} \leq 50$ kN/m^2)

6.3.1.2. CIDc(+ν′) Tests ($\sigma'_{c,0} > 50$ kN/m^2)

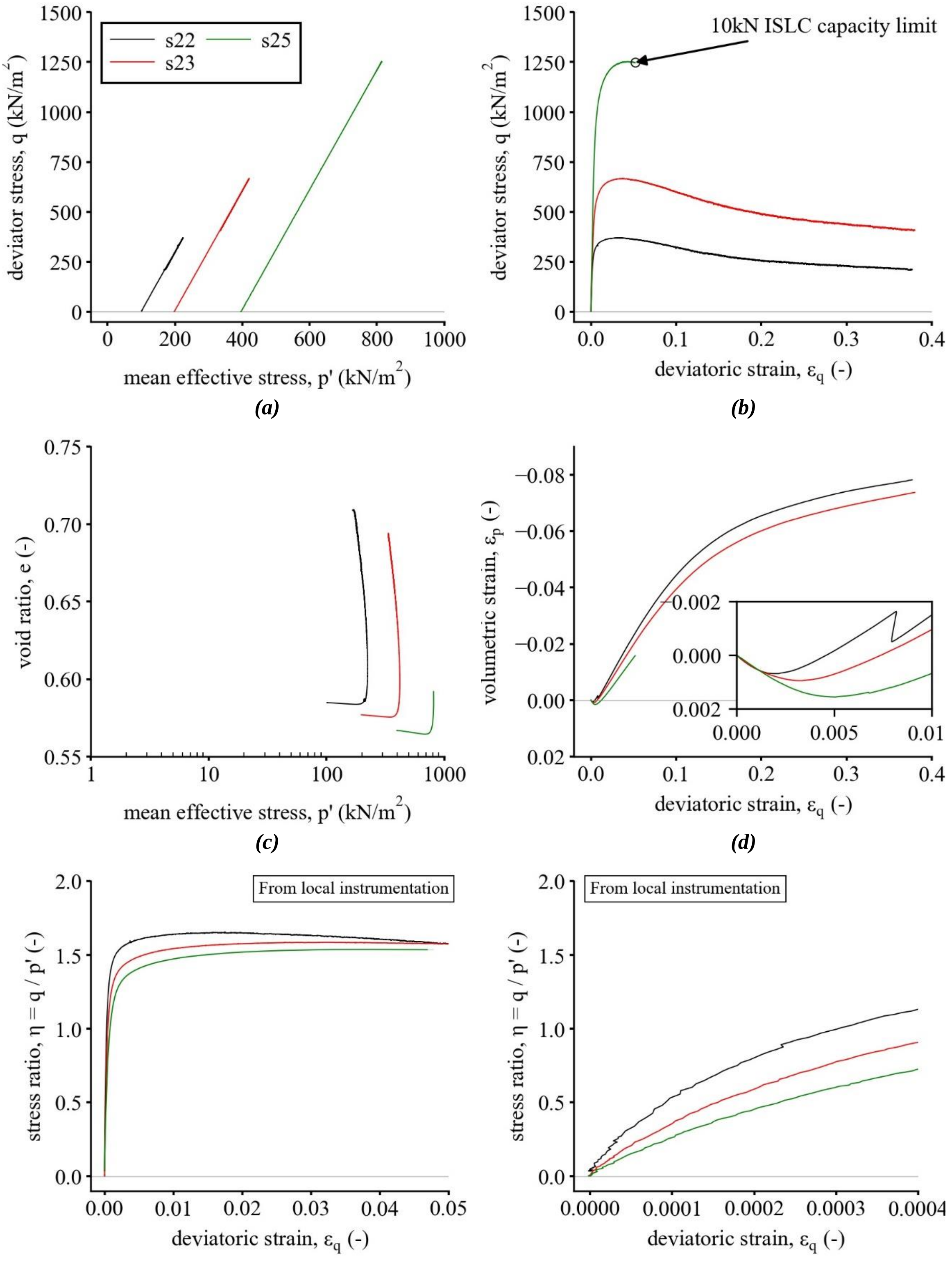

(a) *(b)*

(c) *(d)*

(e) *(f)*

Figure 6.3: Summary of CIDc(+ν′) test results (for $\sigma'_{c,0} > 50$ kN/m^2)

6.3.1.3. CIDc(+q) tests

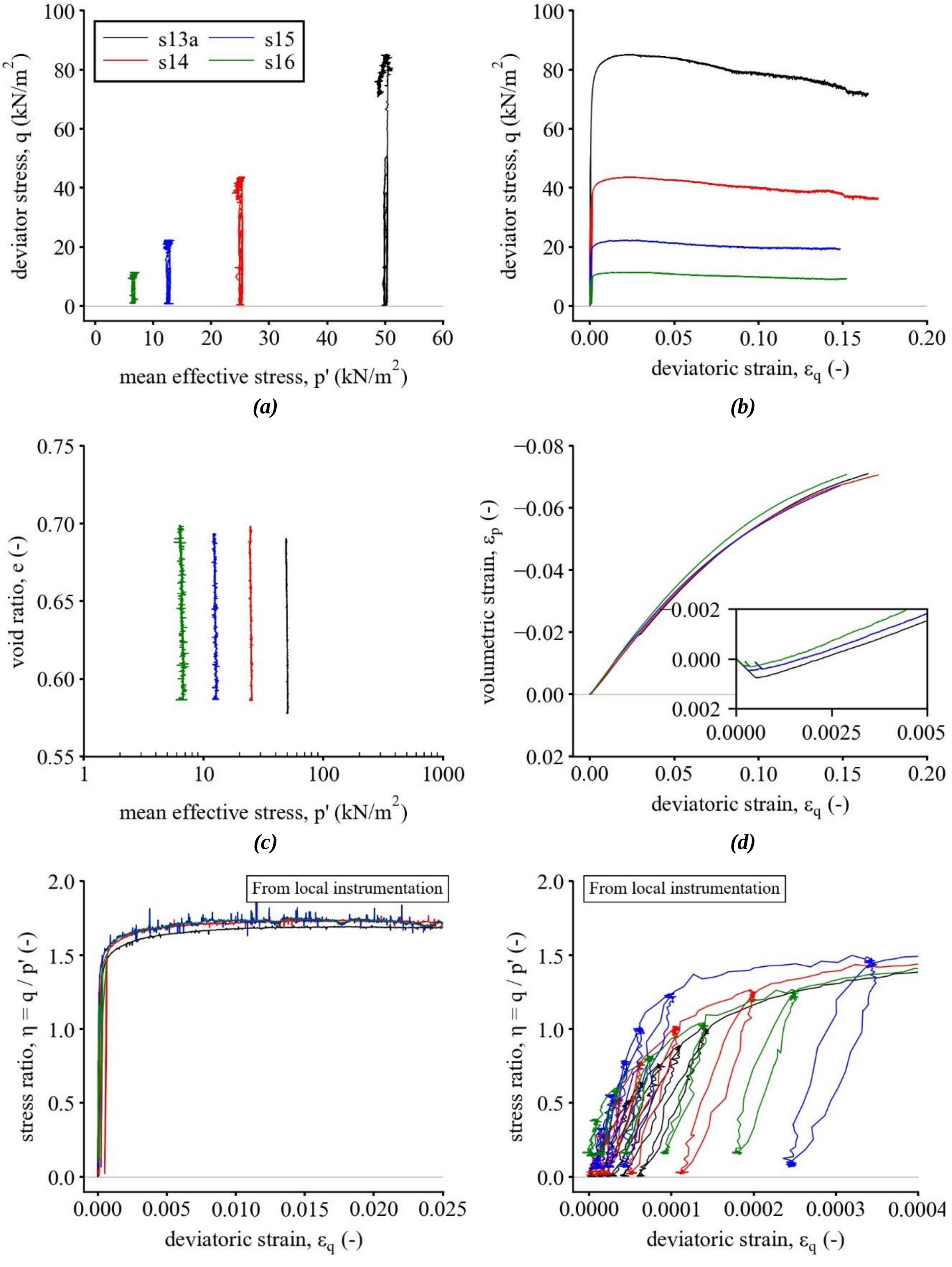

(a) (b) (c) (d) (e) (f)

Figure 6.4: Summary of CIDc(+q) test results

6.3.2. DRAINED ANISOTROPIC COMPRESSION TESTS

6.3.2.1. CADc(+v′) Tests

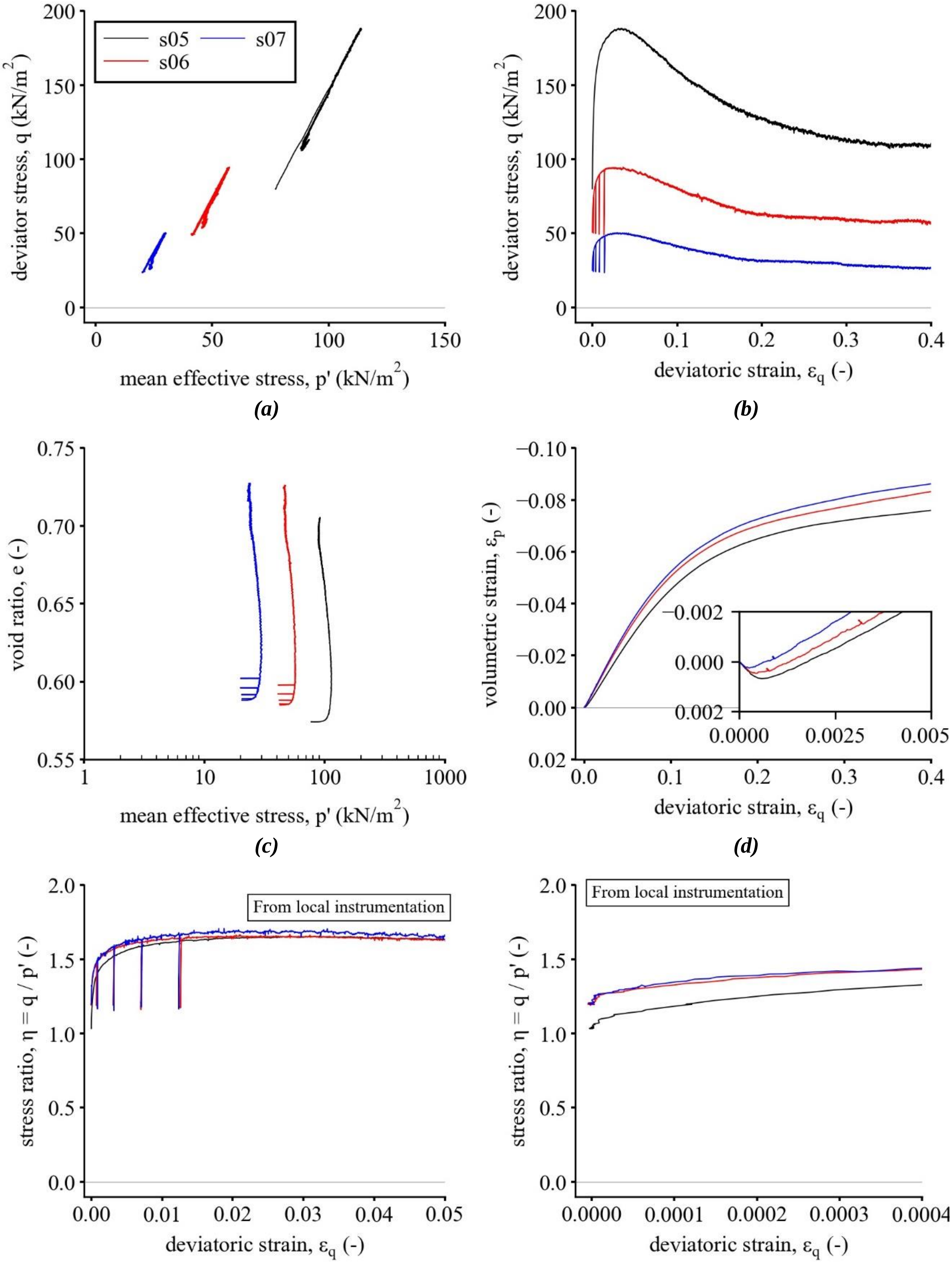

(a) *(b)*

(c) *(d)*

(e) *(f)*

Figure 6.5: Summary of CADc(+v′) test results

6.3.3. DRAINED ISOTROPIC EXTENSION TESTS

6.3.3.1. CIDe(-v') Tests

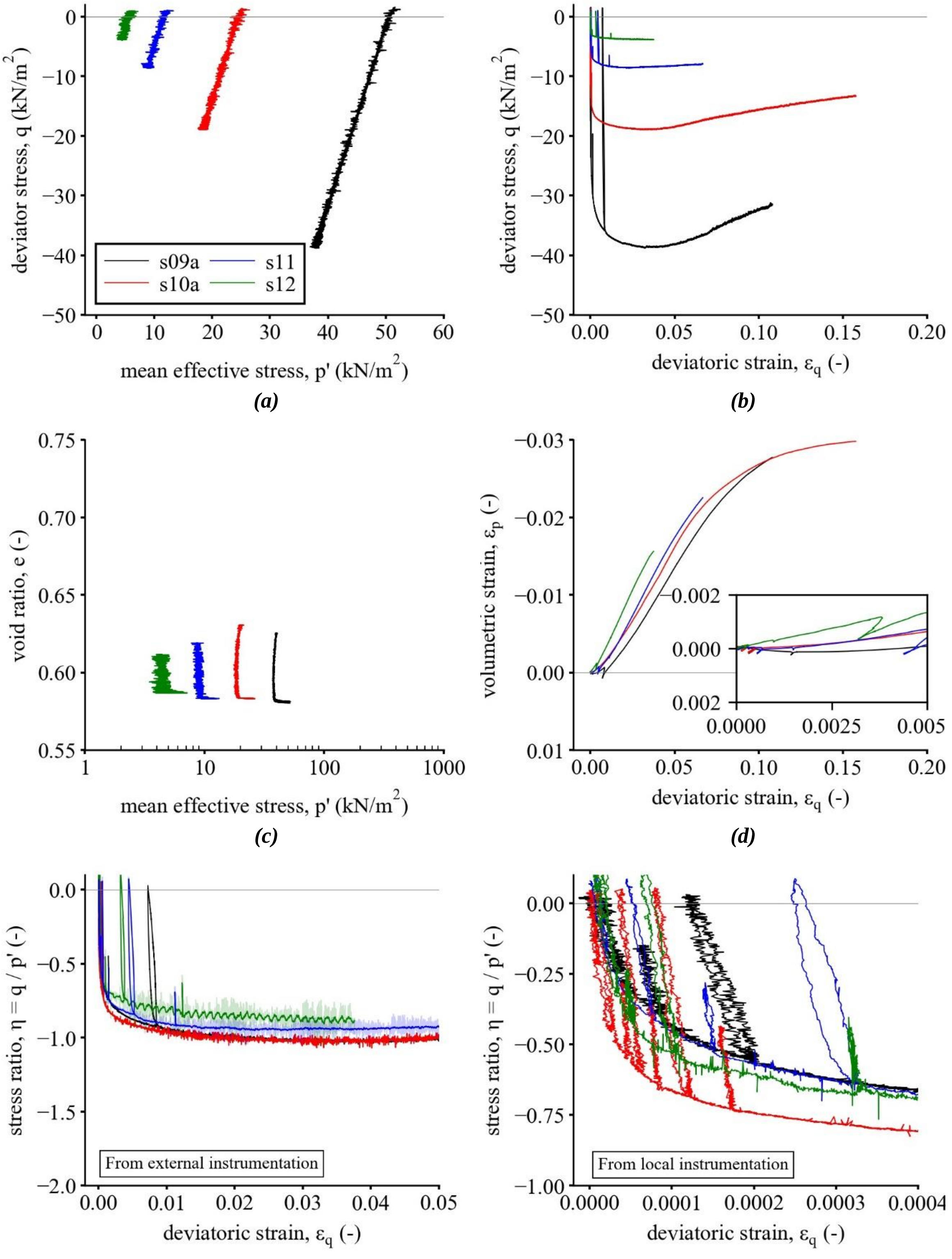

(a) *(b)*

(c) *(d)*

(e) *(f)*

Figure 6.6: Summary of CIDe(-v') test results

6.3.3.2. CIDe(-q) Tests

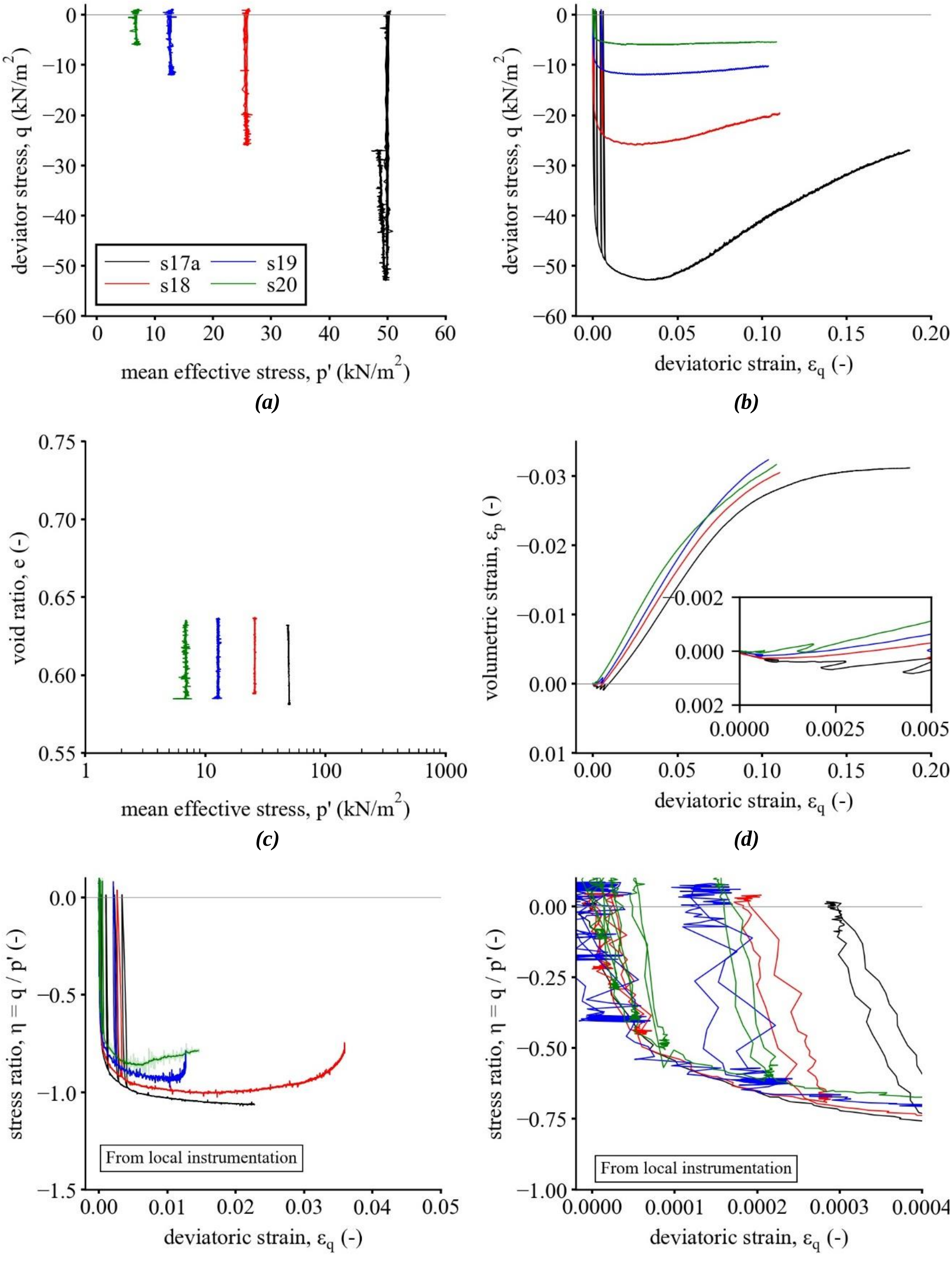

(a) *(b)*

(c) *(d)*

(e) *(f)*

Figure 6.7: Summary of CIDc(-q) test results

Table 6.3: Summary of effective stress strength parameters determined from drained triaxial stress-path tests

Test ID	**Test type**	**void ratio**	**relative density**	**initial mean effective stress**	**maximum deviator stress**	**mean effective stress at failure**	**maximum stress ratio**	**effective angle of internal friction**		**angle of dilation***		**maximum dilatancy***
-	-	$\boldsymbol{e_c}$†	$\boldsymbol{D_{r,c}}$†	$\boldsymbol{p'_0}$	$\boldsymbol{\lvert q\rvert_{max}}$	$\boldsymbol{p'_f}$	$\boldsymbol{\lvert\eta\rvert_{max}}$	$\boldsymbol{\phi'_{max}}$	$\boldsymbol{\phi'_{cv}}$	$\boldsymbol{\psi^D_{(1)}}$	$\boldsymbol{\psi^D_{(2)}}$	$\boldsymbol{D_{min}}$
(-)	**(-)**	**(-)**	**(%)**	**(kN/m^2)**	**(kN/m^2)**	**(kN/m^2)**	**(-)**	**(°)**	**(°)**	**(°)**	**(°)**	**(-)**
s01	CIDc(+v’)	0.584	81.9	50.7	188.7	93.0	1.653	40.3	31.5	23.1	15.5	-0.55
s02a	CIDc(+v’)	0.585	81.7	25.1	95.8	45.4	1.680	41.0	30.8	25.9	17.2	-0.63
s03	CIDc(+v’)	0.586	81.0	14.1	46.3	24.3	1.616	39.6	29.3	26.1	17.3	-0.65
s04a	CIDc(+v’)	0.583	82.2	5.4	24.6	12.4	1.798	44.0	30.6	27.7	18.1	-0.68
s05	CADc(+v’)	0.575	85.0	77.3	188.3	91.7	1.656	40.3	30.9	22.5	15.2	-0.54
s06	CADc(+v’)	0.586	81.2	42.4	94.6	47.2	1.649	40.4	31.2	26.1	17.3	-0.65
s07	CADc(+v’)	0.588	80.4	20.5	50.5	23.9	1.685	41.1	29.9	27.2	18.0	-0.68
s09a	CIDe(-v’)	0.585	81.7	51.3	1.6	40.1	1.024	38.1	-	17.4	14.2	-0.39
s10a	CIDe(-v’)	0.585	81.7	25.1	1.4	20.2	1.029	38.4	-	18.9	15.2	-0.42
s11	CIDe(-v’)	0.583	82.3	12.2	1.1	8.7	0.951	34.4	-	19.7	16.0	-0.46
s12	CIDe(-v’)	0.587	80.9	6.0	1.0	4.4	0.902	32.1	-	20.9	17.8	-0.52
s13a	CIDc(+q)	0.581	82.8	50.1	85.1	48.9	1.691	41.2	-	28.8	18.8	-0.71
s14	CIDc(+q)	0.587	80.7	25.2	43.6	24.6	1.730	42.2	-	28.6	18.6	-0.69
s15	CIDc(+q)	0.587	80.9	12.3	22.3	12.3	1.716	42.5	-	29.9	19.3	-0.73
s16	CIDc(+q)	0.586	81.2	6.6	11.4	6.4	1.672	41.1	-	30.6	20.1	-0.76
s17a	CIDe(-q)	0.586	81.3	50.2	0.8	48.3	1.063	40.2	-	17.4	14.0	-0.43
s18	CIDe(-q)	0.584	82.0	25.9	1.2	25.8	1.003	37.0	-	18.0	14.5	-0.42
s19	CIDe(-q)	0.585	81.5	13.0	1.1	12.8	0.932	33.5	-	18.4	14.9	-0.43
s20	CIDe(-q)	0.584	81.8	7.0	1.1	6.9	0.860	30.1	-	19.8	16.1	-0.48
s21	CIDc(+v’)	0.581	82.9	50.4	188.8	87.1	1.676	40.9	32.4	25.8	17.1	-0.64
s22	CIDc(+v’)	0.590	79.7	101.2	369.9	170.5	1.650	40.3	31.5	23.1	15.5	-0.55
s23	CIDc(+v’)	0.581	82.9	197.7	666.2	335.5	1.586	38.8	31.2	20.9	14.2	-0.49
s25	CIDc(+v’)	0.575	85.2	395.6	1252.2	813.0	1.538	37.7		18.5	12.7	-0.42

Notes:

† subscript ‘c’ represents values at the end of consolidation

* See Section 6.5.3 for definitions of $\psi^D_{(1)}$ and $\psi^D_{(2)}$ and D_{min}

6.4. GENERAL OBSERVATIONS

Despite the use of enlarged and lubricated end platens, barrelling and shear bands were still observed in the compression tests, a typical example of which is shown in Figure 6.8a.

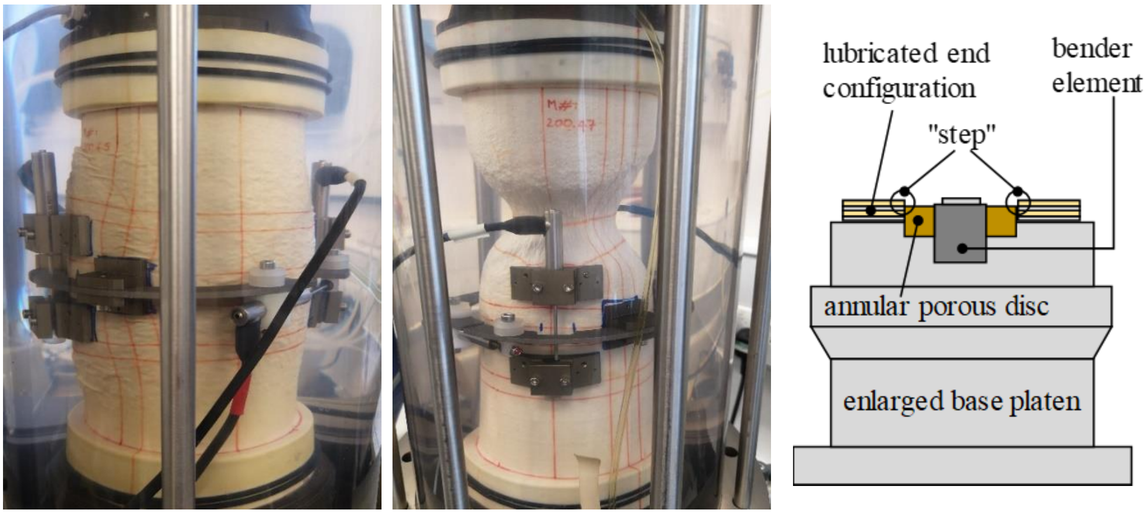

(a) *(b)* *(c)*

Figure 6.8: Deformed specimens at end of shearing from (a)CIDc(+q) 85.50; and (b) CIDe(-q) 85.50; and (c) sketch of development of step in dual-skin lubricated end set-up.

Causes of the barrelling are thought to be due to the following:

- The inclusion of bender elements requires relatively large annular porous discs, which, when added to the surface area of the bender element, reduce the effective ‘frictionless’ area of the platen;
- Despite best efforts to select appropriately thick latex discs for use in the dual-skin lubricated end set-up, a ‘step’ often developed between the finished height of the upper latex disc and porous disc (see Figure 6.8c), thereby reducing the effectiveness of the ‘frictionless’ ends.
- Dense specimens with 2:1 height to diameter ratios are highly susceptible to developing shear bands in drained triaxial compression tests, as can be seen in Figure 6.8a.

However, Lade (2016) comments that as the specimen is expected to deform away from its central axis, centrally located rough porous discs have negligible influence on the soil behaviour. Figure 6.9 shows photographs taken of the lower latex discs following careful excavation of the test specimen, and clearly show the circumferential cuts having deformed outwardly, indicating that the lubricated end set-up is performing to some extent.

(a) *(b)*

Figure 6.9: Excavation of (a) the base pedestal; and (b) the top cap allowing post-test inspection of the lower latex disc from lubricated end set-up.

Improvement could be obtained by reducing the $H:D$ ratio of the specimen to 1:1, which would promote the development of more uniform strains in the sample (Rowe & Barden, 1964). Furthermore, because shear bands are less likely to develop in 1:1 $H:D$ specimens, results of drained compression tests yield more appropriate failure conditions that better represent the soil strength at the final, uniform void ratio (Lade, 2016).

To further improve the effectiveness of the set-up, the bender elements could be removed, permitting the use of smaller porous discs, and thereby maximising the ‘frictionless’ area. This configuration, if incorporated into a modular/detachable pedestal set-up, would also permit ‘end of sample freezing’. This has been shown to significantly improve the accuracy of end-of-test void ratio estimations (Sladen & Handford, 1987), which is critically important for testing campaigns concerned with determination of the CSL (Reid et al., 2020).

It is therefore recommended that future researchers performing tests on sand with this apparatus adopt 1:1 $H:D$ ratio specimen sizes. Abandoning platen-mounted bender elements is not recommended, as they provide a valuable means of determining G_0. However, fabricating a second set of modular, ‘bender-free’, enlarged end platens is also recommended given the importance of reliable predictions of the CSL and its associated use in modern constitutive models.

EXTENSION TESTS

Figure 6.8b shows a photograph of a drained triaxial extension test specimen after approximately $\varepsilon_q \approx 19\,\%$. The deformed shape shown in Figure 6.8b was found to be typical of extension test specimens in that significant necking was observed, with strain localisations tending to develop in the upper third of the sample. This is outside the area where the local small-strain instrumentation was installed, meaning that calculations of parameters based on these measurements (i.e. shear stiffness) are unreliable.

Furthermore, cylindrical triaxial test specimens are typically assumed to deform as right cylinders, so that all parts of the specimen contribute equally in the overall strains. The problem associated with the relatively severe strain localisations typical to triaxial extension tests, is that computations of axial and volumetric strain become erroneous, as does the assumed calculated cross-sectional area on which estimations of axial stresses are based.

The shortcomings associated with triaxial extension tests are well-known to researchers, with Lam & Tatsuoka (1988), Roscoe *et al*. (1963), and Lade (2016) all concluding that results of such tests cannot be relied upon for evaluating failure criteria. However, quantifying the different behaviour of cohesionless soils in compression and extension is an important component of constitutive models, and in the absence of other methods, triaxial extension test data can still provide useful information.

VOLUME CHANGE BEHAVIOUR

The CIDc(+v′) and CADc(+v′) tests were sheared to deviatoric strains in excess of 30 % in an attempt to achieve critical state conditions, and enable the determination of useful parameters such as ϕ'_{cv} and e_{cs}. However, the formation of shear bands results in deformations and volume changes that occur along complex localisation zones (Desrues *et al*., 1996). Within these zones, the local void ratio tends towards critical state conditions and is greater than the global average void ratio measured from conventional volume change instrumentation. The practical consequence of this behaviour is illustrated in Figure 6.10, which shows that the critical state line determined from dense specimens (path C) does not coincide with that estimated from loose specimens.

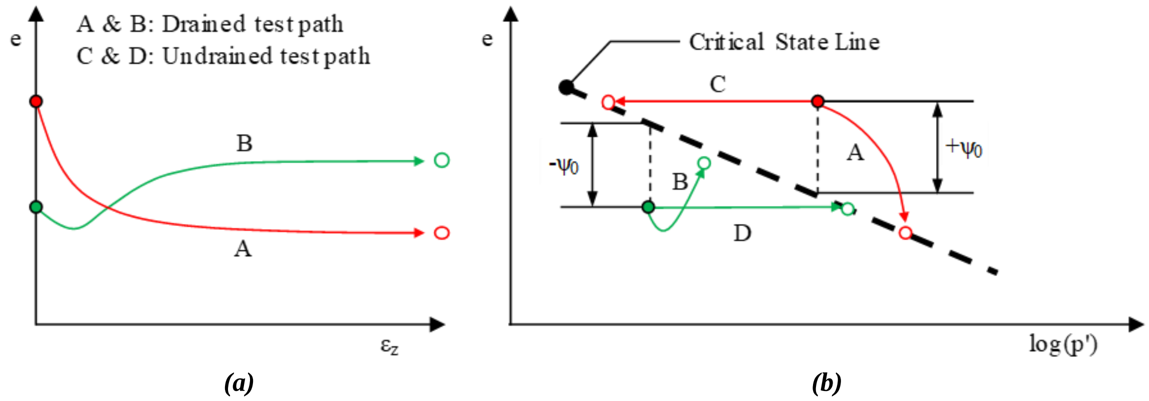

Figure 6.10: Idealised profiles of mobilised void ratio vs. axial strain; and (b) mean effective stress during conventional drained and undrained triaxial compression tests (modified from Jefferies & Been (2015)).

Shear bands were observed in all the CIDc(+v′) tests, which may explain why calculated values of volumetric strain and void ratio fail to stabilise despite large levels of mobilised strain. It has therefore not been possible to reliably determine values of e_{cs} and thus the location of the critical state line in $e - \ln(p')$ space from these tests.

6.5. STRESS-STRAIN BEHAVIOUR DURING DRAINED LOADING

6.5.1. INFLUENCE OF σ'_c ON SHEAR STRENGTH

The typical variation of the drained shear strength of sand with confining pressure is illustrated schematically in Figure 6.11. For a sand of a given initial density, the shear strength is considered to comprise two components (Taylor, 1948):

- The first is due to the basic inter-particle friction between sand grains, which is a combination of rolling and sliding friction. The resulting strength is calculated as the constant volume friction angle, ϕ'_{cv}.
- The second component arises from the contribution of dilation during shearing, and tends to occur in dense sands (i.e. $\psi_0 < 0$).

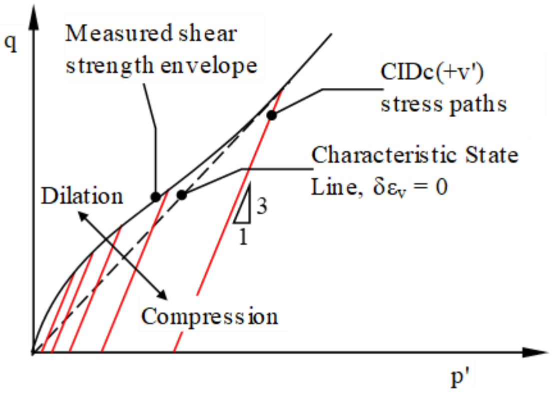

Figure 6.11: Idealised drained shear strength envelope for sand (modified from Lade & Ibsen, 1997).

Very high pressures (e.g. $p' > 2$ MN/m^2) tend to cause particle crushing and suppress dilation, meaning that the contribution due to the rate of dilation at very high pressures reduces to zero. A curved failure surface in $p' - q$ space is thus often observed in experimental data (Stroud, 1971). The stress-strain plots for the 23 drained stress path tests are presented in sub-plot (b) of Figure 6.2 to Figure 6.7, and show typical behaviour associated with dense sands. The plots show that the peak deviator stress increases with effective confining stress, with both compression and extension tests exhibiting brittle behaviour, with post-peak strain softening continuing until the test termination.

To better investigate the influence of confining stress, Figure 6.12 presents stress-strain plots normalised by the current mean effective stress, p'. Similar stress-strain plots are obtained for triaxial compression and extension tests. However, results from CIDc(+v′) 80.6 and CIDc(+q) 80.6 plot above and below the grouped compression test profiles, respectively. While the results from CIDc(+v′) 80.6 do agree with the expected behaviour of lower effective confining stresses yielding higher stress ratios, this behaviour is not validated by the tests undertaken at incrementally higher effective confining stresses, and is further contradicted by the results from CIDc(+q) 80.6. These results are therefore considered anomalous.

The cause of the anomalies is not clear, but are thought to be due to estimates of axial stress becoming increasingly sensitive to the internal load cell measurements, which are dependent on the selection of an initial ‘zero offset’. Temperature fluctuations in the laboratory were found to influence the measured load cell reading by approximately ±1 N, which although relatively small, are found to have a significant influence on the deviator stress for tests undertaken at such low confining pressures.

Considering the influence of OCR, the stress-strain curve of CIDc(+v′)80.50 is practically indistinguishable from that of a similar test isotropically consolidated to an OCR = 8.0 prior to shearing (CIDc(+v′)80.50.8). This implies that concerns associated with samples sheared at effective confining pressures less than 25 kN/m^2 being overconsolidated (due to unavoidable factors associated with setting up the specimen) may therefore be considered negligible.

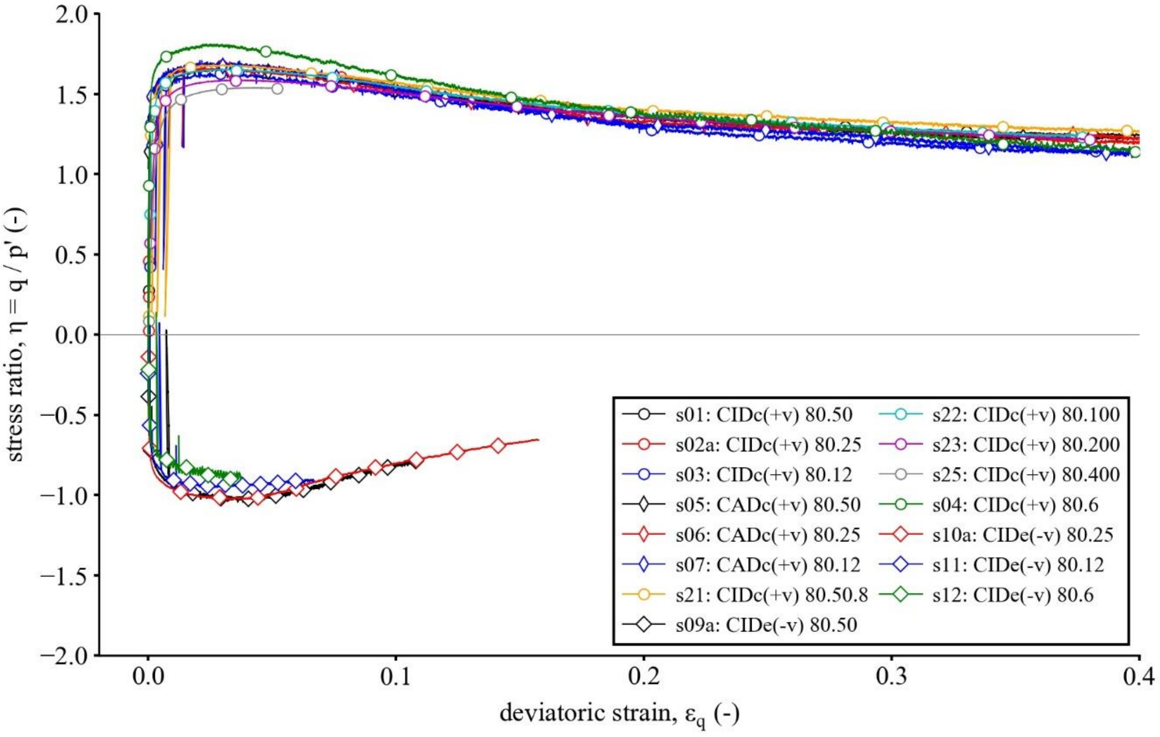

(a)

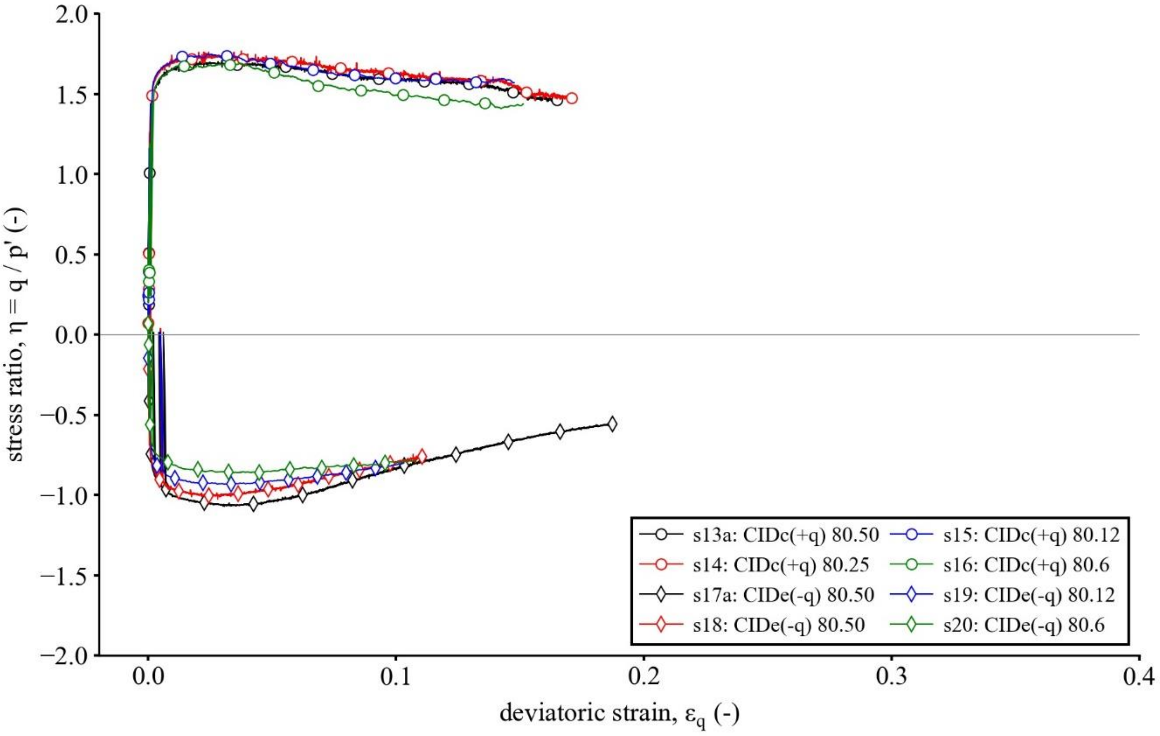

(b)

Figure 6.12: Normalised stress-strain curves calculated from external instrumentation from (a) ± v'; and (b) ± q stress path tests.

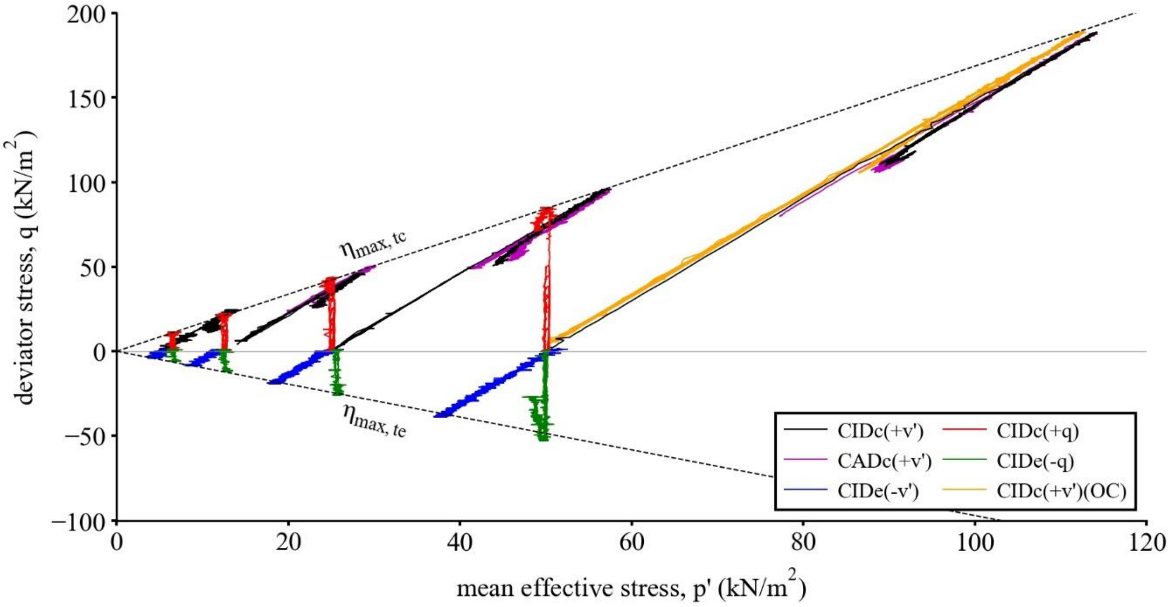

Figure 6.13: Stress paths for triaxial tests undertaken at $\sigma'_{c,0} \leq$ 50kN/m^2

In triaxial extension, similar post-peak strain-softening behaviour is observed in tests sheared at $\sigma'_{c,0} \geq$ 25 kN/m^2. However, results from tests sheared at $\sigma'_{c,0} \leq$ 25 kN/m^2 appear to show strain hardening behaviour, with no observable peak obtained before significant necking occurred, resulting in termination of the test. The displayed behaviour is thought to be a result of erroneous deviator stress calculations arising from unrealistic cross-sectional area assumptions.

Figure 6.13 shows the stress paths for tests sheared at $\sigma'_{c,0} \leq$ 50 kN/m^2. Initial inspection of the stress paths indicate that a linear failure envelope may enclose both the compression and extension tests, the slope of which can be quantified by the peak stress ratio, η_{max}, defined as:

$$\eta_{max} = \frac{q_f}{p'_f} \tag{6-1}$$

where:

q_f = deviator stress at failure
p'_f = mean effective stress at failure

However, tests performed at higher $\sigma'_{c,0}$ (Figure 6.14) show that η_{max} tends to progressively decrease with increasing confining stresses. meaning that the linear failure envelope drawn in Figure 6.13 for $\sigma'_{c,0} \leq$ 50 kN/m^2 is no longer appropriate for higher stress levels. Based on the limited data for $\sigma'_{c,0} >$ 50 kN/m^2, a bi-linear failure envelope is tentatively sketched on Figure 6.14 for triaxial compression

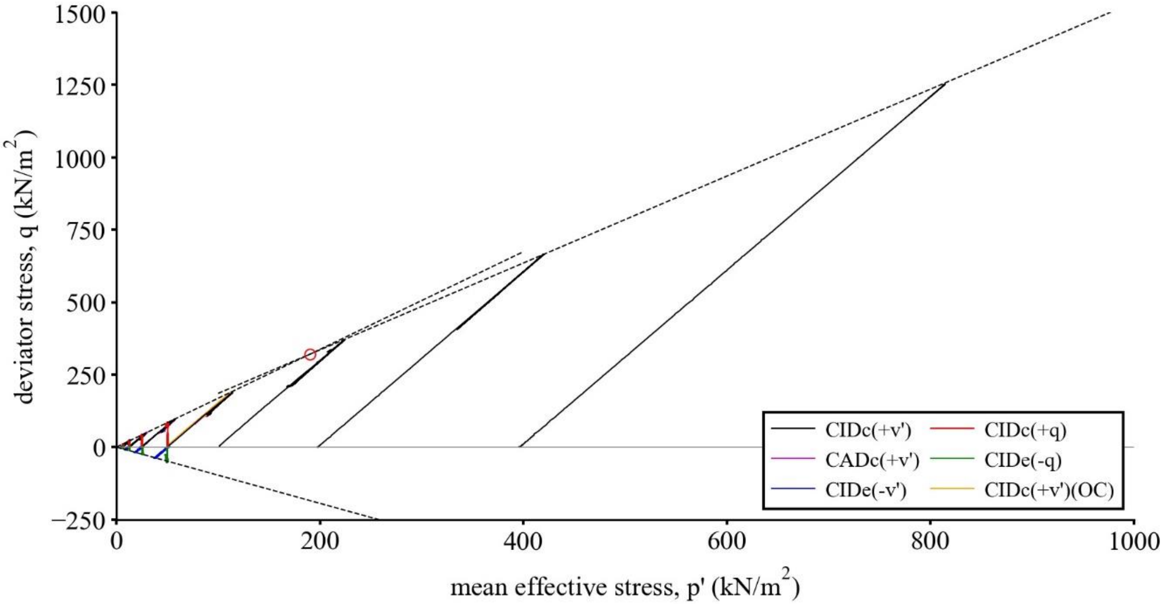

Figure 6.14: Stress paths for all triaxial tests

tests, with the two envelopes intersecting at 190 kN/m^2. A curved failure envelope may also capture the response; however, tests at higher $\sigma'_{c,0}$ values would be required to confirm this.

Figure 6.15 shows estimates of η_{max} plotted against the mean effective stress at failure, p'_f, and indicates that at relatively low effective confining stresses (e.g. $p' < 100$ kN/m^2) the value of p' has little influence on the mobilised η_{max} for LBS-B in triaxial compression, and yield an average value of $\eta_{max} = 1.686 \pm 0.03$ for $25 \leq p'_f \leq 100$ kN/m^2. η_{max} also appears to be independent of both stress path and OCR.

At $p' \leq 25$ kN/m^2, factors such as the accuracy of applied corrections, temperature fluctuations within the laboratory and electrical noise become increasingly influential on measured data. Despite best efforts to minimise these factors, the calculated η_{max} exhibits increased scatter at these stress levels ($1.62 \leq \eta_{max} \leq 1.80$), making it difficult to reliably quantify the effect of p' on η_{max} at very low stress levels.

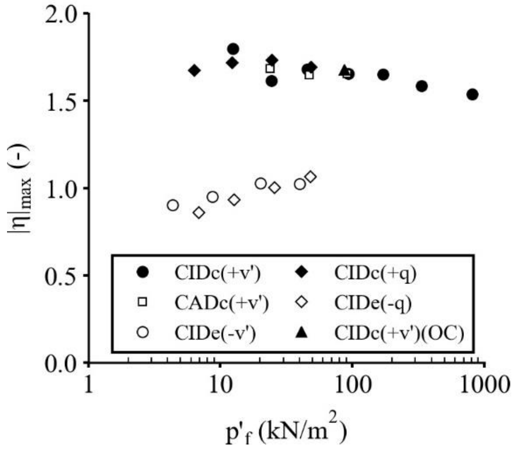

Figure 6.15: Effect of the initial mean effective confining stress, p'$_f$ on η_{max}

However, the relatively narrow band of η_{max} show that the effect of confining stress at very low stress levels is small and potentially negligible for triaxial compression conditions. Conversely, for p'_f >100 kN/m^2, η_{max} is found to decrease from 1.65 to 1.54 at p'_f =11 and 813 kN/m^2, respectively.

Both the conventional triaxial extension stress path tests (tests s09a to s12), and the 'constant p'' stress paths (tests s17a to s20) show the magnitude of η_{max} to decrease with decreasing confining stress, from -1.02 at p'_f = 40 kN/m^2 (s09a) to -0.902 at p'_f = 4.4 kN/m^2 (s12). Similar results were obtained from the constant p' stress path tests. This yields a shear stress ratio between extension and compression (i.e. $|\eta|_{\mathrm{max,te}}$ / $\eta_{max,tc}$) of approximately 60 %, which is less than the typical value of 2/3 commonly assumed by numerical modelling practitioners (Cerfontaine, 2014).

The lower (absolute) values of η_{max} mobilised in the extension tests contradict the results of the triaxial compression tests performed at similar confining stresses, and are treated with caution. The differing behaviour is thought to be related to the known issues associated with triaxial extension tests (sample necking etc.), and the experimental accuracy of the instrumentation.

6.5.1.1. *Influence of Effective Confining Stress on ϕ'*

The previous discussion has focused on characterising shear strength in terms of a dimensionless ratio of stress invariants, $\eta = q\ /\ p'$; however, much of the historic literature uses a 'friction angle' notation, so it is useful to frame the results within that context. In drained tests, this angle, termed the effective angle of internal shearing resistance, ϕ', is determined from Eq. (4-20), and may be related to η by Eqs. (4-21) and (4-22), for compression and extension conditions, respectively.

Figure 6.16(a & b) show measured values of ϕ'_{max}, and ϕ'_{cv}, plotted against p'_f, and p'_{cv}, respectively. As previously discussed, it was not possible to determine ϕ'_{cv} from every test due to premature termination following shear band development. However, the CIDc(+v′) and CADc(+v′) tests were sheared to large strains ($\varepsilon_q \geq 35$ %), from which relatively reliable estimates of ϕ'_{cv} are possible.

Given the relationship between ϕ' and η, similar conclusions to those described in Section 6.5.1 can be drawn. Results from CIDc(+v′) and CADc(+v′) tests show reasonable agreement ($\phi'_{max,tc} \approx 41.2$

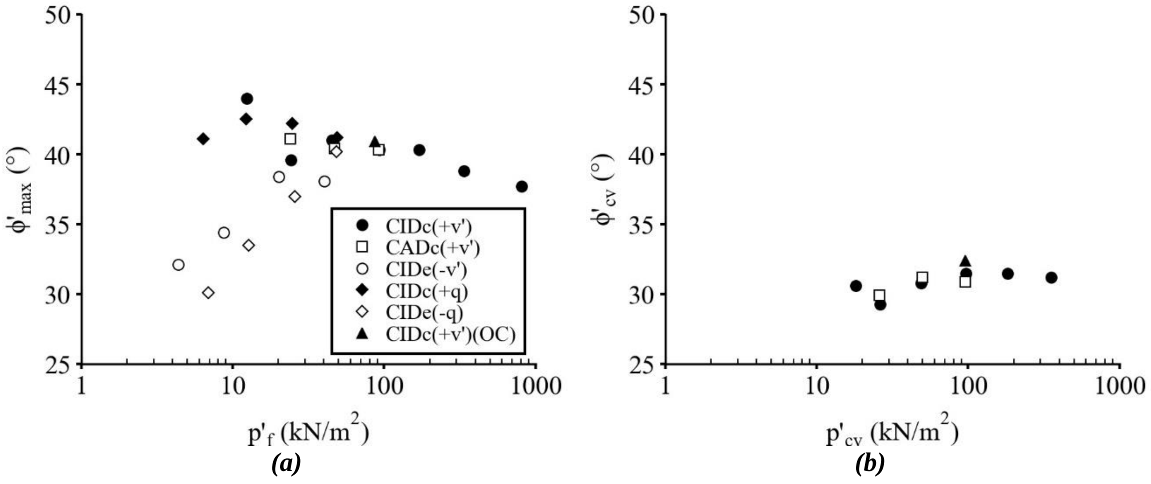

(a) *(b)*

Figure 6.16: (a) Maximum, ϕ'_{max}; and (b) constant volume, ϕ'_{cv}, effective angle of internal shearing resistance, versus mean effective stress

±1.7° for $12 \leq p'_f \leq 100$ kN/m^2), while results from the constant p' suite of compression tests show less scatter ($\phi'_{max,tc} \approx 41.8 \pm 0.7°$). Both stress paths suggest a modest increase in ϕ'_{max} with decreasing values of p'. Values of ϕ'_{max} determined from triaxial extension show wide scatter, ranging from $30.1° \leq \phi'_{max,te} \leq 40.2°$.

As discussed in Chapter 2, experimental evidence for the drained strength of granular media at very low stress levels is both limited and conflicting. Results presented here tend to agree with the work of Tatsuoka (Fukushima & Tatsuoka, 1984; Tatsuoka, 1987; Tatsuoka *et al.*, 1986), who concluded that the magnitude of ϕ'_{max} is independent of the effective confining stress for pressures less than approximately 50kN/m^2. Figure 6.16a supports this conclusion to some extent; however, results show that for LBS-B, notable reductions in ϕ'_{max} only mobilise once $\sigma'_{c,0} > 100$ kN/m^2.

The behaviour observed in these tests may also be explained in terms of the state parameter, ψ, and supports the notion of a critical state line that curves towards a horizontal asymptote in the $e:\ln(p')$ plane at low stress values (see Section 5.1.3). For example, given that all test specimens were sheared from initially similar void ratios, the magnitude of the initial state parameter, $|\psi_0|$, will tend towards a similar value as the initial confining stress, $\sigma'_{c,0}$, (and p'_0) decreases, and therefore exhibit similar behaviour once the shape of the CSL begins to plateau at low stress levels.

To achieve critical state conditions from drained triaxial tests on dense sands requires large strains to be mobilised. This, together with the strain localisation issues, is one of the reasons why undrained tests undertaken on loose samples, are typically the preferred option for obtaining critical state properties (Jefferies & Been, 2015). Inspection of Figure 6.12 shows that even at ε_q > 30 %, the development of shear bands results in stress-strain curves that fail to plateau, meaning estimates of ϕ'_{cv} continue to decrease with strain and fail to stabilise.

For consistency, the values of ϕ'_{cv} presented in Figure 6.16b represent the average ϕ' value mobilised over the strain range $0.30 \leq \varepsilon_q \leq 0.35$. Relatively consistent estimates of ϕ'_{cv} are obtained: $\phi'_{cv} \approx$ 30.9 ±0.9°, which is less than both the value of $\phi'_{cv} \approx$ 35° reported by Stroud (1971) determined from simple shear tests undertaken on similar LBS 14/25, and the more general value of $\phi'_{cv} \approx$ 33° reported by Bolton (1986) for quartz sand in triaxial compression.

However, given that the calculation of ϕ'_{cv} is dependent on the estimated value of axial stress, σ'_z, the accuracy of ϕ'_{cv} is therefore also influenced by the accuracy of the adopted area correction, which at such large strains becomes increasingly questionable. ϕ'_{cv} values calculated from drained triaxial tests on dense samples that exhibit significant barrelling may therefore be inaccurate.

6.5.2. INFLUENCE OF σ'_c ON VOLUMETRIC RESPONSE

Subplots (d) of Figure 6.2 through Figure 6.7 show plots of volumetric strain vs deviatoric strain for the 23 drained stress path tests. The results show that all tests initially undergo a very small compression before dilating towards critical state conditions. The plots show the rate of dilation, D, decreases with mobilised strain; however, despite mobilising strains in excess of 35 % in some cases, the curves fail to plateau, indicating critical state conditions were not achieved. As discussed in Section 6.4, the development of shear bands leads to localised zones of shearing in which local void ratios tend towards critical state conditions, and are greater than the global average void ratio estimated from conventional volume change instrumentation.

With a few exceptions (CIDc(+v′) 80.12; CIDc(+v′) 80.50.8; CIDc(+q) 80.6), the plots show that the magnitude of mobilised compressive volumetric strain increases with effective confining stress;

while the rate of dilation generally increases with decreasing confining stress. The mobilised strain at which the soil transitions from compressive to dilative behaviour is also found to increase with stress level. This point of separation between regions of compression and dilation was termed the “characteristic state” by Luong (1980), and defined as the point at which the ratio $\delta\varepsilon_v$ / $\delta\varepsilon_q$ tends towards zero for any chosen loading path.

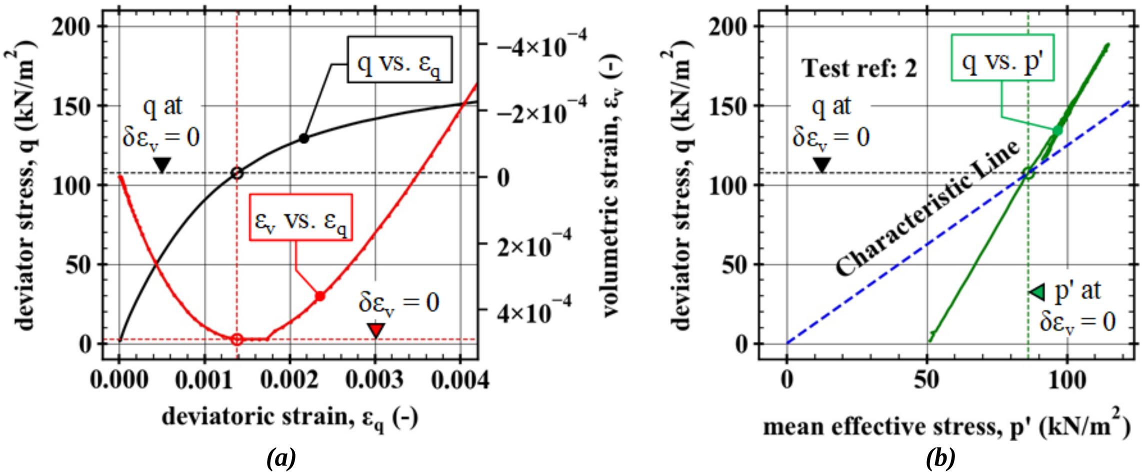

(a) *(b)*

Figure 6.17: Schematic diagram illustrating the determination of the characteristic state line.

Transferring the characteristic state conditions into $p' - q$ space (see Figure 6.17) defines a line that passes through the stress origin with slope, η_{Ch}, where the Ch subscript denotes characteristic state:

$$\eta_{Ch} = \frac{q_{Ch}}{p'_{Ch}} \tag{6-2}$$

Alternatively, this stress ratio may also be characterised by an angle, ϕ'_{Ch}, such that:

$$\phi'_{Ch} = Arcsin\left(\frac{3|\eta|_{Ch}}{\eta_{Ch} + 6}\right) \tag{6-3}$$

For loose sand or sand at very high confining stresses (i.e. sands with a positive state parameter, ψ > 0), the characteristic state is reached at the critical state, and so may be considered equivalent. According to Luong (1980), although not being strictly equivalent, the characteristic state and critical state angles are similar, which is advantageous when testing dense sands at low confining stresses, as while the critical state requires the mobilisation of large strain magnitudes, the characteristic state is achieved much sooner.

It is often considered that the characteristic line and phase transformation line (Ishihara *et al.*, 1975) described in Section 5.1.7, as determined from undrained tests, are equivalent (Lade & Ibsen, 1997). However, examining the definitions mathematically:

Characteristic state occurs when: $$\delta\varepsilon_p = 0 \tag{6-4}$$

$$\delta\varepsilon_p = \delta\varepsilon_p^e + \delta\varepsilon_p^p = 0 \tag{6-5}$$

$$\delta\varepsilon_p^p = -\delta\varepsilon_p^e \tag{6-6}$$

From Hooke's law for isotropic materials, with K_{tan} denoting the tangent bulk modulus:

$$\delta\varepsilon_p^e = \frac{dp'}{K_{tan}};\ \delta\varepsilon_p^p = -\frac{dp'}{K_{tan}};\ \therefore\ \delta\varepsilon_p^p \neq 0 \tag{6-7}$$

According to Ishihara *et al.* (1975), the phase transformation marks the point at which "the stress path turns its direction in $p' - q$ space", therefore:

Phase transformation occurs at: $$p' = p'_{min} \tag{6-8}$$

$$dp' = 0 \tag{6-9}$$

From Hooke's law for isotropic materials:

$$dp' = \delta\varepsilon_p^e K_{tan} = 0 \tag{6-10}$$

For an undrained material: $$\delta\varepsilon_p^e = 0 \tag{6-11}$$

$$\delta\varepsilon_p = \delta\varepsilon_p^e + \delta\varepsilon_p^p = 0 \tag{6-12}$$

$$\delta\varepsilon_p^p = -\delta\varepsilon_p^e = 0 \tag{6-13}$$

Despite experimental evidence supporting the notion of equivalence between the characteristic state and point of phase transformation, comparison of Eq. (6-7) with Eq. (6-13) shows that the two definitions are dissimilar. The characteristic line is also considered to represent a much less fundamental aspect of soil behaviour and is a function of the material's assumed elastic properties; whereas the phase transformation line on the other hand, is considered non-unique and may be more easily characterised by the simple condition of zero incremental plastic strains (Taborda, 2014). This has implications for numerical modelling, which is perhaps why current modelling approaches include the phase transformation line explicitly (e.g. the "dilatancy surface" of Taborda *et al.*, 2014).

Lade & Ibsen (1997) investigated the effect of relative density and effective confining stress on the characteristic angle of Santa Monica Beach sand, and found that ϕ'_{Ch} is independent of relative density but reduces with decreasing confining pressure or minor principal effective stress. Figure 6.18 presents values of ϕ'_{Ch} determined from drained compression tests undertaken as part of this study, as well as estimates of ϕ'_{cv}. Results are summarised in Table 6.4.

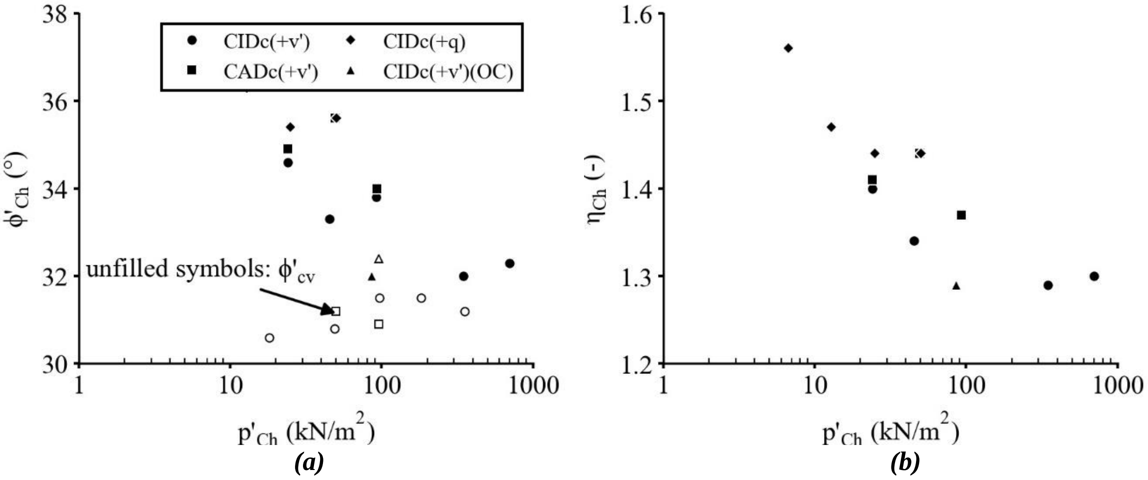

Figure 6.18: Variations of (a) estimated characteristic state angles, ϕ'_{Ch}; and (b) characteristic line gradient, η_{Ch}, vs. mean effective stress at the characteristic state, p'_{Ch}.

Table 6.4: Summary of estimated characteristic state angles and characteristic line slope

Test ID (-)	p'_0 (kN/m^2)	$\varepsilon_{p,Ch}$ (-)	$\varepsilon_{q,Ch}$ (-)	q_{Ch} (kN/m^2)	p'_{Ch} (kN/m^2)	η_{Ch} (-)	ϕ'_{Ch} (°)	ϕ'_{cv} (°)
s01	50.7	1.03E-03	7.43E-04	126.3	92.4	1.37	33.8	31.5
s02a	25.1	7.09E-04	4.34E-04	60.4	45.0	1.34	33.3	30.8
s03	14.1	1.01E-03	7.43E-04	33.7	24.1	1.40	34.6	29.3
s04a	5.4	Local strain instrumentation results spurious						35.0
s05	77.3	6.84E-04	5.89E-04	128.1	93.3	1.37	34.0	30.9
s06	42.4	4.71E-04	4.67E-04	71.4	49.4	1.44	35.6	31.2
s07	20.5	2.54E-04	2.69E-04	34.0	24.0	1.41	34.9	29.9
s13a	50.1	7.62E-04	5.29E-04	72.8	50.5	1.44	35.6	-^{1}
s14	25.2	4.82E-04	3.23E-04	35.7	24.9	1.44	35.4	-^{1}
s15	12.3	3.26E-04	3.71E-04	18.9	12.8	1.47	36.3	-^{1}
s16	6.6	1.08E-03	1.36E-03	10.4	6.7	1.56	38.2	-^{1}
s21	50.4	2.20E-04	4.24E-04	110.7	86.1	1.29	32.0	32.4
s22	101.6	Local strain instrumentation results spurious						32.0
s23	197.7	1.09E-03	1.13E-03	446.0	346.8	1.29	32.0	31.2
s25	395.6	1.50E-03	2.15E-03	909.0	699.7	1.30	32.3	-^{1}

Notes:

1. Tests terminated before critical state conditions achieved

Figure 6.18a shows that ϕ'_{Ch} tends to increase with decreasing confining stress. Similarly, Figure 6.18b shows that for LBS-B, the characteristic stress ratio, η_{Ch}, appears to increase at relatively lower effective confining stresses, with tests undertaken at higher $\sigma'_{c,0}$ values mobilising lower ϕ'_{Ch} and η_{Ch} values. In terms of the comparison with the constant volume state friction angle, ϕ'_{Ch} is found to show reasonable agreement with ϕ'_{cv} determined at large strains for those tests performed at relatively high initial confining stresses (i.e. $\sigma'_{c,0} > 50$ kN/m^2), where $\phi'_{Ch} \approx 32.7°$.

However, while ϕ'_{Ch} obtained at relatively low stresses (i.e. $\sigma'_{c,0} < 50$ kN/m^2) tends to show closer agreement with the $\phi'_{cv} \approx 35°$ value reported by Stroud (1971), the average characteristic stress ratio of η_{Ch} = 1.40 ±0.01 is higher than the range of triaxial compression critical friction ratios, M_{tc}, reported by Jefferies & Been (2015) for quartz sands ($1.25 \leq M_{tc} \leq 1.35$), where:

$$M_{tc} = \frac{q_{cv}}{p'_{cv}} = \frac{6 \sin \phi'_{cv}}{3 - \sin \phi'_{cv}} \tag{6-14}$$

Table 6.4 shows that characteristic state conditions are typically mobilised at $\varepsilon_q \leq 0.1$ %. ϕ'_{Ch} may therefore be determined with a much higher degree of accuracy than ϕ'_{cv}, given that estimates are based on specimen dimensions that can be reliably tracked from initial measurements via local strain instrumentation. Results of tests performed at conventional initial confining stresses therefore support the findings of Luong (1980) and suggest that, in the absence of undrained tests on loose sand specimens, reasonably accurate estimations of ϕ'_{cv} and M_{tc} may be obtained from drained triaxial tests without needing to mobilise large strain magnitudes. However, at lower confining stresses, using ϕ'_{Ch} and η_{Ch} to estimate ϕ'_{cv} and M_{tc} may result in values being overpredicted.

6.5.3. DILATANCY AT LOW STRESS LEVELS

Dilatancy is a measure of the change in volume that occurs with shear distortion of a material, and must be accounted for in constitutive models if reliable predictions of soil deformation and pore pressure development are to be made. Historically, dilatancy was characterised by a dilation angle, ψ^D, which is an expression of the ratio of the plastic volume change to plastic shear strain, and is an important input parameter of the Mohr-Coulomb model. (Note: the superscript “D” is used here to differentiate between the shared notation with state parameter, ψ).

The dilation angle varies during shearing, but is found to be greatest near and at peak strength, and for soils the maximum instantaneous dilation angle is known to be significantly smaller than ϕ'_{max}. According to Vermeer & de Borst (1984), dense sands typically exhibit maximum dilation angles of approximately 15°, while looser sands tend to have lower values (< 10°).

The angle of dilation is conventionally defined for plane strain conditions (e.g. Hansen, 1958; Roscoe, 1970; Bolton, 1986; Houlsby, 1991):

$$\sin\psi^D = -\left(\frac{\delta\varepsilon_p^p}{\delta\gamma_{max}^p}\right) = -\left(\frac{\delta\varepsilon_1^p + \delta\varepsilon_3^p}{\delta\varepsilon_1^p - \delta\varepsilon_3^p}\right) \tag{6-15}$$

where:

$\delta\varepsilon_p^p$ = volumetric plastic strain increment
$\delta\gamma_{max}^p$ = maximum plastic shear strain increment
$\delta\varepsilon_1^p$ = major principal plastic strain increment
$\delta\varepsilon_3^p$ = minor principal plastic strain increment

However, for loading other than plane strain conditions, other definitions have been suggested for determining ψ^D In triaxial compression, Houlsby (1991) and Vaid & Sasitharan (1992) proposed:

$$\sin\psi^D = -\left(\frac{\delta\varepsilon_1^p + \delta\varepsilon_2^p + \delta\varepsilon_3^p}{\delta\varepsilon_1^p - \delta\varepsilon_3^p}\right) = -\left(\frac{\delta\varepsilon_z^p + 2\delta\varepsilon_r^p}{\delta\varepsilon_z^p - \delta\varepsilon_r^p}\right) \tag{6-16}$$

where:

$\delta\varepsilon_z^p$ = vertical strain increment (plastic component)
$\delta\varepsilon_r^p$ = radial strain increment (plastic component)

and in triaxial extension:

$$\sin\psi^D = -\left(\frac{\delta\varepsilon_z^p + 2\delta\varepsilon_r^p}{\delta\varepsilon_r^p - \delta\varepsilon_z^p}\right) \tag{6-17}$$

However, an alternative definition of ψ^D has been suggested by Vermeer (Schanz & Vermeer, 1996; Vermeer & de Borst, 1984) for plane strain and triaxial compression conditions, of the form:

$$\sin\psi^D = -\left(\frac{\delta\varepsilon_p^p}{2\delta\varepsilon_1^p - \delta\varepsilon_p^p}\right) \tag{6-18}$$

In plane strain Eq. (6-18) reduces to Eq. (6-15); therefore, for plain strain conditions there is compatibility between the two definitions. However, in triaxial compression, Eq. (6-18) becomes:

$$\sin\psi^D = -\left(\frac{\delta\varepsilon_1^p + 2\delta\varepsilon_3^p}{\delta\varepsilon_1^p - 2\delta\varepsilon_3^p}\right) = -\left(\frac{\delta\varepsilon_z^p + 2\delta\varepsilon_r^p}{\delta\varepsilon_z^p - 2\delta\varepsilon_r^p}\right) \tag{6-19}$$

Vermeer & de Borst (1984) did not refer to triaxial extension, but according to Frydman *et al*. (2007), the form of their development leads to the following relation for triaxial extension:

$$\sin\psi^D = -\left(\frac{2\delta\varepsilon_1^p + \delta\varepsilon_3^p}{2\delta\varepsilon_1^p - \delta\varepsilon_3^p}\right) = -\left(\frac{2\delta\varepsilon_r^p + \delta\varepsilon_z^p}{2\delta\varepsilon_r^p - \delta\varepsilon_z^p}\right) \tag{6-20}$$

Alternatively, the mobilised angle of dilation may also be determined graphically from results of triaxial tests. Rearranging Eq. (6-15) in terms of the gradient of the line determined from a volumetric strain vs. axial strain plot ($d\varepsilon_p$ / $d\varepsilon_z$), Vaid & Sasitharan (1992) derived the following expression:

$$\psi^D = Arcsin\left[\frac{2}{\frac{3}{(d\varepsilon_p/d\varepsilon_z)} - 1}\right] \tag{6-21}$$

Similarly, rearranging Eq. (6-19) in terms of the slope of the volumetric strain vs axial strain curve:

$$\psi^D = Arcsin\left[\frac{\frac{d\varepsilon_p}{d\varepsilon_z}}{\frac{d\varepsilon_p}{d\varepsilon_z} - 2}\right] \tag{6-22}$$

The above illustrates that while there exists a universally accepted definition of the angle of dilation in plane strain (Eq. (6-15)), multiple definitions are available when considering triaxial stress conditions. While the adopted definition of ψ^D is somewhat arbitrary, the lack of a unique, universally agreed-on relationship is cause for confusion and may have significant implications on design without due care.

This is exemplified by the numerical modelling work undertaken by Lee (2000), who measured dilation angles of up to 45°, obtained from drained triaxial compression tests by “measuring the slope of the linear portion of the volumetric strain versus axial strain”. It is not clear from the above exactly which method Lee adopted to determine the values of ψ^D; however, he goes on to note that the magnitude of ψ^D used in the numerical analyses had an enormous effect on the predicted deformations of geosynthetic reinforced retaining walls under investigation.

Furthermore, Frydman *et al*. (2007) point out that the commonly used numerical codes PLAXIS (Plaxis, 2018) and FLAC (Itasca Consulting Group Inc., 2015), recommend that ψ^D used in plane strain analyses be estimated from triaxial compression tests according to Eq. (6-19); however, without appreciation of the above, calculating ψ^D according to Eq. (6-16) would yield a different value for input into the plane strain analyses, leading to a different result.

Figure 6.19a presents angles of dilation determined from external strain measurements based on the two methods described above, with $\psi^D_{(1)}$ based on 'method 1' (Eqs. (6-16) and (6-17)), and $\psi^D_{(2)}$ calculated from 'method 2' (Eqs. (6-19) and (6-20)). Results are summarised in Table 6.3.

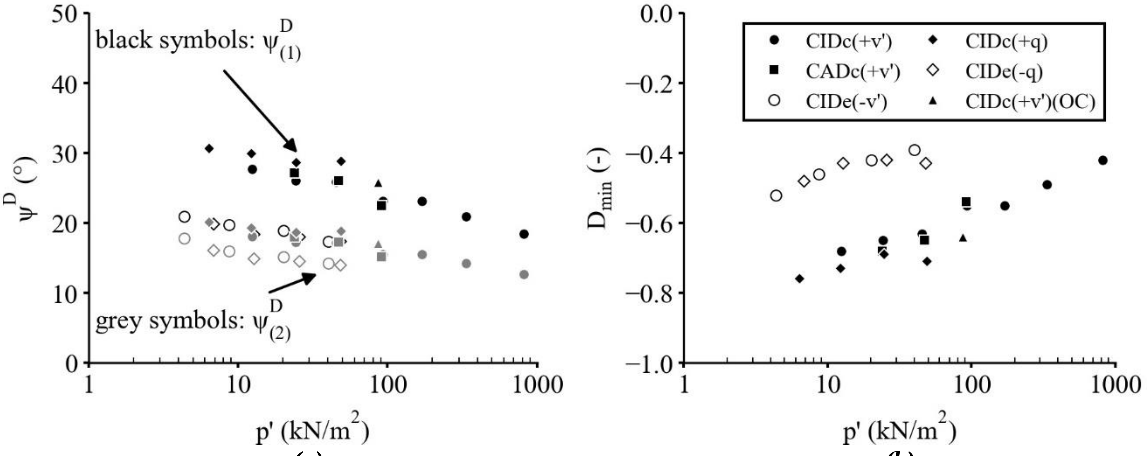

(a) *(b)*

Figure 6.19: (a) Maximum dilation angle, ψ^D, calculated from the two definintions given in the literature; and (b) maximum dilatancy, D_{min}, versus mean effective stress, p'.

Figure 6.19a shows that samples sheared at lower mean effective stresses mobilise higher values of ψ^D. Mobilised ψ^D values are also found to be higher in compression than in extension tests undertaken at similar $\sigma'_{c,0}$ values. Two distinct groups are clearly visible in Figure 6.19a, with results from Eq. (6-16) yielding ψ^D values approximately 10° higher than those from Eq. (6-19).

Figure 6.19b presents the maximum dilatancy rate, D_{min}, (subscript min because of the compression positive sign convention used in soil mechanics), defined by Jefferies & Shuttle (2002) as the ratio between the two plastic strain increment invariants:

$$D = \frac{\delta\varepsilon_p^p}{\delta\varepsilon_q^p} \approx \frac{\delta\varepsilon_p}{\delta\varepsilon_q} \tag{6-23}$$

where:

$\delta\varepsilon_p^p$ = plastic component of the incremental volumetric strain
$\delta\varepsilon_q^p$ = plastic component of the incremental deviatoric strain

These curves show a similarly linear trend in both compression and extension, indicating that the magnitude of the dilatant response increases with decreasing mean effective stress.

The adopted definition of ψ^D also influences the outcome of predictions of ϕ'_{max} made from Bolton's empirical flow rule (Bolton, 1986). From compilation of an extensive database, Bolton proposed an empirical relationship for determining ϕ'_{max} from soil state variables for both triaxial and plane-strain compression conditions, where:

$$\phi'_{max} = \phi'_{cv} + A_\psi I_R \tag{6-24}$$

where:

A_ψ = constant (5 for plane-strain; 3 for triaxial conditions)
I_R = relative dilatancy index (function of density and mean effective stress)

This relationship was later modified following work and comments made by Tatsuoka (1987) to account for the behaviour of sands at relatively small confining stresses:

for $p' > 150kN/m^2$:
$$I_R = D_r\left[5 - \ln\left(\frac{p'}{150}\right)\right] - 1 \tag{6-25}$$

for $p' \leq 150kN/m^2$:
$$I_R = 5D_r - 1 \tag{6-26}$$

Bolton (1986) found that for plane strain conditions, Eq. (6-24) could be simplified to:

$$\phi'_{max} = \phi'_{cv} + 0.8\psi^D_{max} \tag{6-27}$$

where the maximum dilation angle is defined according to plane strain definitions as:

$$\sin\psi^D_{max} = \left(-\frac{\delta\varepsilon_p^p}{\delta\gamma^p}\right) = -\frac{(\delta\varepsilon_1/\delta\varepsilon_3)_{max} + 1}{(\delta\varepsilon_1/\delta\varepsilon_3)_{max} - 1} \tag{6-28}$$

Eq. (6-24) and Eq. (5-2) suggest that for plane strain compression, $0.8\psi^D_{max}$ is equivalent to $\phi'_{max} - \phi'_{cv} = A_\psi I_R$, with $A_\psi = 5$. Considering triaxial conditions, where $A_\psi = 3$, and a similar value for I_R, then the difference between ϕ'_{max} and ϕ'_{cv} should be 60 % of the value of this difference for plane strain compression, or $0.6(0.8\psi^D_{max}) = 0.48\psi^D_{max}$. For triaxial compression conditions, Bolton's (1986) expression may therefore be presented as

$$\phi'_{max} = \phi'_{cv} + 0.48\psi^D_{max} \approx \phi'_{cv} + 0.5\psi^D_{max} \tag{6-29}$$

or: $$\phi'_{max} - \phi'_{cv} = 3I_R \tag{6-30}$$

Figure 6.20a presents values of ϕ'_{max} determined from the drained triaxial compression tests at mean effective stresses coinciding with failure conditions, p'_f. Also shown are values of ϕ'_{max} calculated from Eq. (6-29) using ψ^D_{max} values estimated from both Eq. (6-16) and Eq. (6-19), $\psi^D_{(1)}$ and $\psi^D_{(2)}$, respectively. In situations where test-specific values of ϕ'_{cv} were unavailable, the average value defined in Section 6.5.1 was adopted (ϕ'_{cv}= 30.9°). Figure 6.20a shows that the definition of ψ^D proposed by Vermeer & de Borst (1984) yields ϕ'_{max} values that agree more closely with the experimental data than those calculated from Eq. (6-16).

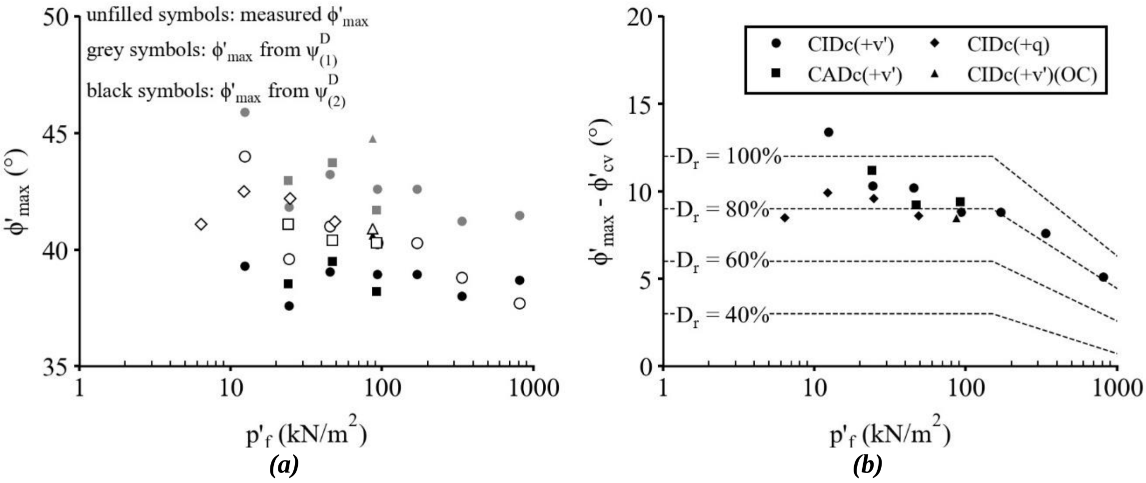

(a) *(b)*

Figure 6.20: (a) ϕ'_{max} determined both experimentally and from Eq. (6-29); and (b), comparison of experimentally determined ϕ'_{max} - ϕ'_{cv} values with Bolton's (1987) modified empirical prediction, versus mean effective stress at failure, p'_f

Figure 6.20b presents Bolton's modified empirical profile (Tatsuoka, 1987) of I_R (= $\phi'_{max} - \phi'_{cv}$) against the mean effective stress at failure, p'_f, for various relative densities, following the modification to account for small effective confining stresses (Eqs. (6-25) and (6-26)). The experimental data obtained from this investigation shows good agreement with the modified empirical prediction, further supporting the notion of a low stress 'threshold' at approximately p' = 150 kN/m^2.

6.6. STIFFNESS AT LOW STRESS LEVELS

The small-strain, elastic behaviour is an important part of constitutive modelling, an accurate determination of which is essential if realistic predictions of soil deformations are required. Jardine *et al*. (1986) and Mair (1993) have shown that the strain levels around typical geotechnical structures fall in the range where soil stiffness changes most dramatically with strain, and are normally in the range 0.01 to 0.1 %, as illustrated in Figure 6.21.

Therefore, in addition to estimates of small strain elastic stiffness moduli, stiffness degradation data are also required for accurate ground movement predictions. Laboratory testing plays an important role in the determination of stiffness parameters. With appropriate instrumentation, the triaxial test can provide a complete history of the degradation of soil stiffness with increasing strain level.

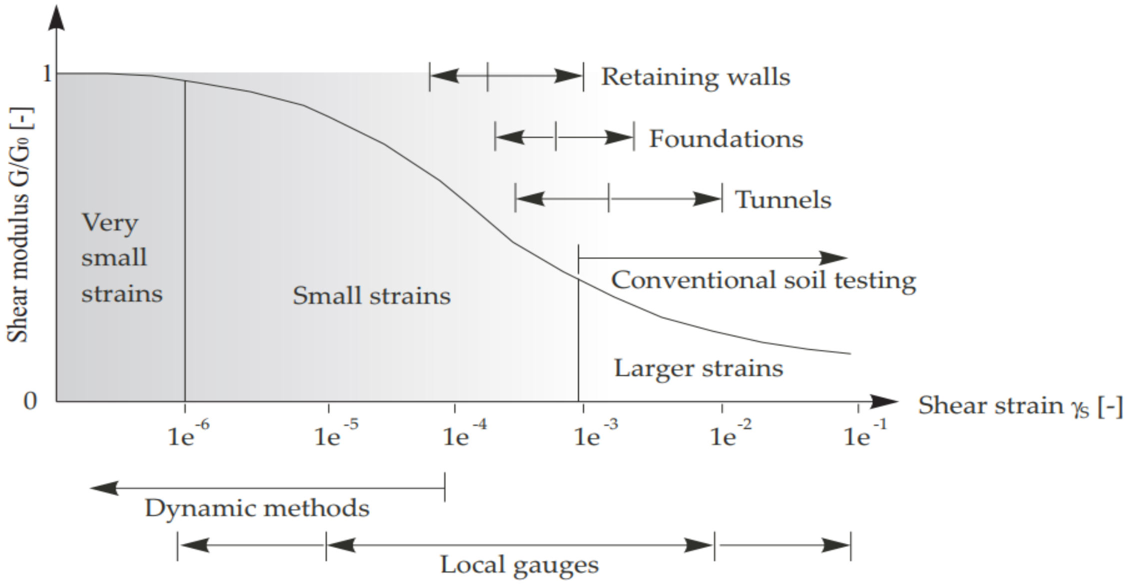

Figure 6.21: Characteristic stiffness degradation profile for soils with typical strain ranges for laboratory tests and structures (from Atkinson & Sallfors, 1991).

6.6.1. ESTIMATION OF G_0 FROM BENDER ELEMENT TESTS

Figure 6.22(a-d) shows transmitted and received data stacked from four bender element pulses from various tests undertaken as part of this study, via bender elements mounted in the top and bottom platens. The tests were carried out at the end of the creep stage and immediately prior to shearing, and comprised firing a single 12 V amplitude shear wave pulse through the sample.

Time domain methods ***Cross correlation method***

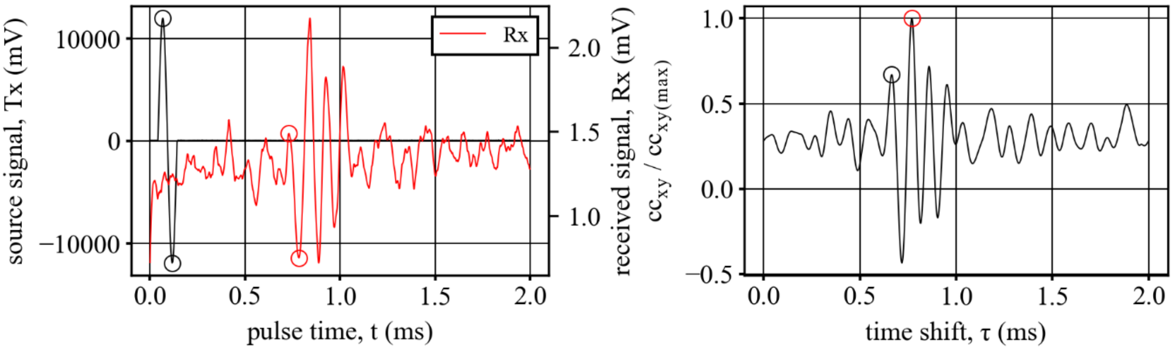

(a) s01 CIDc(+v′) 80.50: G_0 = 172.2 MN/m^2 ***(b) s01 CIDc(+v′) 80.50: G_0 = 172.2 MN/m^2***

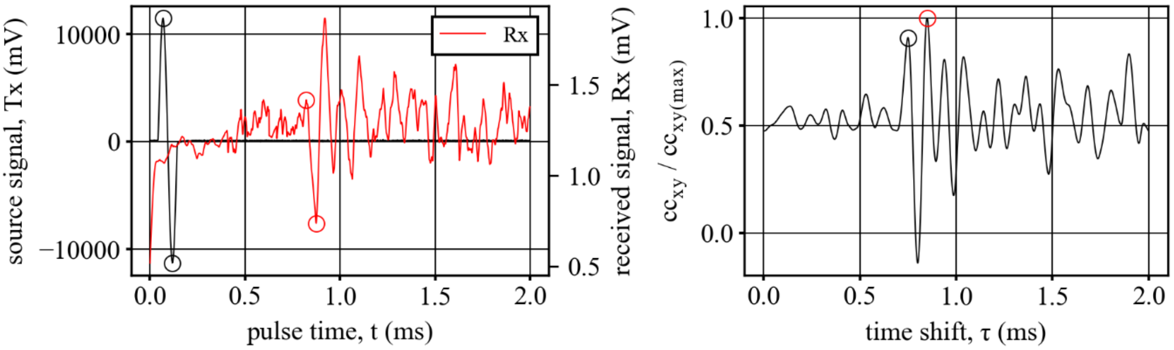

(c) s02a CIDc(+v′) 80.25: G_0 = 133.3 MN/m^2 ***(d) s02a CIDc(+v′) 80.25: G_0 = 135.2 MN/m^2***

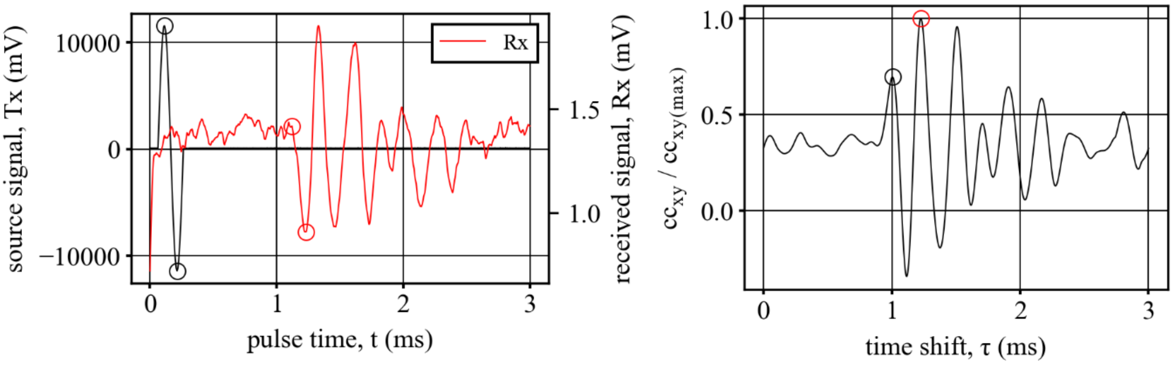

(e) s03 CIDc(+v′) 80.12: G_0 = 75.5 MN/m^2 ***(f) s03 CIDc(+v′) 80.12: G_0 = 75.5 MN/m^2***

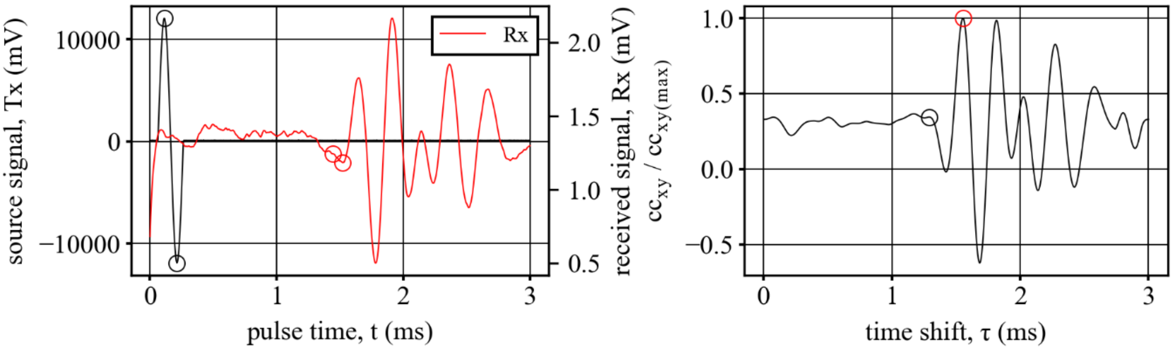

(g) s12 CIDe(-v′) 80.6: G_0 = 43.6 MN/m^2 ***(h) s12 CIDe(-v′) 80.6: G_0 = 45.6 MN/m^2***

Figure 6.22: Bender element test results comparing time domain (i.e. first major peak to peak) and cross-correlation methods at different mean effective stresses for Leighton Buzzard sand (Fraction B).

The bender testing apparatus allows for various input frequencies to be selected; however, to avoid near-field effects, input frequencies of 10 kHz were typically adopted to ensure wavelength ratios greater than 3.33 (as recommended by Leong *et al*., 2005 and Arroyo *et al*., 2006). Lade (2016) presents an overview of the various methods typically employed for interpreting bender element signal data, and comments that reliability in results depends upon employing the same method throughout a study, coupled with consistent user judgement during interpretation. Clayton (2011) suggests that the “First break” and the “First peak-to-peak” methods be adopted in routine triaxial testing, as significant differences were found in cases adopting the more complex cross correlation and phase/frequency methods (Ferreira & da Fonseca, 2005; Yamashita *et al*., 2009). However, there is no clear consensus regarding which approach yields the most reliable results.

Several features can be seen from Figure 6.22:

- Well-defined peaks are clearly visible in the received signal data, and the time histories indicate that the shear wave velocity increases with increasing mean effective stress.
- The signals are subject to significant background noise, resulting in multiple random and localised peaks both before and after the received trace.
- It is not possible to reliably determine the ‘first break’ given the extent of noise in the data
- Several peaks are observed in the received trace. Determination of the ‘first major peak’ therefore requires judgement.

As shown in Figure 6.22, the ‘First break’ is not well defined and so this method was not considered further. However, the profiles do show reasonably well-defined peaks that are clearly distinguishable from the background noise. The ‘First major peak-to-peak’ method was therefore initially adopted for determining estimates of the shear wave velocity, v_s, and small-strain shear modulus, G_0.

However, the location of the first major peak was not always clearly identifiable, particularly at very low stress levels which leads to unreliable estimates of G_0. The cross correlation method was therefore also implemented, and was found to provide a more robust means of determining the arrival of the shear wave, as shown in Figure 6.22. Full details of the cross-correlation method are provided by Mohsin (2008). G_0 values estimated using this method are summarised in Table 6.6.

Determining the small-strain shear modulus of soils has been the focus of much research, and has led to the development of numerous empirical relationships. Clayton (2011) states that the shear modulus of granular material at very small strains is affected by three main factors:

- the void ratio of the specimen;
- the effective stress, and interparticle contact stiffness (related to particle mineralogy, angularity and roughness);
- deformation and flexing within individual particles (related to particle mineralogy and shape).

A comprehensive list of published relationships was compiled by Benz (2007), who found that most empirical equations adopt a similar form, where:

$$\mathrm{G}_0 = A_G p_{ref} f(e) OCR^k \left(\frac{p'}{p_{ref}}\right)^{n_G} \tag{6-31}$$

where:

$f(e)$ = some function of void ratio

A_G, k, n_G = dimensionless material constants

p_{ref} = reference pressure (usually taken as atmospheric pressure = 101.3kN/m^2)

For cohesionless soils, the factor k (a function of the plasticity index) reduces to 0, meaning that G_0 depends only on the mean effective stress and void ratio, and not on OCR. To account for the influence of void ratio, Hardin & Black (1966) proposed:

$$f(e) = \frac{\left(e_g - e\right)^2}{(1+e)} \tag{6-32}$$

where e_g = 2.17 and 2.97 for rounded and angular particles shapes, respectively. Different values for the material constant, A_G have been proposed for sands with various grading, particle size, surface roughness, and minerology. The exponent n_G is often taken as 0.50, which has the advantage of conforming to Hertzian theory for pressure dependence of conical contacts (Goddard, 1990).

Figure 6.23 summarises values of G_0 determined from bender element tests carried out on samples of LBS-B at various mean effective stresses. Figure 6.23 also presents predictions of G_0 vs p', determined from empirical relationships based on the results of tests undertaken on silica sands. These relationships use Eq. (6-31), and are summarised in Table 6.5.

Figure 6.23 shows that the experimentally determined G_0 values are generally higher than would be estimated from empirical relationships for silica sands. However, relatively good agreement is achieved with the Hoque & Tatsuoka (2004) and Penna *et al*. (2016) profiles, both of which are based on element tests undertaken on LBS. Hoque & Tatsuoka (1998) also observed that the axial Young's modulus of silver LBS is much larger than that of other clean uniform sands and gravels at similar states. This is encouraging, as despite the silver LBS used by Hoque & Tatsuoka having different grading characteristics to the LBS-B used in this study, it originates from the same geological formation and thus shares similar geotechnical characteristics, suggesting that relatively higher values of G_0 are to be expected.

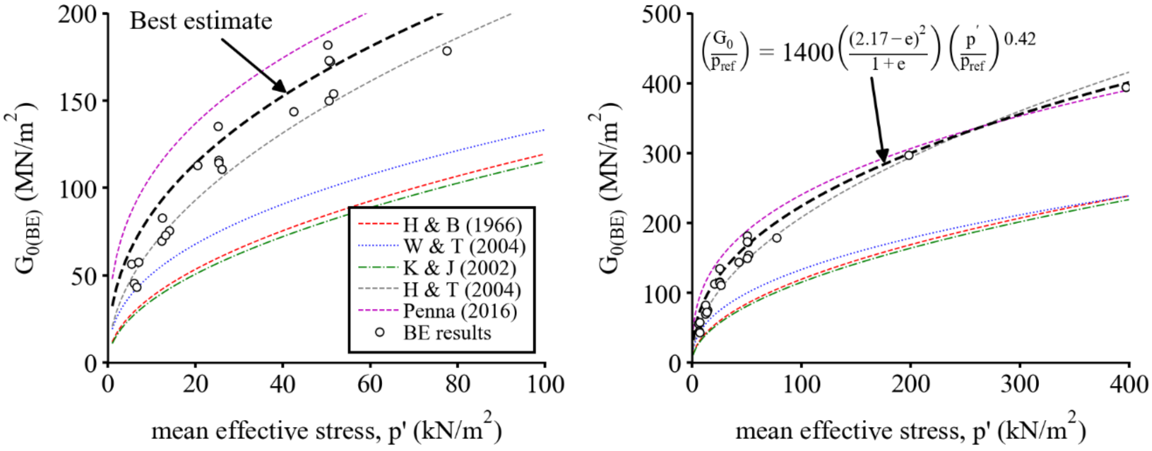

(a) ***(b)***

Figure 6.23: Small-strain shear modulus, G_0, vs mean effective stress, p', estimated from bender element test results and empirical relationships found in the literature

Table 6.5: Summary of select empirical relationships used to estimate G_0 (modified from Benz, 2007)

soil tested **(-)**	d_{50} **(mm)**	C_U **(-)**	A_G **(-)**	$f(e)$ **(-)**	n_G **(-)**	**Reference** **(-)**
crushed sand	-	-	330	$(2.97 - e)^2/(1 + e)$	0.5	(Hardin & Black, 1966)
Ham River sand	0.27	1.67	720-810	$(2.17 - e)^2/(1 + e)$	0.50-0.52	(Kuwano & Jardine, 2002b)
silica sand	0.55	1.66	2750	$(1.46 - e)^2/(1 + e)$	0.42	(Wichtmann & Triantafyllidis, 2004)
silver LBS	0.62	1.11	820-1300	$(2.17 - e)^2/(1 + e)$	0.44-0.53	(Hoque & Tatsuoka, 2004)
LBS-B	0.82	-	1500	$(1.85 - e)^2/(1 + e)$	0.35	(Penna *et al*., 2016)

The Hoque & Tatsuoka (2004) profile shown in Figure 6.23 uses A_G = 1300 (and m = 0.5), and therefore represents an upper bound in terms of the range of A_G values appropriate for silver LBS, but also in comparison to the material constants quoted in the other empirical relationships listed in Table 6.5. One reason as to why silver LBS exhibits higher values of G_0 may be on account of its relatively larger median particle size, d_{50}. Bui (2009) investigated the effect of particle size on the small strain behaviour of granular material and found that G_0 increased significantly with increasing particle size. The relatively larger particle size of the LBS tested in this study (d_{50} = 0.85 mm) and associated higher G_0 values appear to support Bui's (2009) findings.

However, there is also research to support the idea that estimates of G_0 are independent of particle size, as the effects of particle size are intrinsically accounted for within the void ratio function (Hardin & Drnevich (1972), Iwasaki & Tatsuoka (1977) and Wichtmann & Triantafyllidis (2010)). Iwasaki & Tatsuoka (1977) also indicated that differences in normalised G_0 values of various clean sands with different particle shapes are generally less than 10 %. The higher shear moduli observed in this study may therefore be attributable to differences in the mineralogy or the surface roughness of the grains influencing individual particle contact stresses. More research in this area is needed to clarify the issue.

The analysis also emphasizes the problems associated with using empirical relationships to determine G_0, which may lead to significant underpredictions if the material under consideration differs from that used in the formulation of the empirical relationship. However, for LBS-B, Eq. (6-33) is found to provide a satisfactory fit to the experimental data as shown in Figure 6.23:

$$\frac{G_0}{p_{ref}} = 1400\frac{(2.17-e)^2}{(1+e)}\left(\frac{p'}{p_{ref}}\right)^{0.42} \tag{6-33}$$

6.6.2. ESTIMATION OF G0 FROM LOCAL STRAIN INSTRUMENTATION

One of the key advantages of triaxial testing is that the full non-linear stiffness degradation curve may be determined if local small-strain instrumentation is installed on test specimens. Scholey *et al*. (1995) recommended that local strain instrumentation must be capable of measuring strains to an accuracy of at least 10^{-5}; however, to accurately measure purely elastic behaviour, higher resolution local strain instrumentation may be required.

Details of the submersible on-sample LVDTs used in this study are presented in Chapter 4. In summary, they have a working range of ±5 mm, and were found to output a stable signal to a resolution of 0.001 mm. Figure 6.24 illustrates that when installed over the central third of the test specimen, the bracket distance covers a length of approximately 70 mm for extension tests, and 90 mm for compression tests. This distance is taken as the reference length for strain calculations.

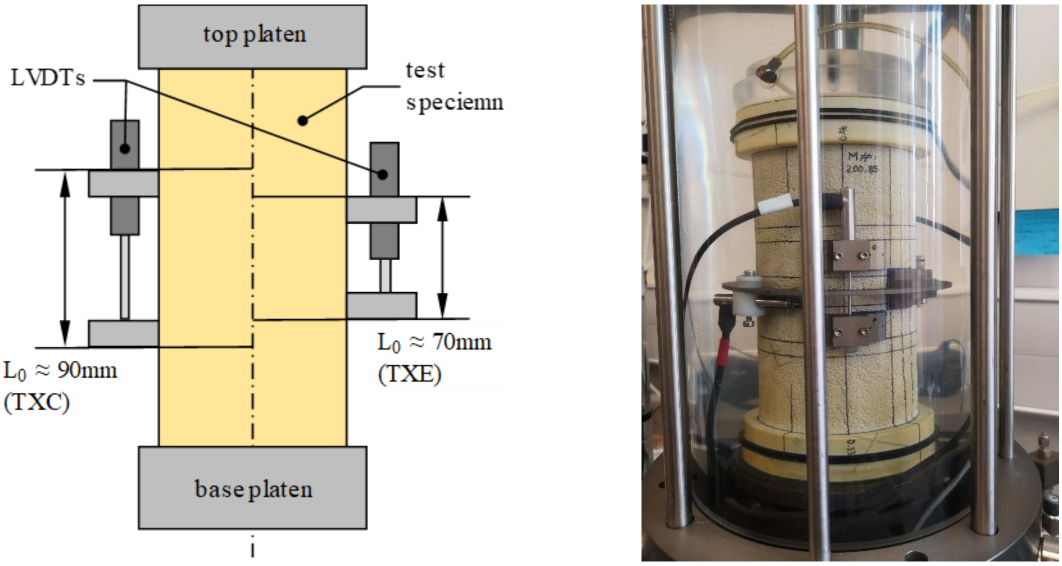

(a) *(b)*

Figure 6.24: Sketch showing (a) defintion of reference lengths in determination of axial strains from small-strain instrumentation; and (b) photograph of a typical specimen set-up.

Based on this set-up, reliable estimates of axial strain to 10^{-5} are considered achievable ($\varepsilon_z = \delta z \,/\, L_0 = 0.001 / 70 = 1.43 \mathrm{x} 10^{-5}$). While the LVDTs may display to resolutions less than 1 μm, it was found that the fourth decimal place (when displayed in mm) suffered from fluctuations of the order ±0.5 μm. Therefore, estimations of strains to an accuracy of less than 10^{-5} are potentially misleading.

In hindsight, acquiring on-sample LVDTs with a reduced range (e.g. ±2.5 mm) may have been prudent, as the reduced working range would serve to improve the accuracy of measurements in the very small strain, elastic range, while still having sufficient range to capture the majority of the stiffness degradation profile (i.e. maximum measurable strain range = $\delta z \,/\, L_0$ = 5 / 90 ≈ 5 %.).

With local strain instrumentation, the secant shear stiffness, G_{sec}, may be calculated directly from plots of deviatoric stress, q, vs. deviatoric strain, ε_q, (see Section 4.8.4). Figure 6.25 shows secant stiffness degradation profiles for the drained triaxial stress path tests undertaken as part of this study (for $\sigma'_{c,0} \leq$ 50 kN/m^2), calculated from local strain instrumentation, together with G_0 values determined from bender element tests. The unload-reload loops are not shown for clarity.

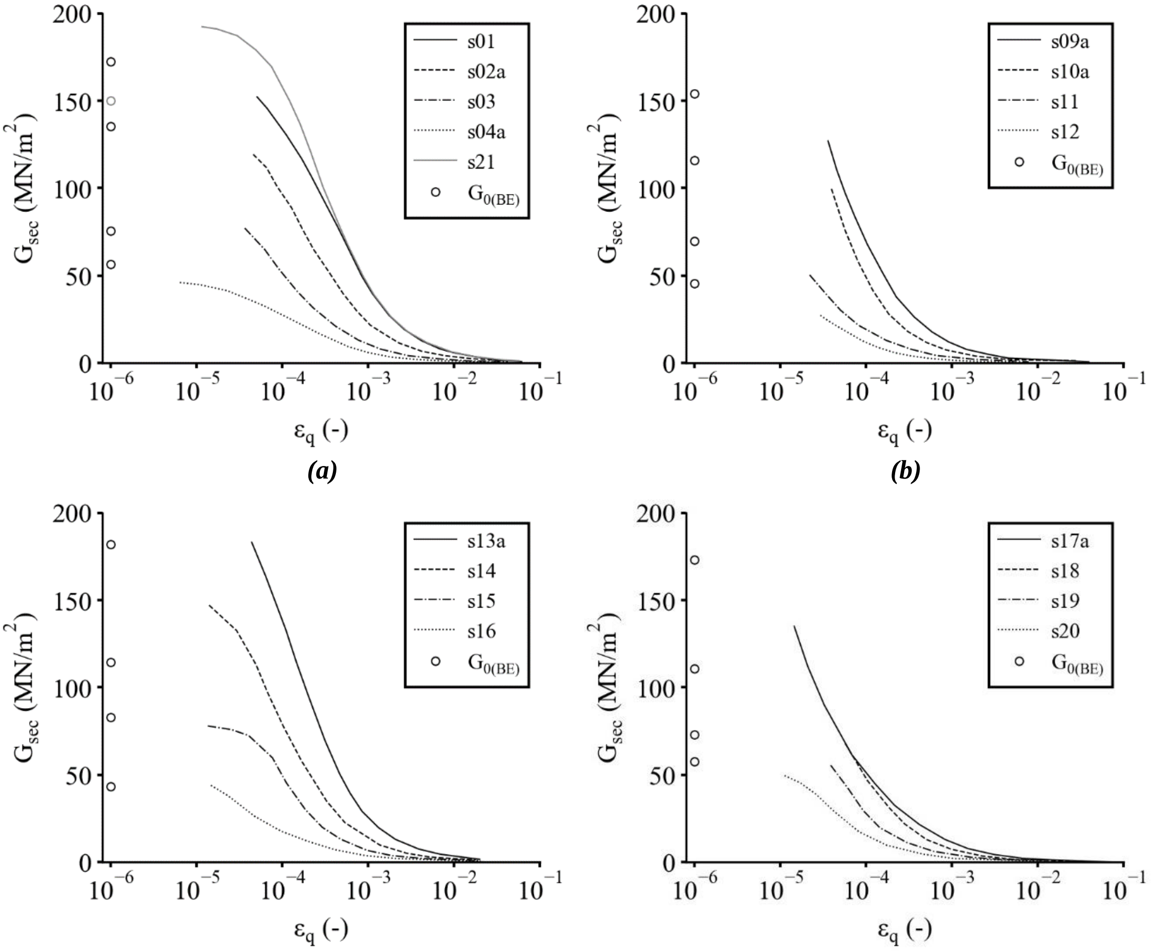

(a) ***(b)***

(c) ***(d)***

Figure 6.25: Secant shear stiffness, G_{sec} vs. deviatoric strain, ε_q, from (a) CIDc(+v′) tests; (b) CIDe(-v′) tests; (c) CIDc(+q) tests; and (d) CIDe(-q) tests.

The plots show the influence of effective confining stress, with higher confining stresses yielding higher estimates of G_{sec} as expected. However, while the initial portions of some of the curves do show signs of plateauing, the data becomes increasingly noisy at strain levels less than approximately 3x10^{-5}, making reliable estimates of G_0 difficult.

Table 6.6 summarises values of G_0 estimated from local small-strain instrumentation, together with values determined from bender element tests. Values are also presented graphically in Figure 6.26, indicating that despite the difficulty in determining G_0 values from local strain instrumentation, reasonable agreement is achieved with the bender element test results.

However, it is evident from Figure 6.26 that despite conservative values of G_0 being estimated from the local strain instrumentation, these values often exceed those determined from the bender element tests by more than 10 %. Reasons for the differences in calculated G_0 values are unclear, but may be associated with the inherent anisotropy of LBS-B, and the different shearing modes associated with each method of calculation.

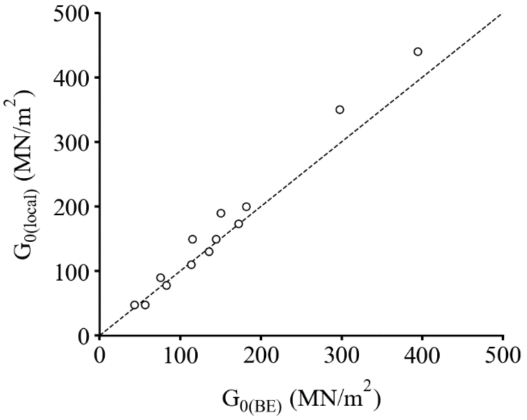

Figure 6.26: Comparison of G_0 values from local strain instrumentation and from bender elements.

Table 6.6: Summary of small-strain shear modulus estimated from local strain instrumentation

Test ID	**Test type**	p'_0	e_c	$G_{0(local)}$*	$G_{0(BE)}$	$\frac{G_{0(local)}}{G_{0(BE)}}$
(-)	**(kN/m^2)**	**(kN/m^2)**	**(-)**	**(MN/m^2)**	**(MN/m^2)**	**(-)**
s01	CIDc(+v’)	50.9	0.584	173	172.2	1.00
s02a	CIDc(+v’)	25.2	0.585	130	135.2	0.96
s03	CIDc(+v’)	14.1	0.586	90	75.5	1.19
s04a	CIDc(+v’)	5.4	0.583	48	56.4	0.85
s05	CADc(+v’)	77.5	0.575	-	178.5	-
s06	CADc(+v’)	42.5	0.586	150	143.9	1.04
s07	CADc(+v’)	20.5	0.588	110	113.1	0.97
s09a	CIDe(-v’)	51.6	0.585	-	154.1	-
s10a	CIDe(-v’)	25.3	0.585	-	116.1	-
s11	CIDe(-v’)	12.2	0.583	-	69.9	-
s12	CIDe(-v’)	6.0	0.587	-	45.6	-
s13a	CIDc(+q)	50.2	0.581	200	181.8	1.10
s14	CIDc(+q)	25.3	0.587	150	114.6	1.31
s15	CIDc(+q)	12.4	0.587	78	82.8	0.94
s16	CIDc(+q)	6.6	0.586	48	43.2	1.11
s17a	CIDe(-q)	50.5	0.586	-	173.0	-
s18	CIDe(-q)	26.0	0.584	-	110.7	-
s19	CIDe(-q)	13.1	0.585	-	72.9	-
s20	CIDe(-q)	7.0	0.584	-	57.8	-
s21	CIDc(+v’)	50.5	0.581	190	150.0	1.27
s22	CIDc(+v’)	101.6	0.590	-	-	-
s23	CIDc(+v’)	198.1	0.581	350	297.3	1.18
s25	CIDc(+v’)	396.8	0.575	440	394.1	1.12

Notes:
* = Best estimate from inspection of Figure 6.25

Figure 6.27 presents plots of normalised secant shear stiffness vs deviatoric strain, for each suite of stress path tests undertaken in this study.

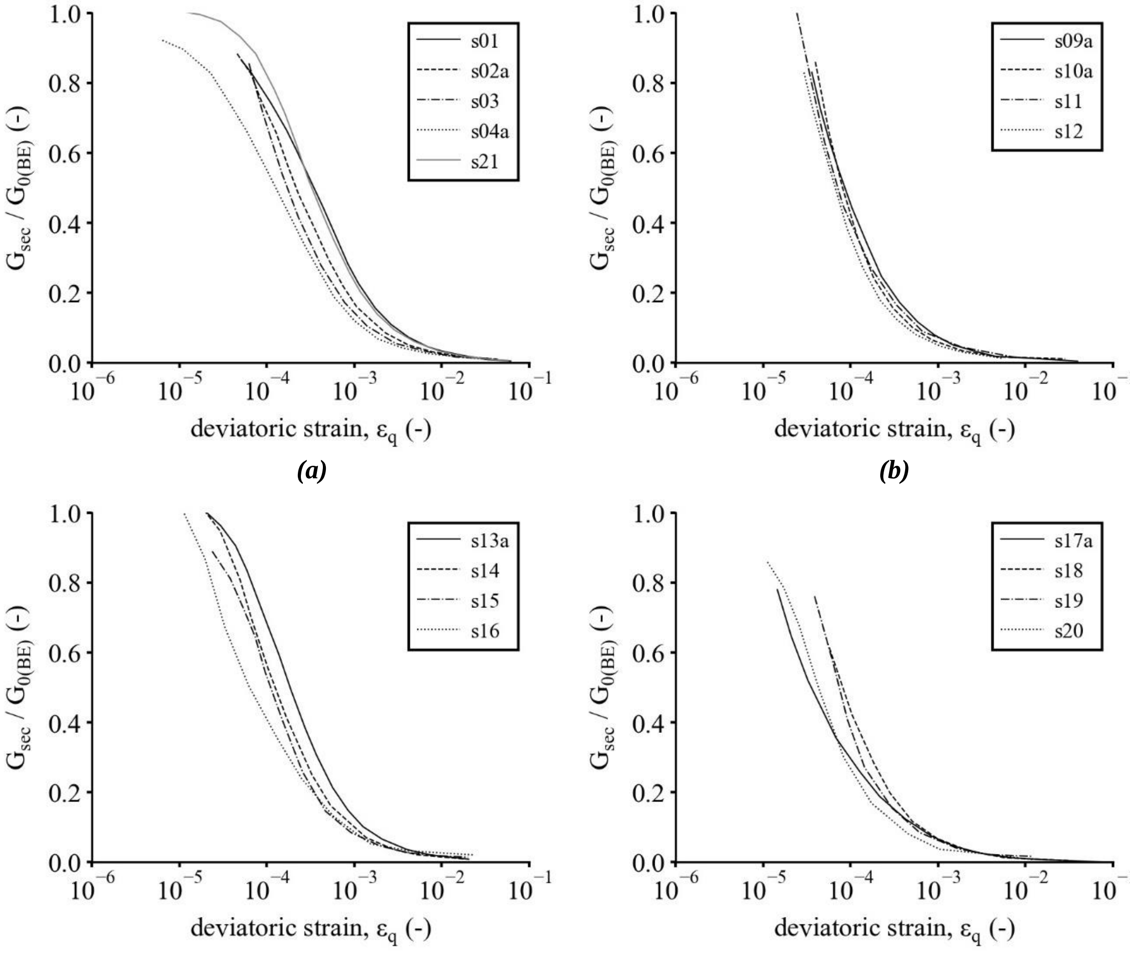

(a) *(b)*

(c) *(d)*

Figure 6.27: Normalised secant shear stiffness, G_{sec} / G_0 vs. deviatoric strain, ε_q, from (a) CIDc(+v') tests; (b) CIDe(-v') tests; (c) CIDc(+q) tests; and (d) CIDe(-q) tests.

The plots show that the shape of the stiffness degradation “S” curve is mildly dependent on the mean effective stress, and indicates that the rate of reduction in shear modulus with strain becomes greater as the confining stress decreases. Thus, tests undertaken at higher confining stresses are shown to plot to the right of tests sheared at lower stresses. This is due to the influence of confining stress on the so-called reference strain, $\varepsilon_{q,ref}$, as defined by Ishihara (1996), who shows that for clean sands, is related to the shear strength properties of the material and the mean effective stress:

$$\varepsilon_{q,ref} = \frac{\eta_{max}}{G_0} \propto (p')^{0.5} \tag{6-34}$$

Figure 6.28 shows idealised and graphical determination of $\varepsilon_{q,ref}$ from the normalised stress-strain curves of tests CIDc(+q)80.50 and CIDc(+q)80.12, and indicates that the magnitude of $\varepsilon_{q,ref}$ increases with increasing mean effective stress. According to Figure 6.28a, the normalised secant shear modulus at reference strain conditions should be similar for both confining stresses. Values of $G_{ref}\ /\ G_0$ = 0.62 and 0.68 for p' = 50 and 12 kN/m^2 respectively, are calculated which is in reasonable agreement with idealised behaviour.

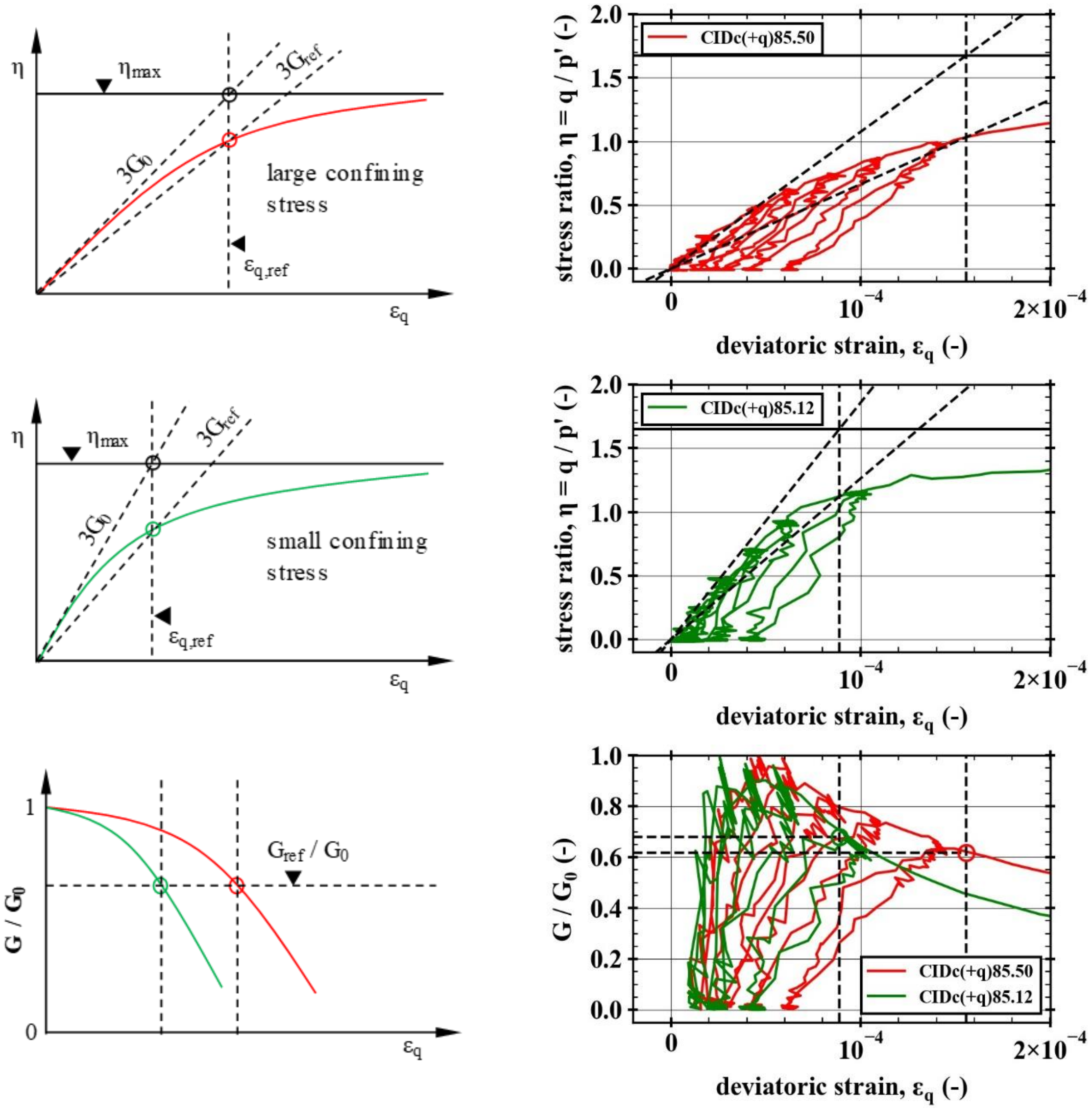

(a) *(b)*

Figure 6.28: (a) idealised and (b) calculated reference strains from CIDc(+q)80.50 and CIDc(+q)80.12, and their influence on the shape of the normalised stiffness degradation curve (after Ishihara, 1996)

The $\varepsilon_{q,ref}$ therefore provides a useful means of evaluating the shape of the stiffness degradation curve, with larger values being mobilised from tests undertaken at higher σ'_c. Such tests tend to have stiffness degradations curves that plot to the right of tests undertaken at lower mean effective stresses (which mobilise smaller values of $\varepsilon_{q,ref}$); therefore, the increase in effective confining stress results in an increase to the normalised G_{sec} at a given strain level, as shown in Figure 6.28.

Figure 6.29 shows normalised stiffness degradation curves for tests sheared at similar p_0' values, illustrating the influence of stress path on the shape of the ‘S’ curve. Conventional triaxial compression and extension tests (i.e. CIDc(+v′) and CIDe(-v′) tests, respectively) are shown to bracket the (+q) stress path tests. This is thought to be due to reasons described above, as the change in p' that occurs during compression/extension acts to shift the curve right/left with mobilised strains.

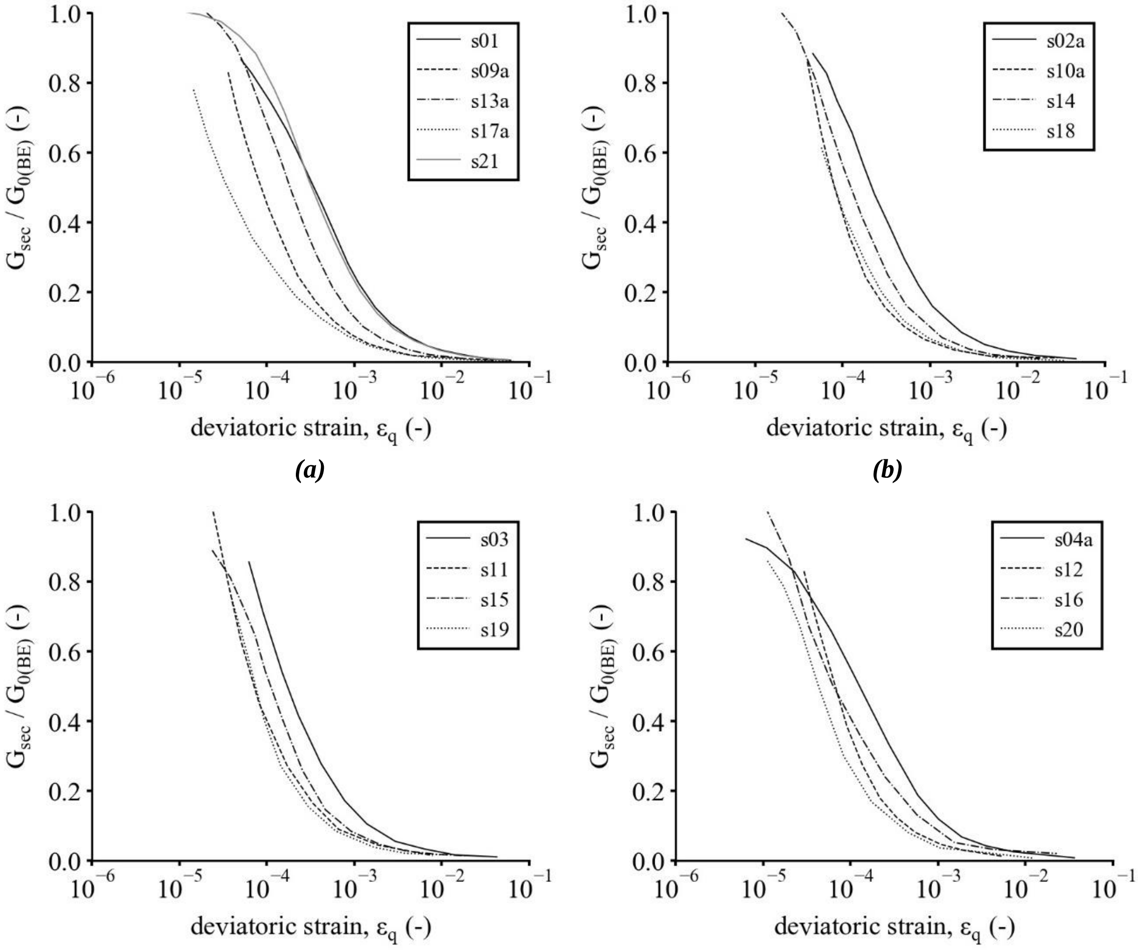

(a) *(b)* *(c)* *(d)*

Figure 6.29: Normalised secant shear stiffness, G_{sec} / G_0 vs. deviatoric strain, ε_q, from (a) $p'_0 = 50kN/m^2$; (b) $p'_0 = 25kN/m^2$; (c) $p'_0 = 12kN/m^2$; and (d) $p'_0 = 6kN/m^2$ tests.

The magnitude of $\varepsilon_{q,ref}$ is also linked to the shear strength properties of the soil (Eq. (6-34)), represented by the maximum shear stress ratio η_{max}. Section 6.5.1 showed that $\eta_{max,te}$ is approximately 60 % of $\eta_{max,tc}$; therefore, $\varepsilon_{q,ref}$ in extension tests will be less than in compression, resulting in stiffness degradation curves plotting to the left of an equivalent compression test.

6.6.3. ESTIMATION OF G_{ur} FROM UNLOAD-RELOAD CYCLES

The true elastic stiffness may also be approximated by performing unloading-reloading cycles, as illustrated in Figure 6.30. The slope of the straight line between point A (the point at which unloading begins) and point B (the point at which reloading begins) is taken as the unloading-reloading modulus, G_{ur}. According to Lade (2016), G_{ur} captures the average soil behaviour during unloading and reloading and may be sufficiently accurate for many situations involving elastic deformations.

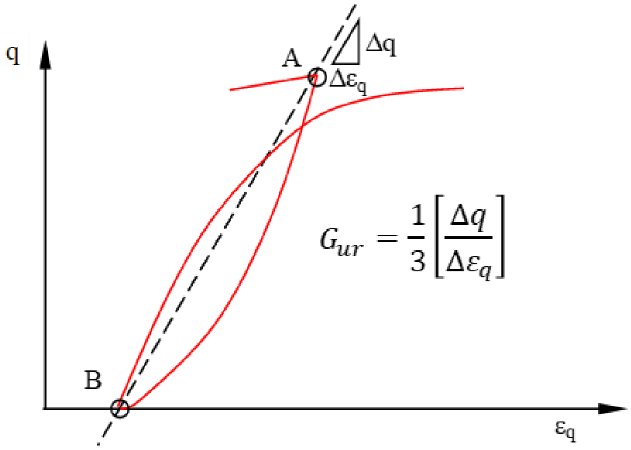

Figure 6.30: Schematic illustration of determination of the unloading-reloading modulus, G_{ur}, and the true elastic modulus, G_0 (modified from Lade, 2016).

While reliable estimates of peak behaviour constitute an important aspect of constitutive models for sand, their ability to accurately model the stress-strain behaviour at small strains may be equally (or more) important in some applications. Figure 6.31 therefore presents the initial profiles of η vs. ε_q obtained from local, small-strain instrumentation, to better identify the effect of confining stress on the shape of the stress-strain profile at the very start of shearing.

The plots show that the initial slope of the normalised stress-strain curves generally increases with decreasing effective confining stress. This suggests that while the peak stress appears to be independent of p' for stress levels less than approximately 50 kN/m^2, the value of p' may still influence the stiffness response. However, the hysteresis loop obtained from the loading-unloading cycle implies that some inelastic behaviour is included in the estimation of G_{ur}. To investigate whether G_{ur} provides a reasonable approximation of G_0 (as determined from bender elements), many of the present tests incorporated unloading-reloading cycles.

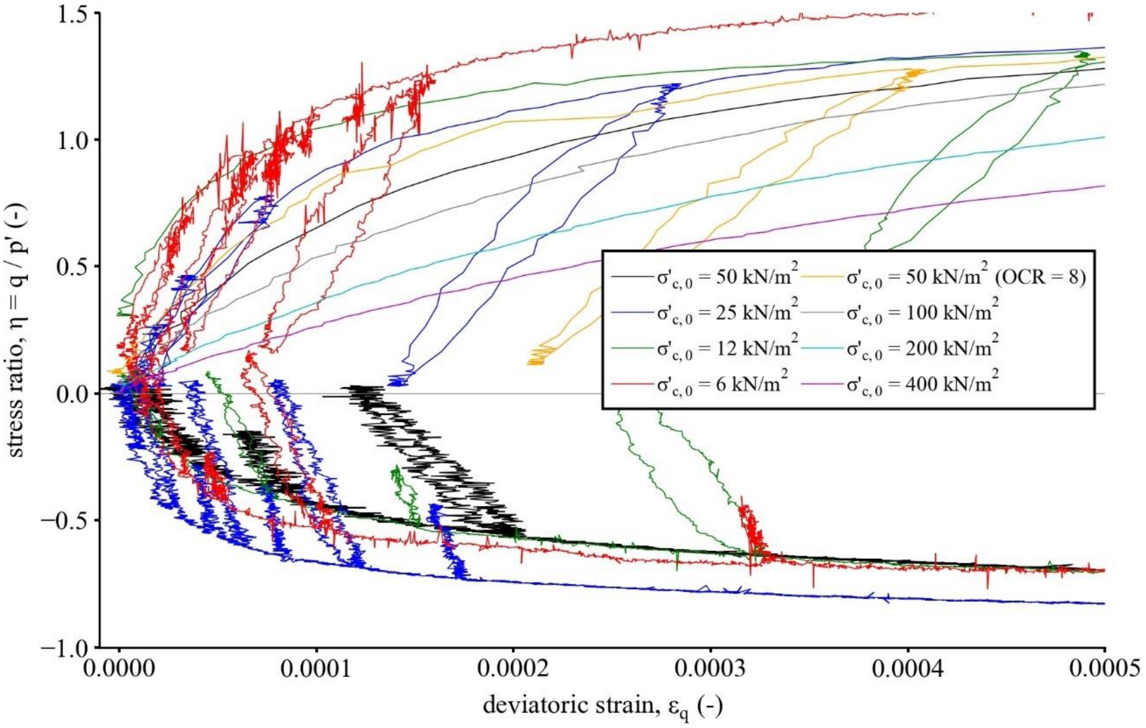

(a)

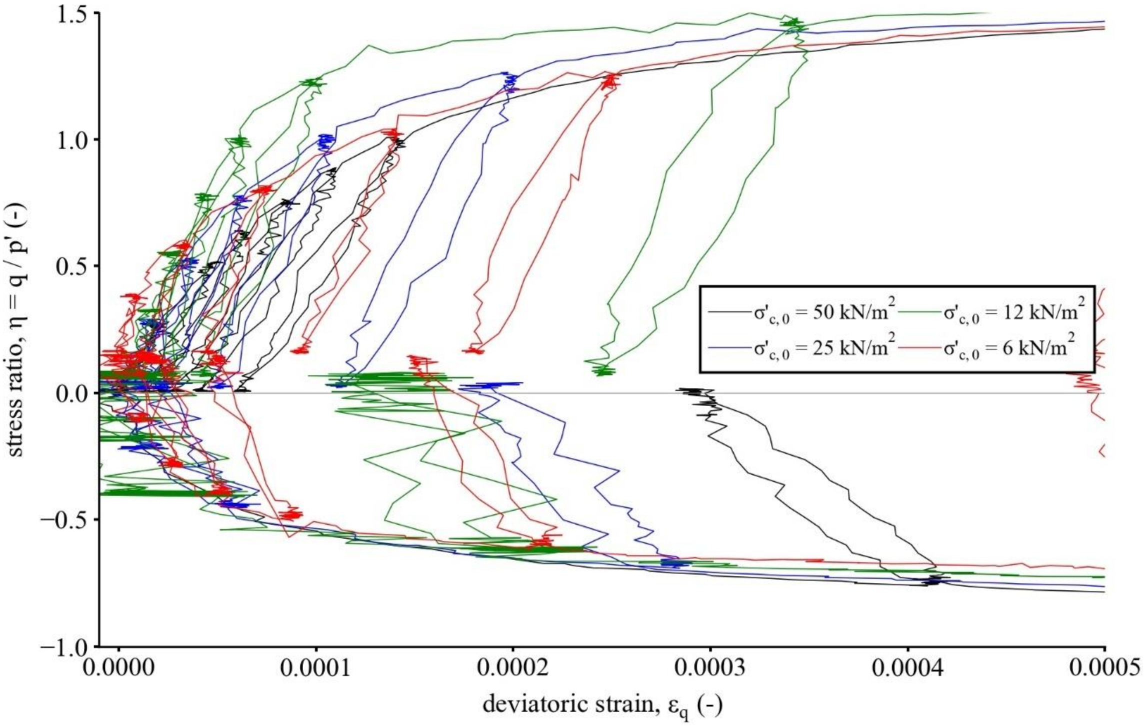

(b)

Figure 6.31: Initial normalised stress-strain response with ε_q calculated from local small-strain instrumentation from (a) ± v′; and (b) ± q stress path tests

G_{ur} also constitutes one of the key input parameters in the Plaxis 'Hardening Soil Model' and 'HSSmall' models (Plaxis, 2018); however, there is relatively little guidance on how to determine G_{ur} both in terms of at what axial strain or stress ratio to commence unloading, and how large the unloading-reloading cycle needs to be.

Appendix B contains plots of deviator stress, q, vs, ε_q for the drained triaxial stress path tests that incorporated unload-reload loops, and corresponding estimates of the unload-reload shear stiffness, G_{ur}. Results are summarised in Figure 6.32, and normalised by G_0 obtained from bender elements.

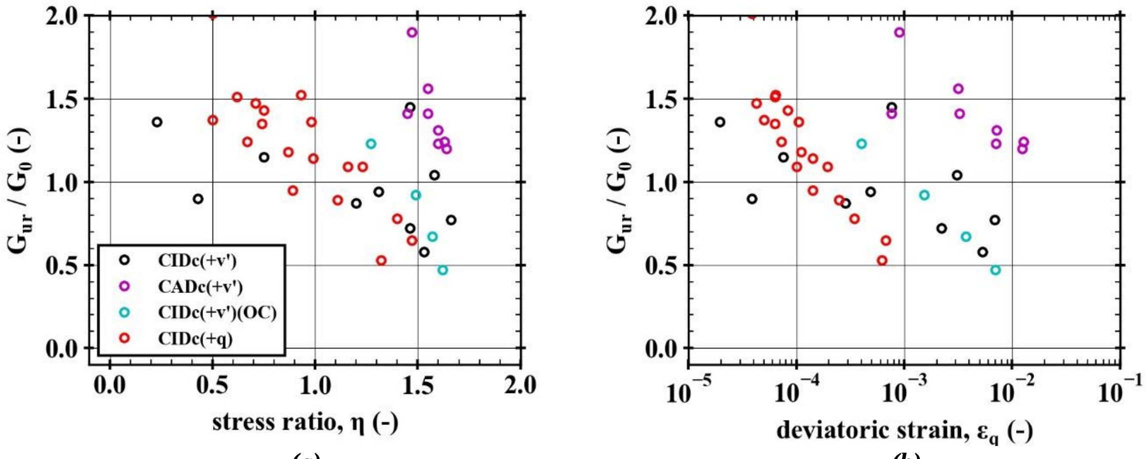

(a) *(b)*

Figure 6.32: Unload-relaod to small strain-shear modulus ratio, G_{ur} / G_0 vs. (a) mobilised stress ratio, η; and (b) mobilised deviatoric strain, ε_q

Figure 6.32a shows a clear trend, indicating that for $\eta \leq 0.8$, shear stiffness estimated from unload-reload loops are likely to yield values greater than G_0 determined from bender element tests. Furthermore, once η exceeds approximately 1.2, the shear stiffness ratio generally falls below 0.85, suggesting that the optimal stress ratio range in which to conduct unload-reload loops lies between 0.8 < η < 1.2. Similarly, from Figure 6.32(b) it may be seen that there is a small window of strain ($1\text{x}10^{-4} < \varepsilon_q < 4\text{x}10^{-4}$) in which unload-reload loops appear to provide the best estimates of G_0.

Inspection of individual unload-reload loops undertaken at stress ratios or strain magnitudes less than those recommended above are found to suffer from excessive noise, and given that the calculation of G_{ur} is sensitive to small changes in ε_q, estimations of G_{ur} based on such data may be unreliable.

6.7. SUMMARY

This chapter presents results of 23 drained triaxial extension and compression tests undertaken at low stress levels on newly acquired soil testing apparatus. It is shown that the commercially available equipment is able to perform conventional compression and extension tests, as well as relatively straightforward stress paths, from which reliable results have been obtained. These results provide the basis of a new database of tests from which advanced constitutive models may be calibrated.

The focus of this chapter has been on the drained behaviour of sand at low stress levels. Experimental data obtained from this study indicates that the mean effective confining stress has minor influence on the effective stress shear strength properties (η_{max} and ϕ'_{max}) for tests undertaken at initial effective confining stresses, $\sigma'_{c,0}$, less than 50 kN/m^2. These results therefore provide further experimental evidence in support of the findings presented by Tatsuoka (Fukushima & Tatsuoka, 1984; Tatsuoka *et al*., 1986), and support the notion of a critical state line that curves towards a horizontal asymptote in the $e\colon \ln(p')$ plane at low stress levels. Tests undertaken at higher stress levels (i.e. $\sigma'_{c,0} \geq$ 100 kN/m^2) show a stress level effect, with decreasing η_{max} and ϕ'_{max} values mobilised with increasing $\sigma'_{c,0}$ values.

This is a useful finding as it indicates that the behaviour at low stress levels may be adequately captured from tests undertaken at relatively high $\sigma'_{c,0}$ values (i.e. $\sigma'_{c,0} =$ 50 kN/m^2), negating the need for performing more challenging low stress tests (i.e. $\sigma'_{c,0} \leq$ 12 kN/m^2) where testing issues (e.g. applied corrections, instrumentation accuracy, temperature fluctuations etc.) become increasingly influential on the calculated response.

The characteristic state has been investigated, and results showed that the characteristic stress ratio (and friction angle) tends to increase with decreasing σ'_c. For tests performed at relatively large effective confining stresses (i.e. $\sigma'_{c,0} >$ 50 kN/m^2), characteristic angles were found to be within 5 to 10 % of ϕ'_{cv} determined from tests at large strains. It was therefore proposed that in the absence of undrained tests on loose sand specimens, reasonably accurate estimations of ϕ'_{cv} and M may be obtained from drained triaxial tests, based on estimations of ϕ' and η at the characteristic state.

The chapter has highlighted the potential confusion regarding the different definitions commonly adopted for determining the angle of dilation, ψ^D, from triaxial tests. Calculations using commonly adopted methods found that differences in ψ^D of up to 10° were obtained, which obviously has significant implications on any subsequent design calculation. It was shown that the set of equations proposed by Vermeer (Schanz & Vermeer, 1997; Vermeer & de Borst, 1984) provided closer agreement with Bolton's (1986) commonly used empirical relationship (modified for triaxial compression conditions), and is therefore recommended.

The test results were compared against Bolton's empirical relationship (modified following the work of Tatsuoka to account for the changing behaviour at stress levels less than 150 kN/m^2 (Tatsuoka, 1987). The modified empirical relationship yielded improved agreement with the test data.

The small-strain shear modulus, G_0, has been examined via bender elements, local small-strain instrumentation, and unload-reload cycles. Estimations of G_0 based on bender element test results yield significantly higher values than would be predicted from commonly used empirical relationships. It was found that a relatively high material constant parameter, $1200 \leq A_G \leq 1600$, is required to accurately predict G_0 values. Reasons for the high G_0 values are uncertain, but may be associated with the relatively high median particle size of the tested material (as suggested by Bui, 2009), or due to differences in the mineralogy and surface roughness of the grains influencing individual particle contact stresses (Iwasaki & Tatsuoka, 1977).

The effect of mean effective stress on the shape of the stress-strain and stiffness degradation curves has been investigated. It was found that tests undertaken at lower mean effective stresses exhibit a comparatively stiffer response than those tests sheared at higher pressures. It was shown that this behaviour may be explained by considering the so-called reference strain, $\varepsilon_{q,ref}$ (Ishihara, 1996), which is found to be dependent on both the maximum stress ratio and mean effective stress.

The magnitude of small-strain shear modulus estimates based on local strain instrumentation was investigated. It was found that the instrumentation suffered from excessive noise in the very small strain range (ε_q < 3x10^{-5}) making reliable estimates of G_0 difficult. Improving the performance of the local instrumentation to capture the response in the very small strain range is therefore considered critical for future researchers utilising the apparatus.

Finally, analysis of large unload-reload loops found that reasonably accurate estimates of G_0 can be obtained from local strain instrumentation if unloading cycles are undertaken within the stress ratio window $0.8 < \eta < 1.2$, or in terms of deviatoric strain, within $1\text{x}10^{-4} < \varepsilon_q < 4\text{x}10^{-4}$.

7. CYCLIC TRIAXIAL TESTS

7.1. INTRODUCTION

In the previous chapter, the stress-strain characteristics of dense Leighton Buzzard sand - Fraction B (LBS-B) subjected to monotonic shear were investigated. This chapter investigates how LBS-B behaves when subjected to cyclic loading with an emphasis on the development of deformations and the number of cycles it can withstand before failure conditions are reached. Cyclic triaxial tests were undertaken on dense specimens, reconstituted to a relative density of approximately 82 %, to simulate natural offshore soil deposits where in situ relative densities are typically relatively high.

The main objectives of carrying out this series of tests are as follows:

- To further investigate the stress-strain behaviour and strength characteristics of LBS-B under cyclic loading, in terms of the effect of stress amplitude and effective confining stress on the development of excess pore water pressure, and permanent and cyclic strains with number of cycles;
- To correlate the monotonic and cyclic behaviour of LBS-B;

As discussed in Chapter 2, there is a significant lack of cyclic triaxial test data in the cyclic stress-space considered most applicable to offshore monopile foundations. The purpose of this test programme is therefore to populate this region and enable the development of design methods, undertaken within a framework that is consistent with model pile load tests performed on the same material (Richards, 2019), which may then be used to estimate the cyclic bearing capacity of offshore monopile foundations for given stress levels and cyclic loading conditions.

This chapter is arranged in the following order: Firstly, an overview of the cyclic definitions and framework adopted in this investigation are described. The utilised cyclic loading characteristics and test schedule summaries are then presented, followed by an interpretation and discussion of the experimental results. The chapter finishes with an examination of the stiffness and damping characteristics, and presentation of tentative cyclic contour diagrams.

7.2. CYCLIC DEFINITIONS

An aim of this research project was to carry out a set of cyclic triaxial tests within a robust framework that is consistent with both pile loading and model tests. However, cyclic loading and cyclic response definitions differ significantly between element and pile/model testing publications. Cyclic definitions used in this thesis are therefore largely based on those given in Richards (2019), so that researchers might more easily draw parallels between pile and soil element behaviour.

The following expresses the cyclic response in general stress, σ, and strain, ε, terms; however, these terms can represent a number of stress and strain parameters. In element tests, σ typically refers to the deviator stress, q (in triaxial tests), or τ (in shear tests), while for pile tests, σ may represent the applied moment, M, or horizontal load, H. Similarly, ε may correspond to axial or shear strain, ε_z, or γ, in element tests; or pile rotation, θ, or pile displacement, y, in pile tests.

7.2.1. LOAD CHARACTERISATION

The cycle definition shown in Figure 8.1a is adopted to allow both pile response and element tests to be presented in a consistent framework. The cycle is defined in terms of the extreme stress, σ_e, and reversal stress, σ_r, which for constant amplitude loading is defined as the maximum and minimum absolute stress at load reversal, respectively. The cycle numbering convention is similar to that used in pile load testing publications.

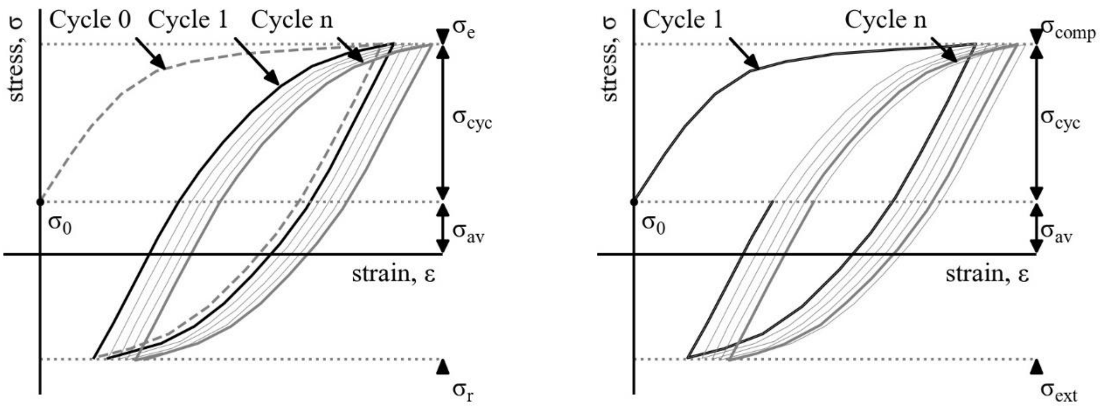

(a) *(b)*

Figure 7.1: (a) Cycle definition adopted in this study (after Richards, 2019); and (b) cyclic definition more commonly used in element testing publications

Cycle 1 is defined as the second load-unload loop to pass through σ_e, while cycle 0 always begins at σ_0 and ε_0, and includes all loading prior to cycle 1. As shown in Figure 8.1, σ_0 may be non-zero (as is the case for anisotropically consolidated tests) and is not necessarily equal to σ_{av}.

In element testing, the cyclic load is characterised by the average shear stress, σ_{av}, and the cyclic deviator stress, σ_{cyc}. The average shear stress comprises two components: the shear stresses associated with in situ conditions, σ_0 (e.g. the static loading caused by the dead-weight of the structure), and the mean stress created by cyclic loading, $\Delta\sigma_{av}$. In terms of the extreme and reversal loads shown in Figure 8.1, the cyclic loads are therefore defined as:

$$\sigma_{cyc} = \frac{\sigma_e - \sigma_r}{2} \tag{7-1}$$

$$\sigma_{av} = \frac{\sigma_e + \sigma_r}{2} \tag{7-2}$$

where, in terms of the average stress, σ_{av}:

$$for\ \sigma_{av} \geq 0: \qquad \sigma_e = \sigma_{av} + \sigma_{cyc}; \quad \sigma_r = \sigma_{av} - \sigma_{cyc} \tag{7-3}$$

$$for\ \sigma_{av} < \ 0: \qquad \sigma_e = \sigma_{av} - \sigma_{cyc}; \quad \sigma_r = \sigma_{av} + \sigma_{cyc} \tag{7-4}$$

The use of σ_e and σ_r allows the framework to consistently capture the behaviour during cyclic triaxial extension tests where the magnitude of the peak cyclic stress in extension may be greater than that in compression, i.e. $|\sigma_{ext}| > |\sigma_{comp}|$. This definition also ensures consistency for all initial load scenarios, particularly for tests involving pre-loading which is typical for cyclic triaxial extension tests (Richards, 2019). Furthermore, the definition allows for a straightforward determination of half cycles which become important when considering multi-amplitude loading.

For pile response, loads are typically characterised in terms of the ratios ζ_b and ζ_c (LeBlanc *et al.*, 2010). Defining the load cycle in terms of σ_e and σ_r, the following is obtained:

$$\zeta_b = \frac{\sigma_e}{\sigma_{ref}}; \quad \zeta_c = \frac{\sigma_r}{\sigma_e} \tag{7-5}$$

The ratio ζ_b gives an indication of the magnitude of the cyclic loading, normalised with respect to some reference stress, σ_{ref}, and lies in the range $0 \leq \zeta_b \leq 1$; while the ratio ζ_c quantifies the characteristics of the cyclic load. With this definition of σ_e and σ_r, the ratio ζ_c is well defined ($-1 \leq \zeta_c \leq 1$), and is independent of load direction.

Figure 8.2 shows graphically the relationship between σ_{av}, σ_{cyc}, ζ_b, and ζ_c using the framework developed by Richards (2019), and offers a convenient way of expressing the interactions between the amplitudes and average loads sustained during a test. Loading type can be extracted by considering areas between limiting ζ_c values of -1, 0, and 1, while contours of increasing ζ_b fan outwards from the origin. Charts similar to this are often used in both pile load testing (e.g. Jardine & Standing, 2000; Poulos, 1988) and element testing (e.g. Andersen & Berre, 1999) to define loading regimes of a suite of cyclic tests, with individual tests represented by a single point located at normalised σ_{av} and σ_{cyc} co-ordinates. Considering cyclic triaxial tests, the left-hand side of the plot represent extension tests with negative initial static bias ($i.e. \sigma_{av} < 0$), while the right-hand side ($\sigma_{av} > 0$) represent compressive tests.

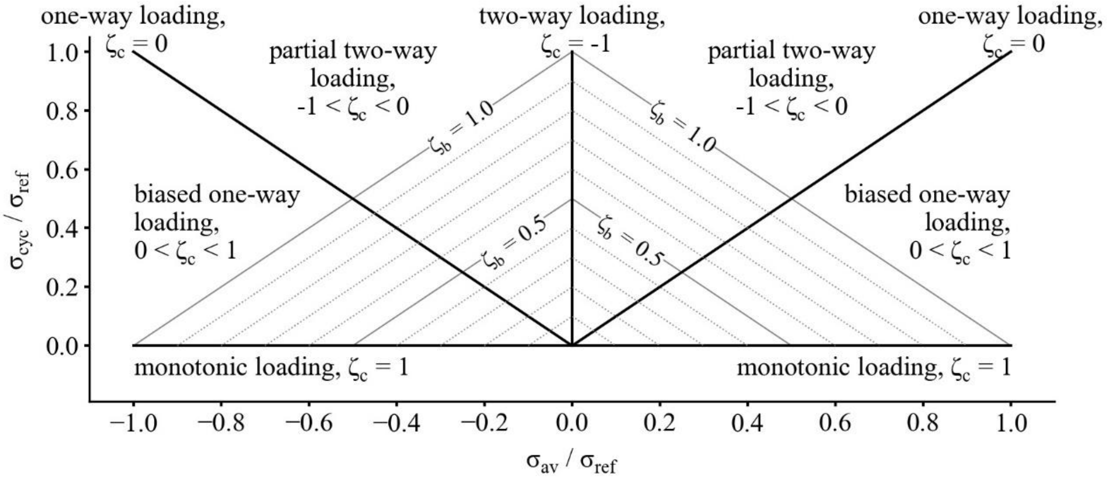

Figure 7.2: Cyclic triaxial test interaction diagram

It should be noted that there is no consistent method for defining σ_{ref}. For laterally loaded piles, the stress mobilised at some limiting rotation or pile head displacement is often adopted. In element testing, some measure of ultimate strength (i.e. s_u or q_{max}) is used. Alternatively, for triaxial stress conditions, the initial effective confining stress, $\sigma'_{c,0}$, is often adopted, while the initial effective overburden pressure, σ'_{z0}, is usually used in cyclic simple shear tests. Adopting these values would yield the 'cyclic stress ratio', CSR, on the y-axis, as defined in Section 5.2.7.

However, the cyclic simple shear and cyclic triaxial tests impose quite different loading conditions, and their cyclic stress ratios are therefore not equivalent, as is the case for axially and laterally loaded piles. It is therefore important to keep in mind that ζ_b may not be directly comparable across sources.

7.2.2. STRAIN PER CYCLE DEFINITIONS

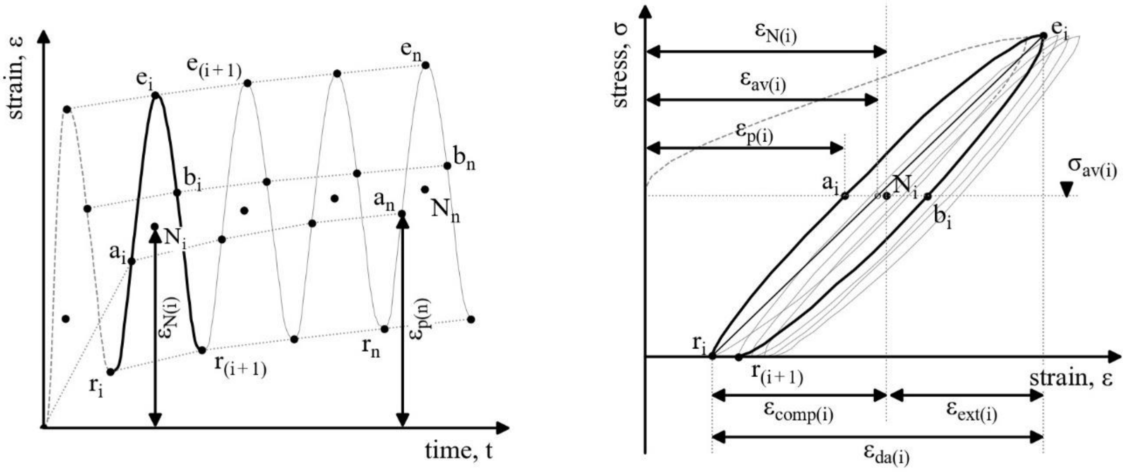

(a) *(b)*

Figure 7.3: Cyclic strains as a function of (a) time and (b) stress

A robust definition of strain per cycle is sought, that is consistent between both element and pile load tests. Figure 7.3 shows graphical representations of some of the strain definitions adopted in element testing publications. The average strain, ε_{av}, is often reported, and is usually defined as the average of the high and low peak values within a cycle (Andersen, 2015). Adopting the cycle numbering and similar definitions for load reversal strains described in Section 7.2.1, then ε_{av} may be defined as:

$$\varepsilon_{av_i} = \frac{1}{2}\left(\varepsilon_{e_i} + \varepsilon_{r_i}\right) \tag{7-6}$$

where:

ε_{av_i} = average cyclic strain mobilised during cycle i
ε_{e_i} = cyclic strain mobilised at σ_e during cycle i
ε_{r_i} = cyclic strain mobilised at σ_r during cycle i

The ‘permanent’ strain, ε_p, is also used, defined as the strain mobilised “at the end of a cycle when the shear stress returns to the value at the start of the cycle” (Andersen, 2015). This definition is similar to ε_{acc} adopted by Wichtmann (2005). Defining the point a_i as the location where the stress-strain cycle intersects σ_{av} on reloading (see Figure 7.3b), then ε_p may be calculated from:

$$\varepsilon_{p_i} = \varepsilon_{a_i} \tag{7-7}$$

where:

ε_{p_i} = permanent cyclic strain mobilised during cycle i
ε_{a_i} = cyclic strain mobilised at σ_{av} on relaoding during cycle i

Richards (2019) reviewed common strain definitions used in both element and pile load testing and recommended the definition given in Eq. (8-8), as it does not combine stiffening or change in hysteresis loop shape with ratcheting:

$$\varepsilon_{N_i} = \frac{1}{2}\left(\varepsilon_{a_i} + \varepsilon_{b_i}\right) \tag{7-8}$$

where:

ε_{N_i} = average cyclic strain mobilised during cycle i
ε_{b_i} = cyclic strain mobilised at σ_{av} on unloading during cycle i

The double amplitude strain, ε_{da}, is often quoted in cyclic element tests, normally in reference to some limiting ‘failure condition’ value (e.g. $\varepsilon_{da} \leq 5$ %). ε_{da} is made up of two components:

$$\varepsilon_{da_i} = \left(\varepsilon_{comp_i} + \varepsilon_{ext_i}\right) \tag{7-9}$$

and:

$$\varepsilon_{comp_i} = \left(\varepsilon_{e_i} - \varepsilon_{N_i}\right);\ \ \varepsilon_{ext_i} = \left(\varepsilon_{N_i} - \varepsilon_{r_i}\right) \tag{7-10}$$

where:

ε_{comp_i} = cyclic strain mobilised during the relaoding part of a given cycle
ε_{ext_i} = cyclic strain mobilised during the unloading part of a given cycle

The cyclic strain, ε_{cyc}, sometimes referred to as the ‘single amplitude’ strain, ε_{sa}, is then the average of the compressive and extensive cyclic strain components, or:

$$\varepsilon_{cyc_i} = \varepsilon_{sa_i} = \frac{\varepsilon_{da}}{2} \tag{7-11}$$

7.2.3. STIFFNESS AND ENERGY LOSS FACTOR

The soil shear stiffness, G, and energy loss factor, ξ, (more commonly known as the damping ratio) are two major cyclic soil parameters specifying the non-linear deformation characteristics of the material. These parameters have historically been defined based on perfectly closing hysteresis loops (e.g. Ishihara, 1996; Kramer, 1996); however, inspection of experimental data (Abadie, 2015) show the accumulation of permanent or residual strains with cycle number, results in non-closing hysteresis loops. Furthermore, the shape and area of the hysteresis loop is also found to evolve with increasing numbers of cycles. Accurate modelling of soil behaviour under long-term cyclic loading is therefore dependent on being able to determine reliably these parameters as they develop.

7.2.3.1. *Secant Stiffness*

As with definitions of stress and strain, a robust definition of stiffness is sought so as to provide a consistent framework between pile load and element testing. A number of alternative definitions for stiffness within a given cycle have been proposed in the literature (Abadie, 2015; LeBlanc *et al.*, 2010). However, these definitions tend to conflate ratcheting with stiffening. The 'central cyclic stiffness' definition given in Richards (2019) is therefore adopted here to avoid these shortcomings.

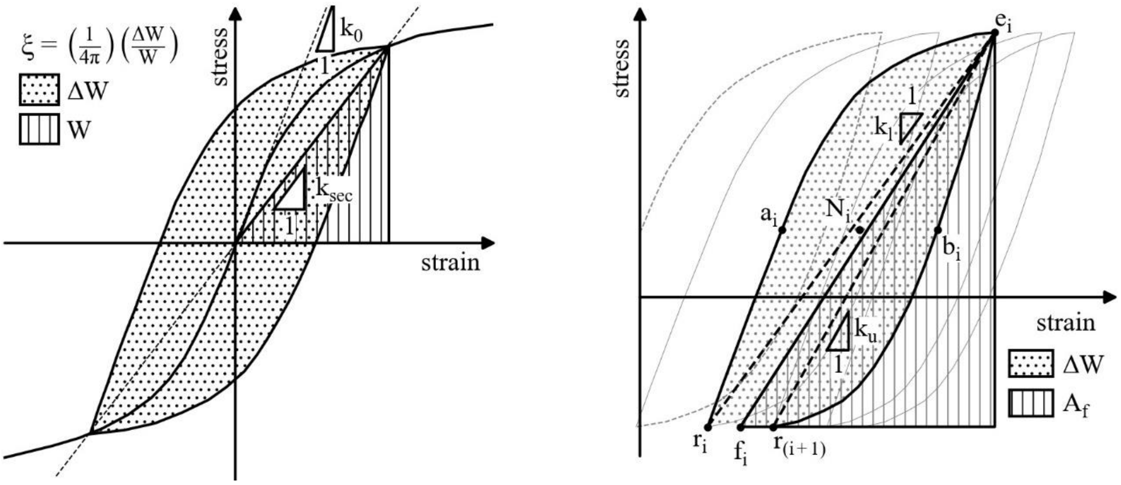

(a) *(b)*

Figure 7.4: Definition of stiffness and elastic stored energy (from Ishihara, 1996); and (b) definition of stiffness and elastic stored energy used in this study

The definition of secant cyclic stiffness used in this study is illustrated graphically in Figure 7.4b, and may calculated from:

$$k_{f_i} = 2\left(\frac{k_{l_i} k_{u_i}}{k_{l_i} + k_{u_i}}\right) \tag{7-12}$$

and:

$$k_{l_i} = \frac{\sigma_{e_i} - \sigma_{r_i}}{\varepsilon_{e_i} - \varepsilon_{r_i}}; \;\; k_{u_i} = \frac{\sigma_{e_i} - \sigma_{r_{i+1}}}{\varepsilon_{e_i} - \varepsilon_{r_{i+1}}} \tag{7-13}$$

where:

k_{f_i} = central cyclic stiffness
k_{l_i} = loading stiffness
k_{u_i} = unloading stiffness

7.2.3.2. Energy Loss Factor

Figure 7.4a shows the methodology used to define the energy loss factor, ξ, for a given load cycle as given by Ishihara (1996), where ξ is a constant factor times the ratio of the energy loss per cycle, ΔW, to the maximum stored energy, W. ΔW is equal to the area enclosed by the hysteresis loop, and W is the area of the triangle bounded by a straight line defining the secant stiffness modulus. As shown by Figure 7.4a, the energy loss factor is typically calculated from perfectly closing stress-strain loops, which is rarely true for real experimental data.

The definition therefore needs to be modified for situations where hysteresis loops are non-closing due to stiffening, softening, or ratcheting behaviour. Several methods for calculating ξ from non-closing hysteresis loops have been proposed in the literature (e.g. Abadie, 2015; Taborda, Potts, & Zdravković, 2016). However, these methods may not correctly capture the hysteretic energy loss for non-closing loops, when ΔW is defined according to:

$$\Delta W = A_{loop} + A_R \tag{7-14}$$

and:

$$A_{loop} = \int_{r_i}^{e_i} \sigma \, d\varepsilon; \quad A_R = \int_{e_i}^{r_{i+1}} \sigma \, d\varepsilon \tag{7-15}$$

where:

ΔW = hysteritic energy loss
A_{loop} = area of the hysteresis loop
A_R = ratcheting area

Figure 7.4b presents a new definition for the energy loss factor proposed by Richards (2019). This definition is based on the rigorous definition of ΔW, where:

$$\xi = \frac{4k_{f_i}}{\pi\left(\sigma_{e_i} - \sigma_{r_i}\right)^2}\left(\int_{r_i}^{e_i} \sigma \, d\varepsilon + \int_{e_i}^{r_{i+1}} \varepsilon \, d\sigma\right) \tag{7-16}$$

The maximum stored energy, A_f, in this case is equal to the area of the triangle defined by the central cyclic stiffness, k_f. For a closed loop system, the conventional soil “damping ratio” (as presented by Ishihara, 1996; Kramer, 1996) is obtained; however, this definition is superior as it remains consistent and robust for situations involving negative ratcheting or convex hysteresis loops.

7.3. TEST PLAN

Cyclic strength and deformation characteristics of sand are important for the design of offshore wind turbine foundations and other offshore structures. However, as discussed in Chapter 2, there is a significant lack of published cyclic element test data conducted at stress levels – both in terms of the confining stress and stress amplitude – appropriate for use in the design of offshore wind energy structures. Furthermore, no industry accepted guidance exists that stipulate how results of cyclic element testing might be applied to the design of such structures, leading to different methods being developed (e.g. Achmus *et al*., 2011; Andersen, 2009).

The contour diagram framework developed by the NGI is one such method, and provides a useful basis for planning cyclic laboratory test campaigns as well as enabling the interpretation of cyclic tests from other test materials to be quantitatively compared. The diagrams also combine measured laboratory data and thus may be used as a tool in both the development of cyclic constitutive models and provide a means of checking such models at different stress conditions (Blaker & Andersen, 2019).

The aim of this testing programme is therefore to populate the area of stress space highlighted in Figure 2.5, and produce and plot data that may be used to inform constitutive model development, as well as potentially enable comparisons to be drawn with recently performed model pile tests conducted at similar stress levels (Richards, 2019).

7.3.1. LOADING FREQUENCY

As discussed in Section 5.3.2, research has found there to be virtually no significant effect of loading rate on the dynamic properties of sands. However, while relatively high frequencies may be desirable when undertaking high-cycle tests, trial tests identified a frequency of $f = 0.1$ Hz as providing the optimum value when considering the trade-off between test duration and control, precision, and data acquisition. Furthermore, this value is similar to the typical cyclic periods (10 to 20 s) developed under storm wave loading (Andersen, 2009), and is also consistent with frequency adopted by the NGI.

7.3.2. NUMBER OF CYCLES

Offshore wind energy structures may be subjected to several millions of cycles over the course of their design life. However, element tests running to over 10^6 cycles are considered unfeasible in terms of both the time and financial cost required to carry out such tests. Such high-cycle tests also have significant data storage implications, and require careful consideration of the sampling rate – sampling needs to be frequent enough to accurately capture the small-strain response, but not so frequent that file sizes become impractical. Sampling rate was therefore typically set to 50 or 100 samples per cycle, with higher values adopted in tests that were predicted to reach failure conditions after relatively few numbers of cycles.

Results presented by Abadie (2015) suggest that there is a diminishing return in undertaking high-cycle element tests beyond 10^4 stress cycles, who found that the first 1000 cycles caused approximately the same magnitude of deformation as the next 9000. All tests in this campaign therefore adopted a target of 10^4 cycles, which was considered to offer a good trade-off in terms of both capturing the long-term behaviour of cyclic soil response, and the number of tests that may be completed within the available timeframe.

7.3.3. CONFINING STRESS, AVERAGE STRESS AND CYCLIC STRESS AMPLITUDE

Cyclic triaxial tests used various combinations of average stress, q_{av}, and cyclic deviator stress, q_{cyc}, to simulate the various dynamic loading conditions applied to offshore wind energy structures. q_{av} and q_{cyc} values were selected to provide similar values of ζ_b and ζ_c used in the 1-g model pile tests undertaken by Richards (2019). The normalising stress, q_{ref}, was taken as q_{max}, which is the peak deviator stress mobilised during a drained monotonic triaxial compression test, undertaken on a sample from a similar initial state. Figure 7.5a summarises the cyclic loading regime, where each circle denotes a cyclic triaxial test with specific stress conditions.

To investigate the influence of the initial effective confining stresses, all test 'locations' shown in Figure 7.5a were undertaken at $\sigma'_{c,0}$ = 50kPa and 12kN/m^2. As discussed in Section 5.2.7, $2\sigma'_{c,0}$ is often used as a normalising stress in cyclic triaxial tests. Figure 7.5b shows the influence of adopting $2\sigma'_{c,0}$ as q_{ref}, and indicates that while the test pattern remains the same, the individual test locations are radially shifted to greater ζ_b values. It is therefore again emphasised that ζ_b values used in this study (Figure 7.5a) may not be directly comparable to those adopted by Richards (2019).

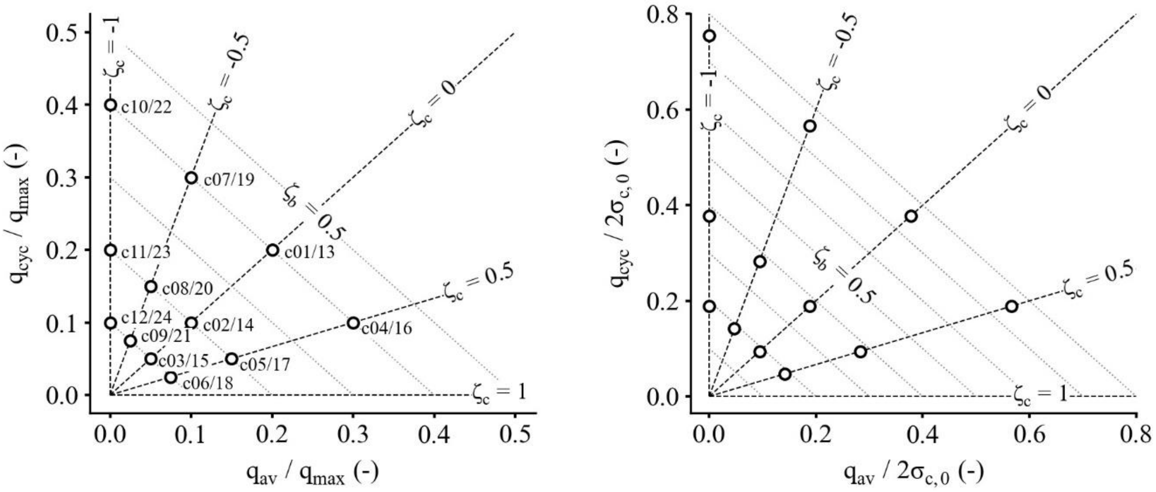

(a) *(b)*

Figure 7.5: Normalised cyclic stress space showing the influence of reference stress, qref, on test location

Target loads for q_{av} and q_{cyc} should be based on the area of the test specimen at the end of the creep-ageing and load-ramping stage, respectively. However, as the control software requires target loads to be input prior to starting the test, initial specimen areas, A_0, were used. This can obviously lead to stresses mobilised during the test deviating from target values; however, comparisons of initial and consolidated specimen areas show relatively small change, and thus the impact of using A_0 is considered minor. Development of a custom test plan for use in the cyclic control software is therefore recommended to overcome this issue in future test campaigns.

7.3.4. CYCLIC TEST SCHEDULES

Detailed test plans for the 20 cyclic triaxial tests undertaken at $\sigma'_{c,0}$ = 50 and 12 kN/m^2 are shown in Table 7.1 and Table 7.2, respectively. All test specimens were prepared using the modified wet pluviation technique to a target initial relative density of 82 %. Test plans followed a similar procedure to that used in the monotonic test campaign (see Chapter 4). Saturation was achieved by simultaneously ramping the cell and back pressures, maintaining an effective cell pressure of

10 kN/m^2. The sample was then isotropically consolidated to the target $\sigma'_{c,0}$, and then left to creep/age for a period of 24 to 36 hours. The target average stress was then applied by ramping the vertical stress under drained conditions over a period of five minutes. The cyclic shearing stage was subsequently performed undrained and under load control.

The cyclic loading stage finished on completion of N = 10^4 stress cycles, or on reaching pre-defined axial deformation limits (governed by the travel limits of the external 50 mm LSCT). Tests that achieved 10^4 stress cycles without failing were subjected to additional cyclic loading stages, as shown in Table 7.3 and Table 7.4. These stages used progressively higher q_{cyc} values (while maintaining the same q_{av} value) until failure conditions were achieved. No drainage was allowed between stages, leading to variable $\sigma'_{c,0}$ values at the start of each additional cyclic stage.

Table 7.1: Cyclic loading characteristics for tests performed at σ'_{c0} = 50 kN/m^2 (q_{ref} = 188.7 kN/m^2; f =0.1Hz)

Test ID (-)	ζ_b (-)	ζ_c (-)	q_{av} / q_{ref} (-)	q_{cyc} / q_{ref} (-)	q_{av} (kN/m^2)	q_{cyc} (kN/m^2)	q_e (kN/m^2)	q_r (kN/m^2)
c01	0.4	0.0	0.20	0.20	37.7	37.7	75.5	0.0
c02	0.2	0.0	0.10	0.10	18.9	18.9	37.7	0.0
c03	0.1	0.0	0.05	0.05	9.4	9.4	18.9	0.0
c04	0.4	0.5	0.30	0.10	56.6	18.9	75.5	37.7
c05	0.2	0.5	0.15	0.05	28.3	9.4	37.7	18.9
c06	0.1	0.5	0.075	0.025	14.2	4.7	18.9	9.4
c07	0.4	-0.5	0.10	0.30	18.9	56.6	75.5	-37.7
c08	0.2	-0.5	0.05	0.15	9.4	28.3	37.7	-18.9
c09	0.1	-0.5	0.025	0.075	4.7	14.2	18.9	-9.4
c10	0.4	-1.0	0.00	0.40	0.0	75.5	75.5	-75.5
c11	0.2	-1.0	0.00	0.20	0.0	37.7	37.7	-37.7
c12	0.1	-1.0	0.00	0.10	0.0	18.9	18.9	-18.9

Table 7.2: Cyclic loading characteristics for tests performed at σ'_{c0} = 12 kN/m^2 (q_{ref} = 45.8 kN/m^2; f =0.1Hz)

Test ID (-)	ζ_b (-)	ζ_c (-)	q_{av} / q_{ref} (-)	q_{cyc} / q_{ref} (-)	q_{av} (kN/m^2)	q_{cyc} (kN/m^2)	q_e (kN/m^2)	q_r (kN/m^2)
c13	0.4	0.0	0.20	0.20	9.2	9.2	18.3	0.0
c15	0.1	0.0	0.05	0.05	2.3	2.3	4.6	0.0
c16	0.4	0.5	0.30	0.10	13.7	4.6	18.3	9.2
c18	0.1	0.5	0.075	0.025	3.4	1.1	4.6	2.3
c19	0.4	-0.5	0.10	0.30	4.6	13.7	18.3	-9.2
c21	0.1	-0.5	0.025	0.075	1.1	3.4	4.6	-2.3
c22	0.4	-1.0	0.00	0.40	0.0	18.3	18.3	-18.3
c24	0.1	-1.0	0.00	0.10	0.0	4.6	4.6	-4.6

7.4. CYCLIC TEST RESULTS

Table 7.3 and Table 7.4 summarise the results of the 20 cyclic triaxial tests undertaken at various values of ζ_b, ζ_c for $\sigma'_{c,0}$ = 50 and 12 kN/m^2, respectively. The stress-strain behaviour and effective stress paths are presented in Figure 7.6 to Figure 7.10. The failure envelopes obtained from monotonic CID compression and extension tests (for $\sigma'_{c,0}$ = 50 and 12 kN/m^2) are included for reference, as is the characteristic / phase transformation line. Cycles at log decades (i.e. n = 1, 10, 100, 1000 etc) are also highlighted in black. The results show that behaviour is predominantly governed by the value of ζ_c, but also influenced by the magnitude of ζ_b.

Engineering parameters have been calculated using the methodology and corrections described in Chapter 4. The loads were controlled via the equipment manufacturer's software csDyna (VJ-Tech, 2017), and typically achieved a stress tolerance of ±0.5 kN/m^2. However, as the cyclic actuator is force (rather than stress) controlled, the accuracy of mobilised target stresses tends to reduce as axial strains accumulate and the specimen area changes.

To avoid system compliance negatively influencing calculated values, all strain, stiffness and damping values presented are based on local, on-sample displacement measurements. Unfortunately, the ±5 mm range of the local strain transducers limits the maximum strain range to $|\varepsilon_z|$ = 5 % for a 200 mm high specimen; therefore, failure criteria based on mobilised double amplitude or permanent strains (i.e. ε_{da} = 5 %, or ε_{av} = 12 %) are unachievable for this equipment set up.

However, inspection of the results show that failure criteria based on 'initial liquefaction' (i.e. R_u = 1) is achieved in several cases, followed by the mobilisation of progressively larger strains. Allowing continued accumulation of strains to some arbitrary value was not permitted, as strain localisation/necking was typically observed in the top third of the specimen during post-liquefaction cyclic loading. Furthermore, strict actuator displacement limits were necessary to avoid the risk of damage to the apparatus. To reduce the development of non-uniform strains and increase the measurable axial strain range, samples with a height to diameter ratio of 1:1 (used in conjunction with enlarged, lubricated end platens) are therefore recommended.

Table 7.3: $\sigma'_{c,0}$ = 50 kN/m^2 cyclic test results summary

Test ID (-)	**e_0 (-)**	**D_r (%)**	**A_0 (cm^2)**	**$A_{c,f}$ (cm^2)**	**$\sigma'_{c,0}$ (kN/m^2)**	**q_{av} (kN/m^2)**	**p'_0 (kN/m^2)**	**q_{cyc} (kN/m^2)**	**q_e (kN/m^2)**	**q_r (kN/m^2)**	**$q_e/q_{e,t}$ (%)**	**$q_r/q_{r,t}$ (%)**	**ζ_b (-)**	**ζ_c (-)**	**CSR (-)**	**$N_{f(Ru = 1)}$ (-)**
c01.1	0.584	81.99	78.04	77.99	51	37.8	63.6	37.6	75.4	0.2	99.9	-	0.4	0	0.296	-
c02.1	0.587	80.92	78.18	78.12	48.4	18.9	54.7	18.9	37.8	0.1	100.2	-	0.21	0	0.173	-
c03.1	0.585	81.57	78.16	78.08	48.6	9.5	51.8	9.4	19	0.1	100.7	-	0.11	0.01	0.091	-
c04.1	0.583	82.41	78.31	78.2	50.7	56.7	69.7	18.8	75.5	37.9	100	100.4	0.41	0.5	0.135	-
c05.1	0.582	82.8	78.07	77.99	50.3	28.3	59.8	9.4	37.7	18.9	99.9	100.2	0.2	0.5	0.079	-
c05.2	0.582	82.8	78.07	78.01	45	28.3	54.6	28.3	56.6	0.1	100	-	0.34	0	0.259	-
c05.3	0.582	82.8	78.07	81.74	16.8	27.6	26	35.2	62.8	-7.5	95.1	79.5	1.02	-0.12	0.677	9
c06.1	0.58	83.33	77.96	77.91	50.1	14.3	54.8	4.7	19.1	9.6	101.2	101.7	0.1	0.5	0.043	-
c06.2	0.58	83.33	77.96	77.92	50	14.3	54.8	14.1	28.5	0.2	100.7	-	0.16	0.01	0.129	-
c07.1	0.582	82.64	77.94	77.68	49.7	19.4	56	56	75.4	-36.5	99.9	96.7	0.41	-0.48	0.5	5
c08.1	0.584	81.89	77.92	77.77	50.2	9.6	53.3	28.2	37.8	-18.7	100.2	99.1	0.21	-0.49	0.265	149
c09.1	0.582	82.67	78.04	77.82	49.7	4.8	51.3	14.2	18.9	-9.4	100.2	99.6	0.1	-0.5	0.138	-
c09.2	0.582	82.67	78.04	77.84	24	4.7	25.8	33.2	37.8	-28.7	100.2	101.4	0.43	-0.76	0.643	8
c10.1	0.587	81.01	78.16	77.98	49.4	-1	49.4	76.2	75.2	-77.1	99.6	102.1	0.42	-1.03	0.771	5
c11.1	0.583	82.27	77.84	76.99	49.4	-0.1	49.3	37.9	37.7	-37.9	99.9	100.4	0.21	-1.01	0.384	6
c12.1	0.578	84.02	77.74	77.61	49.5	0	49.5	19	18.9	-19	100.2	100.7	0.1	-1.01	0.192	3118

Table 7.4: $\sigma'_{c,0}$ = 12 kN/m^2 cyclic test results summary

Test ID (-)	**e_0** (-)	**D_r** (%)	**A_0** (cm^2)	**$A_{c,f}$** (cm^2)	**$\sigma'_{c,0}$** (kN/m^2)	**q_{av}** (kN/m^2)	**p'_0** (kN/m^2)	**q_{cyc}** (kN/m^2)	**q_e** (kN/m^2)	**q_r** (kN/m^2)	**$q_e/q_{e,t}$** (%)	**$q_r/q_{r,t}$** (%)	**ζ_b** (-)	**ζ_c** (-)	**CSR** (-)	**$N_{f(Ru = 1)}$** (-)
c13.1	0.581	82.99	78.1	77.91	12.6	9.1	16	9.1	18.1	0	98.9		0.39	0	0.284	-
c13.2	0.581	82.99	78.1	80.56	4.9	8.8	8.1	11	19.9	-2.2	96.6	95.7	1.11	-0.11	0.679	51
c15.1	0.581	82.94	77.93	78.06	13.1	2.3	14.1	2.3	4.6	0	100		0.1	0	0.082	-
c15.2	0.581	82.94	77.93	78.06	12.5	2.3	13.6	4.6	6.9	-2.3	100	100	0.15	-0.33	0.169	-
c15.3	0.581	82.94	77.93	78.06	11.2	2.3	12.2	6.8	9.1	-4.5	98.9	97.8	0.22	-0.49	0.279	3203
c16.1	0.582	82.55	78.06	78.17	12.7	13.7	17.5	4.5	18.2	9.1	99.5	98.9	0.39	0.5	0.129	-
c16.2	0.582	82.55	78.06	78.22	11.3	13.7	16.1	9.1	22.8	4.6	99.6	100	0.55	0.2	0.283	-
c16.3	0.582	82.55	78.06	78.52	10	13.7	14.8	13.6	27.3	0.2	99.3	-	0.75	0.01	0.459	-
c16.4	0.582	82.55	78.06	80.2	9.1	13.4	13.9	17.6	31.1	-4.3	96.9	93.5	0.93	-0.14	0.633	20
c18.1	0.581	83.1	78.02	78.1	12.6	3.5	14.1	1.1	4.6	2.3	100	100	0.1	0.5	0.039	-
c18.2	0.581	83.1	78.02	78.1	12.9	3.4	14.3	5.7	9.2	-2.3	100	100	0.2	-0.25	0.199	-
c18.3	0.581	83.1	78.02	78.13	6.9	3.6	8.4	10	13.6	-6.3	99.3	91.3	0.54	-0.46	0.595	14
c19.1	0.583	82.18	78.15	77.92	12.7	4.9	14.5	13.1	18	-8.2	98.4	89.1	0.39	-0.46	0.452	8
c21.1	0.583	82.3	78.01	78.14	12.7	1.2	13.3	3.4	4.5	-2.2	97.8	95.7	0.1	-0.49	0.128	-
c21.2	0.583	82.3	78.01	78.16	9.6	1.2	10.2	6.9	8.1	-5.6	101.2	98.2	0.23	-0.69	0.338	224
c22.1	0.583	82.41	78.09	78.08	11.5	0.1	11.8	17.4	17.5	-17.2	95.6	94	0.42	-0.98	0.737	7
c24.1	0.584	82.07	78.18	78.17	11.2	0.2	11.5	4.5	4.7	-4.4	102.2	95.7	0.11	-0.94	0.196	270

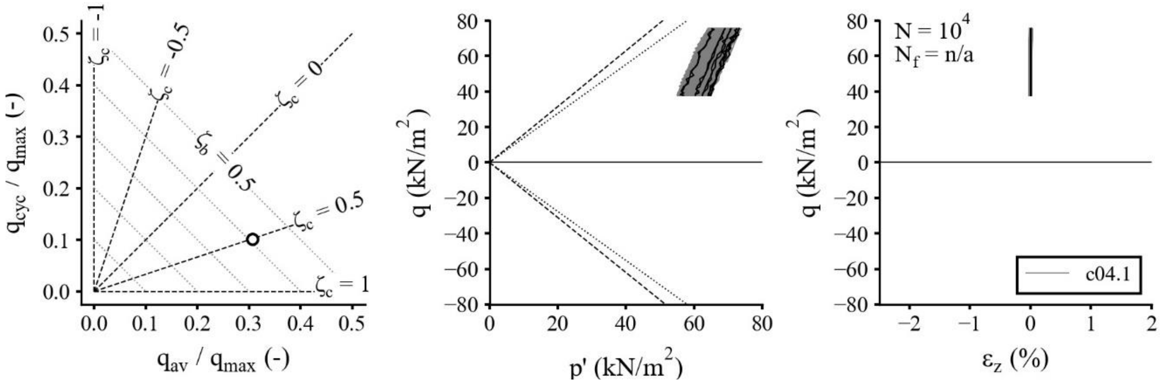

(a) c04: ζ_c = 0.5, ζ_b = 0.4 ***(b) c04*** ***(c) c04***

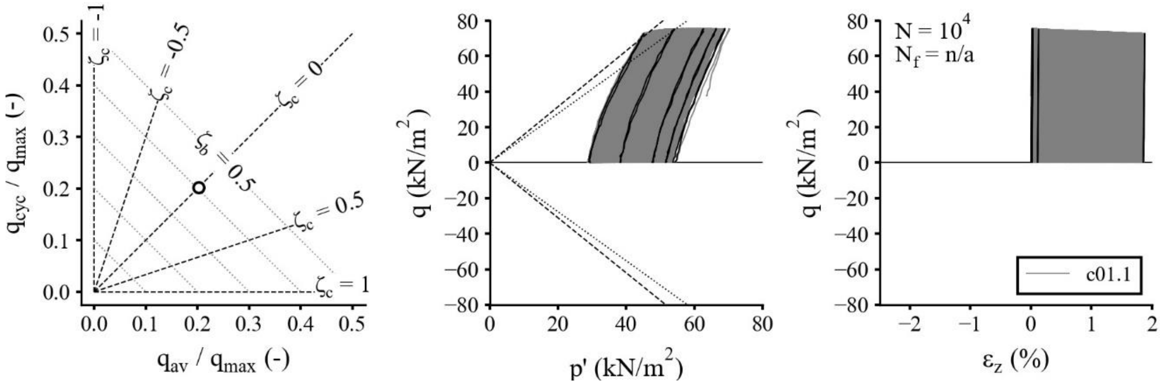

(d) c01: ζ_c = 0.0, ζ_b = 0.4 ***(e) c01*** ***(f) c01***

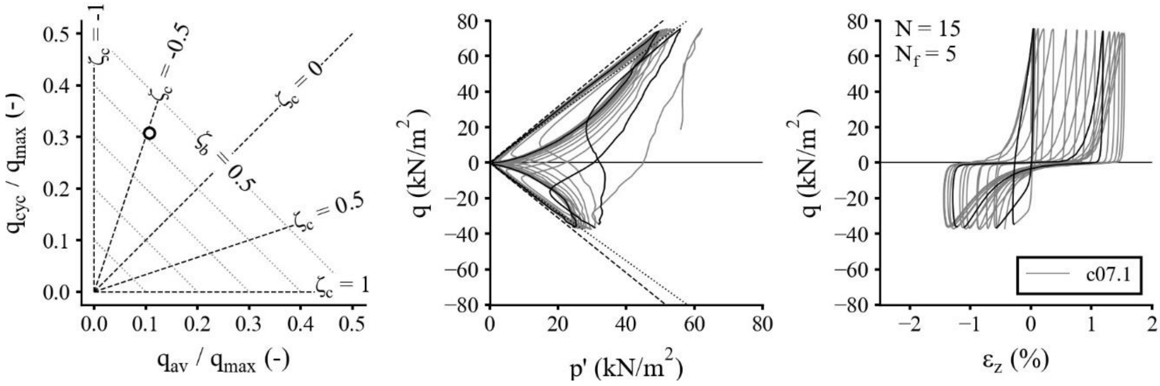

(g) c07: ζ_c = -0.5, ζ_b = 0.4 ***(h) c07*** ***(i) c07***

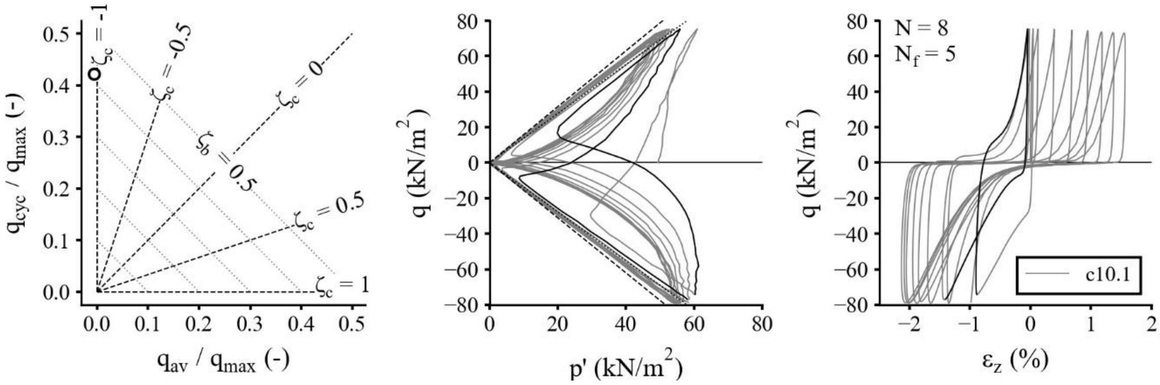

(j) c10: ζ_c = -1.0, ζ_b = 0.4 ***(k) c10*** ***(l) c10***

Figure 7.6: Influence of ζ_c on the effective stress path and stress-strain behaviour for tests sheared at ζ_b = 0.4 and $\sigma'_{c,0}$ = 50kN/m^2

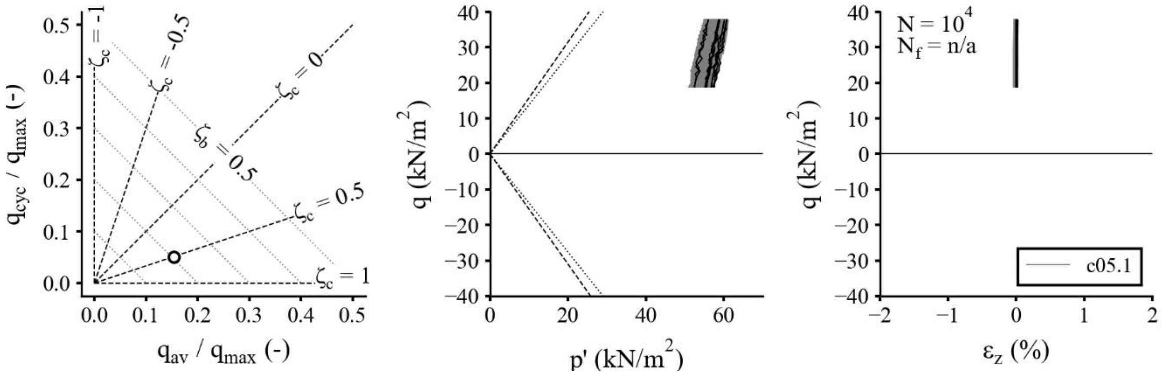

(a) c05: ζ_c = 0.5, ζ_b = 0.2 ***(b) c05*** ***(c) c05***

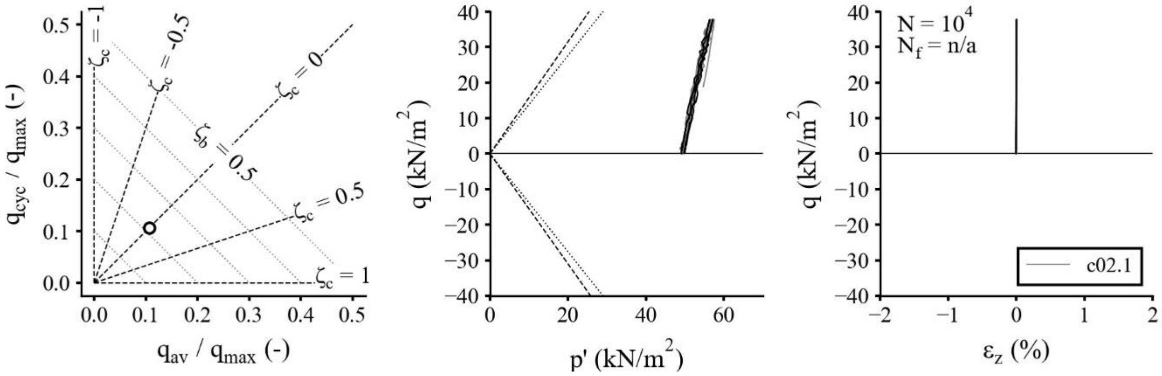

(d) c02: ζ_c = 0.0, ζ_b = 0.2 ***(e) c02*** ***(f) c02***

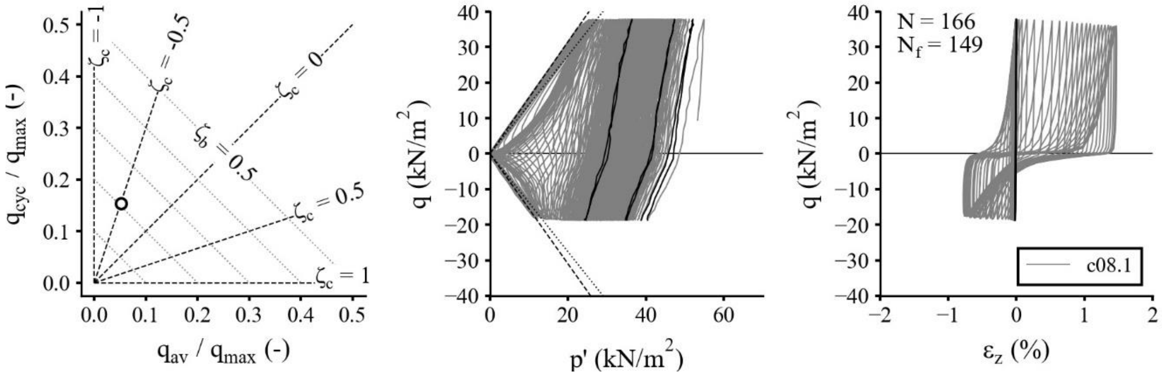

(g) c08: ζ_c = -0.5, ζ_b = 0.2 ***(h) c08*** ***(i) c08***

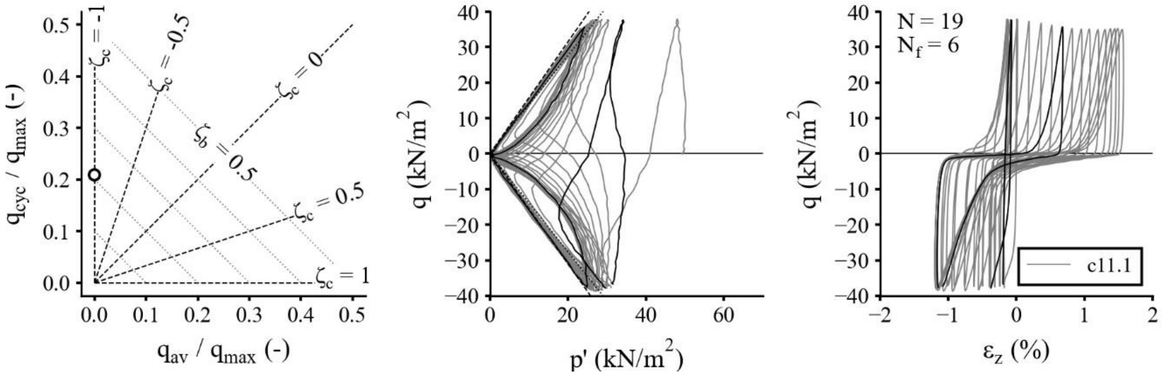

(j) c11: ζ_c = -1.0, ζ_b = 0.2 ***(k) c11*** ***(l) c11***

Figure 7.7: Influence of ζ_c on the effective stress path and stress-strain behaviour for tests sheared at ζ_b = 0.2 and $\sigma'_{c,0}$ = 50kN/m^2

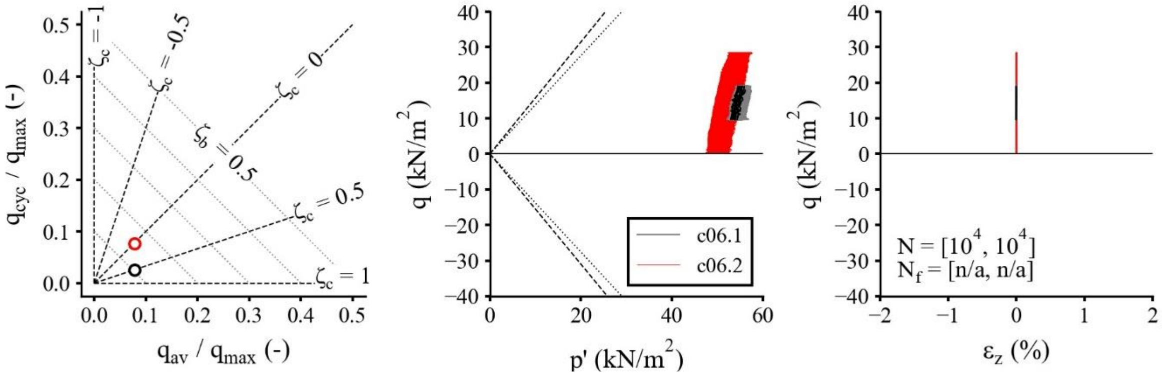

(a) c06: $\zeta_c = 0.5$, $\zeta_b = 0.1$ *(b) c06* *(c) c06*

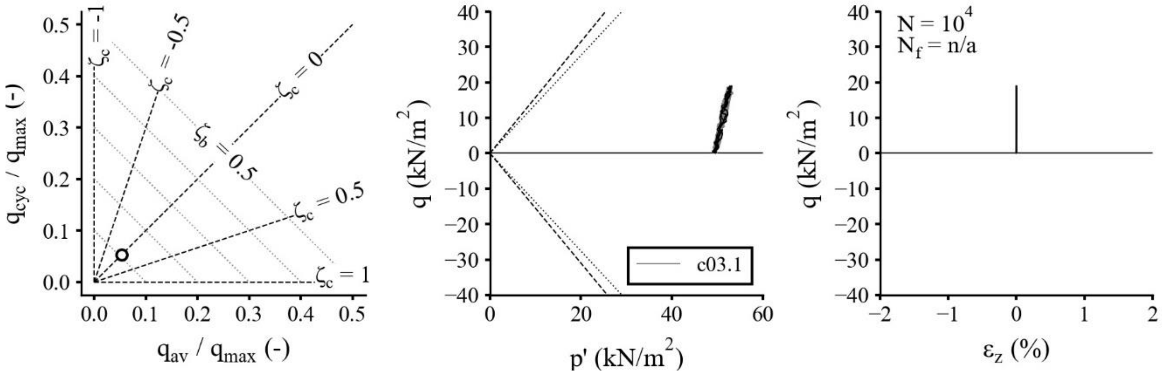

(d) c03: $\zeta_c = 0.0$, $\zeta_b = 0.1$ *(e) c03* *(f) c03*

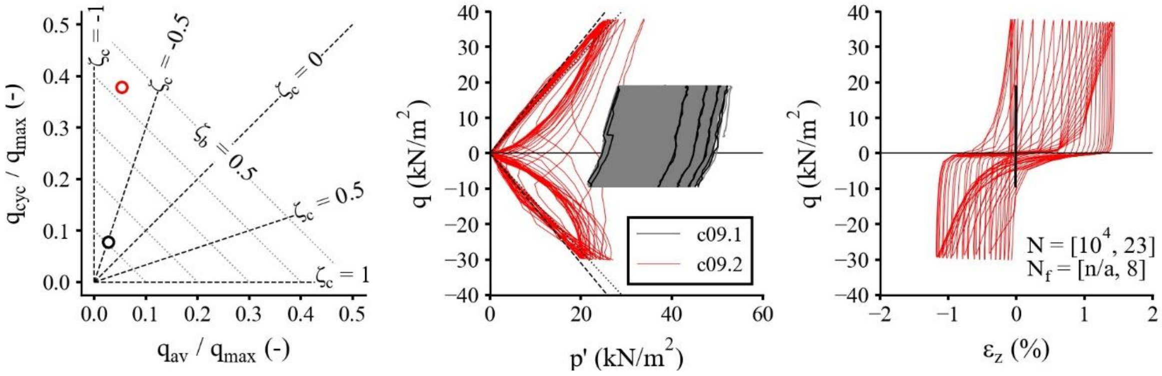

(g) c09: $\zeta_c = -0.5$, $\zeta_b = 0.1$ *(h) c09* *(i) c09*

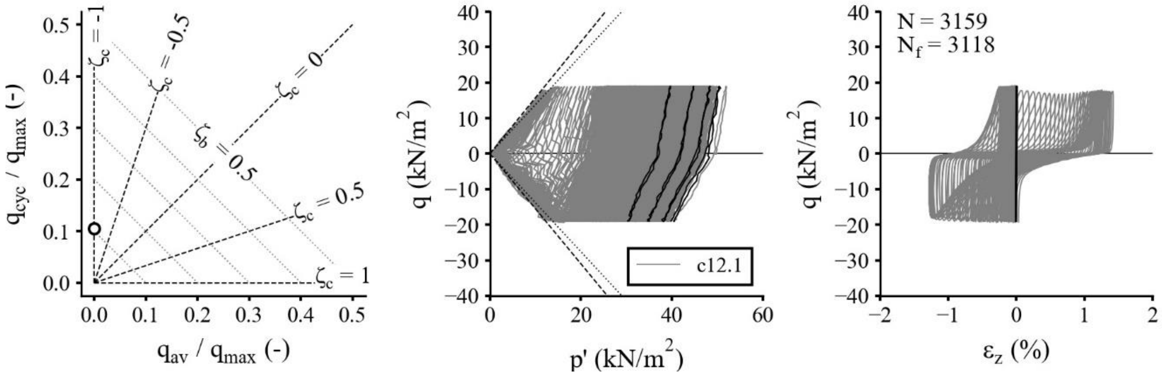

(j) c12: $\zeta_c = -1.0$, $\zeta_b = 0.1$ *(k) c12* *(l) c12*

Figure 7.8: Influence of ζ_c on the effective stress path and stress-strain behaviour for tests sheared at ζ_b = 0.1 and $\sigma'_{c,0}$ = 50kN/m^2

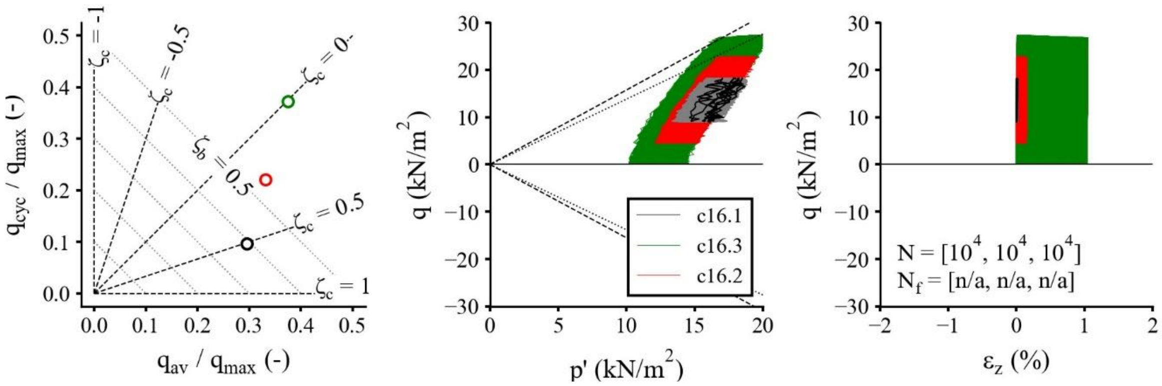

(a) c16: $\zeta_c = 0.5$, $\zeta_b = 0.4$ *(b) c16* *(c) c16*

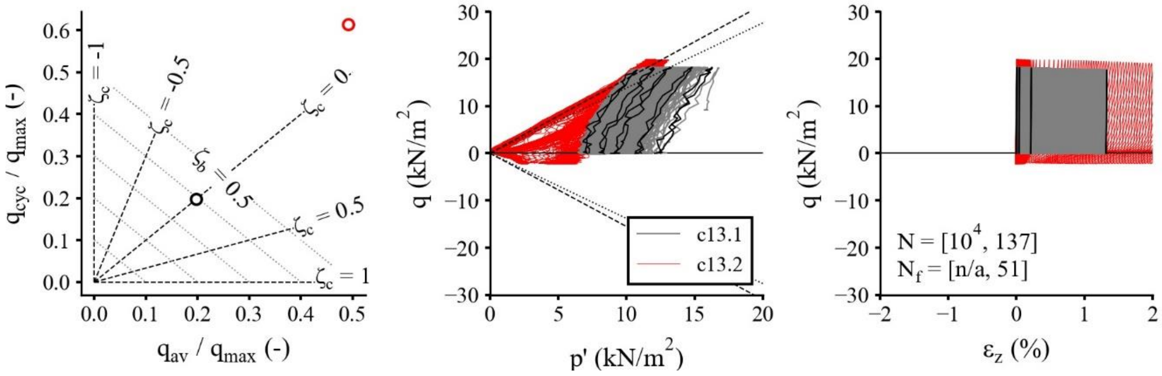

(d) c13: $\zeta_c = 0.0$, $\zeta_b = 0.4$ *(e) c13* *(f) c13*

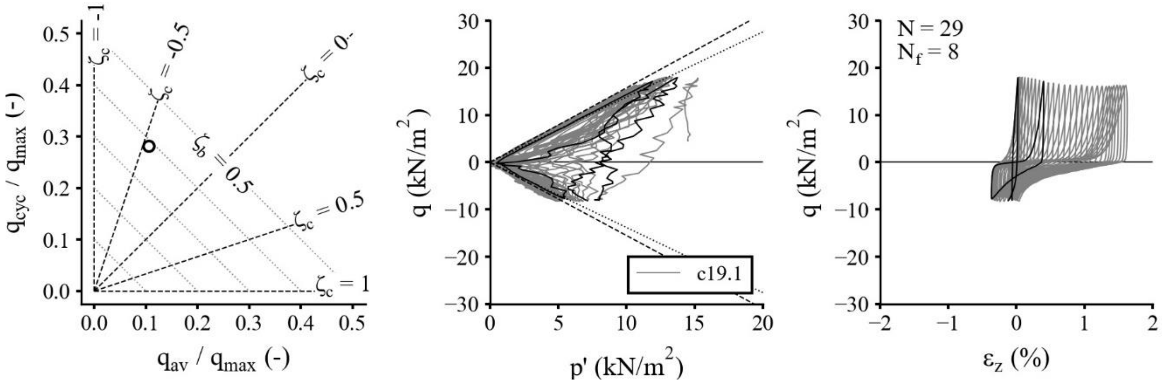

(g) c19: $\zeta_c = -0.5$, $\zeta_b = 0.4$ *(h) c19* *(i) c19*

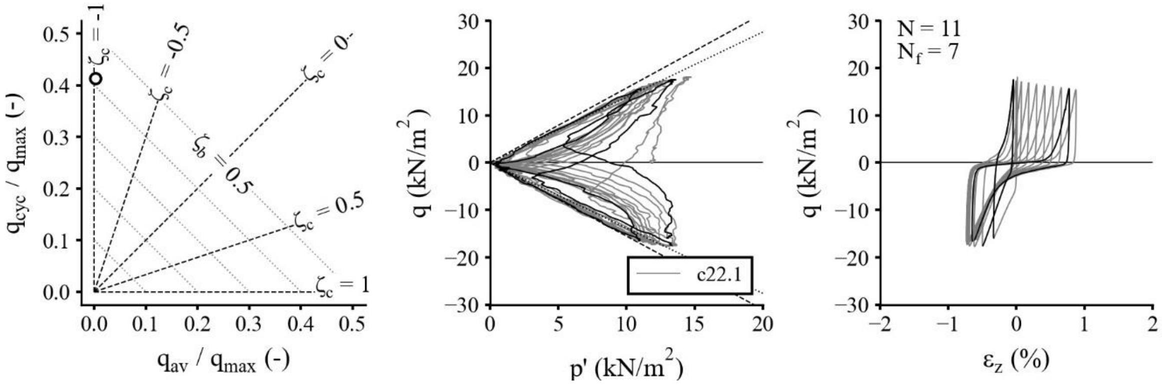

(j) c22: $\zeta_c = -1.0$, $\zeta_b = 0.4$ *(k) c22* *(l) c22*

Figure 7.9: Influence of ζ_c on the effective stress path and stress-strain behaviour for tests sheared at ζ_b = 0.4 and $\sigma'_{c,0}$ = 12kN/m^2

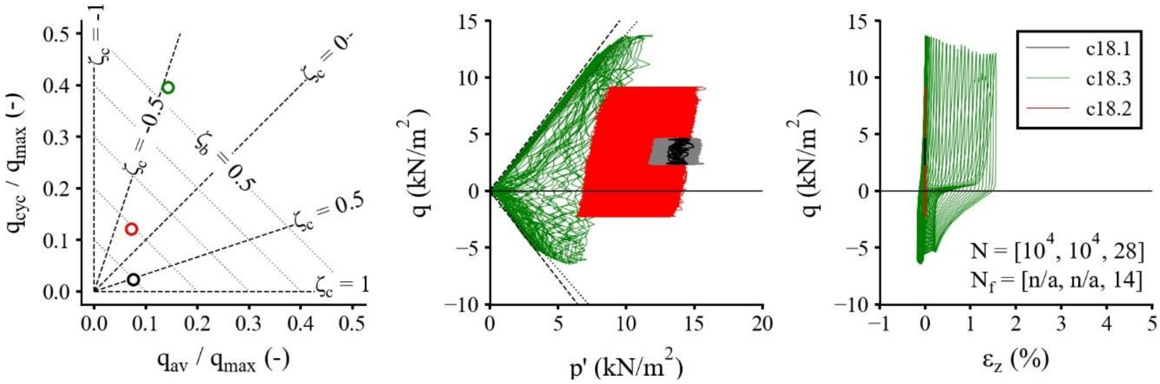

(a) c18: ζ_c = 0.5, ζ_b = 0.1 ***(b) c18*** ***(c) c18***

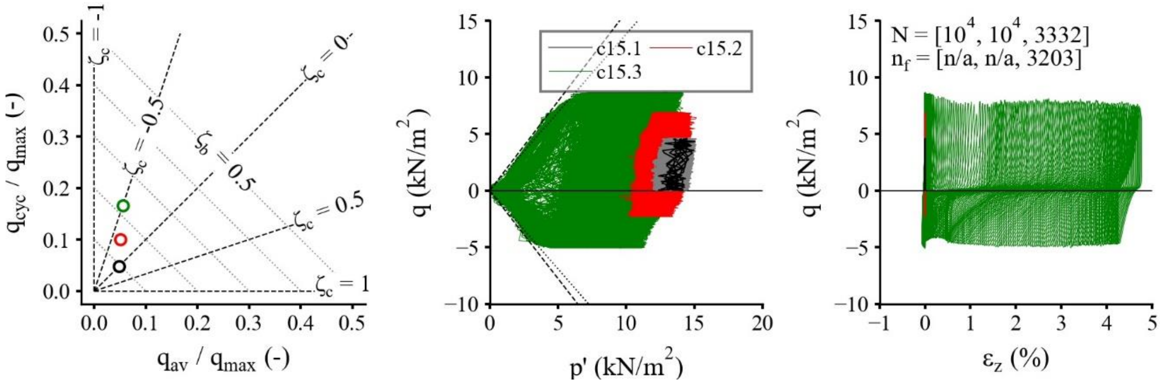

(d) c15: ζ_c = 0.0, ζ_b = 0.1 ***(e) c15*** ***(f) c15***

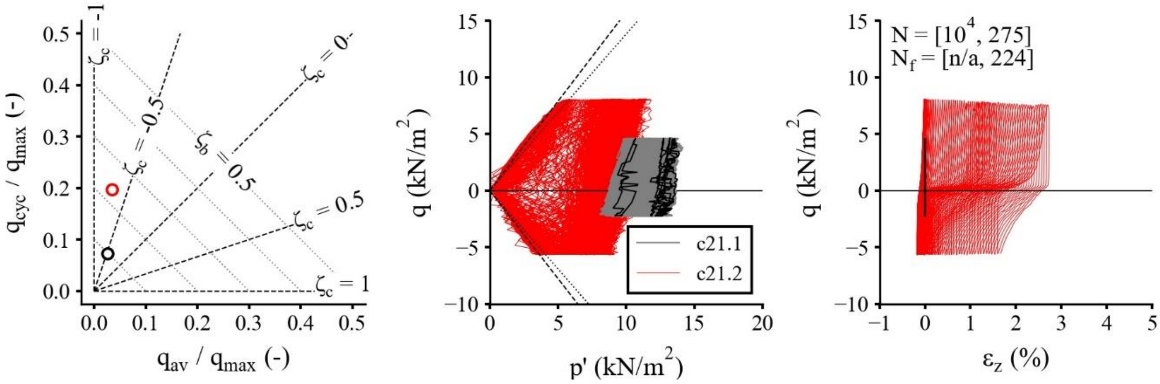

(g) c21: ζ_c = -0.5, ζ_b = 0.1 ***(h) c21*** ***(i) c21***

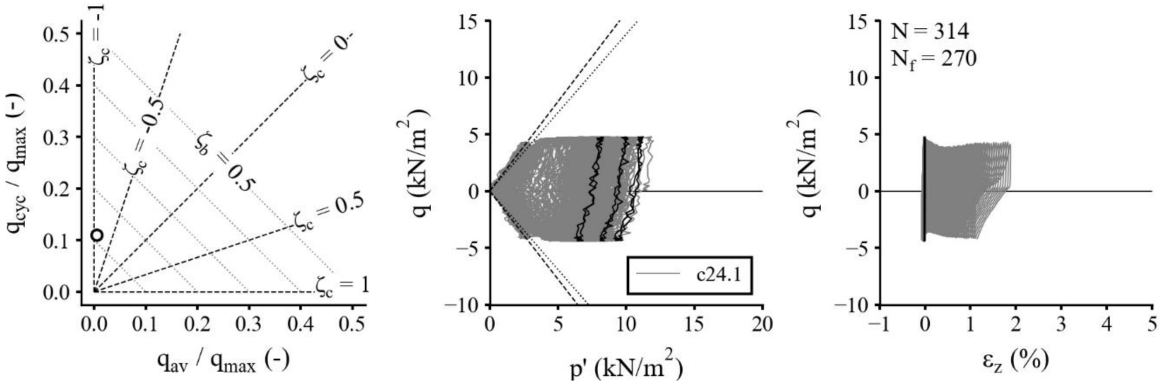

(j) c24: ζ_c = -1.0, ζ_b = 0.1 ***(k) c24*** ***(l) c24***

Figure 7.10: Influence of ζ_c on the effective stress path and stress-strain behaviour for tests sheared at ζ_b = 0.1 and $\sigma'_{c,0}$ = 12kN/m^2

7.4.1. TEST REPEATABILITY

To investigate the repeatability of the test results, tests c08 and c05 were repeated. Figure 7.11b shows the stress paths of the duplicate tests (identified by the letter ‘r’ after the test ID), and shows qualitatively that good repeatability is achieved in terms of the shape of the stress paths, and the performance of the control system.

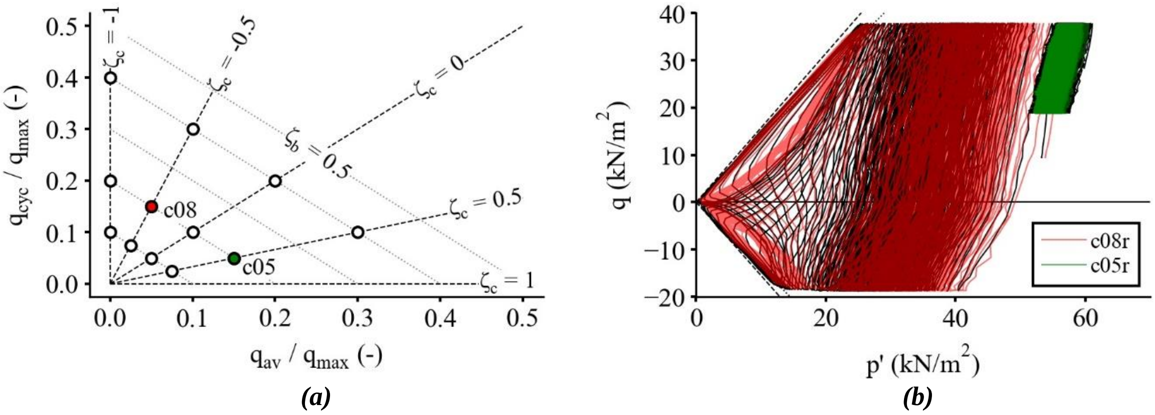

(a) *(b)*

Figure 7.11: Repeatability of cyclic triaxial test results

Figure 7.12 shows plots of pore pressure ratio, R_u, and cyclic shear strain, ε_{cyc}, vs. the number of cycles, n, normalised by either the number of cycles to liquefaction, N_f (for tests c08), or the total number of cycles, N (for tests c05). Very close agreement is obtained for the c05 tests in terms of both R_u and ε_{cyc}. Reasonable agreement is achieved for the c08 repeat tests. Test c08r was able to withstand approximately 30 more load cycles than test c08 before the onset of liquefaction, with N_f^{c08} = 121, and N_f^{c08r} = 149. The reason for this variation is unclear, as similar initial relative densities were obtained for each test (D_r^{c08} = 81.9 % and D_r^{c08r} = 81.5 %). However, the variation is relatively minor and considered to be within satisfactory tolerances.

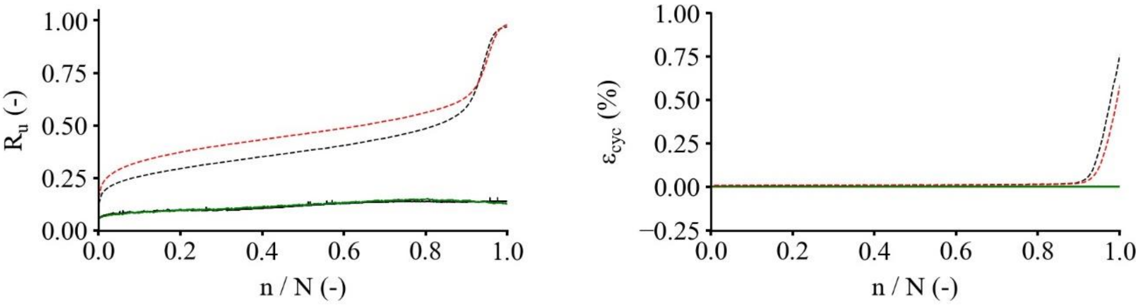

(a) *(b)*

Figure 7.12: Pore pressure ratio and cyclic shear strain measured from similar cyclic triaxial tests

7.4.2. GENERAL CYCLIC BEHAVIOUR

Inspection of tests undertaken at both $\sigma'_{c,0}$ = 50 and 12 kN/m^2 show that for $\zeta_c \geq 0$, tests were generally able to withstand the full 10^4 cycles without mobilising significant permanent axial strains. Tests undertaken at ζ_c = 0.5 are shown to mobilise negligible permanent axial strains (-0.05 % $\leq$ $\varepsilon_z \leq$ 0.05 %) after 10^4 cycles, with observed variations most likely attributable to temperature fluctuations in the laboratory.

Tests undertaken at ζ_c = 0.0 and low ζ_b values (i.e. $\zeta_b \leq$ 0.2) exhibit similar behaviour; however, tests with ζ_b = 0.4 (i.e. tests c01 & c13) show a greater reduction of p' after 10^4 cycles, and intercept the dilatancy surface after approximately 1000 (c01 at $\sigma'_{c,0}$ = 50 kN/m^2, Figure 7.6d) and 100 (c13 at $\sigma'_{c,0}$ = 12 kN/m^2, Figure 7.9d) cycles. Although the effective cyclic stress path appears to intercept the failure envelope in both cases, run-away failure, or 'flow liquefaction' does not occur, instead permanent axial strains are observed to accumulate steadily with increasing numbers of cycles. Similar behaviour was observed by Wichtmann & Triantafyllidis (2016), who also found that the effective stress path of cyclic triaxial tests undertaken on dense sands with high q_{cyc} and q_{av} values were able to cross the undrained failure envelope.

All cyclic effective stress paths for $\zeta_c \geq 0$ are shown to migrate towards the failure envelope, indicating the development of excess pore pressures, thereby suggesting that failure conditions and subsequent accumulation of large strains will inevitably occur given sufficient numbers of cyclic loading. The rate at which excess pore pressures develop is shown to be influenced by the value of ζ_b, with higher values leading to faster accumulation rates. This is exemplified in test c01 (Figure 7.6(d-f)), which shows that for $\zeta_c = 0.0$ and $\zeta_b = 0.4$, the dilatancy surface/PTL is reached after about 1000 cycles, leading to the steady accumulation of approximately 1.8 % of permanent axial strain after 10^4 cycles. However, test c03 undertaken at $\zeta_c = 0.0$; $\zeta_b = 0.1$ (Figure 7.8(d-f)) shows only a modest reduction in the mean effective stress after 10^4 cycles, and negligible mobilised axial strains. Test c02 (Figure 7.7(d-f)), an intermediate test undertaken at $\zeta_c = 0.0$; $\zeta_b = 0.2$ shows an increased reduction in p' after 10^4 cycles compared with test c03; however, the cyclic stress path remains relatively far away from the dilatancy surface, resulting in negligible accumulation of permanent axial strains. Similar behaviour is observed for tests undertaken at $\sigma'_{c,0}$ = 12 kN/m^2.

With the exception of tests c09 and c21, cyclic triaxial tests undertaken with $\zeta_c < 0$ developed sufficient excess pore pressures to trigger 'initial liquefaction' (i.e. p' = 0, or R_u = 1), leading to the characteristic 'butterfly' stress path shape in $q - p'$ space, and accumulation of increasingly large permanent strains. However, despite failure conditions being reached, significantly large strains are not mobilised. This is because dense sands tend to dilate when sheared, which in undrained tests is manifested by the development of negative pore pressures and subsequent increases in p'. Development of large 'runaway' strains are therefore arrested by the onset of dilation and subsequent stiffness increases resulting from the increased p'. As cycling continues, progressively larger strains are required in each load cycle to mobilise dilatancy and associated increases in p'.

The number of cycles required to reach initial liquefaction (shown in Table 7.3 and Table 7.4) is found to be principally influenced by ζ_c, with full, 2-way loading ($\zeta_c = -1$) causing cyclic instability in relatively fewer numbers of cycles than those tests carried out at $\zeta_c = -0.5$. Results also indicate the influence of ζ_b, in that liquefaction conditions were not reached after 10^4 cycles when ζ_b was $\leq$ 0.1, as shown by results from tests c09 (Figure 7.8g) and c21 (Figure 7.10g).

The above behaviour may be explained by considering the shape of the effective stress-path in $q - p'$space, the static bias (q_{av}), and the magnitude of the cyclic deviator stress (q_{cyc}). For 2-way cyclical axial loading with no static bias, the orientation/direction of the stress path means that the extension failure envelope will be intercepted at a lower magnitude of stress than in compression. This type of behaviour is evident in Figure 7.7(k), which shows the stress path intercepting the extension dilatancy surface during the unloading component of cycle 0. Static bias can therefore improve the resistance of the material, by 'shifting' the stress path up in $q - p'$ space, and thus further away from the extension failure envelope.

However, increasing the static bias too much may result in the compression failure envelope being intercepted first. The influence of static bias is shown in the results of tests c02 (Figure 7.7(d-f)), c04

(Figure 7.6(a-c)), and c12 (Figure 7.8(j-l)). These tests trace a horizontal line in the cyclic stress space diagram (i.e. q_{cyc}= constant – see Figure 7.5) but were sheared from different initial static biases. Despite a relatively small cyclic load amplitude, test c12 – which had no static bias – reached initial liquefaction conditions after approximately 3122 cycles. However, liquefaction did not occur in tests c02 and c04, but inspection of the effective stress paths show that test c04 is closer to the compression failure envelope after 10^4 cycles, and would probably intercept the compression failure envelope in fewer cycles than c02. Test c04 may therefore be considered as having a lower 'cyclic resistance' than c02.

This behaviour may be explained in part by comparing the ζ_b values for tests c02 and c04 (0.2 and 0.4, respectively). Despite test c04 having a higher ζ_c value than test c02 (ζ_c = 0.5 and 0.0, respectively), which as previously discussed is shown to generally improve cyclic resistance, test c04 also has a higher ζ_b value (ζ_b= 0.4 compared to 0.2 for test c02).

This is further exemplified in the results of tests c07 (Figure 7.6(h)) and c09 (Figure 7.9(h)). Both tests included some beneficial static bias (exemplified by $\zeta_c \neq -1$); however, the magnitude of the cyclic deviator stress was significantly larger in test c07 than in test c09 ($\zeta_b = 0.4$, and $\zeta_b = 0.1$, respectively), leading to liquefaction after relatively few cycles. Conversely, despite stress reversal, test c09 did not liquefy even after 10^4 cycles as the magnitude of the cyclic deviator stress was sufficiently small.

The use of ζ_b and ζ_c within a normalised cyclic stress-space framework therefore provides a useful and robust tool for not only characterising cyclic loads in a test programme, but also for qualitatively predicting cyclic soil response. ζ_c gives an indication of the type of cyclic loading and amount of static bias. $\zeta_c = -1$ represents full 2-way cyclic loading, and is shown to constitute the most destructive or 'worst case' conditions (for triaxial loading conditions with positive static bias). The 'cyclic resistance', defined broadly as the ability of a soil to withstand cyclic loading, is dependent on the type of cyclic loading and is significantly improved in situations where stress reversal does not occur (i.e. $\zeta_c \geq 0$). ζ_b gives an indication of the magnitude of the applied cyclic stress amplitude.

Higher values of ζ_b therefore become increasingly destructive in terms of the cyclic response, even in one-way loading situations. The cyclic resistance is therefore a balance between relative magnitudes of ζ_c and ζ_b.

As defined in Section 5.1.7, the phase transformation state marks the boundary between contractive and dilative behaviour. Large strains are rapidly mobilised on approach and during transition; however, once the PTL is crossed, the soil tends to dilate, excess pore pressures decrease, mean effective stresses increase and the cyclic stress path moves to the right. The shear strength and stiffness of the material rapidly increases with dilation, thereby limiting the mobilisation of further excessively large strains. Similar behaviour occurs on unloading, leading to the characteristic ‘butterfly’ profile arising from alternate phases of dilation (hardening) and densification (softening).

7.5. INTERPRETATION

7.5.1. EXCESS PORE PRESSURE ACCUMULATION RATE

Figure 7.13 shows graphs of pore pressure ratio, R_u, vs. the number cycles. Each column represents tests carried out at a constant value of ζ_b. Similar colour groupings are employed across each column to denote ζ_c values, with $\sigma'_{c,0}$ = 50 and 12 kN/m^2 shown as solid and dashed lines, respectively. Values of R_u shown represent the maximum value mobilised over the duration of an individual cycle. Similar behavioural trends to that described in Section 7.4 are observed, indicating that the rate and magnitude of accumulated strains are closely related to the build-up of excess pore water pressures and corresponding reduction in mean effective stress.

It is evident from the results that:

- The increase in R_u with cycle number is non-linear, with significant excess pore pressures accumulating in cycle 0.
- The accumulation of R_u is relatively linear between cycle 1 up to about R_u = 40-50 %, after which the rate of accumulation increases significantly.
- The rate of pore pressure accumulation increases with higher ζ_b and lower ζ_c values

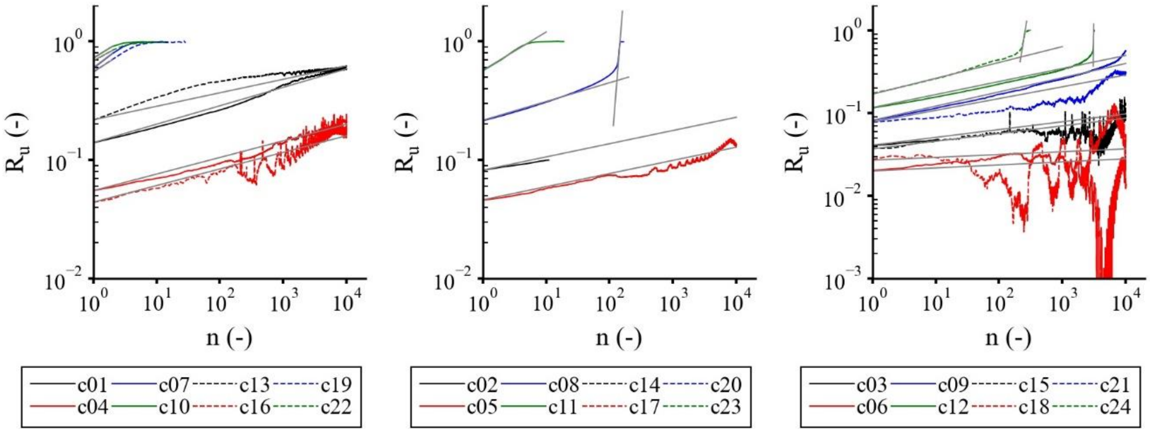

(a) ζ_b = 0.4 ***(b) ζ_b = 0.2*** ***(c) ζ_b = 0.1***

Figure 7.13: Measured pore pressure ratio development with numbers of cycles

Table 7.5 and Table 7.6 shows the rate of pore pressure ratio accumulation for tests sheared at $\sigma'_{c,0}$ = 50 and 12 kN/m², respectively. The results show similar accumulation rates for tests carried out with similar ζ_b and ζ_c values; however, tests undertaken at $\sigma'_{c,0}$ = 50 kN/m² show generally higher accumulation rates than those tests sheared at 12kN/m². Table 7.5 and Table 7.6 also present the higher R_u accumulation rates mobilised during those cycles immediately prior to initial liquefaction, and shows that the accumulation rate generally increases by two to three orders of magnitude.

Table 7.5: Pore pressure ratio accumulation rates for tests sheared at σ'$_{c,0}$ = 50 kN/m²

Test ID (-)	ζ$_b$ (-)	ζ$_c$ (-)	dR_u/dn (-)
c01	0.4	0.0	4.5e-05
c02	0.2	0.0	1.5e-05
c03	0.1	0.0	5.7e-06
c04	0.4	0.5	1.5e-05
c05	0.2	0.5	8.2e-06
c06	0.1	0.5	8.0e-07
c07	0.4	-0.5	0.196*
c08	0.2	-0.5	1.4e-03 | 3.6e-02*
c09	0.1	-0.5	3.2e-05
c10	0.4	-1.0	0.185*
c11	0.2	-1.0	0.07
c12	0.1	-1.0	3.8e-05 | 1.8e-02*

Table 7.6: Pore pressure ratio accumulation rates for tests sheared at $\sigma'_{c,0}$ = 12 kN/m²

Test ID (-)	ζ$_b$ (-)	ζ$_c$ (-)	dR_u/dn (-)
c13	0.4	0.0	4.1e-05
c14	0.2	0.0	
c15	0.1	0.0	5.0e-06
c16	0.4	0.5	1.2e-05
c17	0.2	0.5	
c18	0.1	0.5	1.0e-06
c19	0.4	-0.5	0.147*
c20	0.2	-0.5	
c21	0.1	-0.5	2.1e-05
c22	0.4	-1.0	0.150*
c23	0.2	-1.0	
c24	0.1	-1.0	4.7e-04 | 1.5e-02*

* Maximum rate mobilised

The significant increase in the rate of R_u accumulation (and corresponding axial strains) observed in tests c08, c12 and c24 (Figure 7.13(bc)) emphasises how instability can suddenly occur over relatively few cycles. This behaviour was first reported by Lee & Albaisa (1974) following undrained cyclic triaxial tests on D_r = 30 to 100 % samples of Monterey sand. Seed *et al*. (1975) proposed Eq. (7-17) to describe the observed behaviour.

$$R_u = \frac{1}{2} + \frac{1}{\pi}\arcsin\left(2\left(\frac{N}{N_L}\right)^{\frac{1}{\alpha}} - 1\right) \tag{7-17}$$

where α is a curve fitting parameter. Figure 7.14a presents R_u vs the normalised number of cycles required to cause initial liquefaction, N/N_L, reported by Lee & Albaisa (1974). Also shown are empirical estimates based on Eq. (7-17), indicating the influence of various α values on the calculated pore pressure ratio. Figure 7.14a shows that while the upper bound may be accurately modelled by taking $\alpha = 1.2$, Eq. (7-17) is evidently unable to adequately reproduce the characteristic "S-shape" curve for the lower bound curve.

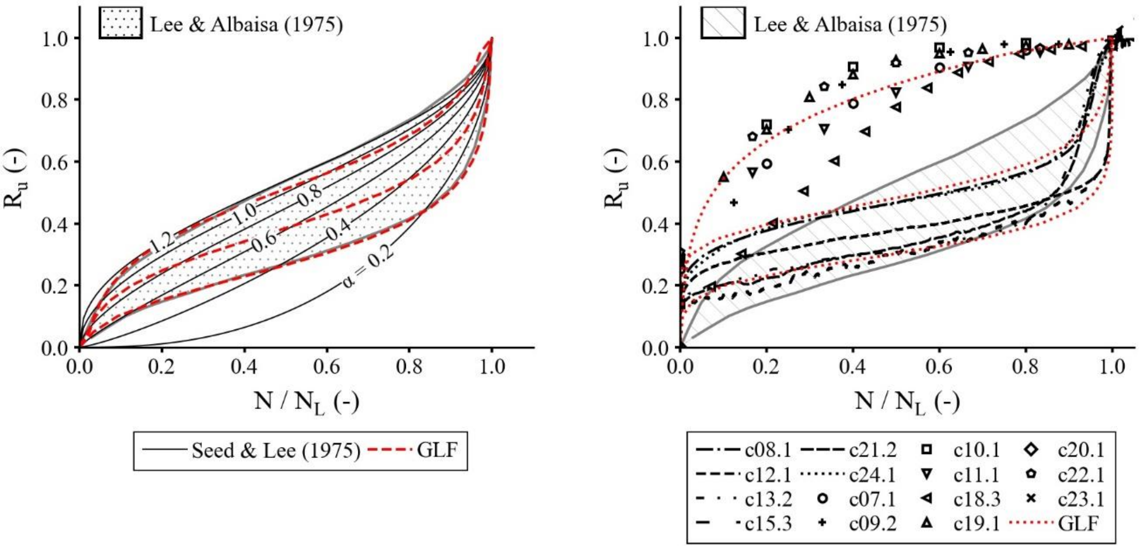

(a) *(b)*

Figure 7.14: (a) Range of pore pressure ratios reported by Lee & Albaisa (1974), and (b) measured pore pressure ratios from tests observed to reach conditions of initial liquefaction

An improvement may be obtained by adopting a generalised logistic (or Sigmoid) function (GLF), as given in Eq. (7-18):

$$\frac{N}{N_L} = \frac{K}{(1 + Qexp^{-BR_u})^{1/v}} \tag{7-18}$$

where K, Q, B, and v are curve fitting parameters. The dashed red lines in Figure 7.14a represent three curves calculated using Eq. (7-18), and show that a very close match to the Lee & Albaisa (1974) range may be achieved. Figure 7.14b presents results obtained from this study and shows that, for tests that took a relatively large number of cycles to liquefy (i.e. c08, c12, c24), qualitatively similar behaviour to that found by Lee & Albaisa (1974) is observed. However, the rate of excess pore pressure accumulation appears to be greater in the first few and last few loading cycles. Furthermore, tests that reached initial liquefaction in relatively few numbers of cycles do not exhibit the same "S-shape" curve, and instead develop significant excess pore pressures in the first few cycles.

Both types of behaviour may be accurately reproduced with Eq. (7-18), as shown by the dotted red lines in Figure 7.14b, indicating the flexibility and improved performance of the GLF in capturing the various responses. The differences in the observed responses may be explained by considering the magnitude of mobilised cyclic shear strains in relation to the cyclic volumetric threshold strain, γ_{tv} (see Section 5.2.3). This concept and its implications are examined further in Sections 7.5.3 and 7.5.4.

7.5.2. STRAIN ACCUMULATION RATE

Figure 7.15 and Figure 7.16 show plots of ε_{da} and ε_N, vs n, respectively, for the 20 cyclic triaxial tests undertaken in this study. Similar qualitative behavioural trends described in Section 7.4.1, in terms of the influence of ζ_b and ζ_c on cyclic response, may also be drawn from inspection of Figure 7.15. Results from additional cyclic shearing stages are not presented for clarity purposes.

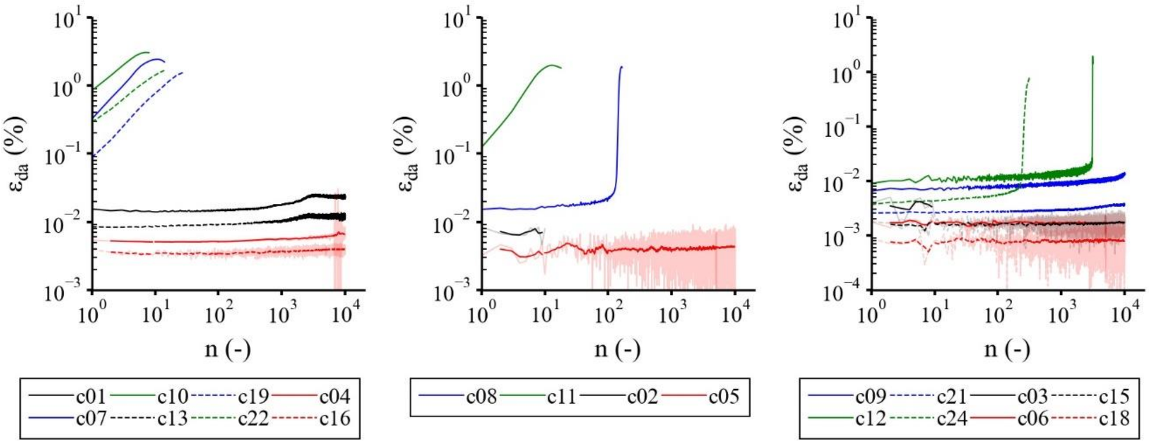

(a) ζ_b = 0.4 *(b) ζ_b = 0.2* *(c) ζ_b = 0.1*

Figure 7.15: Estimated double amplitude vertical strain, ε_{da}, mobilised with cycle number

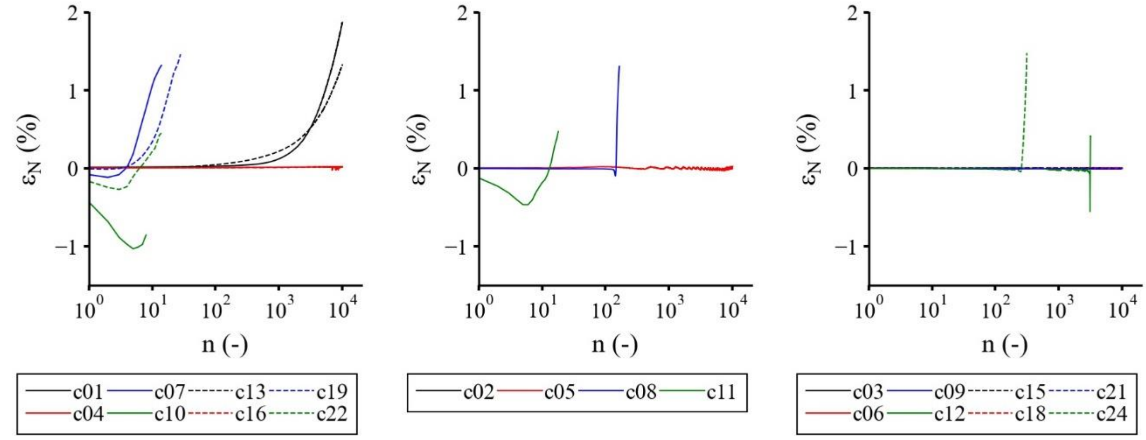

(a) $\zeta_b = 0.4$ (b) $\zeta_b = 0.2$ (c) $\zeta_b = 0.1$

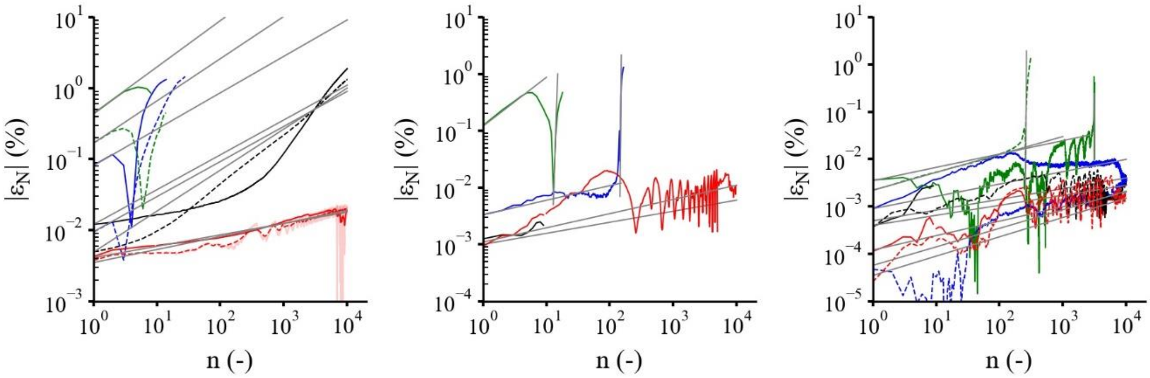

(d) $\zeta_b = 0.4$ (e) $\zeta_b = 0.2$ (f) $\zeta_b = 0.1$

Figure 7.16: Estimated and residual vertical strain, ε_N , mobilised with cycle number

Figure 7.15 and Figure 7.16 show that tests with high ζ_b values are found to mobilise larger strain values in fewer cycles. The same is true for tests with lower ζ_c values. Tests that were found to reach liquefaction conditions are easily identifiable by both the relatively large cyclic and residual axial strains mobilised, and also by their failure in reaching the intended 10^4 cycles.

Figure 7.15(abc) shows that ε_{da} tends to increase with increasing numbers of cycles, before rapidly increasing once liquefaction conditions have been reached (e.g. tests c08, c12, c24). However, once liquefaction has occurred the magnitude of ε_{da} tends to reach a maximum value of approximately 2-3 %, and then decreases on further cycling. This type of behaviour is unexpected, and is thought to be due to the occurrence of necking in the top third of the specimen. Large displacements were observed in this zone during the last few cycles prior to halting a test, which were visibly not being captured by the local strain instrumentation.

Figure 7.16 presents the accumulation of permanent strains with cycle number, and show similar behaviour to that observed for R_u (Figure 7.13). Table 7.5 and Table 7.6 shows the estimated residual vertical strain accumulation rates for tests sheared at $\sigma'_{c,0}$ = 50 and 12 kN/m^2, respectively, and show that tests with relatively high ζ_b and low ζ_c values mobilise relatively higher accumulation rates.

Figure 7.16(abc) shows tests that undergo stress reversal ($\zeta_c < 0$) initially accumulate negative (i.e. extensive) residual strains, but tend to change direction after a certain number of cycles. The accumulation of axial strain on the triaxial extension or compression side is thus found to depend on whether the main portion of the stress path lies above or below the isotropic axis. Analysis of the excess pore pressure ratio profiles for these tests finds that the local minimum generally coincides with values of $R_u \geq 90$ %, and is ≥ 98 % in three cases (test c10, c11 and c12). This change in the direction of strain accumulation is therefore probably associated with the onset of liquefaction.

First inspection of the one-way loading tests ($\zeta_c > 0$) in Figure 7.16(abc) suggests that negligible residual strains are accumulated after 10^4 cycles; however, replotting the data on a log scale (Figure 7.16(def)) shows that modest positive (compressive) strains are accumulated with increasingly large numbers of cycles. However, the displacements seen for tests sheared at lower stress amplitudes (i.e. ζ_b = 0.1 and 0.2) were of comparable magnitude (or less) to the resolution of the on-sample strain instrumentation. Furthermore, temperature fluctuations in the laboratory become increasingly influential at such low displacement amplitudes (see Figure 7.16(e) – test c05), and despite adopting filtering techniques to reduce electrical noise, reliable estimates of strain are difficult in these tests.

Tests c01 and c13, both undertaken at $\zeta_c = 0$ and $\zeta_b = 0.4$, show different behaviour to that described above. Unlike tests which trigger liquefaction conditions, relatively high residual strains are found to progressively accumulate (1.9 and 1.3 %, respectively) over the course of 10^4 cycles. According to Figure 7.6 and Figure 7.9, both effective stress paths appear to have intercepted the maximum failure envelope as determined from monotonic tests. Unstable behaviour is therefore expected (i.e. sudden increase in R_u and associated increases in permanent strains).

Table 7.7: Strain rates for tests sheared at $\sigma'_{c,0}$ = 50 kN/m^2

Test ID (-)	**ζ_b** (-)	**ζ_c** (-)	**$d\varepsilon_N/dn$** (% per cycle)
c01	0.4	0.0	1.1e-04**
c02	0.2	0.0	5.0e-07
c03	0.1	0.0	3.5e-07
c04	0.4	0.5	1.4e-06
c05	0.2	0.5	9.9e-07
c06	0.1	0.5	1.9e-07
c07	0.4	-0.5	-9.0e-04
c08	0.2	-0.5	-5.8e-05 | 3.1e-01*
c09	0.1	-0.5	9.0e-07
c10	0.4	-1.0	-1.8e-02
c11	0.2	-1.0	-8.3e-02 | 4.4e-01*
c12	0.1	-1.0	-9.7e-06 | 7.8e-02*

* Maximum rate mobilised

Table 7.8: Strain rates for tests sheared at $\sigma'_{c,0}$ = 12 kN/m^2

Test ID (-)	**ζ_b** (-)	**ζ_c** (-)	**$d\varepsilon_N/dn$** (% per cycle)
c13	0.4	0.0	1.0e-04**
c14	0.2	0.0	
c15	0.1	0.0	2.4e-07
c16	0.4	0.5	1.6e-06
c17	0.2	0.5	
c18	0.1	0.5	1.5e-07
c19	0.4	-0.5	-8.9e-05
c20	0.2	-0.5	
c21	0.1	-0.5	2.0e-07
c22	0.4	-1.0	-3.9e-03
c23	0.2	-1.0	
c24	0.1	-1.0	-2.8e-05 | 1.8e-01*

However, inspection of the R_u profile for these tests (Figure 7.13a) shows a similar steady increase in excess pore pressure with increasing cycle number to approximately 60 %; however, the sudden collapse observed in other tests following development of $R_u \geq$ 40-50 % is not observed. This behaviour may be explained by again considering the mobilised value of γ_{cyc} in relation to γ_{tv}. Inspection of ε_{da} profiles (related to γ_{cyc} by Eq. (7-11)) for these tests (Figure 7.15a) show small increases in ε_{da} up to about 3000 cycles, after which values stabilise or decrease slightly. Instability conditions are therefore not mobilised as γ_{cyc} remain less than γ_{tv}.

7.5.3. STIFFNESS RESPONSE

Figure 7.17 presents the evolution of the secant shear modulus, G_{sec}, with increasing numbers of cycles, and shows that both the magnitude and rate of degradation of G_{sec} is influenced by a number of factors:

- G_{sec} decreases with increasing numbers of cycles.
- G_{sec} decreases with decreasing $\sigma'_{c,0}$.
- Initial G_{sec} values decrease with decreasing ζ_c.
- The rate of degradation of G_{sec} is non-linear, and is strongly influenced by ζ_b and ζ_c.
- Initial G_{sec} values and degradation rates are higher for smaller values of ζ_b.

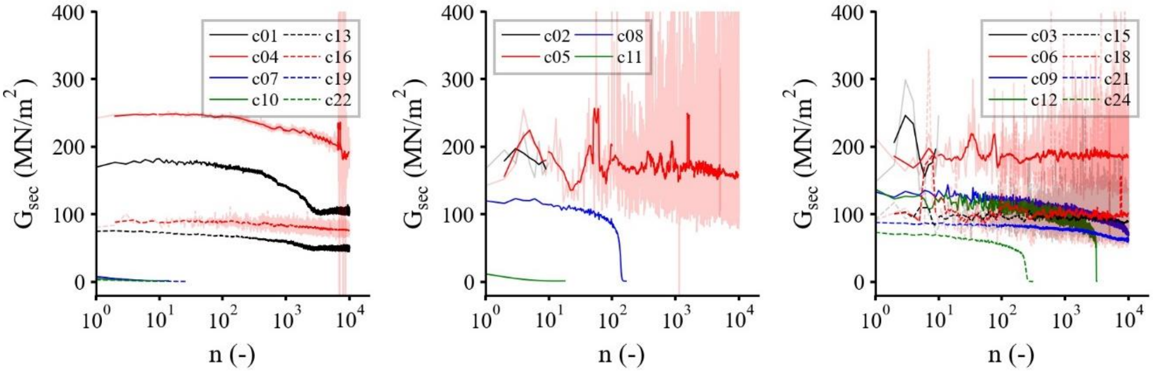

(a) $\zeta_b = 0.4$ ***(b) $\zeta_b = 0.2$*** ***(c) $\zeta_b = 0.1$***

Figure 7.17: Evolution of the secant shear modulus, G_{sec} with increasing numbers of cycles

The behaviour observed in Figure 7.17 may be explained by considering the cyclic stress space diagram presented in Figure 7.5 and the volumetric threshold cyclic shear strain concept described in Section 5.2.3. For tests undertaken at similar ζ_b values, the magnitude of q_{cyc} increases as ζ_c reduces, with higher cyclic stress amplitudes mobilising larger cyclic strains. Similarly, the magnitude of q_{cyc} (and subsequent $\Delta\varepsilon_z$) decreases with decreasing ζ_b. For tests with relatively high q_{cyc} values (e.g. c07, c10), the cyclic volumetric threshold strain, γ_{tv}, is exceeded during the initial load cycle, causing significant excess pore pressures and reductions to initial G_{sec} values.

Similar tests in terms of ζ_c but lower ζ_b values (e.g. c09, c12) are subjected to lower cyclic stress amplitudes, and exhibit a greater initial stiffness. Excess pore pressures and cyclic strains accumulate relatively slowly with increasing numbers of cycles, resulting in modest reductions to G_{sec} over this period. However, once γ_{tv} is exceeded, significant stiffness degradation occurs. This behaviour is not observed for $\zeta_c \geq 0$, as accumulated cyclic shear strains remain below γ_{tv}, even after 10^4 cycles.

Figure 7.17 shows that the data suffer from excessive noise in some tests, particularly for $\zeta_c \geq 0$, and $\zeta_b \leq 0.2$, making reliable estimations of G_{sec} difficult. This is because the magnitude of q_{cyc} decreases with decreasing ζ_b values (see Figure 7.5), and as result smaller cyclic strains are mobilised. Such low cyclic stress and strain amplitudes are challenging to accurately measure and require the use of instrumentation with appropriate capacity/displacement range and resolution. However, the instrumentation must have sufficient capacity/range to adequately capture the response of the material, but also be robust enough to ensure accidental damage/over-ranging does not occur.

Despite utilising filtering methods (e.g. simple moving average techniques) to reduce noise, the data remains erratic in some cases, suggesting that the instrumentation adopted in this study is sub-optimal for the range of cyclic stresses and strains mobilised in some of these tests. Improving the quality of stress measurements may be relatively easily achieved by tailoring the capacity of the ISLC to the anticipated demands of each individual test. However, improving the quality of the local strain instrumentation results, in terms of capturing behaviour in the very small strain range (i.e. for $\varepsilon_z < 10^{-6}$) is more challenging, and would likely require manufacturer input/support.

Figure 7.18 shows stiffness degradation curves for tests undertaken at $\zeta_c \leq 0$, normalised by the small-strain shear modulus, G_0, obtained from bender element tests carried out immediately prior to cyclic shearing. Tests at $\zeta_c \geq 0$ are not presented as the data suffered from excessive electrical noise. Figure 7.18 shows that tests undertaken at $\sigma'_{c,0}$ = 12 kN/m^2 mobilise a lower G_{sec} at the same γ_{cyc} value than similar tests carried out at $\sigma'_{c,0}$ = 50 kN/m^2 (i.e. curves are ‘shifted’ to the left), which is consistent with the findings of Chapter 6.

A similar response is observed for tests carried out at the same ζ_c but decreasing values of ζ_b. This type of behaviour may again be explained by considering the cyclic stress space diagram presented in Figure 7.5, which shows that along lines of constant ζ_c, the magnitude of q_{av} decreases with decreasing ζ_b. Despite $\sigma'_{c,0}$ remaining constant during the drained ramp up to q_{av}, the 3:1 inclination of the stress path in $q - p'$ space, results in different initial mean effective stress, p'_0, values for each test. Tests undertaken at lower ζ_b values are therefore sheared from progressively lower initial mean effective stresses, and thus behave in a manner similar to that described in Chapter 6.

The relatively steep gradient of the stiffness degradation curves in the range $10^{-5} \leq \gamma_{cyc} \leq 10^{-3}$ may be a result of the mean effective stresses decreasing with increasing numbers of cycles and excess pore pressures accumulation. Alternatively, the shape of the curve may be an artefact of constant amplitude cyclic testing, with each amplitude yielding a particular $G - \gamma_{cyc}$ relationship.

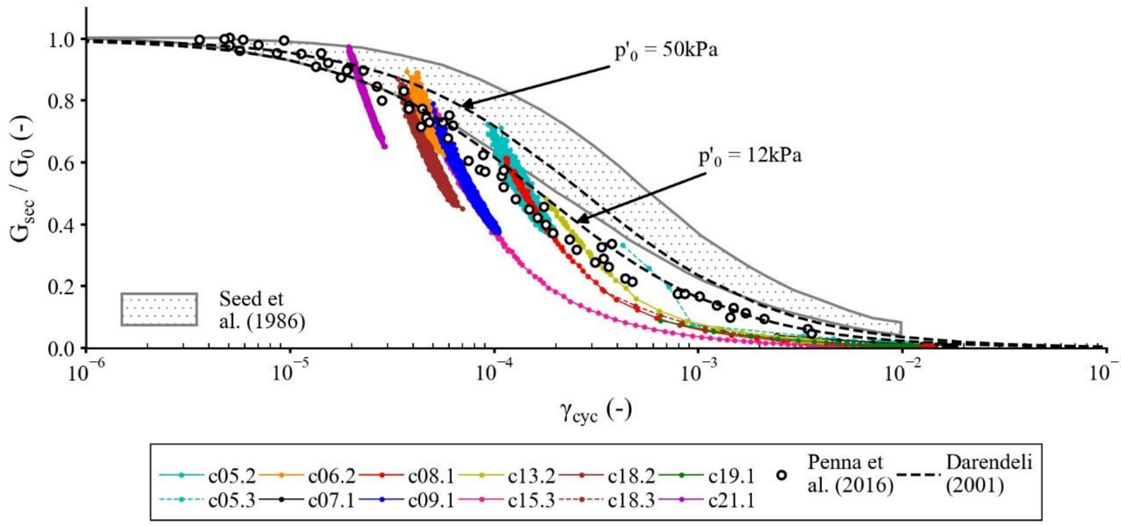

(a) -0.5 ≤ ζ_c ≤ 0

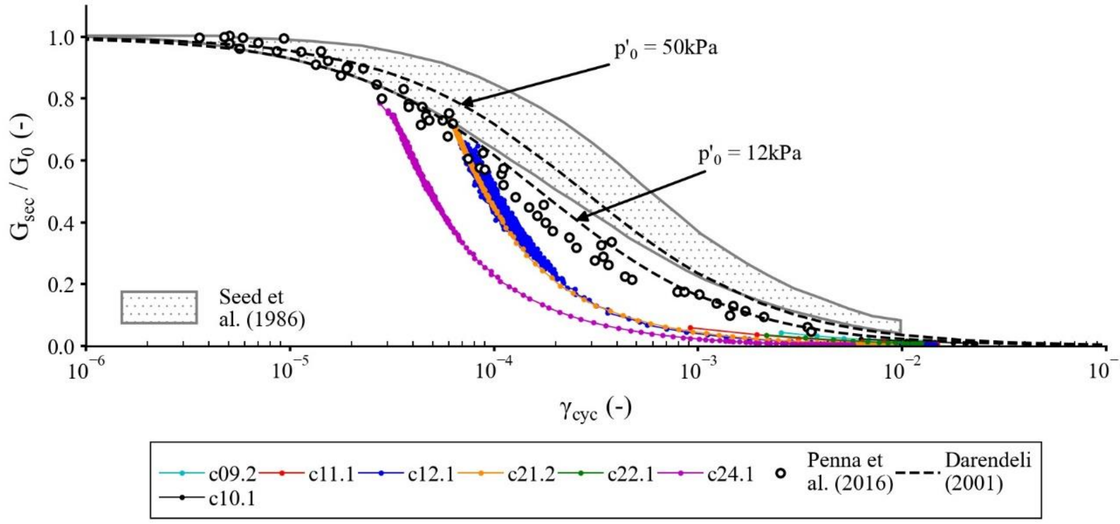

(b) -1.0 ≤ ζ_c < -0.5

Figure 7.18: Stiffness degradation curves

Figure 7.18 includes empirically determined stiffness degradation profiles for p' = 50 and 12 kN/m^2 using the equations proposed by Darendeli (2001), as well as the range of values found by Seed *et al*. (1986), following compilation of a large database of clean sand and gravel test data. Also included are the results of Penna *et al*. (2016), who undertook resonant column and torsional shear tests on samples of LBS-B sand at low mean effective stresses ($p'_0 \leq$ 10 kN/m^2). The results show that for $\gamma_{cyc} <$ 2x10^{-4}, the G_{sec} values associated with cycle 1 show good agreement with results from Penna *et al*. (2016), and the lower bound profile presented by Seed *et al*. (1986). The empirical curves proposed by (Darendeli, 2001) are found to generally overpredict G_{sec} at a given γ_{cyc}.

Furthermore, it is unfortunate that several of the tests were not permitted to continue cycling beyond $N=10^4$, as the results show that accumulated cyclic shear strains may have been close to exceeding γ_{tv}. Therefore, rather than specifying a target total number of cycles *a priori*, an improved test procedure would allow cycling to continue indefinitely, and assess, after some threshold number of cycles (e.g. n = 10,000) whether it is worthwhile (or financially feasible) to continue the test. This assessment should be based on real-time evaluations of both the magnitude and rate of increase of γ_{cyc} (or an equivalent ε_{cyc} for drained tests), and its proximity to the estimated γ_{tv} value.

7.5.4. MATERIAL DAMPING BEHAVIOUR

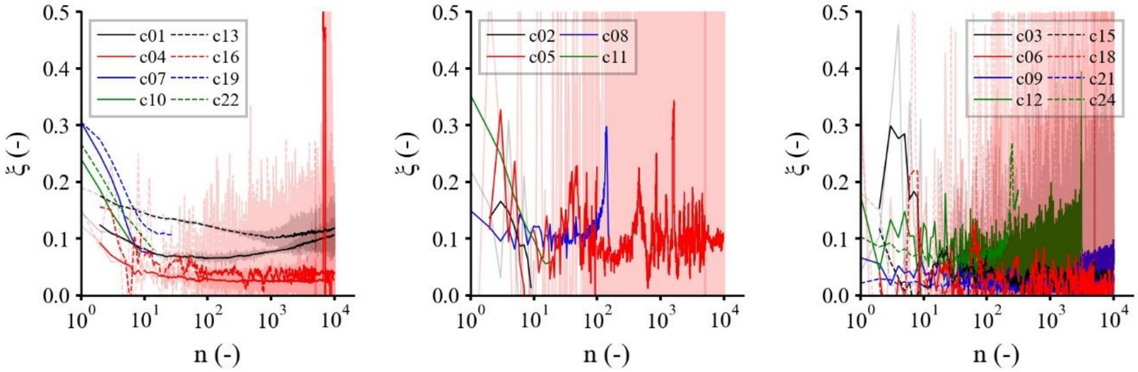

(a) ζ_b = 0.4 **(b) ζ_b = 0.2** **(c) ζ_b = 0.1**

Figure 7.19: Evolution of the energy loss factor, ξ, with cycle number, n

Figure 7.19 shows the evolution of the energy loss factor, ξ, with cycle number and shows that ξ is a function of both the type of cyclic loading (i.e. ζ_b and ζ_c), and the number of stress cycles. However, it is clear that the data suffers from substantial noise, particularly for lower ζ_b values, making reliable estimation of ξ difficult in some tests. Rascol (2009) suggests that there is a log scale difference between accurate measurements of G and ξ, and found that satisfactory estimates could only be obtained when $\gamma_{cyc} \geq 5.5\text{x}10^{-4}$.

Figure 7.20 presents material damping curves estimated from tests which underwent stress reversal (i.e. $\zeta_c \leq 0$), and thus mobilised relatively large cyclic shear stain amplitudes. Empirically determined curves (after Darendeli, 2001) for p' = 50 and 12 kN/m^2, and values obtained from the literature (Penna *et al*., 2016; Seed *et al*., 1986) are also included.

Figure 7.20 shows that the material damping response appears to be governed by the mobilised γ_{cyc} and whether it exceeds the cyclic volumetric threshold shear strain, γ_{tv} (see Section 5.2.3). Results show that when γ_{cyc} is less than approximately 10^{-4}, ξ does not increase greatly (except for c24) and remains relatively constant with cycle number. This is in agreement with findings in the literature (e.g. Dobry & Ladd, 1980; Dobry *et al*., 1982; Ladd *et al*., 1989) where γ_{tv} is found to be essentially 10^{-4}, regardless of confining stress, density and specimen fabric. This type of response where $\gamma_{tl} < \gamma_{cyc} < \gamma_{tv}$ (i.e. $10^{-5} < \gamma_{cyc} < 10^{-4}$), termed 'non-degraded hysteresis' behaviour by Ishihara (1996), is observed for tests c09 and c21 where $\zeta_b = 0.1$ in both cases.

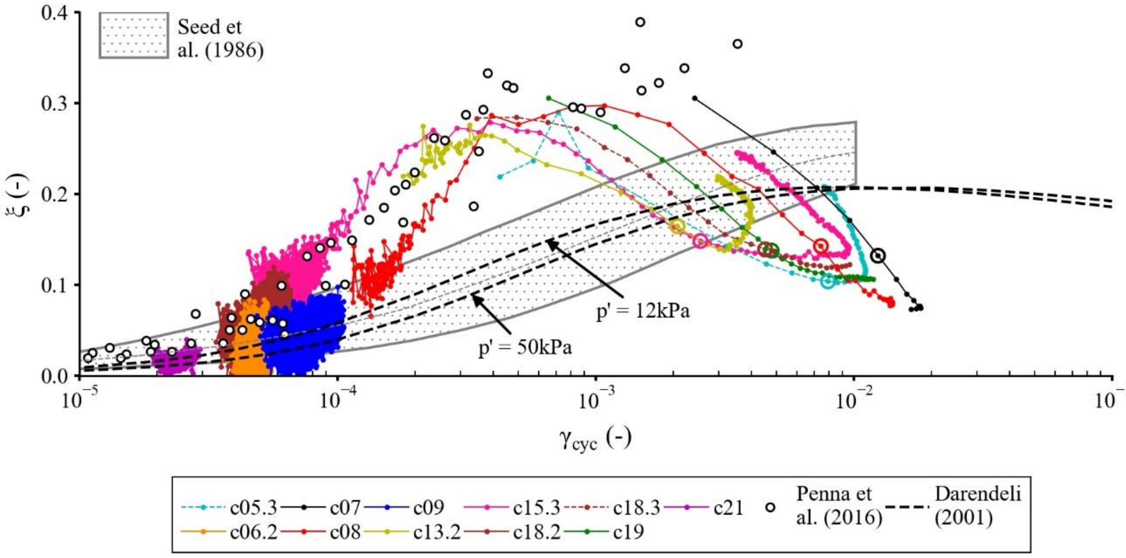

(a) -0.5 ≤ ζ_c < 0

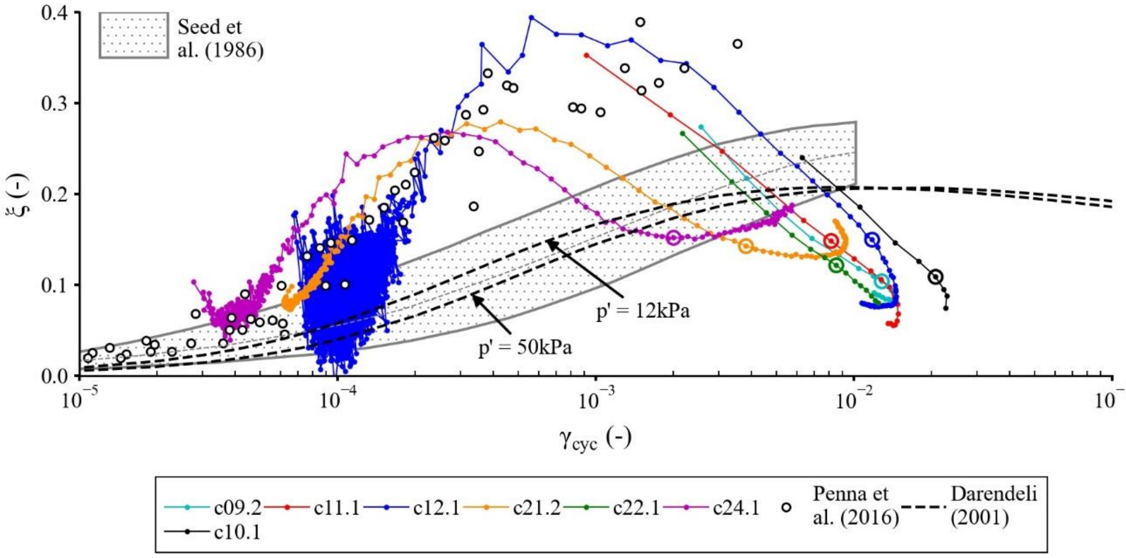

(b) -1.0 ≤ ζ_c < -0.5

Figure 7.20: Material damping curves from tests that underwent stress reversal

Figure 7.20 also shows that once γ_{tv} is exceeded (i.e. $10^{-4} < \gamma_{cyc} < 10^{-2}$), ξ tends to change considerably with both γ_{cyc} and cycle number due to changes in p' resulting from excess pore-water pressure development. ξ increases to a peak value of approximately 0.25 – 0.35 at $\gamma_{cyc} = 10^{-3}$, and then decreases with further stress cycles. The points at which R_u = 1.0 are circled on the plots, and show similar values of ξ = 0.1 – 0.15 at $n = N_L$. This type of response is termed “degraded hysteresis” behaviour by Ishihara (1996). Figure 7.20 also indicates the influence of $\sigma'_{c,0}$ on ξ. Comparison of tests with similar cyclic loading characteristics (in terms of ζ_b and ζ_c) but different $\sigma'_{c,0}$, show that tests undertaken at lower $\sigma'_{c,0}$ are typically shifted left, supporting the findings of Kokusho (1980).

Comparison of the results with the Darendeli (2001) and Seed *et al*. (1986) curves show that LBS-B mobilises significantly larger ξ values, in terms of both the gradient of the material damping curve and ξ_{max}. However, the results do show reasonably good agreement with Penna *et al*. (2016). Using empirical relationships and ranges found in the literature to estimate ξ for LBS-B are therefore not recommended, as they fail to capture the complex response observed in these tests. Similar conclusions were also given by Blaker & Andersen (2019) who found that ξ is significantly more influenced by the number of cycles than indicated by Seed *et al*. (1986), and tend to overestimate ξ at large cycle numbers. This is important, as overestimating ξ will have potentially significant consequences, particularly in fatigue analyses where the number of cycles can be very high.

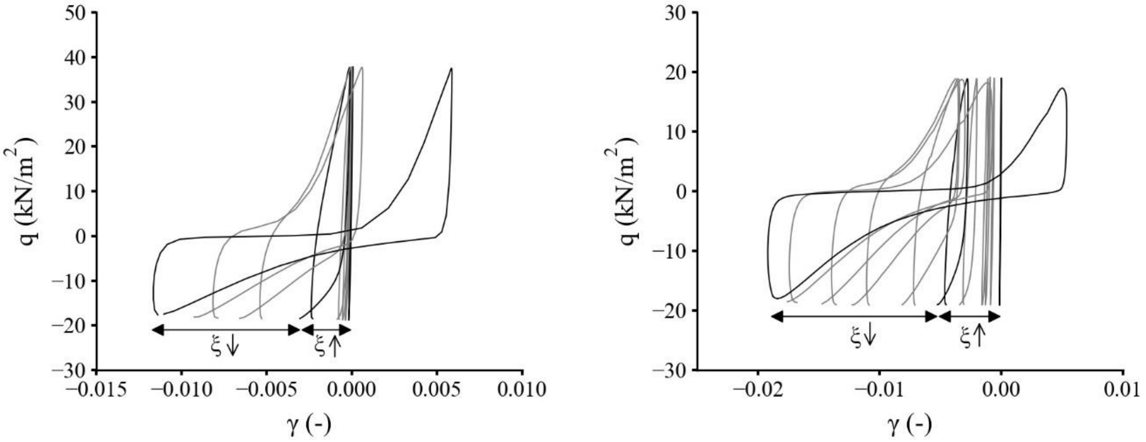

(a) c08 ***(b) c12***

Figure 7.21: Evolution of hyseresis loops for (a) test c08; and (b) test c12

The shape of the material damping curves may be explained by considering the changing shape of the hysteresis loop as the sample accumulates excess pore pressures and begins to dilate with cycle number. Figure 7.21 presents the evolution of the hysteresis loops for tests c08 and c12 for a select number of cycles, and shows that for the initial increase in ξ exhibited in Figure 7.20, the stress-strain curve remains relatively similar in terms of the shape of the hysteresis loop; however, the width of the loop tends to increase with increasing numbers of cycles up to ξ_{max}. As cycling continues, parts of the hysteresis loop become increasingly concave, and the central portion of the loop gets progressively wider. From Eq. (7-16) and Figure 7.4, ξ must therefore decrease as the maximum elastic energy, A_f, increases disproportionately to the enclosed area of the loop, ΔW.

7.6. CYCLIC CONTOUR DIAGRAMS

Contour diagrams represent a convenient way of combining and summarising the results of multiple cyclic triaxial tests, as well as providing a basis for practical foundation of offshore structures (Blaker & Andersen, 2019). The diagrams allow performance checks for stress conditions outside the range of measured laboratory data. Figure 7.22 present tentative contour diagrams for dense LBS-B in terms of pore pressure ratio, and cyclic shear strains, as functions of the cyclic shear stress, τ_{cyc}, and n. Results are normalised by the initial mean effective stress at the end of the drained ramp stage, p'_0. The contour diagrams are valid for stress-controlled cyclic loading with a constant shear stress amplitude and q_{av} / q_{ref} = 0 (i.e. two-way cyclic loading) only.

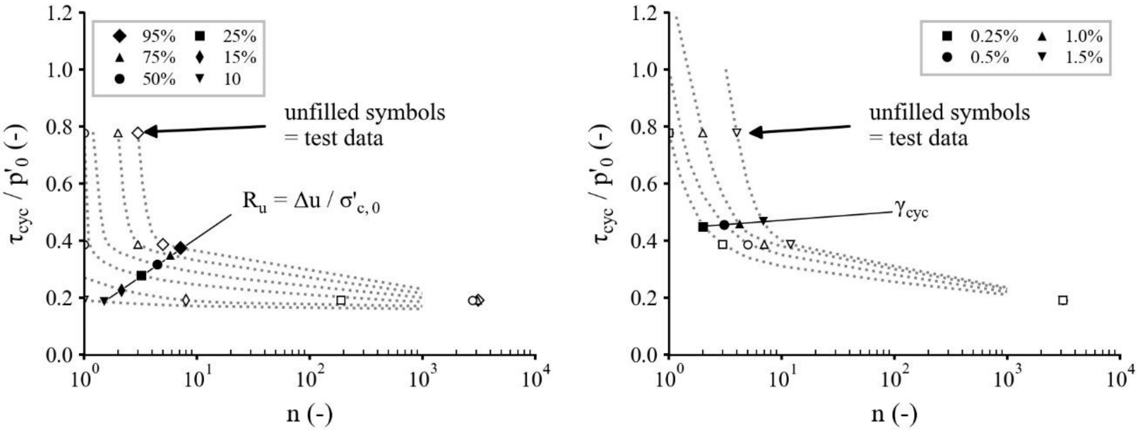

(a) $\boldsymbol{R_u}$ *(b)* $\boldsymbol{\gamma_{cyc}}$

Figure 7.22: Contours of (a) pore pressure ratio; and (b) cyclic shear strain

The contour diagrams enable R_u and cyclic strain values to be predicted for a sand of a given density after a certain number of cycles. The diagrams also show that very small strains (γ_{cyc} <0.25 %) are mobilised in tests with low cyclic stress ratios, (i.e. $\tau_{cyc} \; / \; p'_0$ < 0.2), and therefore represents the lower limit in terms of the cyclic load ratio that should be attempted using the cyclic triaxial apparatus if meaningful results are to be obtained.

When constructing diagrams for use in practical design situations, the average and cyclic shear stresses are often normalised with respect to a certain stress value, yielding the "average load ratio", ALR, and "cyclic load ratio", CLR, respectively (Nielsen *et al*., 2012). However, while the contour diagrams presented in Figure 7.22 are useful for predicting the cyclic response in terms of mobilised cyclic shear strain and pore pressure accumulation, Shajarati *et al*. (2012) found that contour diagrams that only consider CLR are insufficient for predicting the effects of cyclic loading in terms of bearing capacity, as they do not include the capture the influence of the ALR. Nielsen *et al*. (2012) also argue that using an effective stress parameter (e.g. $\sigma'_{c,0}$ or p'_0) to normalise cyclic and average shear stresses for use in design / contour diagrams is inappropriate for the undrained case, as pore pressure is not taken into account, and instead recommend the use of the undrained shear strength, s_u, as the normalising parameter. Such discussions are beyond the scope of this study, and have thus not been investigated further.

7.7. SUMMARY AND CONCLUSIONS

This chapter has presented the results of 20 undrained cyclic triaxial tests, undertaken on samples of dense (D_r ≈ 82 %) Leighton Buzzard sand at different initial effective confining pressures ($\sigma'_{c,0}$ = 50 and 12 kN/m^2). The stress cycles were applied from different initial average shear stresses (q_{av}), and with relatively low cyclic stress amplitudes (q_{cyc}) to investigate the cyclic response and explore the area of cyclic stress space considered appropriate for the design of offshore wind energy structures.

Tests were planned and presented as part of a new, robust cyclic framework, formulated to provide compatibility with pile-load test results. Together with the results from the monotonic stress path tests presented in Chapter 6, the cyclic tests presented in this chapter form the basis of an experimental database which may be used for the development, calibration, and verification of advanced constitutive models with a specific focus on cyclic loading.

The undrained cyclic triaxial tests with isotropic consolidation (i.e. no static bias, q_{av} = 0; and $\zeta_c = -1$) were all found to reach conditions of initial liquefaction (i.e. p' = 0), and show the butterfly-shaped effective stress path characteristic of cyclic mobility conditions. The number of stress cycles required to cause initial liquefaction was found to depend on the magnitude of ζ_b, which was shown to decrease with increasing ζ_b (and q_{cyc}).

Cyclic mobility was also observed in tests with some static bias but stress reversal (i.e. $q_{av} > 0$; ζ_c = -0.5); however, such tests were able to sustain a higher number of stress cycles before developing the characteristic butterfly shape, and in some cases (i.e. where ζ_b = 0.1) cyclic mobility / initial liquefaction was not observed even after the initial 10^4 cycles.

After initial liquefaction (p' = 0), the strain amplitudes were found to progressively increase with subsequent stress cycles. The accumulation of axial strain on the triaxial extension or compression side prevailed, depending on whether the main part of the stress path lay above or below the isotropic axis. Significant necking was often observed in the top third of the test specimen following initial liquefaction; therefore, tests were typically terminated before conventional, strain-based failure criteria were reached to safeguard the apparatus against damage. A pore pressure-based failure criterion was therefore adopted in this study.

For tests that did not cross the isotropic axis (i.e. $\zeta_c > 0$), initial liquefaction / cyclic mobility conditions were not reached after 10^4 cycles. The test specimens generally exhibited very stiff stress–strain behaviour under the imposed load cycling, with cyclic secant stiffnesses reducing only moderately as cycling continued. However, excess pore pressures and cyclic strains continued to accumulate with increasing numbers of cycles, even for relatively small cyclic stress amplitudes (e.g. ζ_b = 0.1). Furthermore, there is some limited data (tests c01 & c13) to support the findings of Wichtmann & Triantafyllidis (2016), who found that for dense samples with relatively large static bias and cyclic stress amplitudes, the effective stress path may exceed the failure envelope (and PTL) as determined from undrained monotonic tests.

Secant stiffness degradation profiles show good agreement with the trends reported in the literature (Penna *et al*., 2016), and may be reasonably predicted with the empirical relationship proposed by Darendeli (2001). However, comparison of material damping curves with both empirically determined and historical values finds that that LBS-B mobilises significantly larger ξ values, in terms of both the gradient of the material damping curve and ξ_{max}. Using empirical relationships and ranges found in the literature to estimate ξ for LBS-B are therefore not recommended, as they fail to capture the complex response observed in these tests.

The results presented in this chapter therefore exemplify the complexities of the material response when subjected to cyclic loading. However, the experiments showed clear and systematic trends, indicating that the cyclic response depends on a combination of both the average and cyclic shear stresses, and the stress path. These factors are adequately and robustly captured by the new cyclic framework adopted in this study. However, the test results have also highlighted some shortcomings with both the apparatus and testing procedure.

The initial effective cell pressure at the end of consolidation, $\sigma'_{c,0}$, has historically been used as a normalising parameter in undrained cyclic triaxial tests, and tests are often anisotropically consolidated to some initial average stress at a fixed effective cell pressure. This is not recommended as for cases other than isotopically consolidated, two-way loading tests (i.e. q_{av} = 0), anisotropic consolidation will generally result in p'_0 > $\sigma'_{c,0}$ due to the shape of the stress path in $p' - q$ space. Given that the number of cycles required to achieve some failure criterion is largely influenced by the proximity of the effective stress path to the undrained failure envelope, analysing the number of cycles to failure therefore becomes inconsistent (for tests with similar q_{cyc} and $\sigma'_{c,0}$ values, but different initial q_{av}) unless samples are anisotropically consolidated in such a way that p'_0 = $\sigma'_{c,0}$. To properly assess the influence of effective confining stress, it is therefore recommended that the role and significance of $\sigma'_{c,0}$ be demoted in favour of the more fundamental mean effective stress, p', when planning cyclic triaxial test programmes and normalising results.

The contour diagrams showed that for tests where the cyclic stress ratios, $\tau_{cyc}/p'_0 < 0.2$, both residual and cyclic shear strains were very small ($\gamma_N < 0.05$ % & $\gamma_{cyc} < 0.1$ %, respectively) even after 10^4 cycles. In terms of the cyclic stress space framework utilised in this study, these tests correspond to one-way loading with some static bias (i.e. $\zeta_c > 0$ and $q_{cyc} \leq q_{av}$), where stress and strain amplitudes were found to be close to or less than the resolution of the instrumentation utilised, particularly for low values of q_{cyc} (i.e. $\zeta_b \leq 0.2$). Results from these tests therefore suffered from excessive electrical noise, making reliable estimates of cyclic strains etc. very challenging, and thus represent the limits of the apparatus in its current state. Attempting further tests in this area of cyclic stress space is therefore not recommended without first improving the capabilities of the local strain instrumentation, and improving the temperature regulation control system in the laboratory.

Significant strain localisation / necking was observed following initial liquefaction, resulting in large displacements. However, it was noted that these displacements were typically located in the top third of the specimen – outside of the zone captured by the local strain instrumentation. The general quality and reliability of results may therefore be significantly improved by adopting a 1:1 ($H{:}D$) ratio sample size. Furthermore, this would enable tests to be sheared to larger cyclic strain magnitudes, enabling conventional strain-based failure criteria to be achieved.

Results showed that the cyclic volumetric threshold shear strain, γ_{tv}, is approximately $\gamma_{cyc} = 2\text{x}10^{-4}$, and thus in close agreement with values in the literature. The cyclic response changes significantly once this threshold is exceeded. However, several tests were found to be relatively close to this threshold after 10^4 cycles, but prevented from evolving further due to the software requirement of specifying a discrete number of cycles before commencing a test. It is therefore recommended that new, bespoke testing scripts be developed, that enable such flexibility and provide real-time estimates of key parameters such as γ_{cyc} and R_u.

8. CONSTITUTIVE MODELLING FRAMEWORKS

8.1. INTRODUCTION

This chapter presents an overview of constitutive models and their associated frameworks developed for cohesionless soils used in research and practice. A review of the various model types developed for sand and current state-of-the-art is provided, followed by a brief review of other modelling frameworks. Background material concerning the formulation and components of elastoplastic constitutive models based on conventional plasticity theory are included in Appendix A.

8.2. OVERVIEW OF SAND CONSTITUTIVE MODELS

Numerous constitutive models have been developed to describe the stress-strain behaviour of soils over the past several decades. For example, a Google Scholar search of “constitutive model sand” yields approximately 22,000 results! It would therefore be impractical to describe every model in detail. However, while an apparently vast number of constitutive models for sand exist, most tend to have been formulated (and further extended) within relatively few theoretical frameworks.

Lade (2005) presents a comprehensive review and evaluation of the various constitutive models and theoretical frameworks published in the literature. The following summarises and extends this work where necessary, by presenting a brief overview of notable models formulated within each of the popular theoretical frameworks. The models presented are also limited to those capable of capturing the behaviour of cohesionless soils, and subsequently evaluated using the ‘category scale’ proposed by Lade (2005), where:

- Category 1: Model is formulated within a (i) transparent and (ii) theoretically sound framework, that may (iii) be easily calibrated from (iv) conventional triaxial compression tests, isotropic compression tests, and conventional (i.e. incremental load) oedometer tests. The model must also (v) exhibit an overall high quality of fitting experimentally observed material behaviour, (vi) including confining stress effects, and (vii) be capable handling 3D stress conditions;
- Category 2: Model lacks one or more of the conditions mentioned above;
- Category 3: Model is deficient in several of the conditions mentioned above.

8.2.1. ELASTIC AND SIMPLE ELASTIC PERFECTLY PLASTIC MODELS

Early constitutive models were predominantly formulated using simple elastic and elastic perfectly plastic theory (e.g. the Hyperbolic model proposed by Duncan & Chang, 1970). Examples of simple elastic perfectly plastic models include the Drucker-Prager model (Drucker & Prager, 1952), traditional Mohr Coulomb based models (Brinkgreve & Vermeer, 1997; Smith & Griffiths, 2013), and the so-called ‘Cap’ models (DiMaggio & Sandler, 1971; Drucker *et al*., 1957).

According to Prévost (1985), Cap models once represented the most popular and widely used constitutive models for modelling sand. However, their inability to capture post-peak, strain softening behaviour, stress-induced anisotropy, and cyclic loading response, means their universal application is limited. As such, Lade (2005) classifies these models according to Categories 2 and 3.

8.2.2. CRITICAL STATE MODELS

The Critical State Soil Mechanics (CSSM) theoretical framework (Schofield & Wroth, 1968) underpins many popular constitutive models in use today. The ‘Clay And Sand Model’, or ‘CASM’ (Yu, 1998; Yu *et al*., 2005, 2007), and NorSand (Jefferies, 1993; Jefferies & Shuttle, 2005, 2011) represent critical state type models, reformulated in terms of the state parameter concept (Been & Jefferies, 1985). State parameter based models are attractive from a modelling point of view because the model parameters for a particular soil are independent of both void ratio and effective stress, with the model itself incorporating the effect of these factors on the predicted response.

According to Jefferies *et al*. (2015), NorSand is able to capture the full range of sand response, including static liquefaction of very loose soils through to dilation of very dense soils. Lade (2005) classifies NorSand according to Category 1, and there are several examples of its successful application in 3D boundary value problems (Jefferies & Been, 2015).

CASM is not included in Lade's (2005) review, but a review of the literature suggests that it may meet all the requirements of a Category 1 model. However, while the model has been successfully implemented in FEA software to solve 3D boundary value problems (Khong, 2004), its wider use in engineering practice appears to be relatively limited. Further investigation into the potential limitations of this model may therefore be beneficial, so that practical guidance in terms of its safe use and application may be determined.

8.2.3. MULTI SURFACE MODELLING CONCEPTS

Single yield surface, isotropic hardening models define the elastic domain using a single state boundary surface. While such models have been shown to offer reasonable stress-strain predictions for soils loaded monotonically, models of this type suffer from significant shortcomings when applied to more complex loading conditions. According to Yu (2006), these shortfalls are due to:

- The elastic domain is too large compared with experimental observations. Furthermore, the instantaneous change from elastic to plastic behaviour predicted by these models contrasts with the gradual transition in stiffness from elastic to plastic states exhibited in experiments;
- The isotropic hardening and early kinematic hardening models (Prager, 1955; Ziegler, 1959) are generally unable to capture the complex behaviour observed in experiments where soil is subjected to cyclic or repeated loading where large stress reversals frequently occur.

Improved hardening rules capable of modelling both cyclic behaviour and the smooth transition from elastic to plastic behaviour were therefore required. To date, the two most successful and widely used theories developed for this purpose are:

1. Multi surface plasticity theory, proposed by Mróz (1967) and Iwan (1966, 1967);
2. Bounding surface plasticity theory, proposed by Dafalias & Popov (1975) and Krieg (1975).

These concepts, collectively known as ‘multi-surface’ frameworks, were initially developed for metals but found application in modelling geomaterials. Notable examples for each type are:

8.2.3.1. Nested Surface Models

Prévost (1985) was the first to propose a nested surface, kinematic hardening model for cohesionless soil, and used Mróz's (1967) mapping rule. The original Prévost (1985) model used a conical (Drucker-Prager) yield surface in stress space with its apex at the origin, resulting in a circular cross section in the deviatoric plane, whose position is determined by the magnitude of the so-called ‘back stress, α. A purely deviatoric, kinematic hardening rule is adopted. The plastic potential is selected such that the deviatoric plastic flow is associative, while a non-associated flow rule is used for the dilational component.

Compared with bounding-surface models, research and development of nested surface type models for sandy soils is more limited. Elgamal *et al*. (2002, 2003) implemented the Prévost (1985) model with modified flow and hardening rules to better simulate the behaviour of dense saturated sand subjected to cyclic loading. Further extensions incorporating Lode angle effects were proposed by Zerfa & Loret (2003) and Yang & Elgamal (2008), who introduced rounded Mohr-Coulomb (Van Eekelen, 1980) and Lade-Duncan (Lade & Duncan, 1975) failure criteria, respectively. The Prévost (1985) model has also been successfully implemented in the finite element code LAGAMINE to model the behaviour of suction caissons installed in dense sands (Cerfontaine *et al*., 2016). However, Cerfontaine (2014) notes that implementation of the model is non-trivial, and observed progressive accumulation of errors when comparing model predictions with cyclic triaxial test results.

Identification of model parameters is relatively straightforward and may be determined from a single triaxial compression and extension test. However, model parameters tend to be calibrated for a specific sand state (void ratio and mean effective stress), though exceptions to this do exist such as the continuous hyperplasticity model presented by Houlsby & Mortara (2004). From a practical design perspective, this is potentially a significant shortcoming given the heterogeneity of in situ soils, and the need to model soil behaviour over a range of depths (and hence effective stress levels). For example, use of such models for large project sites such as offshore wind farms may be impractical due to the number of tests (and expense) required to adequately calibrate the model for all in situ states found on site.

8.2.3.2. Bounding Surface Models

Bounding-surface plasticity models are based on the principles of critical state soil mechanics, formulated within bounding surface plasticity theory, and are perhaps the most well established and researched advanced constitutive models for predicting sand behaviour.

The original two-surface model proposed by Manzari & Dafalias (1997) adopted a state parameter approach to define the peak and dilatancy stress ratios of sand. The model is formulated in a normalised deviatoric plane, using a deviatoric stress ratio tensor given by $\boldsymbol{r} = \boldsymbol{s}/p'$. The model assumes that the hardening modulus is a function of the current stress state and the relative distance of this state from an ‘image’ stress state, located on the bounding surface.

Several extensions to the Manzari & Dafalias (1997) model, collectively known as “SANISAND” (Simple ANIsotropic SAND) models, have since been developed (Dafalias & Manzari, 2004; Dafalias *et al*., 2004; Loukidis & Salgado, 2009; Taborda *et al*., 2014). According to Whyte (2019), the principal differences between these models is with respect to the definition of the hardening law. Dafalias *et al*. (2004) also incorporated a second-order fabric tensor to capture the inherent anisotropy observed in experimental tests.

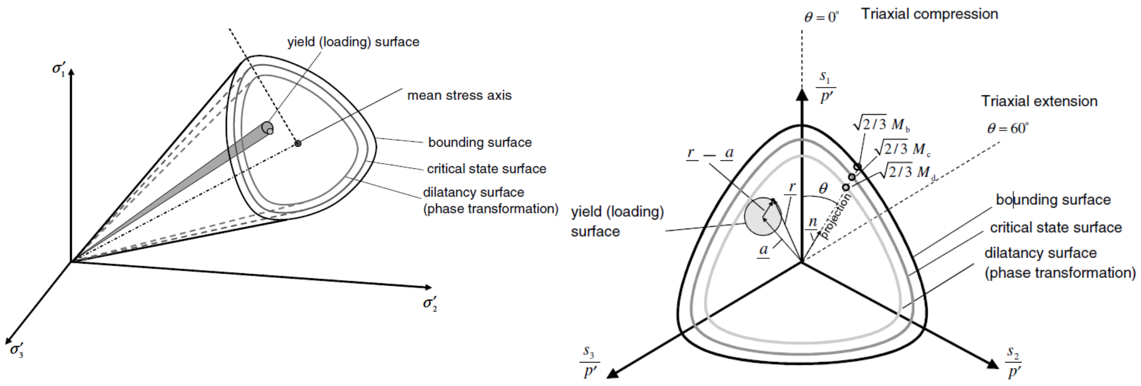

(a) ***(b)***

Figure 8.1: Components of bounding surface plasticity models (Loukidis & Salgado, 2009)

Figure 8.1 shows the key components of modern bounding surface plasticity models. The various surfaces control the evolution of the yield surface and plastic potential function during a strain increment. The evolution of the dilatancy and bounding surfaces is controlled by the state parameter, ψ, with each of them approaching the critical state surface as ψ approaches zero (Whyte, 2019).

Wichtmann *et al*. (2019) tested the performance of a bounding surface model (Dafalias & Manzari, 2004) against element tests, and found that the wedge-type open yield surface made it unable to capture oedometric behaviour. Wichtmann *et al*. (2019) concluded that the model is therefore unsuitable for use in boundary values problems where settlement is of interest. Furthermore, Wichtmann *et al*. (2019) found that while simulations were able to capture fairly well the cyclic mobility effect (see Section 5.2.5.3), the model was less successful at capturing the cyclic response when subjected to small amplitude cycles, and showed overshooting effects on some reloading paths.

Wichtmann *et al*. (2019) also noted that it was impossible to obtain a single set of parameters that delivered accurate simulations for both monotonic and cyclic loading, and found that to better reproduce monotonic test results led to a reduction of the predictive capabilities for cyclic loading.

8.2.4. HYPOPLASTICITY

The Hypoplasticity modelling framework was developed for modelling the response of granular media in terms of rational continuum mechanics. An extensive account of its development and formulation is provided Wu & Kolymbas (2000). The approach aims to model the inelastic behaviour of granular materials without using the manufactured components devised for traditional plasticity-based models (e.g. yield functions, plastic potentials, etc.). Furthermore, the approach does not decompose strains into elastic and plastic components, but rather recognises that inelastic deformations may occur from the very beginning of the loading process.

The attractive feature of hypoplasticity is its simplicity, and it has been adopted by several authors (Niemunis, 2005; von Wolffersdorff, 1996; Wichtmann *et al*., 2019). Hypoplastic models have also been successfully used in boundary value problems to predict the response of foundations subjected to both monotonic and cyclic loading (Fuentes *et al*., 2019; Thieken *et al*., 2014). However, Wichtmann *et al*. (2019) found that these models were also less successful at simulating the behaviour of sand subject to small amplitude cycles.

8.2.5. HYPERPLASTICITY

In the Hyperplasticity framework, the principles of thermodynamics play a central role. The framework originates from the work of Ziegler (1983), and has since been extensively developed by Prof. Houlsby at the University of Oxford as described in Houlsby & Puzrin (2006). The approach assumes that the constitutive behaviour of a dissipative material may be defined by two scalar potential functions: an energy function (either the Gibbs or Helmoholtz free energy); and a dissipation function.

A considerable advantage of adopting this approach is that there are well defined rules that allow for compact development of constitutive models that are guaranteed to obey the laws of thermodynamics. Furthermore, interpretation of this framework in terms of conventional plasticity theory demonstrates that similar yield surfaces, flow and hardening rules are all incorporated within these two scalar potential functions.

8.3. REVIEW

Constitutive modelling provides an understanding of the stress-strain response of soils, based on an appropriate framework derived from mechanics. Modern design approaches are also increasingly requiring the use of detailed 3D finite element analyses (FEA) to enable more accurate predictions of the soil-structure response (e.g. Burd *et al.*, 2019; Byrne *et al.*, 2019). The choice of an appropriate constitutive model is therefore critically important if reliable predictions are to be made.

Several authors have attempted to categorise constitutive models based on their predictive capability and general complexity (Kolymbas, 2000; Muir Wood, 1991). The following is based on the hierarchy adopted by Whyte (2019):

BASIC MODELS:

- Simplistic but very robust;
- Generally provide a poor prediction of the overall constitutive response;
- Examples are linear elastic perfectly plastic Tresca or Mohr-Coulomb models.

ENGINEER DESIGN MODELS:

- Improved predictive capability over basic models
- Additional modelling features incorporated within the constitutive model, which engineers, using their judgement, consider to be needed for the design application;
- Models have been validated by simulating foundation boundary value problems accurately (i.e. prediction compared to foundation load tests) and are suitably robust to be used for design FEA).
- Examples include Modified Cam Clay (Roscoe & Burland, 1968), HSSmall (Plaxis, 2018)

PHILOSOPHER MODELS:

- Mathematically complex models which aim to accurately capture the soil response;
- Implementation of models is an extensive task due to model mathematical complexity;

- Models typically not fully validated, with most publications focusing on single element response, and little evidence in the literature of the model's predictive performance or numerical robustness in (for example) analysis of foundations.

Constitutive models available within commercial FEA packages (e.g Abaqus, Plaxis) typically fall within the *Basic* and *Engineer Design Models* defined above. Whyte (2019) suggests that such models are unlikely to be suitable for modelling the behaviour of dense sand subjected to undrained and/or cyclic loading. For example, while the HSSmall (Plaxis, 2018) and Mohr-Coulomb models may adequately capture the response of loose to medium dense sands that exhibit entirely contractive behaviour, for dense (dilative) sands, such models would typically predict an infinite undrained shear strength due to the use of a fixed (non-zero) dilation angle as one of the model parameters.

Such models may therefore lead to unconservative predictions of the stress-strain response if not appropriately calibrated. Dilatancy 'cut-offs' may be added to prevent unrealistic dilative behaviour; however, for undrained conditions, such cut-offs would not be activated given that they are typically defined in terms of some value of void ratio (e.g. at critical state).

The multi-surface plasticity models offer improved versatility and flexibility for predicting the behaviour of sands subjected to complex loading. At the time of their inception, the computational effort and impractical storage requirements associated with nested surface models resulted in limited development. Conversely, the comparatively cheap (computationally) bounding-surface plasticity models have since undergone considerable development, and are generally considered to represent the current state-of-the-art for modelling sand behaviour (Taborda *et al*., 2019). However, for high-cycle, repeated loading situations (e.g. modelling OWT foundations), Niemunis *et al*. (2005) argue that such frameworks are unsuitable as the requirement for every cycle to be modelled individually leads to both an accumulation of significant errors, and excessively long computation times.

Furthermore, despite the powerful predictive behaviour and oft-cited (by the model developers) 'simplicity' of advanced models, their uptake in the wider geotechnical engineering community appears to be limited. Whyte (2019) undertook a high level review of all constitutive models presented at a recent offshore geotechnical engineering conference (ISFOG 2015), and found that of the 197 papers presented, approximately 30 % (58) involved FEA, of which only 17 % (five) described the use of advanced constitutive models.

Philosopher models have also been considered unsuitable for practical design FEA due to difficulty in implementation, lack of model validation, high computational cost, and lack of robustness under the range of stress paths experienced in boundary value problems (Whyte, 2019). According to Scott (1989), there has also been an undesirable trend in the area of constitutive modelling to increase the number of model parameters, with some models now having as many as 40 material parameters. The large number of parameters, often only determinable from complex laboratory test programmes, therefore make such models hard to apply to practical problems. However, Lade (2005) argues that increasing the number of model parameters is necessary if flexible models, that capture multiple behavioural features, are required. Lade (2005) also suggests that the determination of model parameters represents a small effort compared to the effort and expense involved in obtaining the experimental results.

8.4. CONCLUSION

To satisfy design certification bodies (e.g. DNV), designers must often demonstrate that realistic foundation performance predictions have been made. Predictions made with relatively simple (*Basic*), single surface, isotropic hardening models are unable to capture many important features of sand behaviour under complex loading, and are therefore of limited use in practical design situations. More advanced (i.e. *Philosopher*) constitutive models, implemented within commercial FEA packages, are therefore likely to become increasingly necessary.

The practical use of some advanced constitutive models in design situations has been reviewed. Nested-surface kinematic hardening models (e.g. Houlsby & Mortara, 2004; Prévost, 1985) are identified as powerful constitutive models that are capable of capturing the important features of sand subjected to both monotonic and cyclic loading. However, their development and use in commercial 3D FEA packages has been relatively limited. In addition to the difficulties associated with the implementation of such models (Cerfontaine, 2014), the lack of high-quality experimental test data required for calibration is considered to be a contributing factor associated with their limited development. A secondary aim of the element test programme undertaken in Chapter 6 is therefore to provide a set of triaxial compression and extension tests at different stress states, which may be used by future researchers to calibrate and develop nested-surface kinematic hardening models.

The CASM and NorSand models are identified as representing potentially promising constitutive models based on their ease of calibration, implementation, and predictive capability. The ability of these models to capture the important features of dense sand behaviour is further investigated in Chapter 9, where single element simulations are compared against real monotonic and cyclic test data. Two sophisticated constitutive models – a multi-surface bounding plasticity model (Dafalias & Manzari, 2004), and a nested surface kinematic hardening model (Houlsby & Mortara, 2004) – considered to represent the current state-of-the-art for modelling sand behaviour, are also selected for evaluation.

9. NUMERICAL MODELLING

9.1. INTRODUCTION

The purpose of this chapter is to evaluate the ease of calibration and performance of some advanced constitutive models for sand using single element simulations. Two constitutive models (CASM (Yu *et al*., 2007) and NorSand (Jefferies *et al*., 2015)) have been implemented using the Python (version 3) programming language. While a more straightforward 'triaxial variables' formulation is often adopted in research for developing constitutive models, the general stress space implementation has been adopted here. This approach was adopted to provide increased flexibility, and enable further model evaluation (e.g. in 3D boundary value problems) in the future. Further detail associated with the implementation of elastoplastic constitutive models in general stress space is provided in Appendix A.

These models were selected for implementation following the review of constitutive models presented in Chapter 8, and their perceived ability to capture important features of sand behaviour. Two sophisticated, state-dependent constitutive models, considered to represent the state-of-the-art in terms of predictive capability for modelling sand behaviour, are also examined:

- SANISAND: a state parameter bounding-surface plasticity model (Dafalias & Manzari, 2004);
- HySand: a multi-surface, 'continuous hyperplasticity' model (Houlsby & Mortara, 2004).

The evaluation presented herein therefore aims to provide an assessment of the various types of constitutive models, and yield practical recommendations for their use in the analysis and design of foundations. The chapter consists of five parts:

- First, the additional tests required to calibrate the model-specific parameters are presented, with a particular focus on identifying the critical state line for LBS-B;
- Detailed descriptions of the CASM and NorSand formulations are then provided, followed by calibration of model parameters. The SANISAND and HySand models are then introduced, and model parameters determined;

- Numerical integration techniques commonly used for implementing numerical models are briefly reviewed, and an appropriate integration scheme selected. The Python implementation is then validated against CASM and NorSand simulations published in the literature;
- Single element, monotonic and cyclic triaxial model simulations for a range of initial states and drainage conditions are then presented, and compared with experimental test results excluded from the calibration procedure;
- Finally, the performance of the models in terms of their predictive capability and ease of calibration is critically assessed, and recommendations are provided.

9.2. MODEL CALIBRATION TESTS

Modern constitutive models for sand are typically formulated in terms of the state parameter, ψ, and therefore require the critical state line (CSL) to be accurately determined. Table 9.1 presents the test schedule undertaken to determine the CSL, and the additional model parameters required to calibrate the constitutive models considered in this study. Tests were undertaken using the procedures and reconstitution techniques described in Section 4.7.

Table 9.1: Model calibration testing schedule

test ID (-)	e_0[1] (-)	D_r[1] (%)	p'_0[1] (kN/m^2)	**test type** (-)	**prep. method**[2] (-)	**purpose** (-)
m01	0.781	12.2	300.0	CIUc	MT	CSL
m02	0.754	21.7	346.7	CIUc	MT	CSL
m03	0.726	31.7	396.9	CIUc	MT	CSL
m04	0.754	21.7	299.0	CIDc	MT	CSL
m07	0.739	27.1	596.4	CIUc	MT	CSL
m08	0.770	16.0	247.0	CIUc	MT	CSL
m09	0.694	42.9	49.0	CIDc	WP	M_{tc}, χ_{tc}
m10	0.667	52.6	48.3	CIDc	WP	M_{tc}, χ_{tc}
m11	0.636	63.5	49.2	CIDc	WP	M_{tc}, χ_{tc}
m12	0.614	71.2	48.9	CIDc	WP	M_{tc}, χ_{tc}

Notes:
1. Represents initial values at the start of the shearing phase
2. MT = moist tamping (undercompaction); WP = wet pluviation

9.2.1. CRITICAL STATE LINE

The strategy used to determine the CSL is based on the recommendations given in Jefferies & Been (2015), in which a series of CIUc tests are performed on samples that are markedly looser than the critical state. As discussed in Chapter 4, CIDc tests on dense samples are generally poorly suited for determining the CSL as they have a tendency to form shear bands/zones of strain localisation, and thus tend to underpredict critical state void ratios, e_{cs}. However, researchers have continued to determine CSLs from dense CIDc tests (Zdravković *et al.*, 2019) despite these known shortcomings, and this may result in relatively poor FEA predictions of a laterally loaded pile as part of a 3D boundary value problem (Taborda *et al.*, 2019).

Zdravković *et al.* (2019) justified the use of using exclusively dense CIDc tests by stating that their experimental programme was focussed on characterising the constitutive behaviour of samples at conditions representative of those found in the field. Samples were therefore reconstituted using the wet pluviation technique to representative in situ densities and stresses – as is conventional when scheduling a laboratory test programme in academic research or industry practice. However, with the advent of new, FEA focussed design methods (e.g. Burd *et al.*, 2019; Byrne *et al.*, 2019), this convention is no longer considered appropriate, given the influence of the position of the CSL on predicted soil response. Instead, when it is known that an advanced, state parameter based constitutive model is to be adopted for design, the primary focus of the laboratory testing campaign should focus more on accurately defining the location of the CSL.

As discussed in Section 3.7, the wet pluviation and slurry deposition sample reconstitution methods are able to produce samples that exhibit similar constitutive responses to undisturbed specimens when sheared in the triaxial apparatus (Ghionna & Porcino, 2006). However, a significant shortcoming of these techniques is that they are unable to produce the loose samples (e.g. D_r < 40 %) that are required for easier and more reliable determination of the CSL. A modified undercompaction/moist tamping technique was therefore adopted when necessary (described by Jefferies & Been, 2015), as this method allows for very loose specimens to be produced.

Figure 9.1 presents the results of the 5 CIUc tests outlined in Table 9.1. The stress-strain profiles show that in spite of relatively loose initial densities being achieved, none of the tests exhibits the easily recognisable critical state behaviour illustrated in Figure 5.5f. Instead all tests show the quasi-steady state (QSS) condition described in Section 5.1.7, followed by continuous dilation to high strengths at large mean effective stresses (shown in Figure 5.5e).

The critical friction ratio for triaxial compression conditions, M_{tc}, is typically determined from either multiple CIDc tests on samples with varying density (Bishop, 1966), or from one or more triaxial compression tests on loose samples. Figure 9.1c shows that the critical stress ratio for LBS-B may range between 1.22 and 1.33. However, despite shearing to large strains, all stress-strain profiles fail to plateau (or collapse), suggesting that critical state conditions may not have been achieved. Furthermore, shearing beyond ε_q > 30 % is problematic in terms of the displacement limits of common laboratory apparatus, and estimates of stress become increasingly unreliable due to the distorted shape and applied area correction.

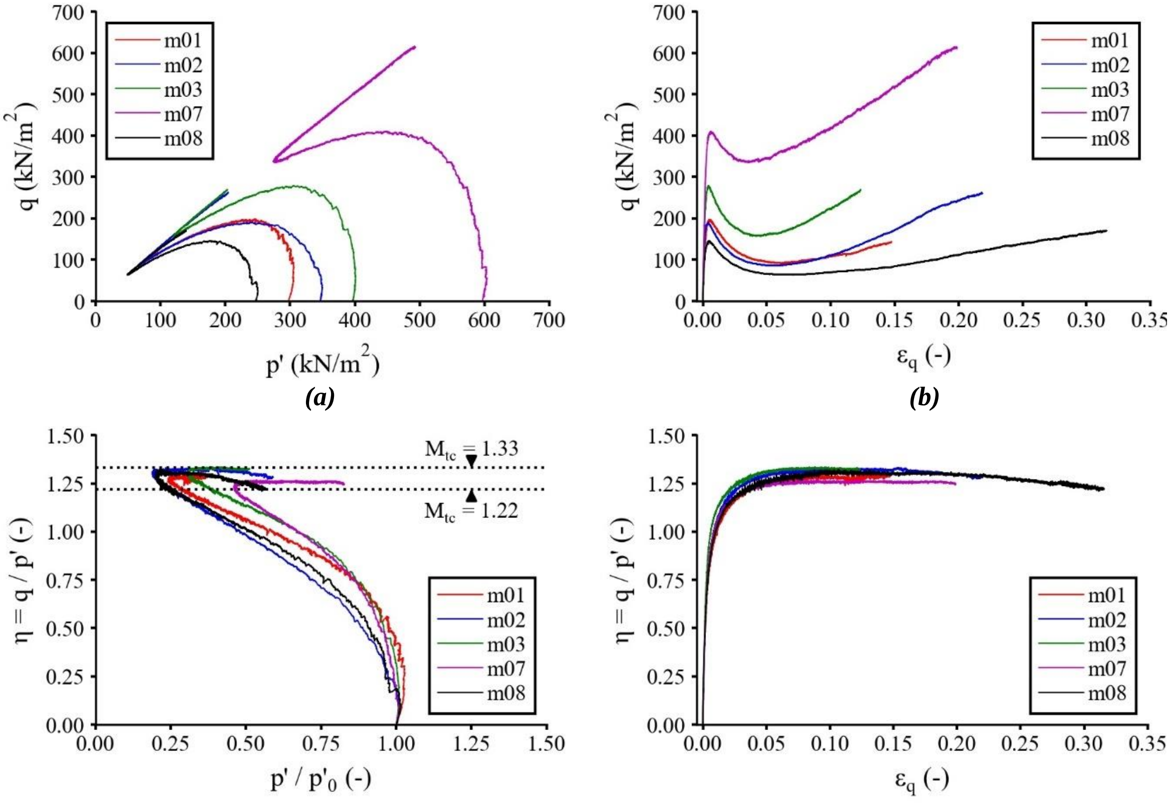

(a) *(b)*

(c) *(d)*

Figure 9.1: Summary of CIUc stress paths and stress-strain behaviour

To determine M_{tc}, the method proposed by Bishop (1966) has been used. Figure 9.2 presents the results of a series of drained triaxial compression tests undertaken at various relative densities ($D_r \approx$ 40 to 70 %), and $\sigma'_{c,0}$ = 50 kN/m^2. Figure 9.2b shows each test reduced to a value of measured peak dilatancy, D_{min}, at peak strength, η_{max}. Projecting the result to zero dilation therefore indicates M_{tc} = 1.31 for LBS-B. Both methods therefore show good agreement with the typical range for quartz sands of 1.2 – 1.35 given by Jefferies & Been (2015).

Accurate estimation of the initial void ratio (immediately prior to shearing) is also essential if the CSL is to be determined reliably, and requires the void ratio to be tracked as it evolves through every test stage. This is not done in routine commercial testing, as it is normally assumed that volumetric strains occurring during the saturation stages are negligible. While this may be reasonable for dense samples, this was found to be a poor assumption for very loose samples (i.e. D_r < 25 %) reconstituted using the moist tamping / undercompaction method, which required very low (<10 %) initial moisture contents to achieve the desired densities.

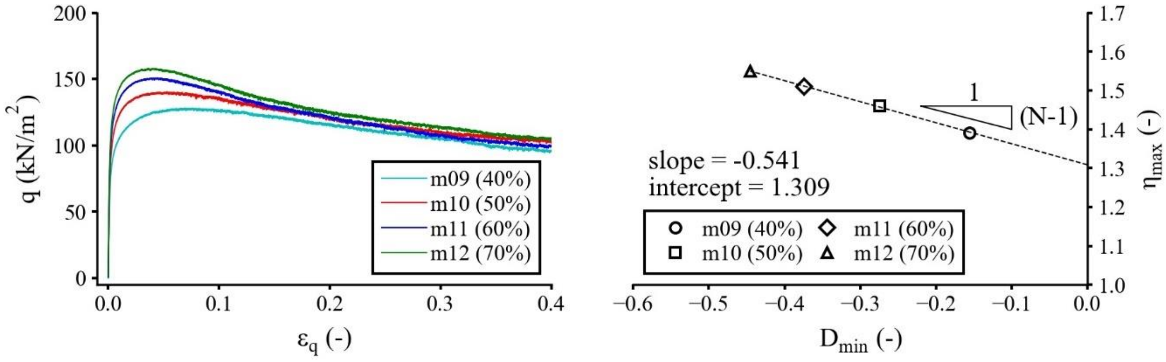

(a) *(b)*

Figure 9.2: (a) Triaxial compression stress-strain curves for LBS-B for various densities undertaken at σ'_c = 50kN/m^2; and (b) relation between peak strength, η_{max}, and peak dilatancy rate, D_{min}.

As a result, additional effort is required to ensure complete saturation of the sample (e.g. longer CO_2 and water flushing periods, higher back pressures), and large volume changes were measured by the volume change measurement instrumentation (APCs) during these stages. However, the large volume changes measured by the APC are thought to be due to the relatively high air content present in the sample following deposition, despite best efforts to remove it by extended CO_2 and de-aired water flushing stages. An additional volume of water must therefore be transferred into the sample to fill these air voids as they compress and dissolve into solution during the saturation ramp.

Estimates of sample volumetric strain and associated void ratio changes based on APC measurements during the saturation stage are therefore unlikely to be reliable. Furthermore, the APCs are isolated during CO_2 flushing, and then used to flush de-aired water through the sample, meaning that any changes in void ratio that occur during these periods are not captured by the external volume change instrumentation.

Sample volume changes may be estimated during saturation stages from cell volume measurements; however, this method requires the cell to be calibrated so that corrections can be made to the measured cell volume for creep/expansion of the cell and for piston movements. The method also relies on the cell being completely free from air, which is difficult to achieve in practice.

Several authors have also recommended end-of-test soil freezing to verify void ratio estimates (Jefferies & Been, 2015; Sladen & Handford, 1987). A recent laboratory testing ‘round robin’ conducted by Reid (2019) to assess how reliably the CSL of sandy silt tailings could be determined, found that of the 15 testing laboratories taking part, those that used both enlarged, lubricated end platens, and end-of-test soil freezing for void ratio measurement produced the most consistent CSLs.

However, end-of-test soil freezing requires modification to the triaxial apparatus, and also cannot be used if the platens incorporate electronic equipment such as bender elements. Soil freezing techniques were therefore not pursued in this project, though it is recognised that reliable void ratio estimates are arguably more important than the ability to undertake bender element tests, if the primary purpose of the test is for determining the location of the CSL.

Table 9.2: Summary of CSL parameters determined for LBS-B

CSL type:	semi log	power function
$\boldsymbol{e_\Gamma}$ **[-]:**	0.950*	0.815^
$\boldsymbol{\lambda}$ **[-]:**	0.035	0.03
$\boldsymbol{\xi}$ **[-]:**	-	0.62
$\boldsymbol{p'_{ref}}$ **[kN/m2]:**	101.3	101.3

Notes:
* void ratio at p'_{ref}
^ void ratio at p' = 0 kN/m^2

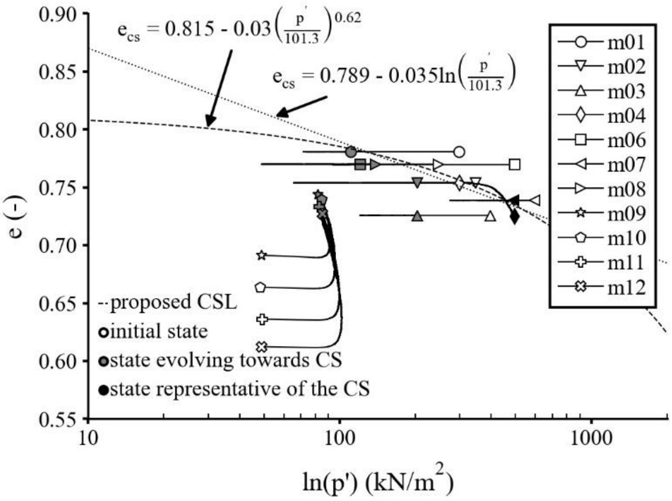

Figure 9.3: Critical stale line proposed for LBS-B

To overcome these issues, local strain instrumentation was used to estimate sample volumetric strains and track the evolution of void ratio throughout the various saturation stages. Figure 9.3 shows the evolution of soil state in $e - \ln(p')$ space during the 10 triaxial compression tests. Red-filled markers denote cases where the state of the soil was continuing to evolve at the end of the test, or where the development of shear bands has led to an assumed underprediction of the critical state void ratio, e_{cs} (i.e. in drained tests). Both a semi-log and curved CSL based on a power law (e.g. Li *et al*., 1999) have been fitted to the data and the parameters are summarised in Table 9.2, such that:

power law: $$e_{cs} = 0.815 - 0.03\left(p'/p'_{ref}\right)^{0.62} \tag{9-1}$$

semi log: $$e_{cs} = 0.789 - 0.035\ln\left(p'/p'_{ref}\right) \tag{9-2}$$

The above relationships are valid for p' < 1 MN/m^2. To validate the shape of the CSL at larger stresses requires high-pressure triaxial apparatus and is beyond the capabilities of the apparatus.

Stroud (1971) also proposed a CSL for LBS 14/25, based on results of simple shear tests. However, Stroud presents the data in terms of the MIT effective stress variable, s', where:

$$s' = \frac{(\sigma'_1 + \sigma'_3)}{2} \tag{9-3}$$

Figure 9.4 shows that the data presented by Stroud (1971) tends to lie above the results obtained in this study.

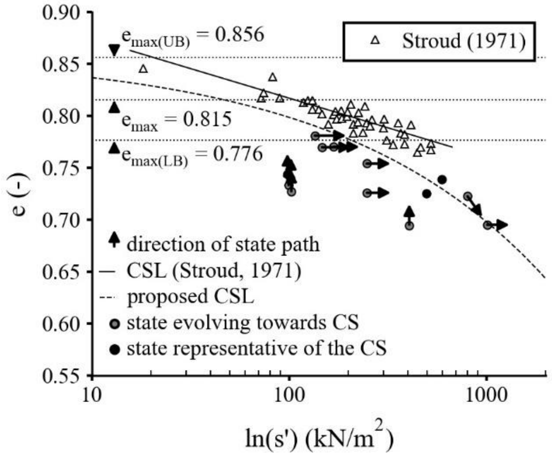

Figure 9.4: Comparison with results and CSL presented by Stroud (1971)

Figure 9.4 also shows the maximum void ratio value, e_{max}, adopted in this study (e_{max}= 0.815), as well as the upper and lower bounds given by Lunne *et al*. (2019) for LBS 14/25. Figure 9.4 shows that many of Stroud's tests mobilise e_{cs} values that are greater than the e_{max} = 0.790 value adopted in his study, which is at odds with Coop (1999), who proposed that the void ratio must tend towards its maximum value (i.e. e_{max}) as p' tends towards zero. This issue further emphasises the need for consistent, robust, and universally accepted limiting density tests for sands.

9.3. NUMERICAL IMPLEMENTATION

Appendix A presents definitions for the various stress and strain invariants required to formulate and implement isotropic elastoplastic constitutive models in general stress space. Implementation of constitutive models involves solving the constitutive equation:

$$\Delta\boldsymbol{\sigma} = \boldsymbol{D}^{ep}\Delta\boldsymbol{\varepsilon} \tag{9-4}$$

where:

$\Delta\boldsymbol{\sigma}$ = increment of the stress tensor
$\boldsymbol{D}^{ep}$ = elastoplastic stiffness matrix
$\Delta\boldsymbol{\varepsilon}$ = increment of the total strain tensor

The numerical integration technique used to determine the updated stress state is known as the stress point algorithm, and can have a significant influence on the accuracy of the computed response. Several numerical techniques are available for implementing non-linear constitutive models in finite element analysis (FEA) packages, the most popular being the tangent stiffness method (Britto & Gunn, 1987), the viscoplastic method (Shuttle, 2004), and the modified Newton Raphson method (Potts, 2003). All methods involve applying boundary conditions incrementally. However, Potts (2003) argued that the tangent stiffness and the viscoplastic approaches are sensitive to increment size, and can lead to inaccurate predictions unless sufficiently small solution increments are adopted.

Potts (2003) shows the modified Newton-Raphson scheme to be a robust and economical means of solving non-linear constitutive equations. It may be used with both explicit and implicit integration schemes, such as the ‘substepping’ (explicit) (Sloan, 1987) and ‘return mapping’ (implicit) stress point algorithms (Borja & Lee, 1990; Ortiz & Simo, 1986). Potts & Ganendra (1994) compared the two approaches and concluded that the substepping approach typically yields more accurate solutions than those based on the return mapping algorithm. Furthermore, implementation of return mapping algorithms is non-trivial for all but the simplest of soil models (Potts & Zdravkovic, 1999; Sloan *et al*., 2001; Zhao *et al*., 2005) given the complex mathematics involved.

Conversely, explicit schemes employ the standard elastoplastic constitutive law and require only first derivatives of the yield function and plastic potential. They can therefore be used as a general purpose integrator for a wide range of models. The automatic substepping stress point algorithms described by Sloan (1987) integrate the constitutive equation by dividing the strain increment, $\Delta\boldsymbol{\varepsilon}$, into smaller strain sub-increments. The error in the integration process is controlled by automatically adjusting the size of each sub-increment, or ‘substep’ using a modified Euler or Runge-Kutta-

Dormand-Prince approach. The number of substeps used is a function of the error tolerance specified, the magnitude of the imposed strain increment, and the non-linearity of the constitutive relations.

The explicit Runge-Kutta-Dormand-Prince scheme is similar to the modified Euler scheme, but uses a pair of fourth and fifth order integration formulae to perform the integration (Sloan & Booker, 1992). This higher order algorithm yields very accurate results and seldom needs correcting back to the yield surface to satisfy prescribed tolerances. Whyte (2019) adopted this method and noted that despite being computationally slower than the modified Euler approach, it was found to be more robust when implemented into 3D FEA boundary value problems. However, the higher order scheme is not considered necessary, as the modified Euler scheme is well suited to applications requiring moderate accuracy, and is the method of choice for most practical analyses (Sloan *et al*., 2001).

9.3.1. MODIFIED EULER SUBSTEPPING SCHEME WITH ERROR CONTROL

The explicit substepping scheme implemented in this thesis therefore uses the Modified Euler approach, with further enhancements for computing the yield surface intersection point, and restoring the updated stress state to the yield surface as described by Sloan *et al*. (2001). The stress point algorithm has been implemented in general (3D) stress space within a single element driver to compare the performance of the constitutive models with the behaviour observed in triaxial tests subjected to various stress boundary conditions. The numerical algorithms used to integrate the constitutive equation (Eq. (9-9)) for drained and undrained conditions are briefly described below.

UNDRAINED TRIAXIAL TEST SIMULATIONS

For undrained triaxial test conditions, $\delta\varepsilon_p = 0$, therefore the constitutive equation (Eq. (9-9)) may be solved by applying a known increment of total strain, $\delta\boldsymbol{\varepsilon}$, as described in the following:

1. Specify an increment of total axial strain, $\delta\varepsilon_z$, to be applied in the current step;
    - For undrained triaxial test conditions: $\gamma_{xy} = \gamma_{yz} = \gamma_{zx} = 0$ and $\delta\varepsilon_p = 0$; therefore $\delta\varepsilon_x = \delta\varepsilon_y = -0.5\delta\varepsilon_z$;
2. Initialise state variables (e.g. $\boldsymbol{\sigma_0}, A_0, p_0', e_0, K, G, \psi$ etc.);
3. Enter the stress update algorithm with the current stress state, $\boldsymbol{\sigma}$, hardening modulus, A, and specified increment of total strain, $\delta\boldsymbol{\varepsilon}$;

4. Solve the constitutive equation using the explicit modified Euler algorithm with automatic substepping and error control procedure described by Sloan *et al*. (2001) to obtain the updated stress state, $\boldsymbol{\sigma}$, and hardening modulus, A, at the end of the current strain increment;
5. Update state variables for new stress state;
6. Repeat steps 3 to 5 for the next increment of total strain.

DRAINED TRIAXIAL TEST SIMULATIONS

For drained triaxial conditions, the radial stresses (σ_x and σ_y) remain constant throughout the test; therefore $\delta\sigma_x = \delta\sigma_y = 0$. As for the undrained case, the calculations are 'strain controlled' and commenced by specifying an increment of total axial strain, $\delta\varepsilon_z$. However, the radial strain increments, ($\delta\varepsilon_x$ and $\delta\varepsilon_y$) are unknown as $\delta\varepsilon_p \neq 0$; and vary with each applied increment of total strain, $\delta\boldsymbol{\varepsilon}$. $\delta\varepsilon_x$ and $\delta\varepsilon_y$ values were therefore computed using an iterative procedure, such that test boundary conditions ($\delta\sigma_x = \delta\sigma_y = 0$) were satisfied at the end of each stress update calculation:

1. Initialise state variables (e.g. $\boldsymbol{\sigma_0}, A_0, p_0', e_0, K, G, \psi$ etc.);
2. Specify an increment of total axial strain, $\delta\varepsilon_z$, to be applied in the current step;
    - For initial stress update calculation, adopt $\delta\varepsilon_x = \delta\varepsilon_y = -0.5\delta\varepsilon_z$, (and $\gamma_{xy} = \gamma_{yz} = \gamma_{zx} = 0$);
3. Enter the stress update algorithm with the current stress state, $\boldsymbol{\sigma}$, hardening modulus, A, and specified increment of total strain, $\delta\boldsymbol{\varepsilon}$;
4. Solve the constitutive equation using the explicit modified Euler algorithm with automatic substepping and error control procedure described by Sloan *et al*. (2001) to obtain trial values of the updated stress state, $\boldsymbol{\sigma_{trial}}$, and hardening parameter, A_{trial}, at the end of the current strain increment;
5. Calculate the change in radial stress based on the current trial stress state and initial values:

$$\delta\sigma_{xx} = \sigma_{xx,trial} - \sigma_{xx,0} \tag{9-5}$$

$$\delta\sigma_{yy} = \sigma_{yy,trial} - \sigma_{yy,0} \tag{9-6}$$

6. Compare calculated $\delta\sigma_{xx}$ and $\delta\sigma_{yy}$ values against a radial stress error tolerance, $RSTOL$ (a value of $RSTOL$ = 0.1 kN/m^2 was used in the simulations):
    - If error is greater than specified tolerance (i.e. $\delta\sigma_{xx} = \delta\sigma_{yy} > RSTOL$):
        - Calculate new trial components of the total strain vector, $\delta\boldsymbol{\varepsilon_{trial}}$ (Eq. (9-7));
        - Enter the stress update algorithm with the current stress state, $\boldsymbol{\sigma}$, hardening modulus, A, and trial increment of total strain, $\delta\boldsymbol{\varepsilon_{trial}}$;
        - Repeat steps 4 to 6 until boundary conditions are satisfied;

- If error is within specified tolerance (i.e. $\delta\sigma_{xx} = \delta\sigma_{yy} \leq RSTOL$):
    - Accept trial stress state and hardening modulus (i.e. $\boldsymbol{\sigma} = \boldsymbol{\sigma_{trial}}, A = A_{trial}$), and update state variables;
    - Repeat steps 2 to 6 for the next applied increment of total strain.

$$\delta\boldsymbol{\varepsilon_{trial}} = (\boldsymbol{D^e})^{-1}\delta\boldsymbol{\sigma} \tag{9-7}$$

where:

$\boldsymbol{D^e}$ = elastic stiffness matrix (based on state variables from the previous step)

$\delta\boldsymbol{\sigma}$ = change in stress state calculated from the current step:

$$\delta\boldsymbol{\sigma} = \boldsymbol{\sigma_{trial}} - \boldsymbol{\sigma_0} \tag{9-8}$$

9.4. CASM

CASM (Clay And Sand Model) is a relatively simple, state parameter based volumetric hardening model developed by Yu (1998). The main feature of CASM is that it adopts a single yield and plastic potential function for predicting the behaviour of both clay and sand under drained and undrained loading conditions. Simplicity is a major advantage of the model, as (in its original form) only two new model constants need be determined over the well-known Cam-clay model parameters.

9.4.1. MODEL SUMMARY AND PARAMETERS

Yu (2006) and Khong (2004) present a comprehensive overview of the CASM model and subsequent extensions, and therefore only a brief summary is provided here. CASM is described in terms of the critical state model parameters $(\lambda, \kappa, \Gamma)$, ψ, and the spacing ratio, r, as shown in Figure 9.5(a), where:

$$r = \frac{p'_0}{p'_\kappa} \tag{9-9}$$

and:

$$\psi = v + \lambda \ln(p') - \Gamma \tag{9-10}$$

The reference state parameter, ψ_{ref}, defines the vertical distance between the critical state line (CSL) and the reference consolidation line, and may be calculated according to:

$$\psi_{ref} = (\lambda - \kappa)\ln(r) \tag{9-11}$$

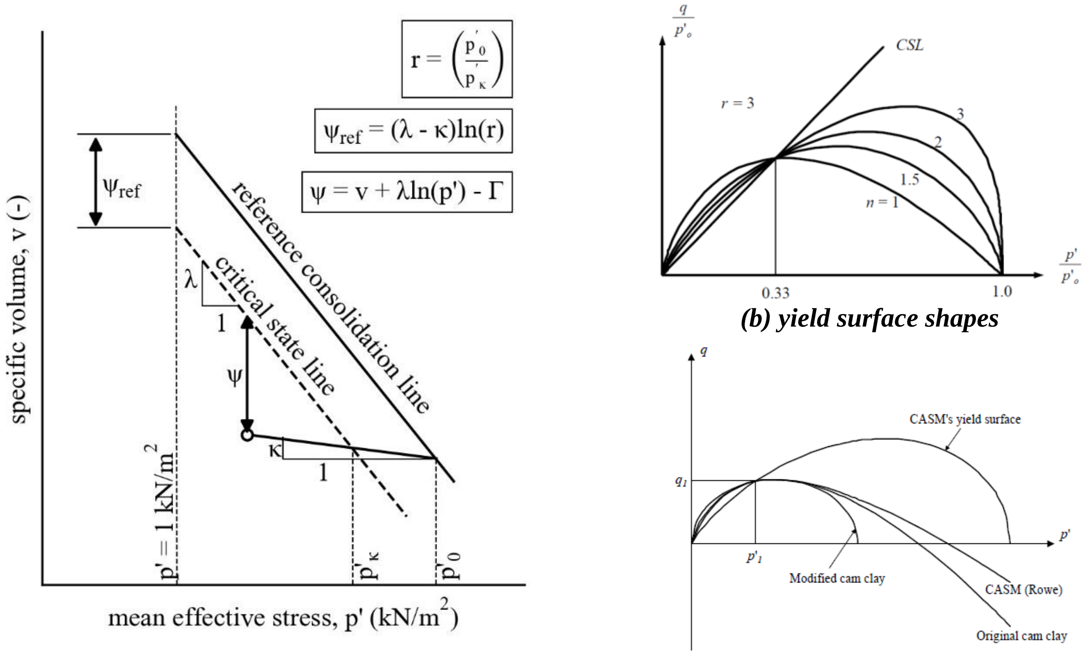

(b) yield surface shapes

(a) definitions

(c) plastic potential shapes

Figure 9.5: Summary of CASM model paramaters and features (modified from Khong, 2004)

While determination of the hardening parameter, p'_c, is relatively straightforward for cohesive soils, it is less clear for sands. According to Wang (2005), p'_c, may be calculated from:

$$p'_c = \exp\left[\frac{\Gamma + \psi_{ref} - v - \kappa\ln(p')}{\lambda - \kappa}\right] \tag{9-12}$$

YIELD SURFACE

The CASM yield function, expressed in terms of conventional triaxial stress invariants, is given by:

$$f = \left(\frac{q}{Mp'}\right)^n + \frac{1}{\ln(r)}\ln\left(\frac{p'}{p'_c}\right) = 0 \tag{9-13}$$

where n is the 'stress state coefficient' and is the second new model parameter required by CASM. n controls the shape of the yield surface as shown in Figure 9.5(b), while the spacing ratio, r, defines the intersection point with the CSL. It is worth noting that adopting n = 1 and r = 2.7183 recovers the original Cam Clay (OCC) model exactly, while selecting r = 2 and an appropriate value of n (typically 1.5 to 2, depending on the material) accurately matches the modified Cam Clay model.

The critical friction ratio, M, varies with Lode angle, and is calculated from Eq. (9-14). When plotted in the deviatoric plane, it forms a shape similar to the Matsuoka & Nakai (1974) yield surface.

$$M_\theta = M_{tc}\left(\frac{2\alpha^4}{1+\alpha^4+(1-\alpha^4)\sin(3\theta)}\right)^{1/4} \tag{9-14}$$

where:

M_θ = critical friction ratio at current Lode angle, θ
M_{tc} = critical friction ratio for triaxial compression stress conditions ($\theta = 30°$)

and:

$$\alpha = \frac{3-\sin\phi'_{cv}}{3+\sin\phi'_{cv}} \tag{9-15}$$

PLASTIC POTENTIAL

CASM adopts the stress-dilatancy rule proposed by Rowe (1962), which for triaxial compression is:

$$\frac{\delta\varepsilon_p^p}{\delta\varepsilon_q^p} = \frac{\partial g}{\partial p'}\Big/\frac{\partial g}{\partial q} = \frac{9(M_\theta-\eta)}{9+3M_\theta-2M_\theta\eta} \tag{9-16}$$

The plastic potential function, g, is then obtained by integration:

$$g = 3M_\theta\ln\left(\frac{p'}{\beta}\right)+(3+2M_\theta)\ln\left(\frac{2q+3p'}{p'}\right)-(3-M_\theta)\ln\left(\frac{3p'-q}{p'}\right)=0 \tag{9-17}$$

where the size parameter, β, may be determined for any stress state by solving the above equations. Figure 9.5(c) presents the shape of CASM's plastic potential, which is similar to the OCC model.

ELASTIC MODEL

CASM uses the same elastic model as the Cam Clay models, where the expressions for the tangent bulk, K_{tan}, and shear, G_{tan}, moduli are obtained by assuming a constant Poisson's ratio, μ, from:

$$K_{tan} = \frac{\partial p'}{\partial\varepsilon_p^e} = \frac{(1+e)}{\kappa}p' = \frac{vp'}{\kappa} \tag{9-18}$$

$$G_{tan} = \frac{3(1-2\mu)K}{2(1+\mu)} = \frac{3(1-2\mu)}{2(1+\mu)}\frac{vp'}{\kappa} \tag{9-19}$$

However, use of constant μ violates the laws of thermodynamics, introduces mild elastic-plastic coupling, and can lead to a non-conservative elastic response (Zytynski *et al.*, 1978). Houlsby *et al.* (2005) proposed a viable, thermodynamically correct alternative based on the hyperelasticity framework, noting that while the effect may be small for relatively simple load cases, significant differences may arise when modelling behaviour over many cycles, and its use is therefore recommended.

HARDENING LAW

In CASM, the size of the yield surface is governed by the hardening parameter, p_c'. CASM is a volumetric hardening model, meaning that the evolution of p_c' (and f) is only related to changes in plastic volumetric strain, $\delta\varepsilon_p^p$, and is estimated from:

$$\delta p_c' = \frac{\nu p_c'}{\lambda - \kappa}\delta\varepsilon_p^p = \frac{\nu p_c'}{\lambda - \kappa}\Lambda\frac{\partial g}{\partial p'} \tag{9-20}$$

where Λ is the non-negative quantity known as the scalar plastic multiplier (see Appendix A.2 for further details). The hardening modulus, A, required in the calculation of the elastoplastic stiffness matrix, $\boldsymbol{D^{ep}}$, is obtained from:

$$A = -\frac{1}{\Lambda}\frac{\partial f}{\partial p_c'}\delta p_c' = -\frac{\partial f}{\partial p_c'}\frac{\nu p_c'}{\lambda - \kappa}\frac{\partial g}{\partial p'} \tag{9-21}$$

such that:

$$\boldsymbol{D^{ep}} = \boldsymbol{D^e} - \frac{\boldsymbol{D^e}\dfrac{\partial g}{\partial \boldsymbol{\sigma}}\dfrac{\partial f}{\partial \boldsymbol{\sigma}}^{\boldsymbol{T}}\boldsymbol{D^e}}{\dfrac{\partial f}{\partial \boldsymbol{\sigma}}^{\boldsymbol{T}}\boldsymbol{D^e}\dfrac{\partial g}{\partial \boldsymbol{\sigma}} + A} \tag{9-22}$$

where $\boldsymbol{D^e}$ is the elastic stiffness matrix defined in Appendix A.2.

9.4.2. CASM MODEL DERIVATIVES

As described in Appendix A.3, the partial derivatives required to form the $\boldsymbol{D^{ep}}$ matrix may be determined by applying the chain rule to the partial derivatives of the stress invariant set $\{p', q, \theta\}$:

$$\frac{\partial f}{\partial \boldsymbol{\sigma}} = \frac{\partial f}{\partial p'}\frac{\partial p'}{\partial \boldsymbol{\sigma}} + \frac{\partial f}{\partial q}\frac{\partial q}{\partial \boldsymbol{\sigma}} + \frac{\partial f}{\partial \theta}\frac{\partial \theta}{\partial \boldsymbol{\sigma}} \tag{A-39 – bis}$$

$$\frac{\partial g}{\partial \boldsymbol{\sigma}} = \frac{\partial g}{\partial p'}\frac{\partial p'}{\partial \boldsymbol{\sigma}} + \frac{\partial g}{\partial q}\frac{\partial q}{\partial \boldsymbol{\sigma}} + \frac{\partial g}{\partial \theta}\frac{\partial \theta}{\partial \boldsymbol{\sigma}} \tag{A-40 – bis}$$

The following CASM specific partial derivatives (along with the partial derivatives presented in Appendix A.3) are therefore required to construct the $\boldsymbol{D^{ep}}$ matrix, and solve the constitutive equation (Eq. (9-4)):

$$\frac{\partial f}{\partial p'} = \frac{1}{p'\ln(r)} - \frac{nq^n}{M_\theta^n p'^{(n+1)}}; \tag{9-23}$$

$$\frac{\partial f}{\partial q} = \frac{nq^{n-1}}{M_\theta^n p'^n} \tag{9-24}$$

$$\frac{\partial f}{\partial p'_c} = -\frac{1}{p'_c \ln(r)} \tag{9-25}$$

$$\frac{\partial g}{\partial p'} = 3\left(\frac{3 + 2M_\theta}{2q + 3p'} - \frac{3 - M_\theta}{3p' - q}\right) \tag{9-26}$$

$$\frac{\partial g}{\partial q'} = \frac{2(3 + 2M_\theta)}{2q + 3p'} + \frac{3 - M_\theta}{3p' - q} \tag{9-27}$$

$$\frac{\partial f}{\partial M_\theta} = -\frac{nq^n}{p'^n M_\theta^{(n+1)}} \tag{9-28}$$

9.4.3. CASM EXTENSIONS

According to Khong (2004), for monotonic conditions the original CASM strikes a good balance between simplicity and practicality. Khong (2004) shows that CASM is able to capture the important features of sand behaviour for both drained and undrained conditions. In particular, the response of dense sands is shown to be satisfactorily modelled. However, CASM is unable to adequately capture cyclic behaviour due to the use of a single yield surface. As described in Chapter 8, such models yield a purely elastic stress range within the yield surface, and offer limited flexibility in terms of describing changes to the plastic hardening modulus following a load reversal. Several extensions to CASM have therefore been proposed (Yu & Khong, 2003; Yu et al., 2005, 2007):

- CASM-b: Reformulates the model using bounding-surface plasticity theory, providing improved predictions of sand behaviour;
- CASM-c: Extension of CASM-b to incorporate cyclic loading predictive capability, by assuming different expressions for the hardening modulus based on the loading conditions;
- CASM-d: Introduces a combined volumetric-deviatoric hardening rule to provide more realistic predictions of material response.

9.4.4. CASM MODEL CALIBRATION

Wang (2005) describes the testing requirements needed to determine the CASM parameters.

9.4.4.1. Elastic constants, μ and κ

The elastic behaviour is modelled by the Poisson's ratio, μ, and the slope of the swelling/recompression line, κ. For uncemented sands, Lade (Lade, 1977; Lade & Duncan, 1975) recommends a constant value of $\mu = 0.20$. Wang (2005) proposes two methods for determining the

Poisson's ratio. The first method uses bender elements to measure the compressional and shear wave velocities, v_p and v_s, respectively, from which μ may be estimated from:

$$\mu = \frac{1}{2}\frac{\left(\frac{v_p}{v_s}\right)^2 - 2}{\left(\frac{v_p}{v_s}\right)^2 - 1} \tag{9-29}$$

Reliable estimates of v_p from bender element tests in saturated soils are often problematic, as such tests tend to yield the v_p of the pore fluid water, rather than the soil itself. The second method described by Wang (2005), using measurements obtained from high-quality, on-sample strain instrumentation taken during conventional CIDc triaxial tests is therefore preferred.

$$\frac{\delta\varepsilon_p^e}{\delta\varepsilon_q^e} = \frac{G}{K} = \frac{3(1-2\mu)}{2(1+\mu)} \tag{9-30}$$

$$\mu = \frac{3 - 2\frac{G}{K}}{6 + 2\frac{G}{K}} \tag{9-31}$$

However, as discussed in Chapters 6 and 7, the on-sample strain instrumentation used in this study was unable to capture the very small strain (i.e. elastic) response; thus accurate determination of μ based on this approach is not possible. Furthermore, given that this study made use of commercially available, unmodified small-strain testing equipment used by several commercial testing laboratories in the UK, this approach is probably beyond the capabilities of such facilities, and therefore a more practical approach is sought. A Poisson's ratio of μ = 0.20 was therefore adopted for LBS-B, which is within the range 0.1 to 0.22 suggested by Loukidis & Salgado (2009) for silica sands.

The critical state constant, κ, determined from a triaxial compression tests with an isotropic consolidation stage including unloading (i.e. test s21), was calculated as κ = 0.003.

9.4.4.2. *Spacing ratio, r, and stress state coefficient, n*

The spacing ratio, r, is required to estimate the reference state parameter, ψ_{ref}:

$$\psi_{ref} = (\lambda - \kappa)\ln r \tag{9-32}$$

Wang (2005) adopts a value of ψ_{ref} = 0.06, which is the value of ψ at the so-called 'threshold' void ratio (Ishihara, 1993), and represents the value of e at which flow liquefaction (i.e. sample 'collapse' to zero residual stress) occurred. Despite preparation of very loose samples (e.g. D_r = 12 %), this type of behaviour was not observed in this study, therefore determining r is not straightforward. Yu (2006) comments that in such circumstances it is acceptable to choose a positive reference state parameter, typically ranging between 0.05 to 0.2.

The parameters r and n have therefore been determined using iterative forward modelling, in which test results are plotted in terms of the abscissa presented in Figure 9.6, and combinations of r and n trialled until a satisfactory envelope to the test data is obtained. Based on this approach, ψ_{ref} = 0.1 (r = 40.6), and n = 4.0 were adopted for LBS-B.

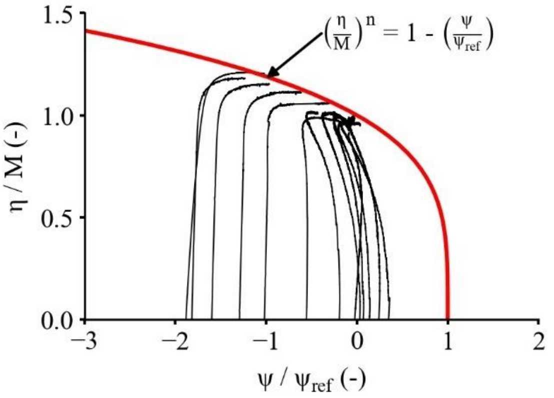

Figure 9.6: Determination of CASM spacing ratio and stress state coefficient

9.5. NORSAND

NorSand is a state parameter based, critical state type constitutive model, developed from the fundamental axioms of critical state theory and results of element tests undertaken on sand. The original NorSand was originally formulated for triaxial compression conditions (Jefferies, 1993), with subsequent refinement and generalisation to three dimensions presented by Jefferies & Shuttle (2002). Jefferies & Shuttle (2011) proposed a simplified, computationally efficient function for calculating the critical friction ratio including Lode angle effects, that yields similar results to the Matsuoka & Nakai (1974) relationship. The version described and implemented in this thesis is based on that presented in Jefferies *et al*. (2015), and is briefly described in the following.

9.5.1. MODEL SUMMARY AND PARAMETERS

NorSand includes the usual elastoplastic constitutive model components of (i) a yield surface, (ii) a flow rule which describes the relative plastic strain increments, and (iii) a hardening law, which controls how the yield surface evolves with plastic strain. However, NorSand differs from other ‘Cambridge type’ models in that it assumes an infinite number of possible normal compression lines

(NCLs) in $e - \ln p'$ space. The implication of this is that the yield surface does not in general intersect the CSL (though it does have a similar shape), and is offset by the state parameter, ψ, with the requirement that:

$$\psi \to 0 \; as \; \varepsilon_q \to \infty \; \forall \; \eta > M$$

Because the yield surface has been decoupled from the CSL, an additional plastic hardening parameter, H (not to be confused with the hardening modulus, A), is also necessary as $\lambda - \kappa$ no longer serves as a plastic compliance (Jefferies & Shuttle, 2002). However, as with CASM, by adopting appropriate values for ψ, H and elastic parameters, the original Cam-clay (and Granta-gravel) Cambridge models may be recovered. NorSand assumes that the maximum dilation rate, D_{min}, is linearly related to ψ (as shown in Figure 5.4b) via a so-called 'state-dilation' coefficient, χ:

$$D_{min} = \chi_i \psi_i \tag{9-33}$$

The concept of an 'image' condition is introduced here (denoted by the subscript, i), defined as the point on a yield surface where the plastic strain rates give D^p = 0, which is one of the two criteria required for satisfying critical state conditions. The image state, ψ_i, is therefore defined as:

$$\psi_i = e - e_{c,i} \tag{9-34}$$

where:

$e_{c,i}$ = critical state void ratio at the image stress, p_i'

In NorSand, p_i' is a further hardening parameter that is controlled by the hardening law, i.e. it evolves with plastic shear strain at a rate that depends on ψ.

PRELIMINARIES

The original NorSand model (Jefferies, 1993) used the flow rule proposed by Nova (1982):

$$D^p = \frac{\delta \varepsilon_p^p}{\delta \varepsilon_q^p} = \frac{M - \eta}{1 - N} \tag{9-35}$$

where N is a density-independent material property relating to volumetric work. However, to account for the observation that M depends on the direction of the major principal stress (i.e. Lode angle, θ), Jefferies & Shuttle (2002) modified the flow rule to:

$$D^p = M_i - \eta \tag{9-36}$$

Eq. (9-36) is similar to the flow rule used in the well-known Original Cam Clay (OCC) model, but differs in using the 'image stress ratio,' M_i. This quantity is a function of both M and ψ, and evolves with shear strain such that $M_i \rightarrow M$ as $\psi \rightarrow 0$, and $\varepsilon_q \rightarrow \infty$, and is calculated from:

$$M_i = M_\theta \left(1 - \frac{\chi_i N |\psi_i|}{M_{tc}}\right) \tag{9-37}$$

The critical friction ratio used in NorSand, M_θ, (subscript θ used to emphasize its variation with Lode angle) is calculated from the simplified relationship proposed by Jefferies & Shuttle (2011):

$$M_\theta = M_{tc} - \frac{M_{tc}^2}{3 + M_{tc}} \cos\left(\frac{3\theta}{2} - \frac{\pi}{4}\right) \tag{9-38}$$

The state-dilatancy coefficient, χ_i, equates the maximum dilation rate, D_{min}, to the current image state parameter, through:

$$D_{min} = D_{min}^p = \frac{M_\theta}{M_{tc}} \chi_i \psi_i \tag{9-39}$$

which is the general form of Eq. (9-33). χ_i may be determined from results of triaxial compression tests undertaken on dense samples (see Section 9.5.3), such that:

$$\chi_i \approx 1.1 \chi_{tc} \tag{9-40}$$

where:

χ_{tc} = NorSand state dilatancy parameter determined from triaxial compression tests

YIELD SURFACE

NorSand is an isotropic, deviatoric hardening model, with the yield surface expanding or contracting while retaining its shape. NorSand adopts a similar 'bullet' shaped yield surface to that adopted by the OCC model. However, one of the aims in the formulation of NorSand was to limit maximum dilation to replicate dense soil behaviour without resorting to non-associated flow rules (Jefferies & Been, 2015).

Realistic maximum dilatancy is obtained via an internal cap, which prevents the soil from unloading to very low stresses without yielding. The internal cap is taken as a flat plane – its location dependent on the current state of the material, as illustrated in Figure 9.7 for both loose and dense states, and controls the limiting stress ratio, η_L, that the soil can sustain.

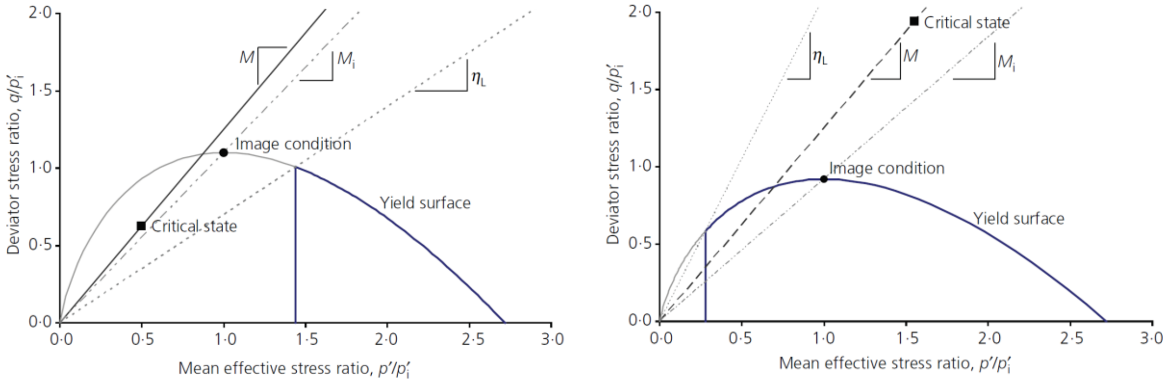

(a) ***(b)***

Figure 9.7: Illustration of NorSand yield surfaces and limiting stress ratios for (a) loose sand, and (b) dense sand (from Jefferies et al., 2015)

The main difference between Figure 9.7a (loose sand) and Figure 9.7b (dense sand) is the location of the critical state relative to the image condition. For sands that are loose of critical (i.e. contractive), the image condition is at a higher mean effective stress, and the yield surface will therefore soften to the critical state. However, for dense, dilative sands, p'_i is less than p' at critical state, and therefore the yield surface must harden to reach the critical state. The yield function, expressed in terms of conventional triaxial stress invariants, is scaled by the ‘image stress’, p'_i, and is given by (Jefferies *et al*., 2015):

$$f = \frac{q}{p'} - M_i + M_i \ln\left(\frac{p'}{p'_i}\right) = 0 \tag{9-41}$$

where:

$$p'_{i,max} = p' \exp\left(\frac{-\chi_i \psi_i}{M_{i,tc}}\right) \tag{9-42}$$

and:

$$M_{i,tc} = M_{tc}\left(1 - \frac{\chi_i N |\psi_i|}{M_{tc}}\right) \tag{9-43}$$

PLASTIC POTENTIAL

NorSand adopts associated flow, therefore the yield and plastic potential functions are similar:

$$g = f = \frac{q}{p'} - M_i + M_i \ln\left(\frac{p'}{p'_i}\right) = 0 \tag{9-44}$$

ELASTIC MODEL

The elasticity model adopted uses the power law relationship developed for LBS-B from bender element tests, as presented in Section 0:

$$\frac{G_0}{p_{ref}} = 1400\frac{(2.17-e)^2}{(1+e)}\left(\frac{p'}{p_{ref}}\right)^{0.42} \qquad \text{(6-33 bis)}$$

HARDENING LAW

The hardening law describes the evolution of the yield surface with plastic strain, and is a simple difference equation between the current maximum allowable value of hardness (Eq. (9-41)) and the current hardness (i.e. size). The rate of change in the size of the yield surface with incremental plastic (deviatoric) strain is therefore:

$$\delta p_i' = H_{tc}\left(p_{i,max}' - p_i'\right)\delta\varepsilon_q^p \qquad \text{(9-45)}$$

where H_{tc} is a dimensionless hardening parameter, obtained from an iterative forward modelling approach as described in Section 9.5.3. Jefferies & Been (2015) express the hardening law in dimensionless form by dividing through by the current image and mean effective stresses:

$$\frac{\delta p_i'}{p_i'} = H_{tc}\left(\frac{M_i}{M_{i,tc}}\right)\left(\frac{p'}{p_i'}\right)\left(\frac{p_{i,max}'}{p'} - \frac{p_i'}{p'}\right)\delta\varepsilon_q^p \qquad \text{(9-46)}$$

where the $M_i/M_{i,tc}$ term is included to account for undefined Lode angles when the stress state is isotropic. To incorporate the influence of shear stress level and obtain closer agreement with realistic sand behaviour, Jefferies & Been (2015) further multiply the RHS of Eq. (9-46) by the ratio p'/p_i', which results in an approximate threefold change in the hardening rate as η changes from zero to η_{max}. The hardening law therefore becomes:

$$\frac{\delta p_i'}{p_i'} = H_{tc}\left(\frac{M_i}{M_{i,tc}}\right)\left(\frac{p'}{p_i'}\right)^2\left(\frac{p_{i,max}'}{p'} - \frac{p_i'}{p'}\right)\delta\varepsilon_q^p \qquad \text{(9-47)}$$

Substituting the equations for $\delta\varepsilon_q^p$ (Eq. (A-31)), and $p_{i,max}'$ (Eq. (9-41)) yields the hardening rule:

$$\delta p_i' = p_i' H_\theta\left(\frac{p'}{p_i'}\right)^2\left[\exp\left(\frac{-\chi_i\psi_i}{M_{i,tc}}\right) - \frac{p_i'}{p}\right]\Lambda\frac{\partial g}{\partial q} \qquad \text{(9-48)}$$

noting that:

$$H_\theta = H_{tc}\left(\frac{M_i}{M_{i,tc}}\right) \qquad \text{(9-49)}$$

However, Jefferies and co-workers found that while Eq. (9-48) performed well for drained tests, unsatisfactory agreement was observed when applied to loose undrained tests. The predicted response was improved by incorporating an additional ‘softening term’:

$$\delta p_i' = p_i' H_\theta \left(\frac{p'}{p_i'}\right)^2 \left[\exp\left(\frac{-\chi_i \psi_i}{M_{i,tc}}\right) - \frac{p_i'}{p}\right] \Lambda \frac{\partial g}{\partial q} + Z \frac{\eta}{\eta_L} \frac{\delta p_{i,max}'}{p_i'} \tag{9-50}$$

where Z is a binary switch operator, and the ratio η/η_L controls the additional softening such that it becomes progressively more important as η approaches its current limiting value, η_L, given by

$$\eta_L = M_i \left(1 - \frac{D_{min}}{M_{i,tc}}\right) \tag{9-51}$$

The hardening modulus, A, required to calculate the $\boldsymbol{D^{ep}}$ matrix, may then be determined from:

$$A = -\frac{1}{\Lambda} \frac{\partial f}{\partial \kappa} \delta\kappa = -\frac{1}{\Lambda} \frac{\partial f}{\partial p_i'} \delta p_i' \tag{9-52}$$

$$A = -\frac{\partial f}{\partial p_i'} \left(p_i' H_\theta \left(\frac{p'}{p_i'}\right)^2 \left[\exp\left(\frac{-\chi_i \psi_i}{M_{i,tc}}\right) - \frac{p_i'}{p}\right] \frac{\partial g}{\partial q} + Z \frac{\eta}{\eta_L} \frac{\delta p_{i,max}'}{p_i'} \right) \tag{9-53}$$

Alternatively, if the current stress state lies on the internal cap, hardening is controlled by:

On the internal cap: $$\delta p_i' = -p_i' \frac{H_\theta}{2} \left|\delta \varepsilon_q^p\right| \tag{9-54}$$

9.5.2. NORSAND MODEL PARTIAL DERIVATIVES

The following partial derivatives (along with the general stress derivatives presented in Appendix A.3) are required to construct the elastoplastic stiffness matrix, $\boldsymbol{D^{ep}}$, and solve the constitutive equations. Note, these derivatives are specific to the yield function given in Section 9.5.1, and must be redefined should an alternative form of Eq. (9-41) be adopted. NorSand adopts an associated flow rule, therefore:

$$\frac{\partial f}{\partial p'} = \frac{\partial g}{\partial p'} = \frac{M_i}{p'} - \frac{q}{p'^2} \tag{9-55}$$

$$\frac{\partial f}{\partial q} = \frac{\partial g}{\partial q} = \frac{1}{p'} \tag{9-56}$$

$$\frac{\partial f}{\partial M_i} = \frac{\partial g}{\partial M_i} = \ln\left(\frac{p'}{p_i'}\right) - 1 \tag{9-57}$$

$$\frac{\partial f}{\partial p_i'} = -\left(\frac{M_i}{p_i'}\right) \tag{9-58}$$

9.5.3. NORSAND MODEL CALIBRATION

Jefferies & Shuttle (2005) provide a description of the testing requirements and methods needed to determine the NorSand model parameters.

9.5.3.1. *Critical Friction Ratio and Volumetric Coupling Coefficient, M_{tc} and N*

The critical friction ratio and volumetric coupling coefficient may be obtained from the 'stress-dilatancy' plot shown in Figure 9.2. A trend line fitted through the data based on the flow rule proposed by Nova (1982) subsequently yields the volumetric coupling coefficient for reference triaxial compression conditions, such that N = 0.46. The critical friction ratio was previously determined (Section 9.2.1) as M_{tc} = 1.31.

9.5.3.2. *State-dilatancy coefficient, χ_{tc}*

The state dilatancy coefficient for reference triaxial compression conditions, χ_{tc}, relates the maximum dilatancy to the state parameter, and may be obtained from the gradient of the state dilatancy plot shown in Figure 9.8. For LBS-B, χ_{tc} is calculated as 3.0 which agrees well with the 2 < χ_{tc} < 5 range given by Jefferies & Been (2015).

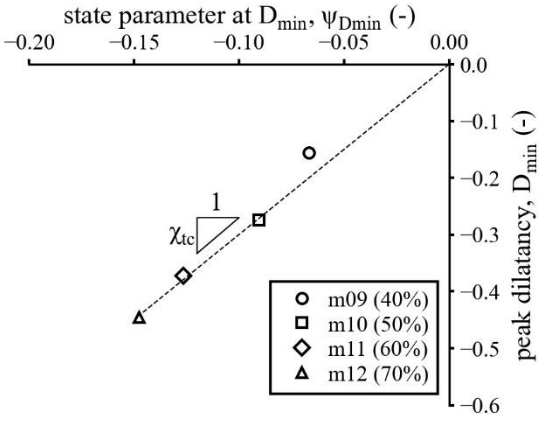

Figure 9.8: State-dilatancy in triaixal compression tests on dense LBS-B

9.5.3.3. *Plastic hardening parameter, H_{tc}*

NorSand uses the dimensionless plastic hardening parameter, H_{tc}, to represent plastic shear hardening. H_{tc} is determined by iterative forward modelling of several CIDc triaxial tests, where an initial value of H_{tc} is used to predict the stress–strain response with NorSand, while keeping the other model parameters fixed. The process is repeated with updated values of H_{tc} until a satisfactory agreement between the computed and measured response is obtained, such that:

$$H_{tc} = H_{\psi}\psi + H_0 \tag{9-59}$$

where H_0 and H_ψ represent the y-intercept and slope of a trendline on a plot of H vs ψ_0, as shown in Figure 9.9. Jefferies & Been (2015) suggest that H_{tc} typically ranges between 50 and 450 for softer and stiffer materials, respectively. Analysis of CIDc tests performed as part of this study indicate that H_0 = 98.2 and H_ψ = -1920 represent appropriate values for predicting H_{tc} for LBS-B at other states.

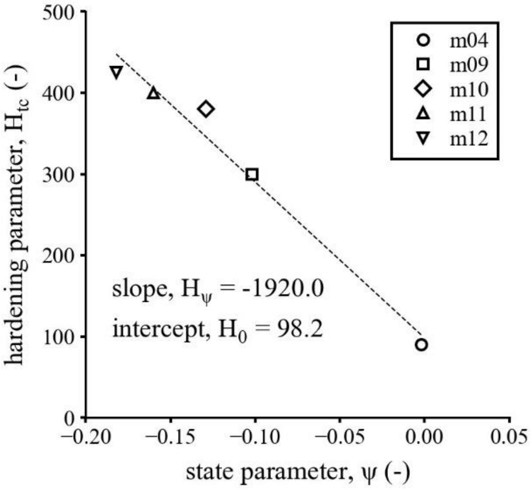

Figure 9.9: Calibration of NorSand hardening parameter, H_{tc}

9.6. SANISAND

SANISAND describes a group of state parameter based constitutive models developed for sand, formulated using bounding surface plasticity theory (Taiebat & Dafalias, 2008). Several variants to the original model proposed by Manzari & Dafalias (1997) exist, as described in Section 8.2.3. The version used in this thesis is based on the model described by Dafalias & Manzari (2004). This model was selected as it is freely available for download as a user defined soil model (UDSM) from SoilModels (2020), and may therefore be implemented within the commercial finite element software, Plaxis. A comprehensive description of the model formulation and model constants is given in Dafalias & Manzari (2004) and Dafalias *et al*. (2004) and is therefore not provided here.

9.6.1. SANISAND MODEL CALIBRATION

Table 9.3 presents the key equations used to formulate the SANISAND model in triaxial stress space, together with the 16 model parameters that must be determined. SANISAND models are often criticised for containing an impractical number of model parameters. However, inspection of Table 9.3 shows that many of the parameters are not exclusive to the SANISAND model (e.g. the critical state parameters $e_\Gamma, \lambda, \xi, M_{tc}, c$), and should be routinely determined as part of an advanced laboratory test programme. Furthermore, several parameters may be ‘switched off’, if the particular aspect of behaviour which they control is not required in the simulation being undertaken.

Table 9.3: SANISAND equations and model parameters (modified from Dafalias & Manzari, 2004)

Model component	Parameters	Governing equation	Eq.
critical state line	e_Γ, λ, ξ	$e_{cs} = e_\Gamma - \lambda\left(\frac{p'}{p_{ref}}\right)^{\xi}$	(9-60)
elastic deviatoric strain increment	-	$\delta\varepsilon_q^e = \frac{\delta q}{3G_0}$	(9-61)
	A_G	$G_0 = A_G p_{ref}\frac{(2.97-e)^2}{1+e}\left(\frac{p'}{p'_{ref}}\right)^{0.5}$	(9-62)
elastic volumetric strain increment	-	$\delta\varepsilon_p^e = \frac{\delta p'}{3K}$	(9-63)
	μ	$K = G_0\frac{2(1+\mu)}{3(1-2\mu)}$	(9-64)
yield surface	m	$f = \lvert\eta-\alpha\rvert - m = 0$	(9-65)
plastic deviatoric strain increment	-	$\delta\varepsilon_q^p = \frac{\delta\eta}{A}$	(9-66)
	-	$A = h(M_b - \eta)$	(9-67)
	c	$M_\theta = \frac{2cM_{tc}}{(1+c)-(1-c)\cos(3\theta)}$	(9-68)
	M_{tc}, M_{te}	$c = \frac{M_{te}}{M_{tc}}$	(9-69)
	n_b	$M_b = M_\theta \exp(-n_b\psi)$	(9-70)
	-	$h = \frac{b_0}{\lvert\eta-\eta_0\rvert}$	(9-71)
	h_0, c_h	$b_0 = A_G h_0(1-c_h e)\left(\frac{p'}{p'_{ref}}\right)^{-0.5}$	(9-72)
plastic volumetric strain increment	-	$\delta\varepsilon_p^p = D\left\lvert\varepsilon_q^p\right\rvert$	(9-73)
	-	$D = A_d(M_d - \eta)$	(9-74)
	n_d	$M_d = M_\theta \exp(n_d\psi)$	(9-75)
	A_0	$A_d = A_0(1+\langle sz\rangle)$	(9-76)
Fabric-dilatancy tensor update	c_z, z_{max}	$\delta z = -c_z\langle -\delta\varepsilon_p^p\rangle(sz_{max}+z)$	(9-77)
Back-stress ratio tensor update	-	$\delta\alpha = \delta\eta$	(9-78)

Notes:

$\langle\ \ \rangle$ = Macaulay brackets, yielding $\langle A\rangle = A$ if $A > 0$, and $\langle A\rangle = 0$ if $A \le 0$
α = yield surface back stress
m = yield surface parameter controlling the size of the cone aperture
h = function of state variables
M_b = gradient of the bounding surface
c = ratio of critical friction ratios in triaxial extension and compression
n_b = model parameter controlling the position of the bounding surface from the CSL
η_0 = initial stress ratio
h_0, c_h = scalar model parameters controlling the magnitude of the hardening modulus, A
A_d = function of state variables
M_d = gradient of the dilatancy surface
n_d = model parameter controlling the position of the dilatancy surface from the CSL
A_0 = model parameter controlling the rate of dilation, D
s = ± 1 according to $\eta = \alpha \pm m$
z = fabric internal variable
c_z, z_{max} = model parameters controlling the rate of evolution of z and the maximum value z can attain

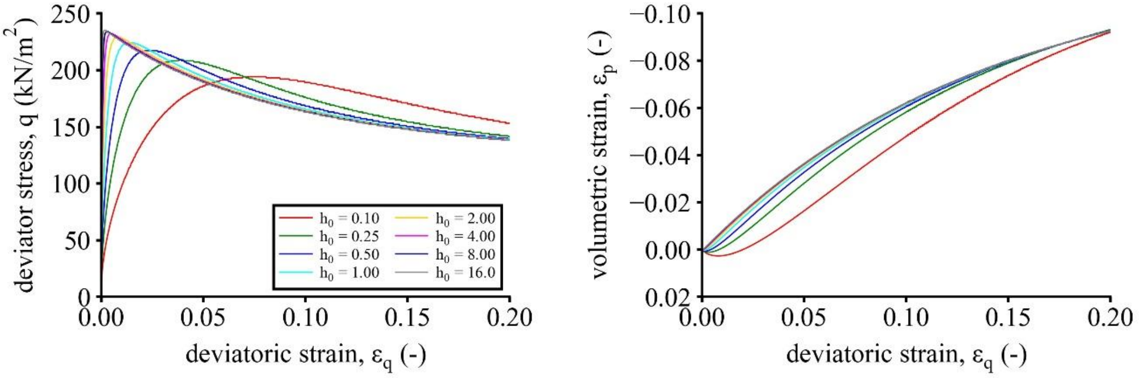

(a) h_0 = varies as shown, c_h = 1.1, A_0 = 1.2, m = 0.0655

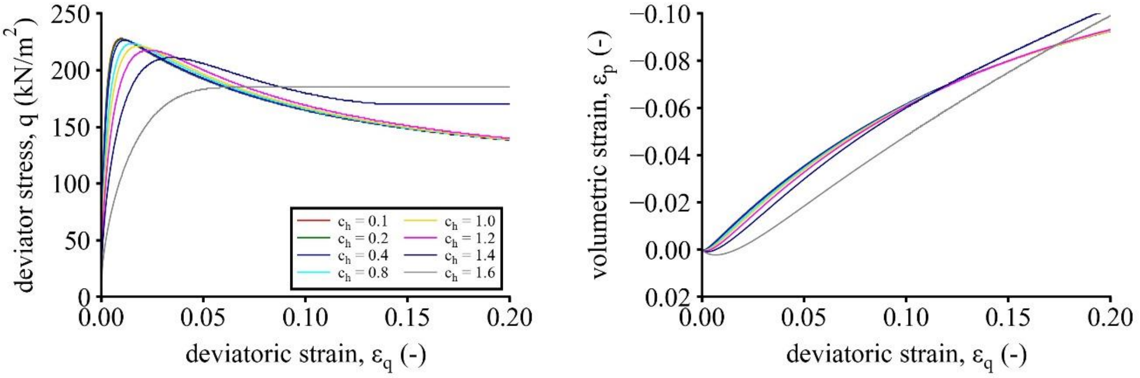

(b) h_0 =0.6, c_h = varies as shown, A_0 = 1.2, m = 0.0655

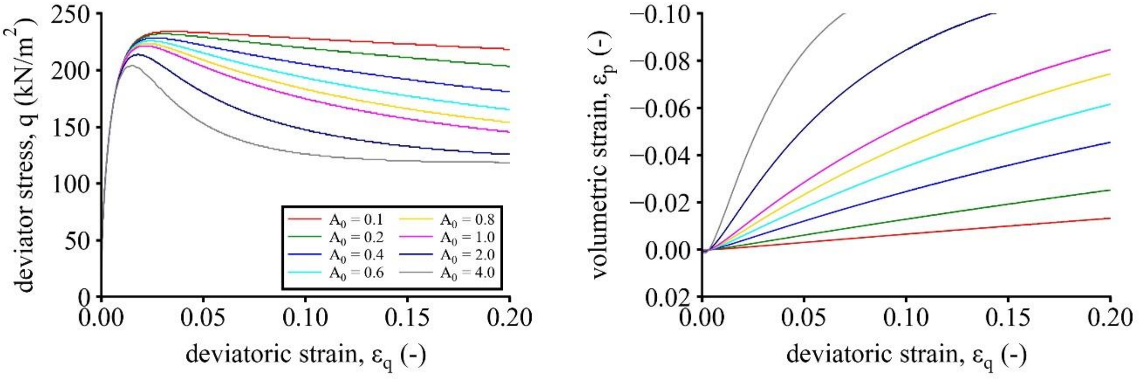

(c) h_0 =0.6, c_h =1.1, A_0 = varies as shown, m = 0.0655

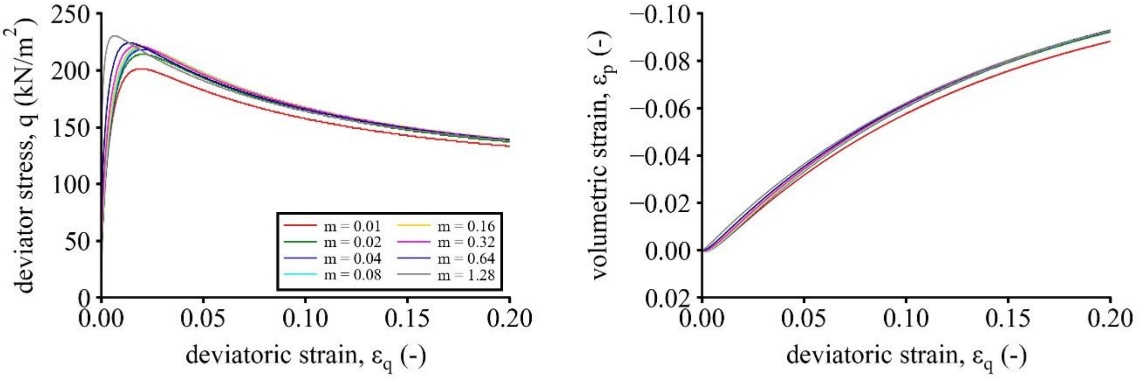

(d) h_0 =0.6, c_h =1.1, A_0 =1.2, m = varies as shown

Figure 9.10: Influence of SANISAND model parameters on simulated constitutive response of a CIDc test

To better understand the influence of varying the SANISAND model parameters on the simulated response, a parameter sensitivity analysis was performed. Results are shown in Figure 9.10, and indicate that relatively minor variations in the model parameters leads to significant changes in both the simulated stress-strain and volumetric responses. Calibration of the model is therefore challenging, with the possibility that multiple calibrated model parameter sets may exist that yield a similar constitutive response.

9.6.1.1. Yield surface parameter, m

The yield surface parameter, m, controls the aperture size of the elastic inner yield surface (a Drucker-Prager cone), and remains constant throughout the simulation (i.e. no hardening is assumed). According to Dafalias & Manzari (2004), m is of the order $M_{tc}/100$, while Papadimitriou $et\ al.$ (2001) suggest setting $m = 0.05M_{tc}$, with typical values for sand ranging between 0.06 and 0.07. For LBS-B, a value of $m = 0.05(1.31) = 0.0655$ is adopted.

9.6.1.2. State dependence parameters, n_b and n_d

These parameters control the gradient of the bounding and dilatancy surfaces, M_b and M_d, respectively. Calibration requires monotonic compression tests sheared from various initial states. Plotting the peak and dilatancy (i.e. characteristic) deviatoric stress ratios, η_{max} and η_{Ch}, against their corresponding values of ψ yields the model parameters n_b and n_d, as shown Figure 9.11a.

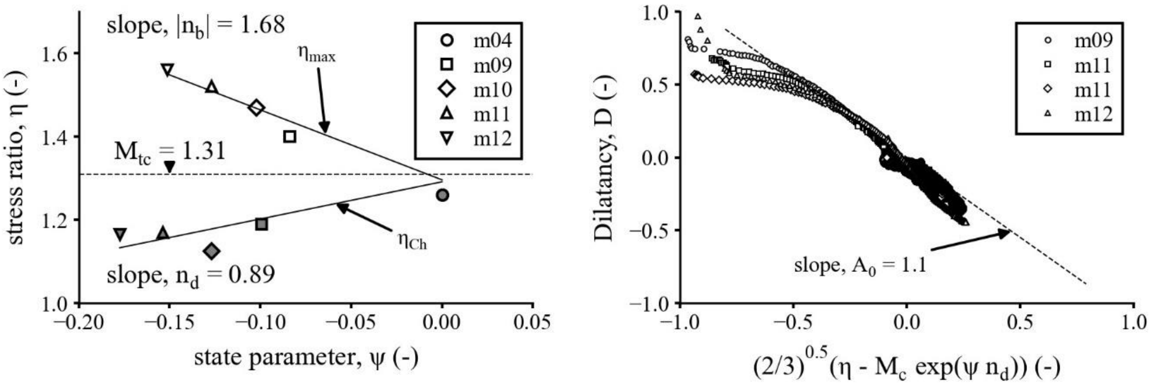

(a) ***(b)***

Figure 9.11: Calibration of SANISAND model parameters n_b, n_d and A_0

However, preliminary calibration simulations using the n_b and n_d values shown in Figure 9.11, yielded consistent overpredictions of the deviator stress at both peak and large strains. A sensitivity analysis found that the magnitude of q_{max} is strongly influenced by the value of n_b. It was found that reducing both n_b and M_{tc} yielded improved comparisons with the measured test data. The following values were therefore adopted in the simulation presented in Section 9.9: n_b = 1.67 and M_{tc} = 1.25.

9.6.1.3. *State dilatancy parameter, A_0*

Whyte (2019) showed that for triaxial stress conditions, the magnitude of the state dilatancy parameter, A_0, may be estimated from the gradient of a plot of dilatancy rate, D, versus $\sqrt{2/3\,(\eta - M_d)}$. Figure 9.11b presents this data for four dense CIDc tests, and indicates A_0 = 1.1 for LBS-B, which is within the range 1 < A_0 < 3.0 suggested by Papadimitriou *et al*. (2001).

9.6.1.4. *Hardening parameters, h_0 and c_h*

Dafalias & Manzari (2004) suggest that the hardening constants, h_0 and c_h, be obtained by trial and error. For LBS-B, h_0 = 1.3 and c_h = 1.3 were found to yield satisfactory agreement with results of CIDc tests. It must be noted that this procedure is not particularly efficient and requires multiple iterations before a reasonable match is obtained.

9.6.1.5. *Fabric parameters, c_z and z_{max}*

The fabric parameters c_z and z_{max} were found to have minimal influence on the predicted response, and therefore for simplicity, these parameters are set to 0.

9.7. HYSAND

Houlsby & Mortara (2004) present a multi-surface kinematic hardening model for sand formulated within the hyperplasticity framework (Houlsby & Puzrin, 2006), henceforth referred to as ‘HySand’ for brevity. A full description of the formulation of the model is provided in Houlsby & Mortara (2004) and is therefore not repeated here.

9.7.1. HYSAND MODEL CALIBRATION

Table 9.4 summarises the 12 model parameters used in HySand. Several of the model parameters are similar to those previously defined for other models (e.g. K, G, M_{tc}, λ, v_Γ, r_{ec}); however, the model parameters v_B, v_D, h, b, A, β_{max} are exclusive to HySand. Houlsby & Mortara (2004) provide minimal calibration guidance; therefore, to better understand the influence of these parameters on the simulated response, a sensitivity analysis was performed.

Table 9.4: HySand model constants defined in Houlsby & Mortara (2004)

HySand constants	**symbol**
bulk modulus	K
shear modulus	G
critical stress ratio in triaxial compression	M_{tc}
slope of the critical state line in $\ln(p') - \ln(v)$ space	λ
specific volume at critical state at $p' = p'_{ref}$	v_Γ
ratio between triaxial compression and extension critical stress ratios	r_{ec}
specific volume at loosest state at $p' = p'_{ref}$	v_B
specific volume at densest state at $p' = p'_{ref}$	v_D
hardening modulus constants	h, b
rate of anisotropy development constant	A
maximum rate of dilation	β_{max}

Figure 9.12 shows the results of a parameter sensitivity analysis for a conventional triaxial CIDc test, and indicate that:

- The shape of the stress strain curve is most influenced by the parameters h and b, with high h and low b values yielding the stiffest response, leading to q_{max} being mobilised at decreasing deviatoric strains;
    - β_{max} is also shown to affect the shape of the stress-strain curve, with initial stiffnesses increasing with increasing β_{max} values;
    - A is shown to have only minor influence on the shape of the stress-strain curve;
- The volumetric response is predominantly controlled by β_{max}; however, A, h and b are also shown to influence the shape of the $\varepsilon_q - \varepsilon_p$ curve;
    - The magnitude of compressive volumetric strain mobilised at the start of shearing is influenced by the value of A, with lower values (i.e. $A < 400$) yielding a greater initially compressive response;
- A has minimal influence on the rate of dilation.

To simulate CIDc tests, the following method was therefore used to calibrate the HySand model parameters:

1. Determine maximum and minimum specific volumes, v_B and v_D;
2. Determine elastic constants, G and K;
3. Determine critical state constants, v_Γ, λ, and M_{tc};
4. Determine r_{ec} from CIDe triaxial tests if available, otherwise assume a value;

5. Run simulation with reasonable ‘starter’ values (e.g. h = 1000, b = 3, A = 200, β_{max} = 0.8);
6. Inspect $\varepsilon_q - \varepsilon_p$ curves, and adjust β_{max} until a satisfactory fit with the test data is obtained;
7. Inspect $\varepsilon_q - \varepsilon_p$ curves, and adjust A until the intersection of the simulated curve with the ε_p = 0 axis yields good agreement with the experimental data;
8. Determine h and b parameters by iterative forward modelling until close agreement with the experimental stress-strain curve is obtained.

9.7.1.1. *Limiting specific volumes, v_B and v_D*

Houlsby & Mortara (2004) define v_B and v_D as the specific volume at a reference mean pressure, p'_{ref}, at the loosest and densest states, respectively, as illustrated in Figure 9.13. It is reasonable to assume that v_B and v_D are similar to the maximum and minimum specific volumes determined from limiting density tests. However, results of such tests may not achieve the absolute limiting densities physically possible for a particular material, and it is therefore recommended that the HySand v_B and v_D parameters be obtained from:

$$v_B = 1 + 1.1(e_{max}) \tag{9-79}$$

$$v_D = 1 + 0.9(e_{min}) \tag{9-80}$$

Results of limiting density tests performed on LBS-B (see Section 4.6.2.1) yield: v_B = 1.897, v_D = 1.480, at a reference mean pressure of p'_{ref} = 101.3 kN/m^2.

9.7.1.2. *Elastic moduli, K and G*

The elastic bulk and shear moduli, K and G respectively, are constant in the original HySand model (Houlsby & Mortara, 2004). Values of G used in the model simulations are therefore calculated according to Eq. (6-33), from which K is subsequently estimated (from Eq. (A-25)) assuming a constant Poisson’s ratio of μ = 0.2.

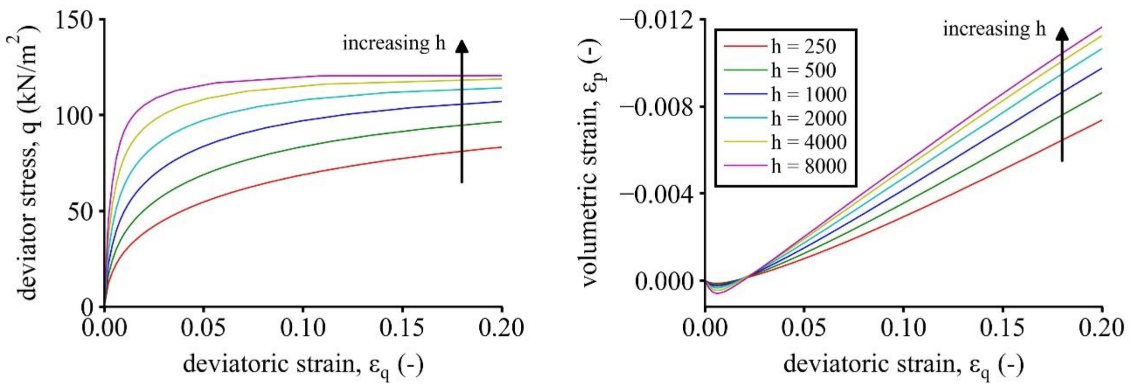

(a) h = varies as shown, b = 3, A = 400, β_{max} = 0.2

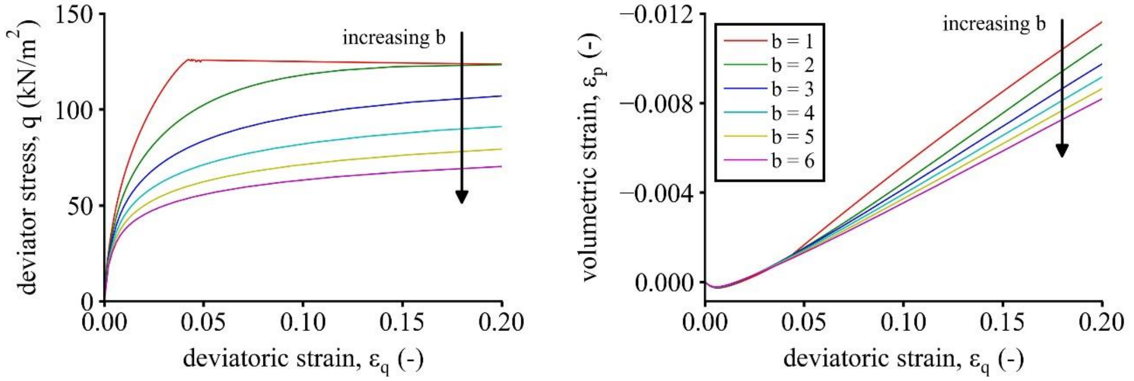

(b) h = 1000, b = varies as shown, A = 400, β_{max} = 0.2

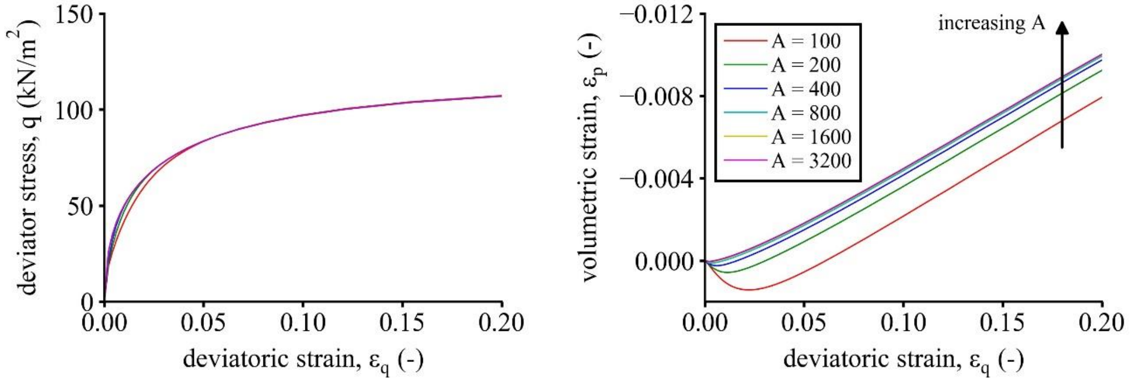

(c) h = 1000, b=3, A = varies as shown, β_{max} = 0.2

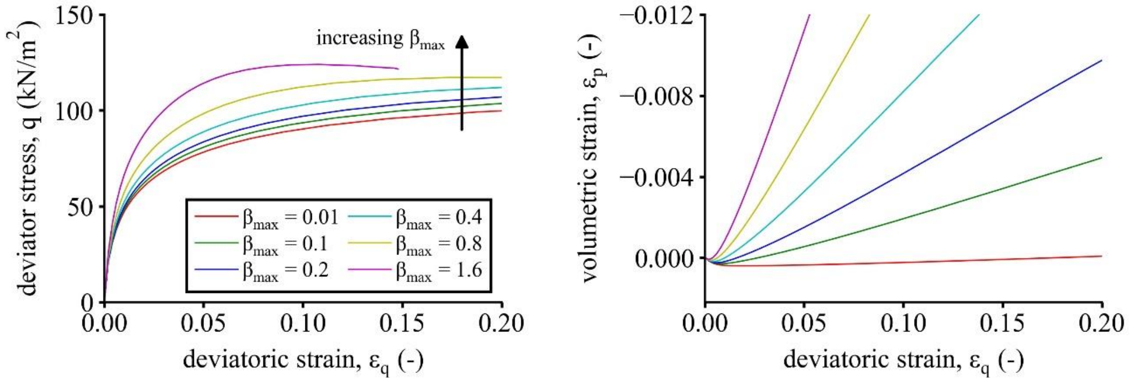

(d) h = 1000, b=3, A = 400, β_{max} = varies as shown

Figure 9.12: Influence of HySand model parameters on simulated constitutive response of a CIDc test

9.7.1.3. Critical state constants, M_{tc} , λ and v_Γ

The slopes of the critical state line in $p' - q$ and $e - p'$ space have been previously determined as M_{tc} =1.31 and λ = 0.035, respectively. v_Γ is shown in Figure 9.13, defined as the specific volume on the critical state line at $p' = p'_{ref}$. Using the value of e_Γ defined in Table 9.2 associated with the semi-log form of the CSL, gives v_Γ = 1.789 for p'_{ref} = 101.3 kN/m^2.

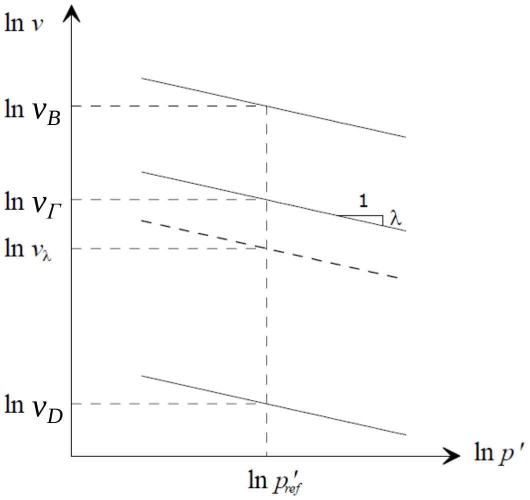

Figure 9.13: Graphical representation of the density and critical state constants used in HySand

9.7.1.4. HySand Model parameters h, b A and β_{max}

Figure 9.14 presents the results of a calibration exercise performed to determine the remaining HySand model parameters, and shows that excellent agreement with the experimental data may be obtained with the HySand model. A summary of the best-fit model parameters is given in Table 9.5.

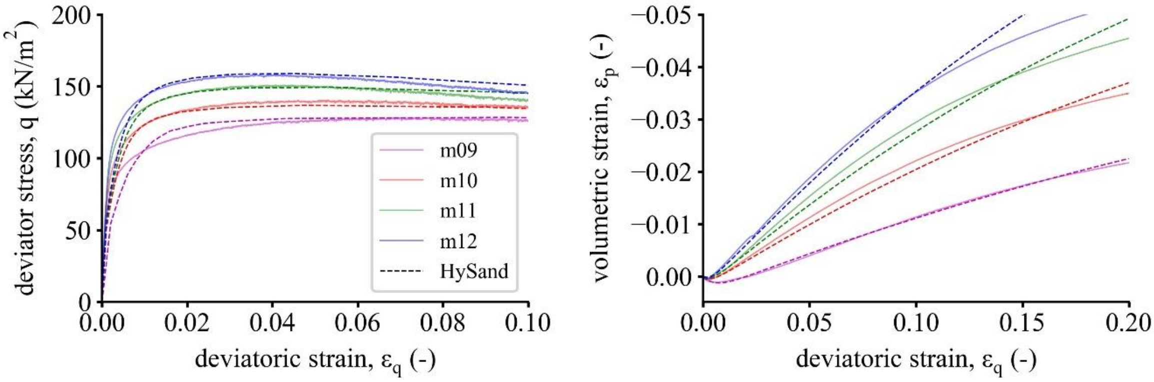

Figure 9.14: Calibration of HySand model parameters from CIDc tests

Table 9.5: Summary of best-fit HySand model parameters determined from CIDc tests

test ID	p'_0 (kN/m^2)	ψ_0 (-)	D_r (%)	h (kN/m^2)	b (-)	A (-)	β_{max}(-)
m09	49.0	-0.102	42.9	80000	4.1	225	0.55
m10	48.3	-0.129	52.6	80000	4.4	400	0.75
m11	49.2	-0.160	63.5	80000	4.7	380	0.85
m12	48.9	-0.182	71.2	80000	5.1	400	1.00

To ease the calibration process, the model parameter h was kept constant in all simulations. A value of h = 80000 yielded good agreement with the initial slope of the stress strain curve, and was therefore adopted for LBS-B. However, inspection of the best-fit model parameters shows that both b and β_{max} appear to increase with decreasing state. This presents a calibration challenge, as adoption of a single value is therefore unlikely to yield a satisfactory response for all states.

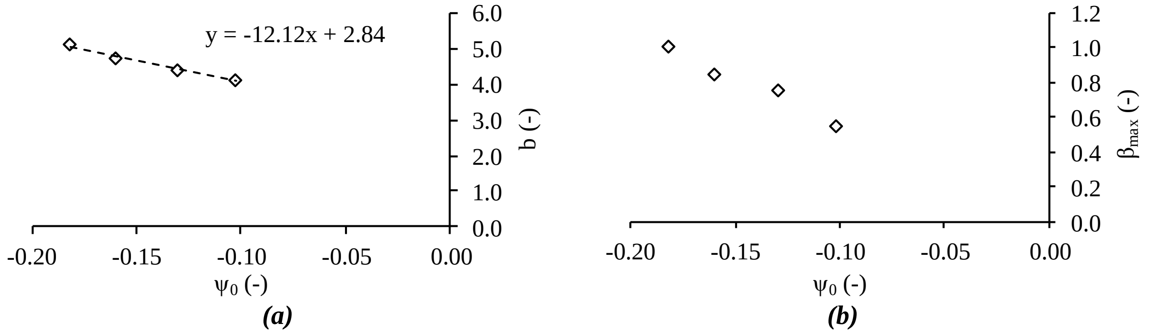

Figure 9.15: Variation of the HySand model parameters b and β_{max} with initial state, ψ_0

Figure 9.12 shows that the shape of the stress-strain curve is influenced by the magnitude of b, with lower values yielding an initially stiffer and more brittle (i.e. increased post-peak strain softening) response. As h is kept constant, it is therefore reasonable to expect that b may vary with ψ_0. The relationship shown in Figure 9.15a was therefore used for determining b in the HySand simulations:

$$b = -12.12\psi_0 + 2.84 \qquad (9\text{-}81)$$

However, despite the apparent relationship with ψ_0 shown in Figure 9.15b, HySand is formulated to be state dependent and therefore a single value of β_{max} must be specified. An average value ($\beta_{max} =$ 0.80) was therefore adopted for the LBS-B simulations. A similar approach was used for determining the rate of anisotropy development model parameter, A ($A =$ 350).

9.8. MODEL VALIDATION

This section presents validation of the CASM and NorSand models, and implementation of the stress update algorithm by comparing CIDc and CIUc triaxial test simulations against those found in the literature. Verification of the SANISAND and HySand code (obtained from external sources) is also presented via comparisons with published source material. These simulations adopted the model parameters provided in the source material.

Figure 9.16 shows results of CIDc triaxial tests for both loose and dense samples of Ersak 330/0.7 sand given in Jefferies & Been (2015). Also shown are CASM and NorSand simulations presented by Yu (2006), and Jefferies & Been (2015), respectively, along with simulations obtained using the Python single element driver developed as part of this thesis.

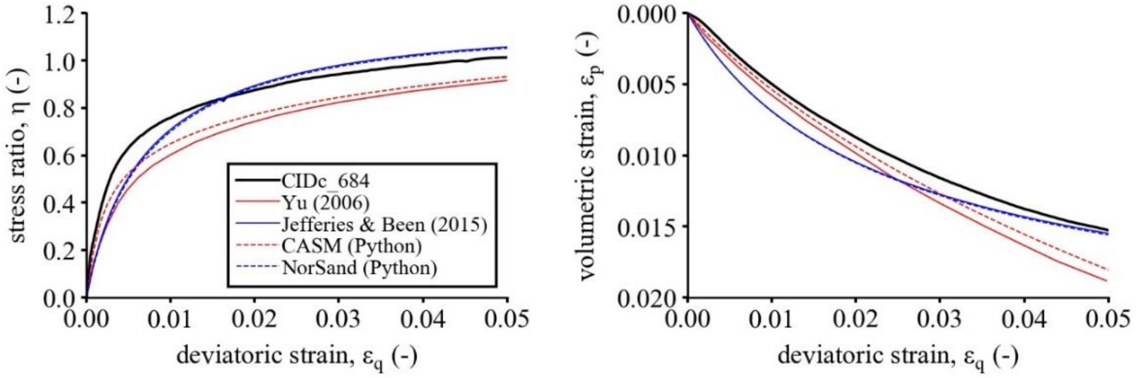

(a) Loose CIDc: e_0 *= 0.82,* p'_0 *= 200 kN/m²*

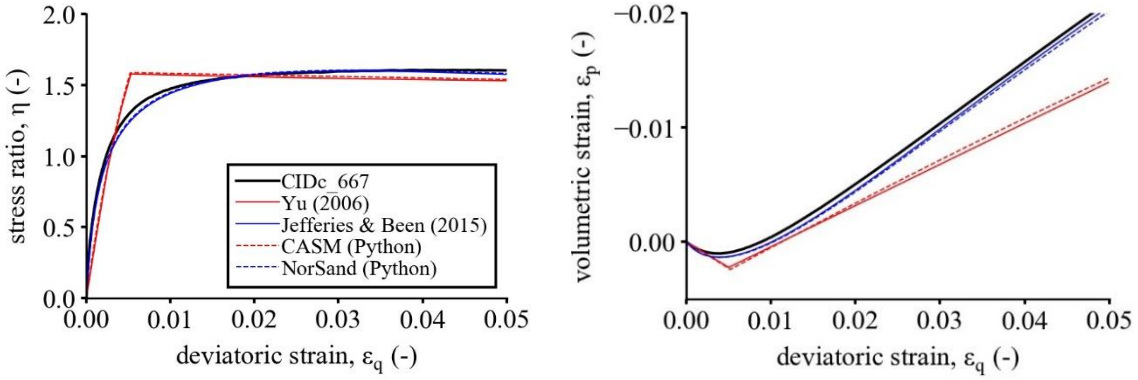

(b) Dense CIDc: e_0 *= 0.59,* p'_0 *= 130 kN/m²*

Figure 9.16: CASM and NorSand model validation of CIDc test simulations for Ersak sand

The CIDc simulations shown in Figure 9.16 yield excellent agreement with the results given in the literature for both CASM and NorSand, indicating that the model equations have been implemented correctly and the numerical integration scheme is performing as intended for CIDc tests. It should be noted that Yu (2006) does not explicitly give values of the hardening parameter, p'_c. Eq. (9-12) was therefore used to estimate initial values of p'_c, and may be the cause of the slight discrepancy observed between the Python simulations and the published curves in Figure 9.16a.

For loose sands, p'_c is generally similar to p'_0 ($p'_c \approx p'_0$ when $\psi_{ref} = \psi_0$); however, for dense sands, p'_c is found to be excessively large (e.g. for the dense CIDc test shown in Figure 9.16b, $p'_{c,0}$ = 1.48x10^{14} kN/m^2). This is a potentially significant issue as it implies that CASM may be unable to appropriately capture realistic material response for stress paths other than conventional triaxial compression and extension tests.

Figure 9.17 shows CASM simulations presented by Yu (2006) for CIUc tests undertaken on loose Ottawa sand by Sasitharan (1994). The CIUc predictions yield excellent agreement with the results presented by Yu (2006). The stress point update algorithm implemented is therefore considered validated for both CIDc and CIUc triaxial tests, and may be used with confidence in subsequent numerical modelling simulations.

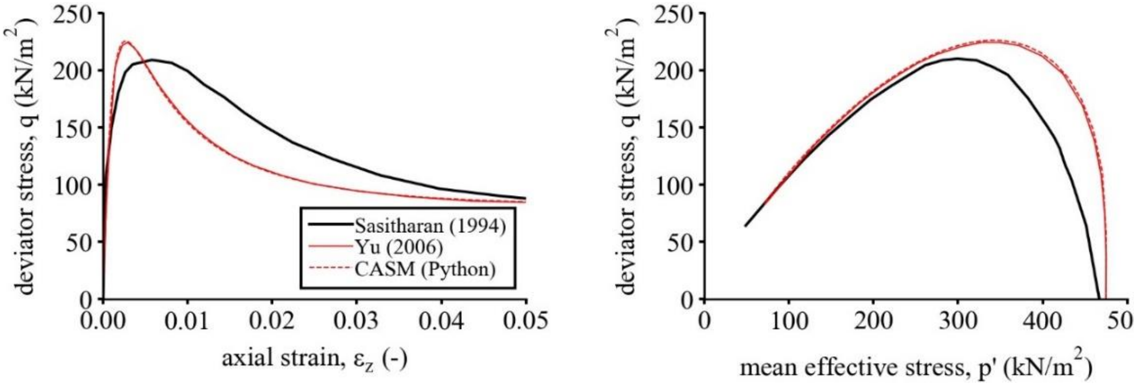

Loose CIUc: $e_0 = 0.793$, $p'_0 = 475$ kN/m^2, $p'_c = 475$ kN/m^2

Figure 9.17: CASM model validation of CIUc test simulations for loose Ottawa sand presented in Yu (2006)

9.8.1.1. SANISAND code verification

The SANISAND code used in this thesis is based on the Dafalias & Manzari (2004) model formulation. The model was implemented in Plaxis as a UDSM (user defined soil model) using the freely downloadable code developed by Dr. D. Mašín (available from https://soilmodels.com/). Plaxis simulations were performed on axisymmetric models, using a 1 m x 1 m square samples comprising two 15-noded triangular elements. Line loads were applied to the right and top model boundaries to simulate the applied confining and axial stresses, as shown in Figure 9.18. With respect to boundary conditions, the top (y_{max}) and right (x_{max}) boundaries were set to *Free*, and the left (x_{min}) and bottom (y_{min}) boundaries were set to *Normally fixed*.

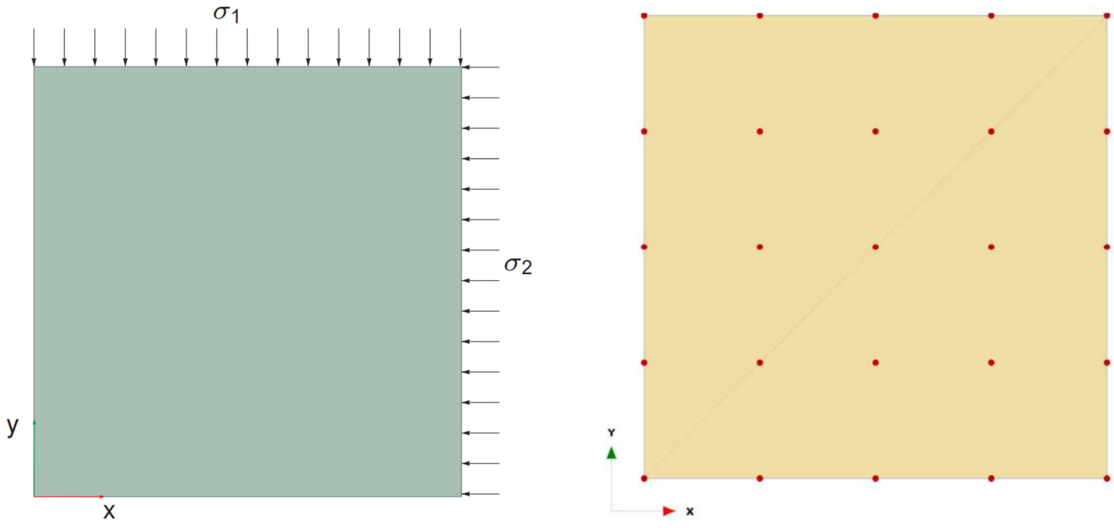

(a) (b)

Figure 9.18: Plaxis 2D triaxial test simulations showing (a) model geometry and loading conditions, and (b) mesh used in FEA simulations

Figure 9.19 shows comparisons of CIDc and CIUc model simulations presented by Dafalias & Manzari (2004) with Plaxis simulations undertaken as part of this study. Figure 9.19 shows excellent agreement between the published and Plaxis-simulated results, indicating that the SANISAND code has been correctly implemented and may therefore be used with confidence in the following sections.

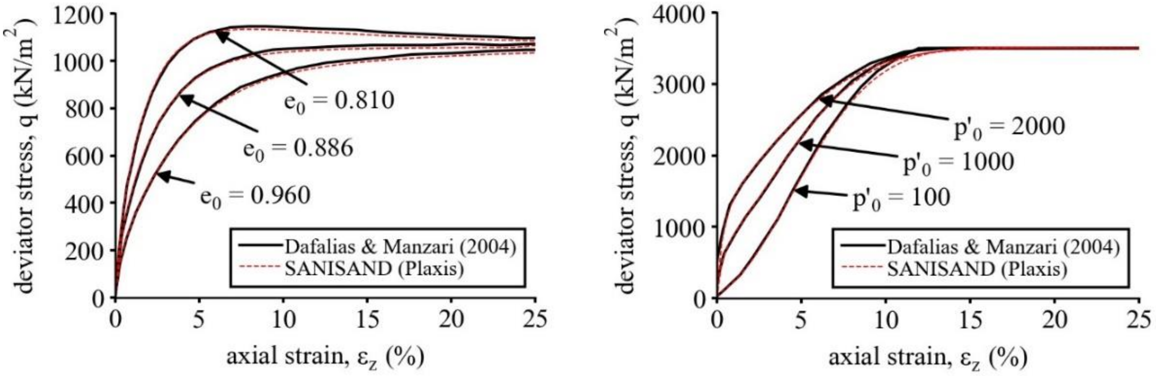

(a) CIDc: σ'_{c0} = 500 kN/m^2 ***(b) CIUc: e = 0.735***

Figure 9.19: SANISAND code verification based on results presented in Dafalias & Manzari (2004)

9.8.1.2. HySand code verification

The HySand code used in this thesis is based on the continuous hyperplasticity model described by Houlsby & Mortara (2004). The model was implemented in Python using code provided by Prof. Houlsby (personal communication). Figure 9.20 shows a comparison of a HySand triaxial test simulation against that presented in Houlsby & Mortara (2004), and shows good agreement between the published and Python-simulated results.

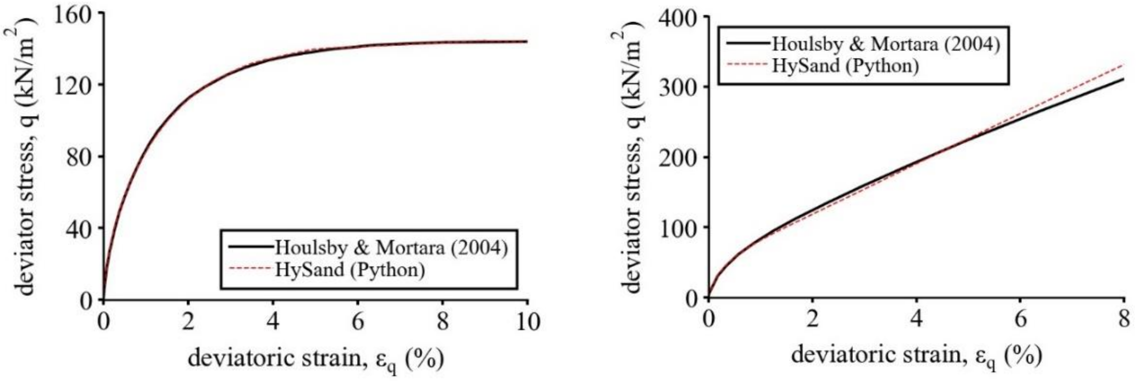

(a) CIDc ($e_0 = 0.85$) ***(b) CIUc ($e = 0.85$)***

Figure 9.20: HySand code verification based on results presented in Houlsby & Mortara (2004)

9.9. MODEL SIMULATIONS

This section presents triaxial test predictions using the CASM, NorSand, SANISAND, and HySand models. Table 9.7 summarises the model parameters determined for LBS-B used in the triaxial simulations. Figure 9.21 to Figure 9.24 show the model predictions compared against results of triaxial tests performed on LBS-B, sheared monotonically from a range of initial states and under different drainage conditions, as summarised in Table 9.6.

Table 9.6: Summary of monotonic triaxial tests performed on LBS-B to compare against model predictions

Test ID	**test type**	**preparation method**	e_0	D_r	p'_0	ψ_0
(-)	**(-)**	**(-)**	**(-)**	**(%)**	**(kN/m^2)**	**(-)**
p01	CIDc	WP	0.581	82.9	198.6	-0.188
p02	CIDc	MT	0.752	22.3	495.0	0.017
p03	CIUc	MT	0.695	42.6	348.9	-0.055
p04	CIUc	MT	0.770	16.1	495.8	0.035

Table 9.7: Summary of calibrated model parameters

model	description	parameter	CASM value	NorSand value	SANISAND value	HySand value
Common	critical state void ratio at p'_{ref}	e_{Γ}	0.950*	0.815^{+}	0.815^{+}	0.789†
	CSL parameter	λ	0.035	0.030	0.030	0.035
	CSL parameter	ξ	-	0.62	0.62	-
	slope of CSL (compression)	M_{tc}	1.31	1.31	1.25	1.31
	slope of CSL (extension)	M_{te}	0.91	0.91	0.91	0.91
	shear modulus constant	A_G	-	1400	1400	1400
	shear modulus exponent	n_G	-	0.42	0.50	0.42
	Poisson's ratio	μ	0.20	0.20	0.20	0.20
	slope of swell line	κ	0.003	-	-	-
CASM	spacing ratio	r	40.6	-	-	-
	stress state coefficient	n	4.0	-	-	-
	reference state parameter	ψ_{ref}	0.1	-	-	-
NorSand	volumetric coupling coefficient	N	-	0.46	-	-
	state-dilatancy coefficient	χ_{tc}	-	3.0	-	-
	hardening parameter	H_0	-	98.2	-	-
	hardening parameter	H_{ψ}	-	-1920	-	-
SANISAND	yield surface parameter	m	-	-	0.0655	-
	bounding surface constant	n_b	-	-	1.67	-
	dilatancy surface constant	n_d	-	-	0.89	-
	dilatancy parameter	A_0	-	-	1.10	-
	hardening parameter	h_0	-	-	1.30	-
	hardening parameter	c_h	-	-	1.30	-
	fabric index constant	z_{max}	-	-	0	-
	fabric index constant	c_z	-	-	0	-
HySand	loosest specific volume at p'_{ref}	v_B	-	-	-	1.897
	densest specific volume at p'_{ref}	v_D	-	-	-	1.480
	maximum rate of dilation	β_{max}	-	-	-	0.80
	rate of anisotropy development	A	-	-	-	350
	hardening parameter	h	-	-	-	80000
	hardening parameter	b	-	-	-	varies^

Notes:
* p'_{ref} = 1 kN/m2
$^{+}$ p'_{ref} = 0 kN/m^2,
† p'_{ref} = 101.3 kN/m^2
^ See Figure 9.15a

9.9.1. Dense CIDc Triaxial Simulations

Figure 9.21 presents CIDc triaxial test model predictions for a dense specimen of LBS-B (p01), and shows that all models are able to capture the general constitutive response of a dense sand subjected drained shearing. However, the accuracy of the model predictions (as compared with measured test data) is found to vary, with the NorSand and SANISAND models considered to yield the closest agreement with the measured test data in terms of both the stress-strain and volumetric responses.

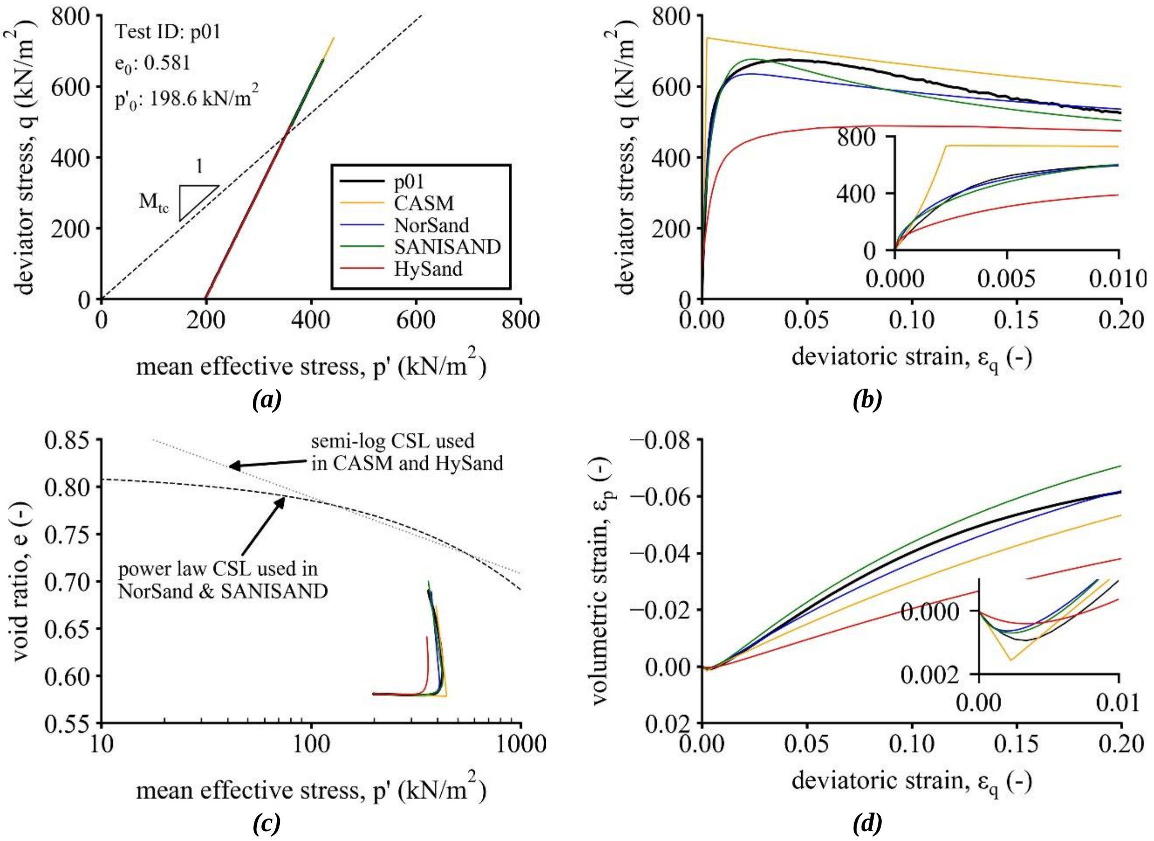

(a) *(b)*

(c) *(d)*

Figure 9.21: Comparison of dense CIDc triaxial test simulations with measured data (Test p01)

While CASM is shown to capture the general behavioural trend observed in the experiment, it is found to overpredict both the peak deviator stress and initial stiffness. This is because the size of the initial yield surface is governed by the magnitude of the initial hardening parameter, which for a dense sand tends to be very large (e.g. $p_c' = 1.4 \times 10^6$ kN/m^2 in this test simulation). The resultant elastic zone is correspondingly large, resulting in CASM significantly overpredicting the initial stiffness. Furthermore, the single yield surface used by CASM results in relatively abrupt ‘corners’ in both the stress-strain and volumetric responses, whereas the other models are shown to more realistically capture the smooth transitions observed in the test data.

The HySand model is also shown to reproduce the general trend; however, it is found to significantly underpredict both the peak deviator stress, initial stiffness, and the rate of dilation. Improved predictions of the measured data may be achieved with further ‘tuning’ of the HySand model parameters (e.g. increasing β_{max} to 1.5); however, doing so violates the purpose of these simulations, and is therefore not performed here.

9.9.2. LOOSE CIDC TRIAXIAL SIMULATIONS

Figure 9.22 shows CIDc triaxial test model predictions for a loose specimen of LBS-B. As for the dense CIDc test, NorSand and SANISAND yield high-quality predictions, and satisfactorily capture the changing stiffness observed in the test data. The CASM and HySand model predictions are less satisfactory, with CASM significantly overpredicting the initial stiffness, and underpredicting the volumetric strains, and HySand failing to capture the observed volumetric response.

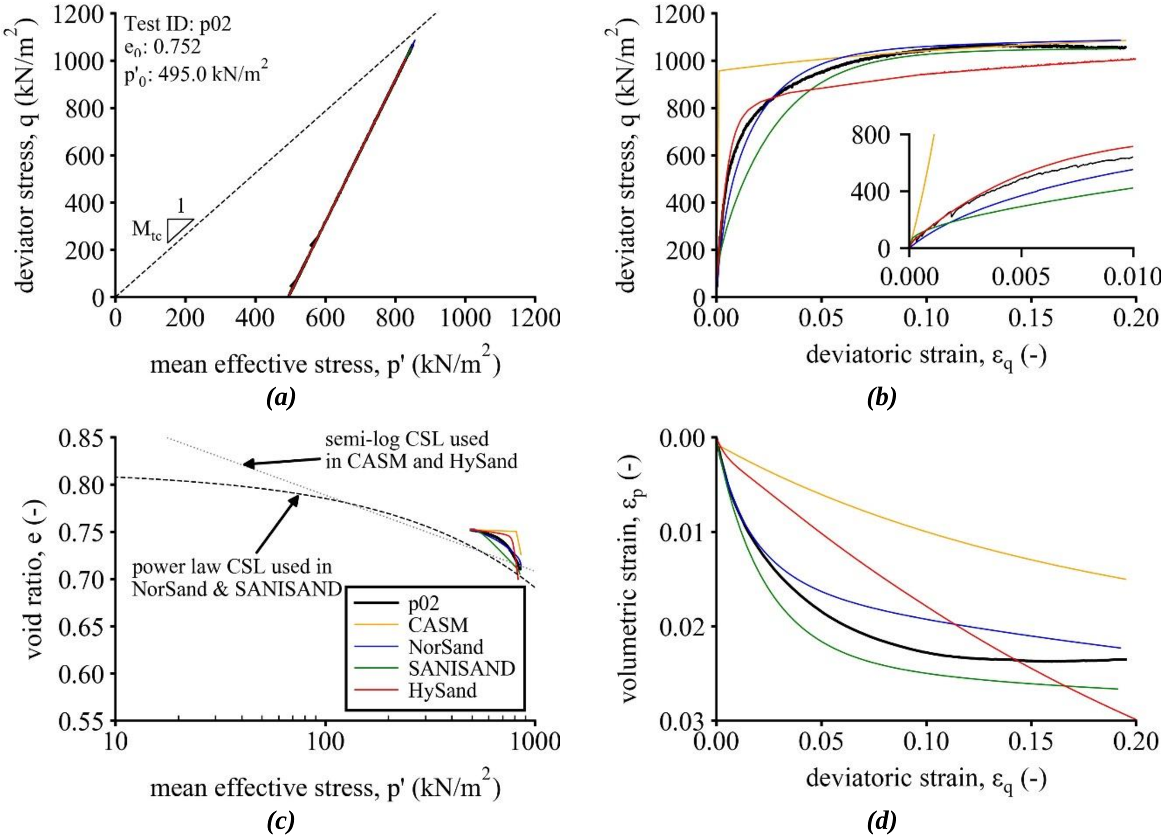

(a) *(b)*

(c) *(d)*

Figure 9.22: Comparison of loose CIDc triaxial tests simulations with measured data (Test p02)

9.9.3. CIUC TRIAXIAL SIMULATIONS

Figure 9.23 and Figure 9.24 show single element CIUc triaxial simulations for samples sheared from relatively dense and loose states, respectively. It is evident that the models are less successful at simulating the behaviour of sands subjected to undrained shearing based on the model parameter sets calibrated in this study. In particular, the HySand and SANISAND models indicate instability and collapse to $p' = 0$ in both instances.

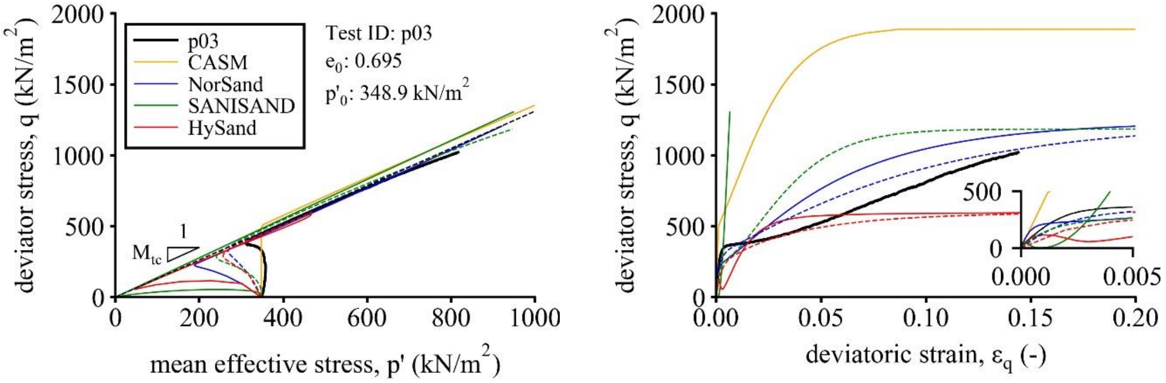

(a) ***(b)***

Figure 9.23: Comparison of dense CIUc triaxial tests simulations with measured data (Test p03)

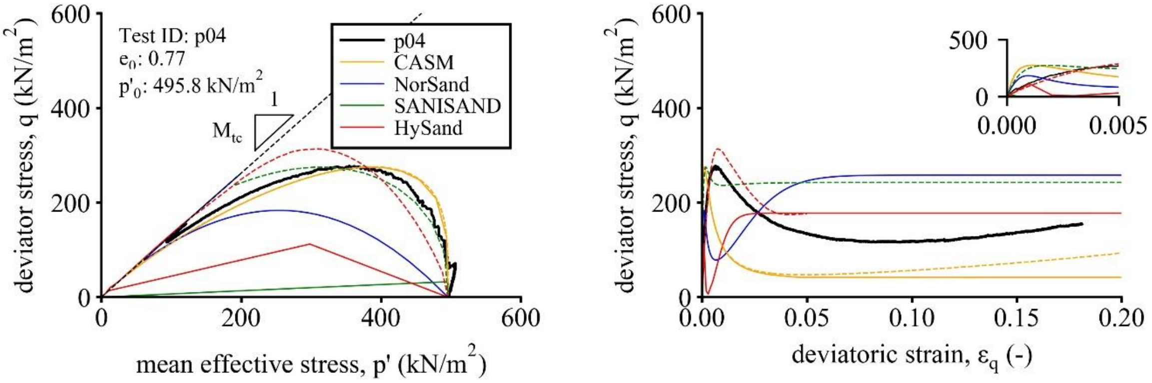

(a) ***(b)***

Figure 9.24: Comparison of loose CIUc triaxial tests simulations with measured data (Test p04)

The NorSand predictions capture the general behavioural trends; however, both the dense and loose simulations are shown to significantly underpredict the deviatoric strain at which critical state conditions are achieved. For example, in the loose CIUc test simulation, the strain softening from the initial peak deviator stress to quasi-steady state, followed by strain hardening towards critical state conditions is correctly captured by the model; however, this transition occurs much too rapidly compared with the experimental data.

Furthermore, the pre-softening peak stress is found to be significantly underpredicted by the model. Improved predictions may be obtained by artificially increasing the OCR and thus the initial image mean effective stress, $p'_{i,0}$, such that:

$$p'_{i,0} = \frac{p'OCR}{r} \tag{9-82}$$

where r is the spacing ratio that defines the offset between the NCL and CSL (Jefferies & Been (2015) suggest adopting r = 2.718 for NorSand). Alternatively, closer agreement with the measured response may be obtained by modifying the shear modulus parameter such that $A_G^u = 0.2A_G$, where A_G^u is the modified 'undrained' stiffness parameter denoted by the 'u' superscript.

Adopting a modified 'undrained' shear modulus parameter in the HySand ($A_G^u = 0.2A_G$) and SANISAND ($A_G^u = 0.075A_G$) models also yielded improved predictions; however, the SANISAND model also required significant modifications to the hardening modulus constants ($h_0 = 12$ and $c_h = 0.95$) to obtain satisfactory predictions. The NorSand, HySand and SANISAND model simulations using the modified 'undrained' stiffness parameter, A_G^u, are shown in Figure 9.23 and Figure 9.24 as dashed lines.

The CASM simulations are shown to closely replicate the shapes of the stress paths in $p' - q$ space, particularly for the loose CIUc test where it accurately predicts the initial 'pre-softening' peak deviator stress. However, as with NorSand, the value of ε_q at which this peak value is mobilised is found to be significantly underpredicted, i.e. the simulated response is much stiffer than anticipated based on the experimental test data. CASM also fails to capture the strain-hardening response following the QSS condition. As noted by Yu (2006), this type of behaviour cannot be captured with a purely volumetric hardening model such as CASM. An improved response may be obtained by incorporating an amended combined volumetric-deviatoric hardening rule of the form:

$$\delta p_c' = \frac{v p_c'}{\lambda - \kappa}\left(\delta\varepsilon_p^p + \omega\delta\varepsilon_q^p\right) \tag{9-83}$$

where ω is an additional model constant, typically ranging from 0 to 0.5. This extension to the original CASM model was termed 'CASM-d' by Yu *et al.* (2005), and is easily implementable within the Python single element driver. Figure 9.24 shows the improved prediction obtained using CASM-d (ω = 0.1); however, the simulation continues to underpredict the value of ε_q at q_{max}.

In the dense CASM simulation, the stress path moves vertically upwards until intercepting the yield surface at approximately q = 500 kN/m^2, emphasising the sensitivity of the model to the magnitude of p_c' (= 37,990 kN/m^2, suggesting an OCR of ≥ 100), and its inability to capture features such as phase transformation. The relatively high deviator stress mobilised at large strains is also significantly greater than that predicted by the NorSand model and experimental results. This difference is predominantly due to CASM's use of a semi-log CSL, leading to the mobilisation of greater p' values before the model intercepts the CSL in $e - \ln(p')$ space.

9.9.4. CYCLIC LOADING

This section presents comparisons of numerical model simulations with both undrained cyclic triaxial test data and monotonic triaxial tests that included unload-reload stages, as summarised in Table 9.8. Cyclic loading is considered beyond the capabilities of the original version of CASM, and therefore CASM predictions are not presented in the following.

Table 9.8: Summary of monotonic and cyclic triaxial tests selected for comparison with model predictions

Test ID (-)	**test type** (-)	e_0 (-)	D_r (%)	$\sigma'_{c,0}$ (kN/m^2)	p'_0 (kN/m^2)	ψ_0 (-)	q_{av} (kN/m^2)	q_{cyc} (kN/m^2)
s03	CIDc	0.586	81.0	14.1	14.1	-0.220	-	-
u01	CIUc	0.580	83.3	49.7	49.7	-0.216	-	-
c01	Cyclic CIU	0.584	82.0	51.0	63.6	-0.211	38.0	38.0
c11	Cyclic CIU	0.583	82.3	49.4	49.4	-0.213	0	38.0

9.9.4.1. CIDc Test with unload-reloading

Figure 9.25 shows model predictions of a dense LBS-B CIDc test (s03, described in Chapter 6) performed at a relatively low confining stress ($\sigma'_{c,0}$ = 14.1 kN/m^2), that included monotonic ($\dot{\varepsilon_z}$ = 0.5 % / hour) unload-reload stages during shear. Dotted lines represent model predictions without inclusion of unload-reload loops.

Figure 9.25c shows that the HySand model accurately simulates both the shape and area enclosed by the hysteresis loop observed in the experimental data in both $\varepsilon_q - q$ and $\varepsilon_q - \varepsilon_p$ space. The SANISAND simulation (Figure 9.25b) also correctly simulates the general trends observed in the experimental data; however, the simulation shows a response that is much too soft on reloading. However, all models tend to overpredict the magnitude of plastic softening mobilised during unloading, indicated by an underestimation of the point of intersection of the unload-reload loop on reloading.

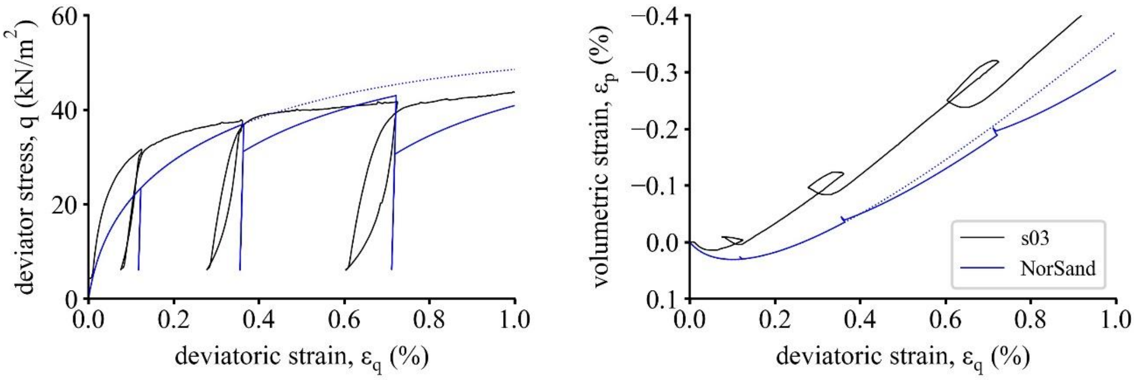

(a) NorSand model prediction

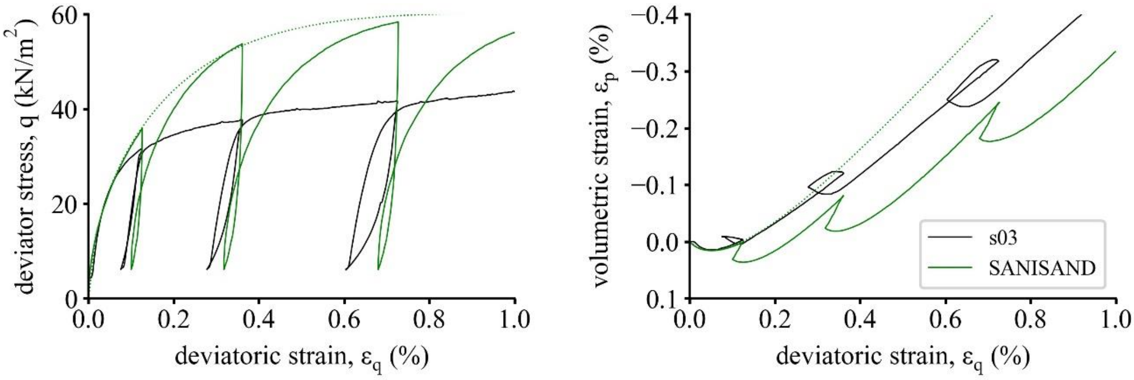

(b) SANISAND model prediction

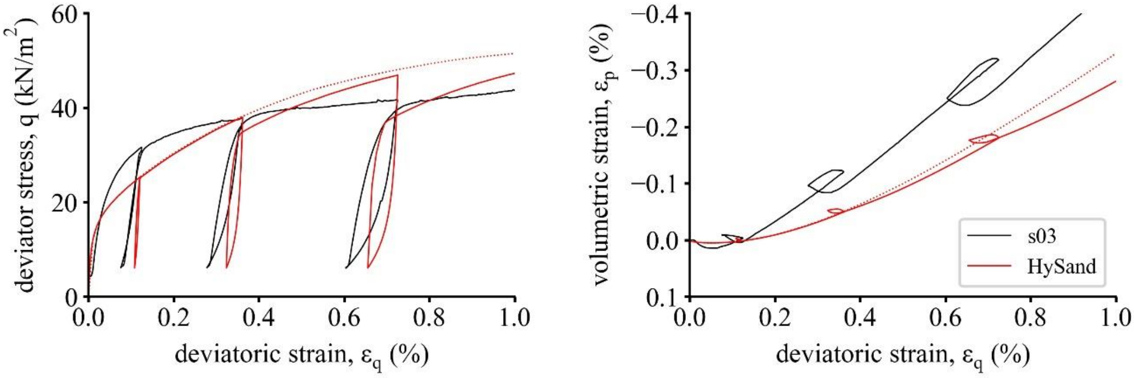

(c) HySand model prediction

Figure 9.25: Comparison of model predictions with CIDc test data (s03) involving unload-reload loops

The NorSand simulation yields the least satisfactory prediction of drained cyclic loading, and predicts purely elastic behaviour during the first unload-reload loop. This is due to the stress path failing to intercept the internal cap used in the NorSand model formulation. However, though not visible at the scale shown in Figure 9.25a, the simulation correctly captures the hysteretic behaviour and characteristic loop shape in the second and third unload-reload loops.

9.9.4.2. *CIUc Test with unload-reloading*

Figure 9.26 shows model predictions of a CIUc test (u01) performed on a dense specimen of LBS-B, that included monotonic ($\dot{\varepsilon}_z$ = 0.5 % / hour) unload-reload stages during undrained shear. Dotted lines represent model predictions without including unload-reload loops. Figure 9.26 shows that none of the model simulations yields particularly satisfactory predictions of the test data. However, while the HySand and SANISAND model simulations are able to at least capture the general trends observed in the experimental data, the NorSand simulation fails to do so.

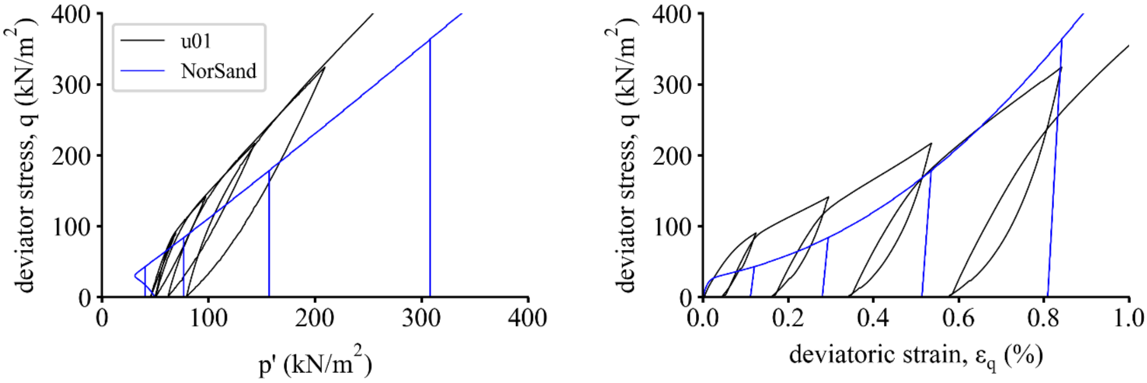

(a) NorSand model prediction

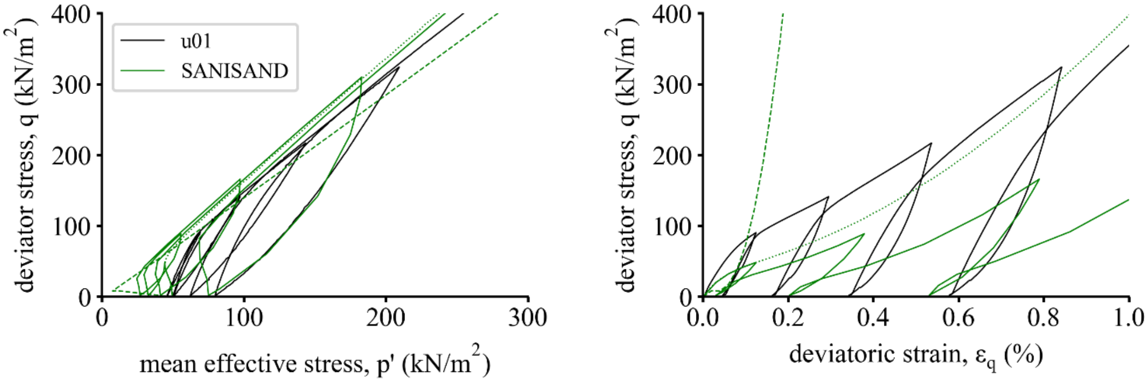

(b) SANISAND model prediction

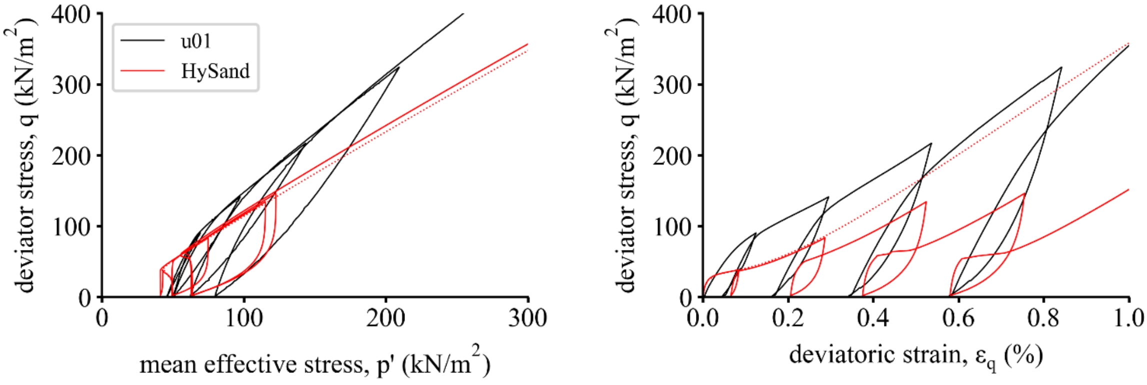

(c) HySand model prediction

Figure 9.26: Comparison of model predictions with CIUc test data (u01) involving unload-reload loops

Furthermore, inspection of the experimental stress path shows a response similar to that idealised in Figure 5.5c. This is expected given the relatively high density of the test specimen (D_r = 83.3 %); however, none of the models captures this type of response, and instead this predicted stress paths that are more consistent with the one idealised in Figure 5.5d, representative of a less dense material initially located closer to the CSL in $e - \ln(p')$ space.

Initial SANISAND predictions using the parameter set defined in Table 9.7 were found to exhibit similar issues to those discussed in Section 9.9.3, i.e. high deviator stresses were mobilised at significantly lower deviatoric strains than observed in the test data (as shown by the dashed line in Figure 9.26b). Therefore, the SANISAND model prediction presented in Figure 9.26b (solid line) was obtained using the ‘undrained’ shear stiffness and modified hardening modulus parameters ($A_G^u = 0.075A_G, h_0 = 12$ and $c_h = 0.95$). The resultant stress path shows reasonable agreement with the test data in terms of both shape and area enclosed by the unload-reload cycle; however, as observed for drained cyclic loading, the point of intersection of the stress-strain loop on reloading is significantly underpredicted in both the SANISAND and HySand model predictions.

The vertical stress paths exhibited during load cycling in the NorSand model predictions are typical of single yield surface constitutive models, and represent a significant shortcoming of such models for predicting undrained cyclic behaviour. Furthermore, given that the stress path is vertical, the internal cap will never be intercepted. As a result, no plastic softening of the outer yield surface occurs, and purely elastic behaviour is simulated during undrained load cycling. This is clearly unrepresentative of the behaviour observed in the test data.

9.9.4.3. Undrained Cyclic Triaxial Tests – One way loading

Figure 9.27 shows the undrained cyclic triaxial model simulations considering one-way loading, compared against experimental data (test c01, described in Chapter 7). Given the inability of the NorSand model to satisfactorily simulate undrained cyclic loading, only HySand and SANISAND model predictions are presented in the following. Furthermore, only the first 10 cycles from the model simulations are shown for clarity.

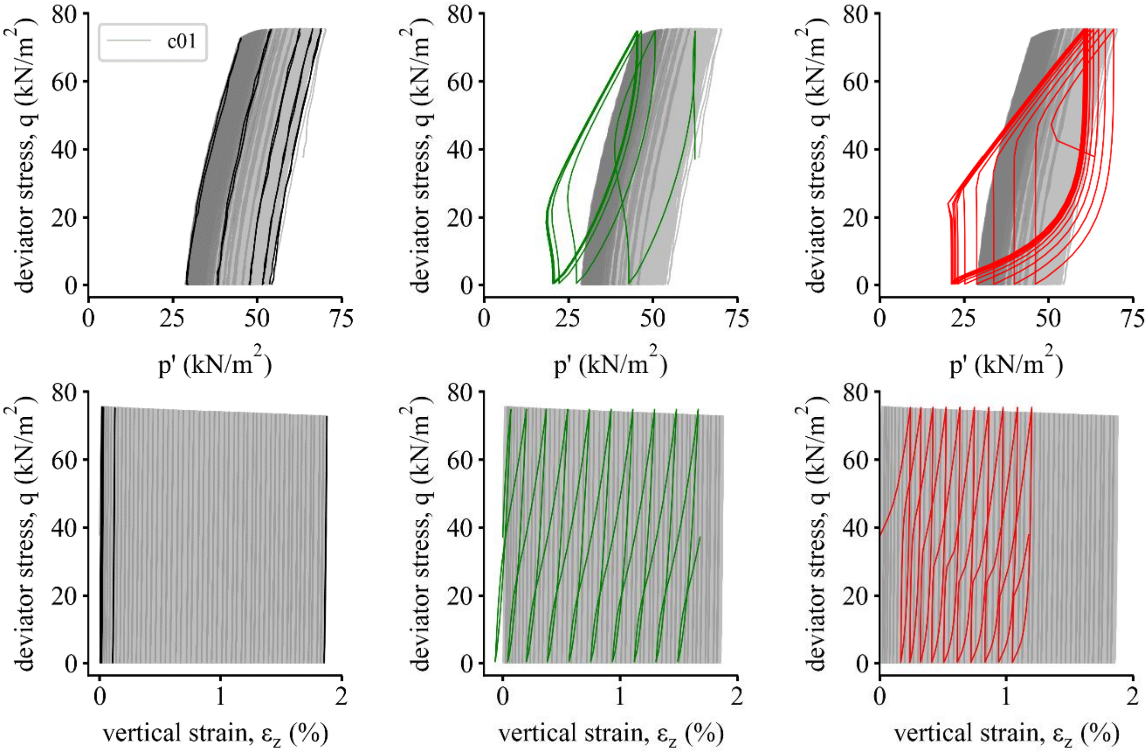

(a) Test data ***(b) SANISAND (N = 10)*** ***(c) HySand (N = 10)***

Figure 9.27: Comparison of model predictions with undrained, one-way loading, cyclic triaxial test (c01)

Test c01 sustained 10,000 load cycles, and exhibited a gradual decrease in mean effective stress with increasing cycle number. Cycle number 1, 10, 100, 1000 and 10000 are highlighted on Figure 9.27a, and indicate that approximately 2 % vertical strain was accumulated at the end of the test. As with previous undrained simulations, the SANISAND model parameters were modified to improve the model performance and reduce numerical stability issues.

Figure 9.27 shows that the models perform poorly in terms of both reproducing the shape and orientation of the stress paths, and significantly overpredict the magnitude and rate of accumulation of vertical strain. Furthermore, both models fail to capture the gradual reduction in mean effective stress exhibited in the test data, and instead rapidly tend towards zero, resulting in conditions of cyclic mobility occurring in less than 10 load cycles.

9.9.4.4. Undrained Cyclic Triaxial Tests – Two way loading

Figure 9.28 shows undrained cyclic triaxial model simulations considering two-way loading, compared against experimental data (test c11, described in Chapter 7). Test c11 reached conditions of initial liquefaction (R_u = 1.0) after approximately six load cycles, and was terminated after 20 load cycles. Cycle numbers 1 and 10 are emphasised in black in Figure 9.28a.

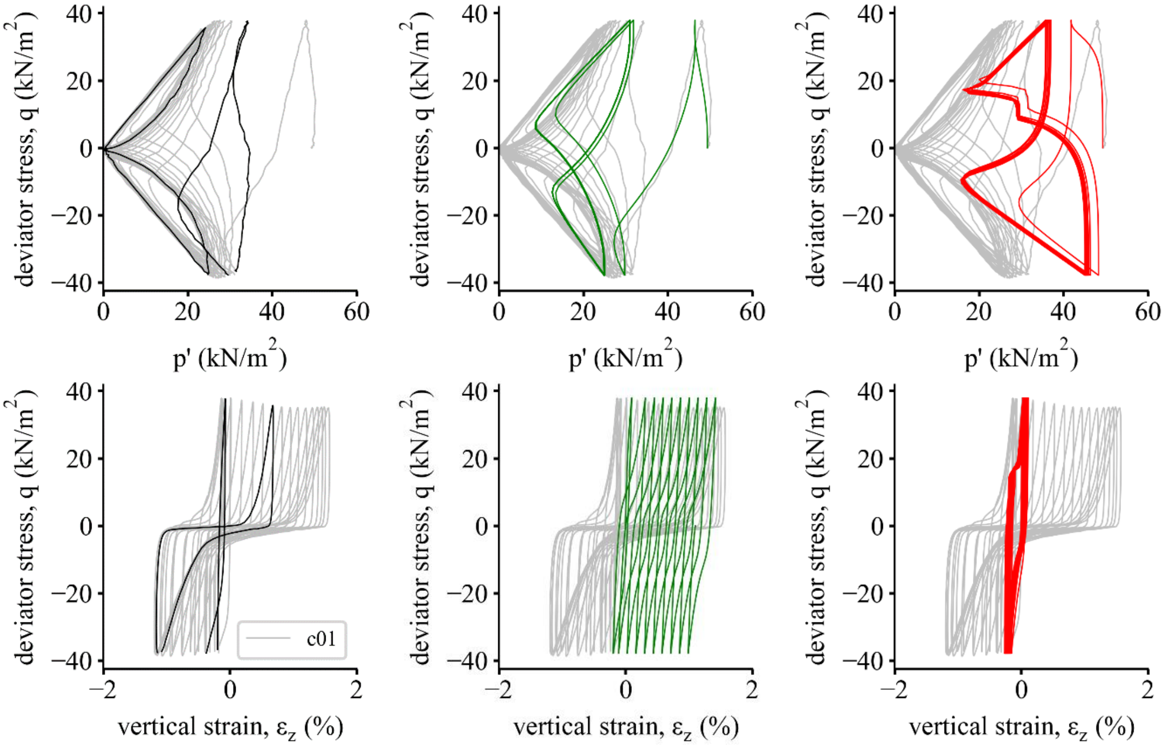

(a) Test data ***(b) SANISAND (N=10), AGU*** ***(c) HySand (N = 10)***

Figure 9.28: Comparison of model predictions with undrained, two-way loading, cyclic triaxial test (c11)

Figure 9.28 shows that the models are able to capture the general trends observed in the test data, and correctly mobilise failure conditions within relatively few cycles. However, neither simulation reaches conditions of zero mean effective stress, and both fail to reproduce the characteristic 'butterfly' shape associated with the initial liquefaction failure criterion. In particular, the 'figure of eight' stress path simulated by the HySand model is considered a poor match compared with the experimental data, and fails to reach the failure envelope indicated in the test data.

Furthermore, both models fail to capture the shape of the stress-strain curves, particularly with respect to the accumulation of negative vertical strain observed in the test data. Figure 9.28b shows that the SANISAND model yields a reasonable prediction of the magnitude of vertical strain mobilised after 10 cycles. However, HySand significantly underestimates both the rate of accumulation and magnitude of vertical strain, which is curious given the overprediction of strain rate accumulation simulated in the one-way loading test (Figure 9.27c).

9.10. SUMMARY AND CONCLUSIONS

9.10.1. CONSTITUTIVE MODEL PERFORMANCE

The purpose of this assessment was to ascertain whether a single set of calibrated model parameters is able to yield satisfactory predictions of dense and loose sand behaviour in both drained and undrained conditions, and for both monotonic and cyclic loading. Comparisons of model simulations with experimental data indicate that this may not be possible, at least, not based on the model parameters determined as part of this study. This is in agreement with Wichtmann *et al.* (2019), who also concluded that it was "impossible" to obtain a single set of model parameters for the three sophisticated, state-dependent constitutive models considered in their analysis.

The relatively poor model predictions obtained in the undrained test simulations may be a result of the calibrated model parameters being determined predominantly from drained triaxial compression tests. As noted by Cerfontaine (2014), independent calibration of model parameters from drained and undrained test data leads to the definition of two distinct sets of parameters. This point is seldom highlighted in numerical modelling publications, which tend to present model simulations for a single drainage condition. To overcome these issues, numerical modelling practitioners appear to have either:

1. Modified parameters beyond normal limits, e.g. Dafalias & Manzari (2004) used μ = 0.05 in their parameter set to obtain satisfactory predictions of drained and undrained tests;
2. Introduced additional elastic stiffness degradation rules to account for the degradation of elastic stiffness that occurs during shearing (Loukidis & Salgado, 2009; Taborda *et al.*, 2014)

The modified 'undrained' shear modulus parameter, A_G^u, proposed in this study and used in the undrained SANISAND model simulations, effectively achieves the same end as item 2 (albeit in a simpler manner), and is conceptually similar to the E_{fact} parameter used by Whyte (2019):

$$\boldsymbol{D^{ep}} = E_{fact}\boldsymbol{D^e} - \frac{E_{fact}\boldsymbol{D^e}\boldsymbol{b}\boldsymbol{a^T}E_{fact}\boldsymbol{D^e}}{\boldsymbol{a^T}E_{fact}\boldsymbol{D^e}\boldsymbol{b} + A} \tag{9-84}$$

It is therefore important to understand what measures are incorporated within a chosen constitutive model when performing undrained FEA in real design situations, as model parameters calibrated predominantly to CIDc test data may overpredict the stiffness response, leading to potentially unconservative designs.

The formulation (e.g. semi-log or power function) and location of the CSL has also been shown to strongly influence the predicted response of drained sands subjected to undrained shearing. As shown in Figure 9.23, adopting a semi-log CSL in the CASM model leads to significantly higher predictions of q_{max} than observed in the test data, and is therefore likely to be highly unconservative. However, as discussed in Section 9.2.1, typical site investigation campaigns and laboratory test programmes tend to focus on reconstituting materials to in situ (usually dense) states. Determining the CSL from such tests is therefore likely to underpredict the location of the CSL in $e - \ln(p')$ space. While this approach is likely to result in conservative estimates of q_{max}, CSLs determined in this way are unlikely to yield realistic predictions of in situ behaviour when used in FEA simulations.

The monotonic model simulations presented in this chapter show that none of the models are able to satisfactorily capture the constitutive response of LBS-B using a single parameter set. However, of the models investigated as part of this study, NorSand is considered to represent the most versatile and user-friendly model in terms of ease of implementation and calibration. Its predictive capability is also found to be comparable to SANISAND for modelling CIDc tests, and was found to be generally more numerically stable when predicting undrained tests. It also offers a significant improvement in terms of predictive capability over less sophisticated models such as CASM (and Mohr-Coulomb). The calibration procedure is also simpler than that required for SANISAND and HySand, which involve considerable ‘trial and error’ to determine several parameters.

The cyclic test simulations presented in this chapter show that both SANISAND and HySand yield reasonable predictions for drained cyclic loading conditions. However, both models produce unsatisfactory predictions of undrained cyclic loading, and are only able to capture basic trends. Improved simulations of the experimental data were possible; however, to achieve this required time-consuming, iterative adjustment of model parameters, which is considered both impractical from a (commercial) design perspective, and in violation of the ideal requirement for a single, robust set of calibrated model parameters.

It is also worth noting that the version of the SANISAND model used in this study (Dafalias & Manzari, 2004) fixed some parameters (e.g. the shear modulus exponent, n_G is set at 0.5), possibly to avoid criticism associated with high numbers of model parameters. However, such practice is not recommended, with increased model parameters being a necessary by-product of flexible models, capable of capturing the complex constitutive behaviour exhibited by sands. Furthermore, in agreement with Lade (2005), the effort and expense involved in obtaining reliable experimental results represents a small effort compared to determining model parameters – provided the correct tests are performed.

NorSand was found to be less successful at simulating cyclic loading, particularly for undrained loading conditions. Realistic model predictions of cyclic behaviour rely on the interception of the internal cap to cause plastic softening of the outer yield surface during unloading. However, it has been demonstrated that this is a significant shortcoming, given that for undrained loading conditions, and certain drained stress paths (e.g. constant mean effective stress), interception of the internal cap will not occur.

9.10.2. TESTING RECOMMENDATIONS FOR CALIBRATION OF ADVANCED CONSTITUTIVE MODELS

This chapter set out to provide practical recommendations and transparent guidelines associated with the selection of constitutive models for sand, and associated calibration processes that are needed for such models for use in FEA. It has been shown that a relatively modest experimental test programme is capable of calibrating four sophisticated constitutive models for sand.

However, it has also been shown that despite the potential predictive capability of these models, calibration is not always straightforward, and a single set of model parameters for all initial states, drainage conditions, and loading conditions is unlikely to exist. Nevertheless, the following summarises the minimum number of laboratory tests considered necessary to provide a reasonable calibration of such constitutive models for sand:

1. Classification tests for index parameters required for sample reconstitution calculations:
    - Limiting density (e_{max} and e_{min}), PSDs, and particle density tests;
2. Triaxial compression tests on loose (ψ > 0) specimens to determine the CSL in $e - ln(p')$ space:
    - Minimum of four CIUc tests, and two CIDc tests, preferably employing sample freezing techniques, and enlarged lubricated end platens;
3. Drained triaxial compression tests with bender elements to develop shear modulus relationship:
    - Minimum of four dense CIDc tests, performed at constant e_0, with increasing p'_0;
4. Constitutive model specific tests:
    - Four CIDc tests, with variable e_0, constant p'_0;
        - To verify M_{tc} obtained from loose CIUc tests, and also obtain state-dilatancy parameters (e.g. $\chi_{tc}, A_0, n_b, n_d, \beta_{max}$ etc.);
    - Optional CIDe / CIUe tests to ascertain the critical stress ratio M_{tc} / M_{te};
        - Such tests should be interrogated and used with caution (see Section 6.4).

The chapter has emphasised the importance of undertaking a bespoke test plan tailored to finding the location of the CSL. It is argued that conventional experimental programmes, focussed on characterising samples subjected to initial conditions representative of those found in the field, should be of secondary importance, if it is known that FEA with an advanced constitutive model is likely to be required during design. Modern commercial testing laboratories therefore need to upskill in terms of available sample reconstitution techniques and equipment, to meet the anticipated demand for the high-quality sand test data needed to reliably calibrate modern constitutive sand models.

10. CONCLUSIONS

This thesis has explored the constitutive response of a dense sand sheared at low effective confining stresses. A comprehensive review of the literature has been presented, including the current state-of-the-art with respect to experimental testing best practice, sample preparation methods, and the various constitutive models and frameworks used to model sand behaviour.

An extensive experimental test programme has been completed. Drained stress path tests allowed the monotonic behaviour at low effective confining stresses to be systematically investigated. High cycle cyclic triaxial tests, incorporating low stress amplitude, undrained cyclic loading have enabled exploration of material behaviour for conditions analogous to the type of loading experienced by offshore renewable energy structures.

Four sophisticated constitutive models have been examined. Issues associated with the ease of implementation, calibration procedure, and predictive capability have been discussed. Recommendations relating to scoping laboratory testing schedules to permit calibration of such models have been proposed.

Summary sections presented at the end of each chapter have presented detailed conclusions. This chapter therefore aims to distil only the key contributions and implications for design. Suggestions for further work are also provided.

10.1. KEY CONTRIBUTIONS

The key contributions arising from this study are presented below:

10.1.1. NEW SOIL TEST DATABASE

According to Cerfontaine (2014), when developing advanced constitutive models, “surprisingly, the hardest step of the calibration of parameters is the finding of data to be calibrated.” It has been shown that the commercially available testing devices used in this thesis are capable of performing both monotonic stress path and cyclic triaxial tests, from which reliable results have been obtained. The results presented in this study therefore provide the basis of a new database of experimental tests, performed in a systematic manner with consistent test procedures and sample preparation methods, which may now be used to inform the calibration, evaluation and development of advanced constitutive models.

10.1.2. MONOTONIC RESPONSE AT LOW CONFINING STRESSES

Experimental data obtained in this study have shown that the mean effective confining stress has a minor influence on the effective stress shear strength properties (η_{max} and ϕ'_{max}) for tests undertaken at initial effective confining stresses, $\sigma'_{c,0}$, less than 50 kN/m^2. This behaviour may be explained in terms of the state parameter, ψ, and supports the notion of a critical state line that curves towards a horizontal asymptote in the e: ln (p') plane at low stress values. Tests undertaken at higher stress levels (i.e. $\sigma'_{c,0} \geq 100$ kN/m^2) show a stress level effect, with decreasing η_{max} and ϕ'_{max} values mobilised with increasing $\sigma'_{c,0}$ values. This has useful implications for practice, as it indicates that the increased shear strength response mobilised at lower stress levels may be adequately characterised from tests performed at relatively high $\sigma'_{c,0}$ values (i.e. $\sigma'_{c,0} = 50$ kN/m^2). Therefore, scheduling tests at more challenging low stresses (i.e. $\sigma'_{c,0} \leq 12$ kN/m^2), where testing issues (e.g. applied corrections, instrumentation accuracy, temperature fluctuations etc.) become increasingly influential on the calculated response, may be unnecessary.

The magnitude of the small-strain shear modulus, G_0, estimated from bender elements, local small-strain instrumentation, and unload-reload cycles has been examined. Results obtained in this thesis have shown that for Leighton Buzzard sand (Fraction B), bender element derived G_0 values are significantly higher than would be predicted from commonly used empirical relationships. This results in the determination of a relatively high material constant parameter, $A_G \approx 1400$.

Similarly, the magnitude of the shear stiffness estimated from unload-reload loops was shown to be influenced by the strain level at which the unload-reloading was performed. This has important implications for practice, as calibration of constitutive models based on such tests may yield unrepresentative and potentially unconservative predictions.

10.1.3. CYCLIC RESPONSE AT LOW CONFINING STRESSES

This study has created a new database of undrained cyclic triaxial tests, performed within a new, robust cyclic framework, that allows for easier comparisons with model and field pile testing publications. Furthermore, the cyclic loading characteristics used in this study cover an area of cyclic stress that was both largely unpopulated, and potentially more representative of the actual loading conditions sustained by offshore renewable energy structures.

The undrained cyclic triaxial tests presented in this thesis exemplify the complexities of the material response when subjected to cyclic loading. However, the experimental results have shown clear and systematic trends, that are adequately and robustly captured by the new cyclic framework adopted in this study. For example, it has been shown that predictions of the general behavioural response under cyclic loading may be obtained using the ζ_b and ζ_c parameters. For Leighton Buzzard sand (Fraction B), failure and subsequent instability was generally observed in all tests where stress reversal occurred (i.e. $\zeta_c < 0$). Conversely, tests performed at relatively low ζ_b values, and which did not undergo stress reversal (i.e. $\zeta_c > 0$) were generally stable and able to sustain 10,000 load cycles without reaching failure conditions.

The secant stiffness and material damping properties of Leighton Buzzard sand (Fraction B) under cyclic loading have been investigated. Results obtained in this study show good agreement with trends reported in the literature, and may be reasonably predicted with empirical relationships (e.g. Darendeli, 2001). However, the experimental data showed a poor match with predictions made using empirical relationships, and found that LBS-B mobilises significantly larger ξ values, in terms of both the gradient of the material damping curve and ξ_{max}.

The results presented in this thesis have therefore shown that use of empirical relationships and generic material damping profiles may fail to capture the complex response. This has significant implications for the design of OWT foundations, given the sensitivity of the structural response to the material damping properties of the foundation material. Use of empirical relationships and generic material damping profiles in the design of these structures is therefore not recommended.

10.1.4. CONSTITUTIVE MODEL EVALUATION

The calibration and evaluation of four sophisticated constitutive models has highlighted several shortcomings associated with the current state-of-the-art. Firstly, it has been shown that use of a single set of calibrated model parameters is unlikely to yield satisfactory predictions of material behaviour for all states and drainage conditions. In particular, undrained model simulations based on calibrated model parameters derived principally from drained triaxial compression tests, have been shown to result in poor predictions compared with real test data.

However, provided these model shortcomings are known and anticipated, additional corrections such as the use of a reduced, ‘undrained’ material stiffness constant, A_G^u, may be employed that result in reasonable model predictions of undrained monotonic behaviour. In terms of ease of implementation, calibration, and predictive capability for monotonic shearing conditions, the NorSand model has been shown to offer good performance, and represents a significant improvement over simpler models such as CASM and the traditional Mohr-Coulomb model.

However, due to the single yield surface adopted by the NorSand formulation, it has been shown to be unsuitable for modelling undrained cyclic loading. More sophisticated bounding surface (e.g. SANISAND) or kinematic hardening (e.g. HySand) models have been shown to offer improved predictive performance and are therefore required to capture the general behavioural trends. However, the model evaluation presented in this study has shown that despite the relative sophistication of such models, simulations of sustained, undrained cyclic loading remain unsatisfactory, and they fail to capture all but the most basic behavioural trends.

Use of such models in engineering practice to predict the long-term behaviour of offshore wind turbine structures should therefore be approached with caution. However, it has been shown that the models tend to overpredict the rate of strain accumulation, and underpredict the cyclic resistance of the soil (i.e. the number of load cycles the soil can sustain before failure conditions are reached), and are therefore likely to provide conservative predictions.

This study has also shown that it is possible to calibrate four distinct constitutive models from a relatively modest experimental test programme. This has useful implications for engineering practice, as the personnel responsible for scheduling laboratory testing programmes are not always aware of the testing requirements associated with a particular constitutive model. Furthermore, the specific constitutive model(s) to be adopted in the detailed design phase is typically not known until after completion of the site investigation campaign, and the subsequent onshore laboratory testing programme. Adherence to the minimum sand laboratory testing programme proposed in Section 9.10.2 would therefore ensure that sufficient tests are undertaken to enable reasonable calibration of some commonly used advanced constitutive models.

This study has also emphasised the importance of undertaking a bespoke test plan tailored to finding the location of the CSL. It has been argued that conventional experimental programmes focussed on characterising samples prepared to initial conditions representative of those found in the field are unlikely to meet the requirements of a robust calibration test programme, and should be of secondary importance if it is known that FEA with an advanced constitutive model is likely to be required during the design phase of a project.

10.2. FUTURE WORK

This section presents suggestions for future work based on findings arising from this study.

10.2.1. INFLUENCE OF FINES CONTENT AND SAMPLE PREPARATION METHOD ON THE BEHAVIOUR AT LOW STRESS LEVELS

All low stress triaxial tests were undertaken on a relatively clean, dense sand, reconstituted using the wet pluviation technique developed as part of this study. This sample preparation method is not suitable for materials containing more than approximately 5 % fines. Given the relatively high silt content of typical natural North Sea sands (Jones *et al.*, 2020), the influence of fines content on the constitutive response needs to be verified. Further tests on cohesionless soils at low stress levels with varying fines content are therefore required to confirm the findings presented in this study.

Preparation of homogenous samples with varying silt content requires adoption of alternative sample reconstitution techniques such as the slurry deposition method described by Dominguez-Quintans *et al.* (2019). Further development of this method to facilitate use of enlarged lubricated end platens and horizontal bender elements is therefore recommended.

10.2.2. EXPANSION OF SAND TEST DATABASE

The creation of a database of tests performed on a single test material is of great value to numerical modelling researchers. While the test programme presented in this thesis is considered to be a useful contribution, expansion of the database to include additional soil element test types (e.g. simple shear, resonant column) would provide further value by enabling constitutive model developers to explore shearing modes other than triaxial stress conditions.

Furthermore, it is the author's opinion that the soil element testing community in both academia and industry lacks a set of universally accepted test results. Historically, universities and soil testing equipment manufacturers have developed their own soil testing apparatus, and subsequently published results without any validation of how their test equipment performs in comparison with other brands / testing laboratories etc. Such practices have therefore led to the current, unsatisfactory situation, where the measured response may be significantly influenced by human factors such as the person responsible for setting up the test, and the particular piece of testing apparatus used (Ramsey *et al.*, 2017). Development of an accepted set of test results on a widely available standard test material will therefore drive up standards in the industry and promote consistency between commercial testing laboratories.

10.2.3. NUMERICAL MODELLING

The findings presented in this thesis indicate that further efficiencies in the design of offshore renewable energy foundations may be realised by exploiting the increased shear strengths that may be mobilised in the shallow, low stress zones of the foundations. It is therefore recommended that finite element analyses be performed, to investigate the influence and potential benefit of accounting for these shallow, higher strength soils, for typical offshore geotechnical structures.

10.2.4. CONSTITUTIVE MODELLING

Further work to develop the performance of sand constitutive models for predicting cyclic and pseudo-random loading is recommended. In particular, while HySand showed promise for predicting the cyclic response, monotonic test predictions were less satisfactory. The fact that the β_{max} model parameter needs to be treated as a constant, despite evidence indicating that it may vary as a function of state, seems to be a key limitation of the current version of the model. More sophisticated functions relating β_{max} to the current state are therefore recommended in future developments of the model.

10.3. OVERVIEW

As the design of geotechnical structures becomes more efficient, some of the inherent conservatism built into the design methods is lost. While this is attractive from an economic perspective, the current trend of using increasingly large wind turbines, and the move to deeper waters with associated harsher met-ocean conditions, brings new challenges to the designer. In such circumstances, the cyclic design and long-term performance of the structure may become critical.

This thesis forms part of a coordinated programme of research at the University of Oxford, which aims to further develop practical cyclic design methods for the next generation of offshore wind turbine foundations. Through acquisition and development of a new soil element testing laboratory, a new high quality database of experimental test results has been created, providing useful insights into the behaviour of dense sands at low stress levels, subjected to both monotonic and cyclic shearing.

The experimental programme of work undertaken as part of this thesis may help bridge the gap between single element laboratory tests, and pile load tests at field and/or 1-g scale. Furthermore, there is often a disconnect in geotechnical engineering between numerical modelling practitioners and experimentalists. The numerical work presented in this thesis therefore aims promote synergy between the two disciplines and prevent occurrence of further divergence. This combined approach has resulted in useful, practical insights that may be used to inform the choice, evaluation, and development of constitutive models used in practice.

11. REFERENCES

Abadie, C. N. (2015). *Cyclic lateral loading of monopile foundations in cohesionless soils*. DPhil Thesis, University of Oxford.

Abate, G., Massimino, M. R., Maugeri, M., & Muir Wood, D. (2010). Numerical modelling of a shaking table test for soil-foundation-superstructure interaction by means of a soil constitutive model implemented in a FEM code. *Geotechnical and Geological Engineering*, *28*(1), 37–59.

Achmus, M., Albiker, J., & Abdel-Rahman, K. (2011). Investigations on the behavior of large diameter piles under cyclic lateral loading. In S. Gourvenec & D. J. White (Eds.), *Frontiers in Offshore Geotechnics II* (pp. 471–476). Taylor & Francis.

Ackerley, S. K., Hellings, J. E., & Jardine, R. J. (1987). Discussion: A new device for measuring local axial strains on triaxial specimens. *Géotechnique*, *37*(3), 413–417.

Ackerley, S. K., Standing, J. R., & Hosseini Kamal, R. (2016). A system for measuring local radial strains in triaxial apparatus. *Géotechnique*, *66*(6), 515–522.

Aghakouchak, A., Sim, W. W., & Jardine, R. J. (2015). Stress-path laboratory tests to characterise the cyclic behaviour of piles driven in sands. *Soils and Foundations*, *55*(5), 917–928.

Alarcon-Guzman, A., Lenoards, G., & Chameau, J. (1988). Undrained Monotonic and Cyclic Strength of Sands. *Journal of Geotechnical Engineering, ASCE*, *114*(10), 1089–1109.

Albiker, J., Achmus, M., Frick, D., & Flindt, F. (2017). 1g Model Tests on the Displacement Accumulation of Large-Diameter Piles Under Cyclic Lateral Loading. *Geotechnical Testing Journal*, *40*(2), 173–184.

Ali, S. R., Pyrah, I. C., & Anderson, W. F. (1995). A novel technique for the evaluation of membrane penetration. *Geotechnique*, *45*(3), 545–548.

Alvarado, G., & Coop, M. R. (2011). On the performance of bender elements in triaxial tests. *Géotechnique*, *62*(1), 1–17.

Andersen, K. H. (2009). Bearing capacity under cyclic loading — offshore, along the coast, and on land. The 21st Bjerrum Lecture presented in Oslo, 23 November 2007. *Canadian Geotechnical Journal*, *46*(5), 513–535.

Andersen, K. H. (2013). Design for cyclic loading : piles and other foundations. In A. Puech (Ed.), *Design for Cyclic Loading: Piles and Other Foudnations. Proceedings of TC 209 Workshop, 18th ICSMGE - Paris, 4 September 2013* (pp. 9–44). Paris.

Andersen, K. H. (2015). Cyclic soil parameters for offshore foundation design - The Third ISSMGE McClelland Lecturer. In V. Meyer (Ed.), *Proceedings of the 3rd International Symposium on Frontiers in Offshore Geotechnics (ISFOG 2015), Oslo, Norway, 10-12 June 2015* (pp. 5–82). CRC Press.

Andersen, K. H., & Berre, T. (1999). Behaviour of a dense sand under monotonic and cyclic loading. In F. B. J. Barends, J. Lindenberg, H. J. Luger, L. de Querlerij, & A. Verruijt (Eds.), *Geotechnical Engineering for Transportation Infrastructure* (Vol. 2, pp. 667–676). Rotterdam: Balkema.

Andersen, K. H., Kleven, A., & Heien, D. (1988). Cyclic soil data for design of gravity structures. *Journal of Geotechnical Engineering, ASCE*, *114*(5), 517–539.

Arroyo, M., Muir Wood, D., Greening, P. D., Medina, L., & Rio, J. (2006). Effects of sample size on bender-based axial G0 measurements. *Géotechnique*, *56*(1), 39–52.

Arulmoli, K., Muraleetharan, K. K., Hossain, M. M., & Fruth, L. S. (1992). *VELACS: Verifications of Liquefaction Analyses by Centrifuge Studies. Laboratory Testing Program. Soil Data Report*.

ASTM. (2011). *ASTM D4767-11 Standard Test Method for Consolidated Undrained Triaxial Compression Test for Cohesive Soils*. *ASTM D4767-11*.

ASTM. (2015). ASTM D5311M-13 Standard Test Method for Load Controlled Cyclic Triaxial Strength of Soil. *ASTM D5311M-13*. West Conshohocken, PA, USA: ASTM International.

ASTM. (2017). Standard practices for cycle counting in fatigue analysis. *ASTM E1049 - 85(2017),* *03*(01), 836–848.

Atkinson, J. H., & Evans, J. S. (1985). Discussion: The measurement of soil stiffness in the triaxial apparatus. *Géotechnique, 35*(3), 378–382.

Atkinson, J. H., & Richardson, D. (1985). Elasticity and normality in soil—experimental examinations. *Géotechnique, 35*(4), 443–449.

Atkinson, J. H., & Sallfors, G. (1991). Experimental determination of soil properties. In *Deformation of soils and displacements of structures - Proceedings of the 10th European Conference on Soil Mechanics and Foundation Engineering, Florence, 26-30 May 1991* (pp. 915–956). Florence, Italy: Balkema.

Baldi, G., Hight, D. W., & Thomas, G. E. (1988). A reevaluation of conventional triaxial test methods. In R. T. Donaghe, R. C. Chaney, & M. L. Silver (Eds.), *Advanced Triaxial Testing of Soil and Rock, ASTM STP 977* (pp. 219–263). ASTM.

Baldi, G., & Nova, R. (1984). Membrane Penetration Effects in Triaxial Testing. *Journal of Geotechnical Engineering, ASCE*, *110*(3), 403–420. https://doi.org/10.1061/(ASCE)0733-9410(1984)110:3(403)

Bayton, S. M., Black, J. A., & Klinkvort, R. T. (2018). Centrifuge modelling of long term cyclic lateral loading on monopiles. In A. McNamara, S. Divall, R. Goodey, N. Taylor, S. Stallebrass, & J. Panchal (Eds.), *Physical Modelling in Geotechnics - ICPMG 2018* (Vol. 1, pp. 689–694). CRC Press.

Been, K., & Jefferies, M. G. (1985). A state parameter for sands. *Géotechnique, 35*(2), 99–112.

Been, K., Jefferies, M. G., & Hachey, J. (1991). The critical state of sands. *Géotechnique, 41*(3), 365–381.

Benz, T. (2007). *Small-Strain Stiffness of Soils and its Numerical Consequences*. *Ph.D. Thesis*. PhD Thesis, University of Stuttgart.

Beuckelaers, W. J. A. P. (2017). *Numerical Modelling of Laterally Loaded Piles for Offshore Wind Turbines*. DPhil Thesis, University of Oxford.

Bishop, A. W. (1966). The Strength of Soils as Engineering Materials. 6th Rankine Lecture. *Géotechnique*, *16*(2), 91–130.

Bishop, A. W., & Green, G. (1965). The Influence of End Restraint on the Compression Strength of a Cohesionless Soil. *Géotechnique*, *15*(3), 243–265.

Bishop, A. W., & Henkel, D. J. (1962). *The Measurement of Soil Properties in the Triaxial Test* (2nd ed.). London: Edward Arnold Ltd.

Bishop, A. W., Kumapley, N. K., & El-Ruwayih, A. A. (1975). The influence of pore-water tension on the strength of clay. *Philosophical Transactions of the Royal Society of London*, *278*(1286), 511–554.

Bjerrum, L. (1973). Geotechnical problems involved in foundations of structures in the North Sea. *Géotechnique*, *23*(3), 319–358.

Blaker, Ø., & Andersen, K. H. (2015). Shear strength of dense to very dense Dogger Bank sand. In V. Meyer (Ed.), *Proceedings of the 3rd International Symposium on Frontiers in Offshore Geotechnics (ISFOG 2015), Oslo, Norway, 10-12 June 2015* (pp. 1167–1172). CRC Press.

Blaker, Ø., & Andersen, K. H. (2019). Cyclic properties of dense to very dense silica sand. *Soils and Foundations*, *59*(4), 982–1000.

Bolton, M. D. (1986). The strength and dilatancy of sands. *Géotechnique*, *36*(1), 65–78.

Borja, R. I., & Lee, S. R. (1990). Cam-Clay plasticity, Part 1: Implicit integration of elasto-plastic constitutive relations. *Computer Methods in Applied Mechanics and Engineering*, *78*(1), 49–72.

Boyce, J. R., & Brown, S. F. (1977). Measurement of elastic strain in granular material. *Géotechnique*, *26*(4), 637–640.

Bredmose, H., Dixen, M., Ghadirian, A., Larsen, T. J., Schløer, S., Andersen, S. J., … Hanson, T. D. (2016). DeRisk - Accurate Prediction of ULS Wave Loads. Outlook and First Results. *Energy Procedia*, *94*, 379–387.

Brinkgreve, R. B. J., & Vermeer, P. A. (1997). *Plaxis: finite element code for soil and rock analyses (version 7)*. Rotterdam: Balkema.

Britto, A. M., & Gunn, M. J. (1987). *Critical state soil mechanics via finite elements*. Chichester:

Ellis Horwood Ltd.

Brown, S. F., Austin, G., & Overy, R. F. (1980). Instrumented Triaxial Cell for Cyclic Loading of Clays. *Geotechnical Testing Journal*, *3*(4), 145–152.

Brown, S. F., & Snaith, M. S. (1974). The measurement of recoverable and irrecoverable deformations in the repeated load triaxial test. *Géotechnique*, *24*(2), 255–259.

BSI. (1990). *BS 1377-8: 1990 Soils for civil engineering purposes - Part 8: Shear strength tests (effective stress)*. *BS 1377-8: 1990*.

BSI. (1998). *BS 1881: Part 131: 1998. Testing Concrete - Part 131. Methods for testing cement in a reference concrete*.

BSI. (1999). *BS 5930: 1999 +A2:2010 Code of practice for site investigations*.

BSI. (2000). *BS 410-1: 2000 Test sieves. Technical requirements and testing. Test sieves of metal wire cloth*.

BSI. (2002). *BS 1377-4: 1990 Soils for civil engineering purposes - Part 4: Compaction-related tests*. *BS 1377-4: 1990*.

BSI. (2016). *BS ISO 3310-1: 2016 Test sieves. Technical requirements and testing. Test sieves of metal wire cloth*.

Bui, M. T. (2009). *Influence of Some Particle Characteristics on the Small Strin Response of Granular Materials*. PhD Thesis, University of Southampton.

Burd, H. J., Taborda, D. M. G., Zdravković, L., Abadie, C. N., Byrne, B. W., Houlsby, G. T., … Potts, D. M. (2019). PISA design model for monopiles for offshore wind turbines: application to a marine sand. *Géotechnique*, (Ahead of print). https://doi.org/10.1680/jgeot.18.p.277

Byrne, B. W., Houlsby, G. T., Burd, H. J., Gavin, K. G., Igoe, D. J. P., Taborda, D. M. G., … Zdravković, L. (2019). PISA design model for monopiles for offshore wind turbines: application to a stiff glacial till. *Géotechnique*, (Ahead of print). https://doi.org/10.1680/jgeot.18.P.255

Byrne, B. W., McAdam, R., Burd, H. J., Houlsby, G. T., Martin, C. M., Zdravkovi, L., … Skov Gretlund, J. (2015). New design methods for large diameter piles under lateral loading for offshore wind applications. In V. Meyer (Ed.), *Proceedings of the 3rd International Symposium on Frontiers in Offshore Geotechnics (ISFOG 2015), Oslo, Norway, 10-12 June 2015* (pp. 705–710). CRC Press.

Çabalar, A. F. (2008). Effect of fines content on the behavior of mixed samples of a sand. *Electronic Journal of Geotechnical Engineering*, *13 D*, 1–11.

Çabalar, A. F., & Clayton, C. R. . (2010). Some observations of the effects of pore fluids on the triaxial behaviour of a sand. *Granular Matter*, *12*(1), 87–95.

Carraro, J. A. H., & Prezzi, M. (2008). A new slurry-based method of preparation of specimens of sand containing fines. *Geotechnical Testing Journal, ASTM*, *31*(1), 1–11.

Casagrande, A. (1936). Characteristics of cohesionless soils affecting the stability of slopes and earth fill. *Journal of Boston Society of Civil Engineers.*, *23*, 257–276.

Casagrande, A. (1975). Liquefaction and cyclic deformation of sands: A critical review. In *Proceedings of the Fifth Pan-American Conference on Soil Mechanics and Foundation Engineering* (pp. 79–133). Cambridge, MA: Pierce Hall.

Castro, G. (1969). *Liquefaction of sands*. PhD Thesis, Harvard University, Cambridge.

Castro, G. (1975). Liquefaction and Cyclic Mobility of Saturated Sands. *Journal of the Geotechnical Engineering Division, ASCE*, *101*(6), 551–569.

Castro, G., Poulos, S. J., France, J. W., & Enos, J. L. (1982). *Liquefaction induced by cyclic loading. Report to National Science Foundation*. Washington D.C.

Cerfontaine, B. (2014). *The cyclic behaviour of sand, from the Prévost model to offshore geotechnics*. PhD Thesis, University of Liège.

Cerfontaine, B., Collin, F., & Charlier, R. (2016). Numerical modelling of transient cyclic vertical loading of suction caissons in sand. *Géotechnique*, *66*(2), 121–136.

Chu, J. (1995). An experimental examination of the critical state and other similar concepts for granular soils. *Canadian Geotechnical Journal*, *32*(6), 1065–1075.

Clayton, C. R. I. (2011). Stiffness at small strain: research and practice. *Géotechnique*, *61*(1), 5–37.

Clayton, C. R. I., & Khatrush, S. A. (1986). A new device for measuring local axial strains on triaxial specimens. *Géotechnique*, *36*(4), 593–597.

Clayton, C. R. I., Khatrush, S. A., Bica, A. V. D., & Siddique, A. (1989). The Use of Hall Effect Semiconductors in Geotechnical Instrumentation. Geotechnical Testing Journal. 12(1) 69-76. *Geotechnical Testing Journal. GTJODJ*, *12*(1), 69–76.

Coop, M. R. (1999). The influence of particle breakage and state on the behaviour of sands. In *International workshop on soil crushability, IWSC '99, Japan*.

Dafalias, Y. F., & Manzari, M. . (2004). Simple plasticity sand model accounting for fabric change effects. *Journal of Engineering Mechanics, ASCE*, *130*(6), 622–634.

Dafalias, Y. F., Papadimitriou, A. G., & Li, X. S. (2004). Sand plasticity model accounting for inherent fabric anisotropy. *Journal of Engineering Mechanics*, *130*(11), 1319–1333.

Dafalias, Y. F., & Popov, E. P. (1975). A model of nonlinearly hardening materials for complex loading. *Acta Mechanica*, *21*(3), 173–192.

Darendeli, M. . (2001). *Development of a new family of normalized modulus reduction and material damping curves.* PhD Thesis, University of Texas at Austin.

Das, B. M., & Ramana, G. V. (2011). *Principles of Soil Dynamics*. (2nd, Ed.). Stanford, USA: Cengage Learning.

Desrues, J., Chambon, R., Mokni, M., & Mazerolle, F. (1996). Void ratio evolution inside shear bands in triaxial sand specimens studied by computed tomography. *Géotechnique*, *46*(3), 529–546.

Dietz, M., & Muir Wood, D. (2007). Shaking table evaluation of dynamic soil properties. In *4th International Conference on Earthquake Geotechnical Engineering, June 25-28, 2007, Thessaloniki, Greece. Paper 1196*.

DiMaggio, F. L., & Sandler, I. S. (1971). Material Model for Granular Soils. *Journal of the Engineering Mechanics Division, ASCE*, *97*(3), 935–950.

Dobry, R. (1991). Soil properties and earthquake ground response. In *Deformation of soils and displacements of structures: Proceedings of the 10th European Conf. on Soil Mechanics and Foundation Engineering, Florence, 26-30 May 1991*.

Dobry, R., & Ladd, R. S. (1980). Discussion of "Soil liquefaction and cyclic mobility evaluation for level ground during earthquakes," by H. B. Seed and "Liquefaction potential: science versus practice," by R. B. Peck. *Journal of the Geotechnical Engineering Division, ASCE*, *106*(6), 720–724.

Dobry, R., Ladd, R. S., Yokel, F. Y., Chung, R. M., & Powell, D. (1982). *Prediction of Pore Water Pressure Buildup and Liquefaction of Sands During Earthquakes By the Cyclic Strain Method*. *NBS Building Science Series 138*. Washington.

Dominguez-Quintans, C., Santiago Quinteros, V., Carraro, J. A. H., Zdravkovic, L., & Jardine, R. J. (2019). Quality assessment of a new in-mould slurry deposition method for triaxial specimen reconstitution of clean and silty sands. *E3S Web of Conferences*, *92*, 1–6. https://doi.org/10.1051/e3sconf/20199202010

Drucker, D. C., Gibson, R. E., & Henkel, D. J. (1957). Soil Mechanics and Work-Hardening Theories of Plasticity. *Transactions of the American Society of Civil Engineers*, *122*(1), 338–346.

Drucker, D. C., & Prager, W. (1952). Soil mechanics and plastic analysis or limit design. *Quarterly of Applied Mathematics*, *10*(2), 157–165.

Duncan, J. M., & Chang, C.-Y. (1970). Nonlinear Analysis of Stress and Strain in Soils. *Journal of the Soil Mechanics and Foundation Division, ASCE*, *93*(SM5), 1629–1653.

Duncan, J. M., & Seed, H. B. (1967). Corrections for strength test data. *Journal of the Soil Mechanics and Foundation Division, ASCE*, *93*(SM5), 121–137.

Dyvik, R., Dobry, R., Thomas, G. E., & Pierce, W. G. (1984). Influence of consolidation shear stresses and relative density on threshold strain and pore pressure during cyclic straining of saturated sands. *Miscellaneous Paper GL-84-15, Department of the Army, U.S. Army Corps of Engineers, Washington, D.C.*, 73.

El-Ruwayih, A. A. (1976). Design manufacture and performance of a lateral strain device. *Géotechnique*, *26*(1), 215–216.

Elgamal, A., Yang, Z., & Parra, E. (2002). Computational modeling of cyclic mobility and post-liquefaction site response. *Soil Dynamics and Earthquake Engineering*, *22*(4), 259–271.

Elgamal, A., Yang, Z., Parra, E., & Ragheb, A. (2003). Modeling of cyclic mobility in saturated cohesionless soils. *International Journal of Plasticity*, *19*(6), 883–905.

Erten, D., & Maher, M. H. (1995). Cyclic undrained behavior of silty sand. *Soil Dynamics and Earthquake Engineering*, *14*(2), 115–123.

Fannin, R. J., Eliadorani, A., & Wilkinson, J. M. T. (2005). Shear strength of cohesionless soils at low stress. *Geotechnique*, *55*(6), 467–478.

Ferreira, C., & da Fonseca, A. V. (2005). *International Parallel Tests on Bender Elements at the University of Porto, Portugal*. *Internal Report*. Porto.

Finn, W. D. . (1981). Liquefaction potential: Developments since 1976. In *Proceedings of the 1st International Conference on Recent Advances in Geotechnical Earthquake Engineering and Soil Dynamics, April 26-May 3, 1981, St. Louis, Missouri* (pp. 655–681).

Frydman, S., Talesnick, M., Nawatha, H., & Schwartz, K. (2007). Stress-Dilation of Undisturbed Sand Samples in Drained and Undrained Triaxial Shear. *Soils and Foundations*, *47*(1), 27–32.

Frydman, S., Zeitlen, J. G., & Alpan, I. (1973). The membrane effect in triaxial testing of granular soils. *Journal of Testing and Evaluation*, *1*(1), 37–41.

Fuentes, W., Wichtmann, T., Gil, M., & Lascarro, C. (2019). ISA-Hypoplasticity accounting for cyclic mobility effects for liquefaction analysis. *Acta Geotechnica*, 1–19.

Fukushima, S., & Tatsuoka, F. (1984). Strength and Deformation Characteristics of Saturated Sand at Extremely Low Pressures. *Soils and Foundations*, *24*(4), 30–48.

Georgiannou, V. N., Tsomokos, A., & Stavrou, K. (2008). Monotonic and cyclic behaviour of sand under torsional loading. *Géotechnique*, *58*(2), 113–124.

Ghionna, V. N., & Porcino, D. (2006). Liquefaction resistance of undisturbed and reconstituted samples of a natural coarse sand from undrained cyclic triaxial tests. *Journal of Geotechnical and Geoenvironmental Engineering, ASCE*, *132*(2), 194–202.

Goddard, J. D. (1990). Nonlinear Elasticity and Pressure-Dependent Wave Speeds in Granular Media. *Proceedings of the Royal Society A: Mathematical, Physical and Engineering Sciences*, *430*(1878), 105–131.

Goto, S., Tatsuoka, F., Shibuya, S., Kim, Y.-S., & Sato, T. (1991). A simple gauge for local small strain measurements in the laboratory. Soils and Foundations. *Soils and Foundations*, *31*(1), 169–180.

Graham, J., & Houlsby, G. T. (1983). Anisotropic elasticity of a natural clay. *Géotechnique*, *33*(2), 165–180.

Grammatikopolou, A., Schroeder, F. C., Brosse, A. M., Andersen, K. W., & Potts, D. M. (2017). On the use of COnstituive Models in Numerical ANalyses of Offshore Structures. In *Proceedings of the 8th International Conference on Offshore Site Investigation and Geotechnics, 12-14 Sept., 2017, London, UK* (Vol. 1, pp. 423–430).

Hansen, B. (1958). Line ruptures regarded as narrow rupture zones, basic equations based on kinematic considerations. In *Proc. Conf. Earth Pressure Problems, Brussels* (pp. 39–48). Brussels.

Hanzawa, H., Itoh, Y., & Suzuki, K. (1979). Shear Characteristics of a Quick Sand in the Arabian Gulf. *Soils and Foundations*, *19*(4), 1–15.

Hardin, B. O. (1965). The Nature of Damping in Sands. *Journal of the Soil Mechanics and Foundations Division, ASCE*, *91*(1), 63–98.

Hardin, B. O., & Black, W. L. (1966). Sand Stiffness Under Various Triaxial Stresses. *Journal of the Soil Mechanics and Foundations Division, ASCE*, *92*(2), 27–42.

Hardin, B. O., & Drnevich, V. . P. (1972). Shear Modulus and Damping in Soils: Measurement and Parameter effects. *Journal of the Soil Mechanics and Foundation Division, ASCE*, *98*((SM6)), 603–624.

Head, K. H., & Epps, R. J. (2011). *Manual of Soil Laboratory Testing. Volume 2: Permeability, Shear Strength and Compressibility Tests.* (3rd ed., Vol. 2). Dunbeath: Whittles Publishing.

Head, K. H., & Epps, R. J. (2014). *Manual of Soil Laboratory Testing. Volume 3: Effective Stress Tests.* (3rd ed., Vol. 3). Dunbeath: Whittles Publishing.

Henkel, D. J., & Gilbert, G. D. (1952). The Effect Measured of the Rubber Membrane on the Triaxial Compression Strength of Clay Samples. *Géotechnique*, *3*(1), 20–29.

Hight, D. W., Gens, A., & Symes, M. J. (1983). The development of a new hollow cylinder apparatus for investigating the effects of principal stress rotation in soils. *Géotechnique*, *33*(4), 355–383.

Hird, C. C., & Hassona, F. A. K. (1990). Some factors affecting the liquefaction and flow of saturated sands in laboratory tests. *Engineering Geology*, *28*, 149–170.

Hird, C. C., & Yung, P. (1989). The use of proximity transducer for local strain measurements in triaxial tests. *Geotechnical Testing Journal*, *12*(4), 292–296.

Høeg, K., Dyvik, R., & Sandbækken, G. (2000). Strength of Undisturbed versus Reconstituted Silt and Silty Sand Specimens. *Journal of Geotechnical and Geoenvironmental Engineering, ASCE*, *126*(7), 606–617.

Holtz, W. G., & Gibbs, J. (1956). Triaxial shear tests on pervious gravelly soils. *Journal of the Soil Mechanics and Foundation Division, ASCE*, *82*(1), 1–22.

Hoque, E., & Tatsuoka, F. (1998). Anisotropy in Elastic Deformation of Granular Materials. *Soils and Foundations*, *38*(1), 163–179.

Hoque, E., & Tatsuoka, F. (2004). Effects of stress ratio on small strain stiffness during triaxial shearing. *Geotechnique*, *54*(7), 429–439.

Houlsby, G. T. (1991). How the dilatancy of soils affects their behaviour. In *10th European Conference on Soil Mechanics and Foundation Engineering, 27-30th May, 1991, Florence, Italy,* (pp. 1189–1202).

Houlsby, G. T. (2016). Interactions in offshore foundation design. *Géotechnique*, *66*(10), 791–825.

Houlsby, G. T., Amorosi, A., & Rojas, E. (2005). Elastic moduli of soils dependent on pressure: A hyperelastic formulation. *Géotechnique*, *55*(5), 383–392.

Houlsby, G. T., & Mortara, G. (2004). Continuous Hyperplasticity model for sand under cyclic loading. In T. Triantafyllidis (Ed.), *Cyclic Behaviour of Soils and Liquefaction Phenomena: Proceedings of the International Conference, Bochum, Germany, 31 March - 2 April 2004* (pp. 21–26).

Houlsby, G. T., & Puzrin, A. M. (2006). *Principles of Hyperplasticity. An Approach to Plasticity Theory Based on Thermodynamic Principles*. Springer.

Hu, W., Dano, C., Hicher, P.-Y., Le Touzo, J.-Y., Derkx, F., & Merliot, E. (2011). Effect of Sample Size on the Behavior of Granular Materials. *Geotechnical Testing Journal, ASTM*, *34*(3), 1–27.

Hyodo, M., Murata, H., Yasufuku, N., & Fujii, T. (1991). Undrained cyclic shear strength and residual shear strain of saturated sand by cyclic triaxial tests. *Soils and Foundations*, *31*(3), 60–76.

Hyodo, M., Tanimizu, H., Yasufuku, N., & Murata, H. (1994). Undrained cyclic and monotonic triaxial behaviour of saturated loose sand. *Soils and Foundations*, *34*(1), 19–32.

Ishihara, K. (1993). Liquefaction and flow failure during earthquakes. 33rd Rankine Lecture. *Géotechnique*, *43*(3), 351–451.

Ishihara, K. (1996). *Soil Behaviour in Earthquake Geotechnics*. New York: Oxford University Press.

Ishihara, K., Tatsuoka, F., & Yasuda, S. (1975). Undrained deformation and liquefaction of sand under cyclic stresses. *Soils and Foundations*, *15*(1), 29–44.

Itasca Consulting Group Inc. (2015). *FLAC 8 Basics*.

Iwan, W. D. (1966). A distributed-element model for hysteresis and its steady-state dynamic response. *Journal of Applied Mechanics, ASME Transactions*, *33*(4), 893–900.

Iwan, W. D. (1967). On a Class of Models for the Yielding Behavior of Continuous and Composite Systems. *Journal of Applied Mechanics*, *34*(3), 612–617.

Iwasaki, T., & Tatsuoka, F. (1977). Effects of Grain Size and Grading on Dynamic Shear Moduli of Sands. *Soils and Foundations*, *17*(3), 19–35.

Jaky, J. (1944). The coefficient of earth pressure at rest. *J. Soc. Hungarian Architects and Engineers, Appendix 1 (Transl)*, *78*(22), 355–388.

Jardine, R. J., Potts, D. M., Fourie, A. B., & Burland, J. B. (1986). Studies of the influence of non-linear stress–strain characteristics in soil–structure interaction. *Géotechnique*, *36*(3), 377–396.

Jardine, R. J., & Standing, J. R. (2000). *Pile load testing performed for HSE cyclic loading study at Dunkirk, France. Offshore Technology Report OTO 2000 007*.

Jardine, R. J., Symes, M. J., & Burland, J. B. (1984). Measurement of soil stiffness in the triaxial apparatus. *Géotechnique*, *34*(3), 323–340.

Jefferies, M. G. (1993). Nor-Sand: a simple critical state model for sand. *Géotechnique*, *43*(1), 91–103.

Jefferies, M. G., & Been, K. (2015). *Soil Liquefaction- A Critical State Approach* (2nd ed.). CRC Press.

Jefferies, M. G., Been, K., & Hachey, J. E. (1990). The influence of scale on the constitutive behaviour of sand. In *Proceedings of the 43rd Canadian Geotechnical Conference, Quebec City, Canada, Vol. 1* (pp. 263–273).

Jefferies, M. G., & Shuttle, D. A. (2002). Dilatancy in general Cambridge-type models. *Géotechnique*, *52*(9), 625–637.

Jefferies, M. G., & Shuttle, D. A. (2005). NorSand: Features, Calibration and Use. In J. A. Yamamuro & V. N. Kaliakin (Eds.), *Geo-Frontiers Congress 2005, January 24-26* (pp. 204–236). Austin, Texas.

Jefferies, M. G., & Shuttle, D. A. (2011). On the operating critical friction ratio in general stress states. *Géotechnique*, *61*(8), 709–713.

Jefferies, M. G., Shuttle, D., & Been, K. (2015). Principal stress rotation as cause of cyclic mobility. *Geotechnical Research*, *2*(2), 66–96.

Jones, L., White, J. R. F., & Truong, L. (2020). On the triaxial testing of sand for offshore wind turbine foundation design. In *Proceedings of the 4th International Symposium on Frontiers in Offshore Geotechnics*. (Ahead of print).

Khong, C. D. (2004). *Development and numerical evaluation of unified critical state models*. PhD Thesis, University of Nottingham.

Kim, D.-S., Stokoe, K. H., & Hudson, W. R. (1992). *Deformational characteristics of soils at small to intermediate strains from cyclic tests*. *Report No: FHWA/TX-92+1177-3*. Austin, Texas: Texas Department of Transportation.

Kirkpatrick, W. M., Seals, R. K., & Newman, F. B. (1974). Stress Distributions in Triaxial Compression Samples. *Journal of the Geotechnical Engineering Division, ASCE*, *100*(GT2), 190–196.

Klotz, E. U., & Coop, M. R. (2002). On the Identification of Critical State Lines for Sands. *Geotechnical Testing Journal, ASTM*, *25*(3), 289–302.

Klotz, U. (2000). *The influence of state on the capacity of driven piles in sands*. PhD Thesis, City University, University of London.

Kokusho, T. (1980). Cyclic Triaxial Test of Dynamic Soil Properties for Wide Strain Range. *1Soils and Foundations*, *20*(2), 45–60.

Kolbuszewski, J. (1965). *Sand particles and their density: Lecture given to the Materials Science Clubs Symposium on Densification of Particulate Materials, London, February 26*.

Kolymbas, D. (2000). *Constitutive Modelling of Granular Materials*. (D. Kolymbas, Ed.). Berlin: Springer.

Konrad, J. M. (1993). Undrained response of loosely compacted sands during monotonic and cyclic compression tests. *Géotechnique*, *43*(1), 69–89.

Kramer, S. L. (1996). *Geotechnical Earthquake Engineering*. Prentice Hall.

Kramer, S. L., Sivaneswaran, N., & Davis, R. O. (1990). Analysis of membrane penetration in triaxial test. *Journal of Engineering Mechanics*, *116*(4), 773–789.

Krieg, R. D. (1975). A Practical Two Surface Plasticity Theory. *Journal of Applied Mechanics*, *42*(3), 641–646.

Kuerbis, R., & Vaid, Y. P. (1988). Sand Sample Preparation-the Slurry Deposition Method. *Soils and Foundations*, *28*(4), 107–118.

Kulhawy, F. H., & Mayne, P. W. (1990). *Manual on Estimating Soil Properties for Foundation Design*. *Electric Power Research Institute, EPRI EL-6800, Project 1493-6*. Palo Alto, California.

Kuwano, R. (1999). *The stiffness and yielding anisotropy of sand*. PhD Thesis, Imperial College London.

Kuwano, R., Connolly, T. M., & Jardine, R. J. (2000). Anisotropic Stiffness Measurements in a Stress-Path Triaxial Cell. *Geotechnical Testing Journal, ASTM*, *23*(2), 141–157.

Kuwano, R., & Jardine, R. J. (2002a). On measurnig creep behaviour in granular materials through triaxial testing. *Canadian Geotechnical Journal*, *39*(5), 1061–1074.

Kuwano, R., & Jardine, R. J. (2002b). On the applicability of cross-anisotropic elasticity to granular materials at very small strains. *Géotechnique*, *52*(10), 727–749.

Ladd, R. S. (1974). Specimen preparation and liquefaction of sands. *Journal of the Geotechnical Engineering Division, ASCE*, *100*(GT10), 1180–1184.

Ladd, R. S. (1977). Specimen preparation and cyclic stability of sands. *Journal of the Geotechnical Engineering Division, ASCE*, *103*(GT6), 535–547.

Ladd, R. S. (1978). Preparing Test Specimens Using Undercompaction. *Geotechnical Testing Journal. GTJODJ*, *1*(1), 16–23.

Ladd, R. S., Dobry, R., Dutko, P., Yokel, F. Y., & Chung, R. M. (1989). Pore-Water Pressure Buildup in Clean Sands Because of Cyclic Straining. *Geotechnical Testing Journal, ASTM*, *12*(1), 77–86.

Lade, P. V. (1977). Elasto-plastic stress-strain theory for cohesionless soil with curved yield surfaces. *International Journal of Solids and Structures*, *13*(11), 1019–1035.

Lade, P. V. (2005). Overview of constitutive models for soils. In *Geo-Frontiers Congress 2005, January 24-26, Austin, Texas* (pp. 1–34). ASCE.

Lade, P. V. (2016). *Triaxial Testing of Soils*. Wiley Blackwell.

Lade, P. V., & Duncan, J. M. (1975). Elastoplastic Stress-Strain theory for cohesionless soil. *Journal of the Geotechnical Engineering Division, ASCE*, *101*(GT10), 1037–1053.

Lade, P. V., & Ibsen, L. B. (1997). A study of the phase transformation and the characteristic lines of sand behavior. In *Proceedings of the International Symposium on Deformation and Progressive Failure in Gemechanics* (pp. 353–359). Nagoya, Japan.

Lam, W.-K., & Tatsuoka, F. (1988). Effects of initial anisotropic fabric and σ2 on strength and deformation characteristics of sand. *Soils and Foundations*, *28*(1), 89–106.

LeBlanc, C., Houlsby, G. T., & Byrne, B. W. (2010). Response of stiff piles in sand to long-term cyclic lateral loading. *Géotechnique*, *60*(2), 79–90.

Lee, K. H., & Seed, H. B. (1967). Cyclic stress conditions causing liquefaction of sand. *Journal of the Soil Mechanics and Foundations Division, ASCE*, *93*(SM1), 47–70.

Lee, K. L. (1978). End Restraint Effects on Undrained Static Triaxial Strength of Sand. *Journal of the Geotechnical Engineering Division, ASCE*, *104*(GT6), 687–704.

Lee, K. L., & Albaisa, A. (1974). Earthquake induced settlements in saturated sands. *Journal of the Geotechnical Engineering Division, ASCE*, *100*(GT4), 387–406.

Lee, W. F. (2000). *Internal Stability Analyses of Geosynthetic Reinforced Retaining Walls.* PhD Thesis, University of Washington.

Lentz, R. W., & Baladi, G. Y. (1980). Simplified procedure to characterize permanent strain in sand subjected to cyclic loading. In *International Symposium on soils under cyclic and transient loading* (pp. 89–95).

Leong, E. C., Yeo, S. H., & Rahardjo, H. (2005). Measuring shear wave velocity using bender elements. *Geotechnical Testing Journal*, *28*(5), 488–498.

Leps, T. M. (1970). Review of shearing strength of rockfill. *Journal of the Soil Mechanics and Foundation Division, ASCE*, *96*(SM4), 1159–1170.

Li, X.-S., Dafalias, Y. F., & Wang, Z.-L. (1999). State-dependant dilatancy in critical-state constitutive modelling of sand. *Canadian Geotechnical Journal*, *36*(4), 599–611.

Li, X. S., & Dafalias, Y. F. (2012). Anisotropic Critical State Theory: Role of Fabric. *Journal of Engineering Mechanics, ASCE*, *138*(3), 263–275.

Lin, S.-S., & Liao, J.-C. (1999). Permanent Strains of Piles in Sand due to Cyclic Lateral Loads. *Journal of Geotechnical and Geoenvironmental Engineering, ASCE*, *125*(9), 798–802.

Long, J. H., & Vanneste, G. (1994). Effects of Cyclic Lateral Loads on Piles in Sand. *Journal of the Geotechnical Engineering Division, ASCE*, *120*(1), 225–244.

Loukidis, D., & Salgado, R. (2009). Modeling sand response using two-surface plasticity. *Computers and Geotechnics*, *36*(1–2), 166–186.

Lunne, T., Knudsen, S., Blaker, Vestgården, T., Powell, J. J. M., Wallace, C. F., … Ghanekar, R. K. (2019). Methods used to determine maximum and minimum dry unit weights of sand: Is there a need for a new standard? *Canadian Geotechnical Journal*, *56*(4), 536–553.

Luong, M. P. (1980). Stress-Strain Aspects of Cohesionless Soils Under Cyclic and Transient Loading. In G. N. Pande & O. C. Zienkiewicz (Eds.), *Proceedings of the International Symposium on Soils under Cyclic and Transient Loading. Swansea, 7-11 Januray, 1980* (Vol. 1, pp. 315–324). Balkema.

Mair, R. J. (1993). Developments in geotechnical engineering research: Applications to tunnels and deep excavations. Unwin Memorial Lecture 1992. *Proceedings of the Institution of Civil Engineers - Civil Engineering*, *93*(1), 27–41.

Manzari, M. T., & Dafalias, Y. F. (1997). A critical state two-surface plasticity model for sands. *Géotechnique*, *47*(2), 255–272.

Martin, C. M., & Burd, H. J. (2018). *Numerical Analysis for Offshore Geotechnics, course notes*. Oxford, UK: University of Oxford.

Matsuishi, M., & Endo, T. (1968). Fatigue of Metals Subjected to Varying Stress – Fatigue Lives Under Random Loading. *Proceedings of the Kyushu District Meeting, Japanese Society of Mechanical Engineering*, 37–40.

Matsuoka, H., & Nakai, T. (1974). Stress-deformation and strength characteristics of soil under different principal stresses. *Proceedings of the Japanese Society of Civil Engineers,* (232), 59–70.

Menzies, B. K. (1988). A computer Controlled Hydraulic Triaxial Testing System. In R. T. Donaghe, R. C. Chaney, & M. L. Silver (Eds.), *Advanced Triaxial testing of Soil and Rock, ASTM STP 977* (pp. 82–94). Philadelphia: ASTM.

Miura, S., & Toki, S. (1982). A Sample Preparation Method and Its Effect on Static and Cyclic Deformation-Strength Properties of Sand. *Soils and Foundations*, *22*(1), 61–77.

Mohamad, R., & Dobry, R. (1986). Undrained Monotonic and Cyclic Triaxial Strength of Sand. *Journal of the Geotechnical Engineering Division, ASCE*, *112*(10), 941–958.

Mohsin, A. K. M. (2008). *Automated Gmax Measurement to Explore Degradation of Artificially Cemented Carbonate Sand*. PhD Thesis, University of Sydney.

Molenkamp, F., & Luger, H. J. (1981). Modelling and minimization of membrane penetration effects in tests on granular soils. *Géotechnique*, *31*(4), 471–486.

Molenkamp, F., & Tatsuoka, F. (1983). Discussion of "Compression of Free-ends During Triaxial Testing." *Journal of Geotechnical Engineering, 109*(5), 766–771.

Mróz, Z. (1967). On the description of anisotropic workhardening. *Journal of the Mechanics and Physics of Solids*, *15*(3), 163–175.

Muir Wood, D. (1991). Approaches to Modelling the Cyclic Stress-Strain Response of Soils. In M. P. O'Reilly & F. Brown (Eds.), *Cyclic Laoding of Soils. From Theory to Design* (pp. 19–69). Glasgow: Blackie & Son Ltd.

Mulilis, J. P., Seed, H. B., & Chan, C. K. (1977). Effects of sample preparation on sand liquefaction. *Journal of the Geotechnical Engineering Division, ASCE,* (GT2), 91–108.

Newland, P. L., & Allely, B. H. (1957). Volume changes during drained triaxial tests on granular materials. *Geotechnique*, *7*(1), 17–34.

Newland, P. L., & Allely, B. H. (1959). Volume changes during undrained triaxial tests on saturated dilatant granular materials. *Géotechnique*, *9*(4), 174–182.

Nicholson, P. G., Seed, R. B., & Anwar, H. A. (1993). Elimination of membrane compliance in undrained triaxial testing. I. Measurement and evaluation. *Canadian Geotechnical Journal*, *30*(5), 727–738.

Nielsen, S. D., Shajarati, A., Sørensen, K. W., & Ibsen, L. B. (2012). Behaviour of Dense Frederikshavn Sand During Cyclic Loading. *Aalborg: Department of Civil Engineering, Aalborg University. DCE Technical Memorandum No. 15 Aalborg University*, 1–9.

Niemunis, A., Wichtmann, T., & Triantafyllidis, T. (2005). A high-cycle accumulation model for sand. *Computers and Geotechnics, 32*(4), 245–263.

Norén-Cosgriff, K., Jostad, H. P., & Madshus, C. (2015). Idealized load composition for determination of cyclic undrained degradation of soils. In V. Meyer (Ed.), *Proceedings of the 3rd International Symposium on Frontiers in Offshore Geotechnics (ISFOG 2015), Oslo, Norway, 10-12 June 2015* (pp. 1097–1102). London, UK: CRC Press.

Nova, R. (1982). A constitutive model under monotonic and cyclic loading. In G. N. Pande & O. C. Zienkiewicz (Eds.), *Soil Mechanics – Transient and Cyclic Loads* (pp. 343–373). Wiley.

Oda, M., Koishikawa, I., & Higuchi, T. (1978). Experimental study of anistotropic shear strength of sand by plane strain tests. *Soils and Foundations*, *18*(1), 25–38.

Olson, S. M., & Stark, T. D. (2003). Use of Laboratory Data to Confirm Yield and Liquefied Strength Ratio Concepts. *Canadian Geotechnical Journal*, *40*(6), 1164–1184.

Omar, T., & Sadrekarimi, A. (2014). Effects of multiple corrections on triaxial compression testing of sands. *Journal of GeoEngineering*, *9*(2), 75–83.

Omar, T., & Sadrekarimi, A. (2015). Specimen Size Effect on Shear Behavior of Loose Sand in Triaxial Testing. *Canadian Geotechnical Journal*, *52*(6), 732–746.

Ortiz, M., & Simo, J. C. (1986). An analysis of a new class of integration algorithms for elastoplastic constitutive relations. *International Journal for Numerical Methods in Engineering*, *23*(3), 353–366.

Papadimitriou, A. G., Bouckovalas, G. D., & Dafalias, Y. F. (2001). Plasticity model for sand under small and large cyclic strains. *Journal of Geotechnical and Geoenvironmental Engineering, ASCE*, *127*(11), 973–983.

Peacock, W. H., & Seed, H. B. (1968). Sand Liquefaction Under Cyclic Loading Simple Shear Conditions. *Journal of the Soil Mechanics and Foundations Division, ASCE*, *94*(3), 689–708.

Penna, A., Sorrentino, G., D'Onofrio, A., Silvestri, F., & Simonelli, A. L. (2016). Dynamic behaviour of the Leighton Buzzard Sand-B under very low confining stresses. In *1st IMEKO TC4 International Workshop on Metrology for Geotechnics (MetroGeotechnics 2016), 17-18 March 2016, Benevento, Italy.* (pp. 200–203). International Measurement Confederation (IMEKO).

Peralta, P. (2010). *Investigations on the Behavior of Large Diameter Piles under Long-Term Lateral Cyclic Loading in Cohesionless Soil*. PhD Thesis, University of Hanover.

Peralta, P., & Achmus, M. (2010). An experimental investigation of piles in sand subjected to lateral cyclic loads. In L. Springman, S. Laue, J. Sewards (Ed.), *Proceedings of the 7th International Conference on Physical Modelling in Geotechnics (ICPMG 2010), 28th June - 1st July, Zurich, Switzerland* (pp. 985–990). CRC Press.

Peralta, P., Ballard, J. C., Rattley, M. R., & Erbrich, C. E. (2017). Dynamic and Cyclic Pile-Soil Response Curves for Monopile Design. In *Proceedings of the 8th International Conference on Offshore Site Investigation and Geotechnics, 12-14 Sept., 2017, London, UK* (Vol. 2, pp. 1054–1061). London: Society for Underwater Technology.

Pietruszczak, S. (2010). *Fundamentals of Plasticity in Geomechanics*. CRC Press.

Plaxis. (2018). *2D Material Models Manual*.

Ponce, V. M., & Bell, J. M. (1971). Shear strength of sand at extremely low pressures. *Journal of the Soil Mechanics and Foundation Division, ASCE*, *97*(SM4), 625–638.

Potts, D. M. (2003). Numerical analysis: a virtual dream or practical reality? *Géotechnique*, *53*(6), 535–573.

Potts, D. M., & Ganendra, D. (1994). An evaluation of substepping and implicit stress point algorithms. *Computer Methods in Applied Mechanics and Engineering*, *119*(3–4), 341–354.

Potts, D. M., & Zdravkovic, L. (1999). *Finite element analysis in geotechnical engineering - Theory* (Vol. 1). London: Thomas Telford Ltd.

Poulos, H. G. (1988). Cyclic Stability Diagram for Axially Loaded Piles. *Journal of Geotechnical Engineering, ASCE*, *114*(8), 877–895.

Poulos, S. J. (1981). The steady state of deformation. *Journal of Geotechnical Engineering, ASCE*, *107*(GT5), 553–562.

Poulos, S. J., Castro, G., & France, J. W. (1988). Closure to "Liquefaction Evaluation Procudure." *Journal of Geotechnical Engineering, ASCE*, *114*(2), 251–259.

Prager, W. (1955). The Theory of Plasticity: A Survey of Recent Achievements. *Proceedings of* *the Institution of Mechanical Engineers*, *169*, 41–57.

Prévost, J. H. (1985). A simple plasticity theory for frictional cohesionless soils. *International Journal of Soil Dynamics and Earthquake Engineering*, *4*(1), 9–17.

Quinteros, V. S., Lunne, T., Dyvik, R., Krogh, L., Bøgelund-Pedersen, R., & Bøtker-Rasmussen, S. (2017). Influence of Pre-Shearing on the Triaxial Drained Strength and Stiffness of a Marine North Sea Sand. In *Proceedings of the 8th International Conference on Offshore Site Investigation and Geotechnics, 12-14 Sept., 2017, London, UK* (pp. 338–345). London.

Rad, N. S., & Tumay, M. T. (1987). Factors Affecting Sand Specimen Preparation By Raining. *Geotechnical Testing Journal*, *10*(1), 31–37.

Raju, V. S., Sadsivan, S. K., & Venkatamaran, M. (1972). Use of lubricated and conventional end platens in triaxial tests on sands. *Soils and Foundations*, *12*(4), 25–43.

Ramsey, N., Sharma, S., & Lee, F. (2017). Multi-laboratory assessments of cyclic soil behaviour. In *Proceedings of the 8th International Conference on Offshore Site Investigation and Geotechnics, 12-14 Sept., 2017, London, UK* (Vol. 2, pp. 1232–1237). Society for Underwater Technology.

Rascol, E. (2009). *Cyclic Properties of Sand: Dynamic Behaviour for Seismic Applications*. PhD Thesis, École Polytechnique Fédérale de Lausanne.

Reid, D. (2019). Preliminary results of critical state testing round robin. Retrieved May 21, 2019, from https://www.linkedin.com/pulse/preliminary-results-critical-state-testing-round-robin-david-reid/

Reid, D., Fourie, A., Ayala, J. L., Dickinson, S., Ochoa-Cornejo, F., Fanni, R., … Suazo, G. (2020). Results of a Critical State Line Testing Round Robin Programme. *Géotechnique*, (Ahead of print). https://doi.org/10.1680/jgeot.19.P.373

Richards, I. A. (2019). *Monopile foundations under complex cyclic lateral loading*. DPhil Thesis, University of Oxford.

Richards, I. A., Byrne, B. W., & Houlsby, G. T. (2019). Monopile rotation under complex cyclic lateral loading in sand. *Géotechnique*, (Ahead of print). https://doi.org/10.1680/jgeot.18.p.302

Roscoe, K. H. (1970). The influence of strains in soil mechanics. *Géotechnique*, *20*(2), 129–170.

Roscoe, K. H., Schofield, A. N., & Thurairajah, A. (1963). An evaluation of test data for selecting a yield criterion for soils. In *Laboratory Shear Testing of Soils, ASTM STP 361* (pp. 111–128). ASTM.

Roscoe, K. H., Schofield, A. N., & Wroth, C. P. (1958). On the yielding of soil. *Géotechnique*, *8*(1), 22–53.

Rowe, P. W. (1962). The Stress-Dilatancy Relation for Static Equilibrium of an Assembly of Particles in Contact. *Proceedings of the Royal Society A*, *269*, 500–527.

Rowe, P. W., & Barden, L. (1964). Importance of free ends in triaxial testing. *Journal of the Soil Mechanics and Foundation Division, ASCE*, *90*(SM1), 1–27.

Roy, M., & Lo, K. Y. (1971). Effect of End Restraint on High Pressure Tests of Granular Materials. *Canadian Geotechnical Journal*, *8*(4), 579–588.

Sarsby, R. W., Kalteziotis, N., & Haddad, E. H. (1980). Bedding error in triaxial tests on granular media. *Géotechnique*, *30*(3), 302–309.

Sasitharan, S. (1994). *Collapse behaviour of very loose sand*. PhD Thesis, University of Alberta.

Schanz, T., & Vermeer, P. A. (1996). Angles of friction and dilatancy of sand. *Géotechnique*, *46*(1), 145–151.

Schanz, T., & Vermeer, P. A. (1997). Discussion: Angles of friction and dilatancy of sand. *Géotechnique*, *47*(4), 887–892.

Schnaid, F. (1990). *A study of the pressuremeter test in sand*. DPhil Thesis, University of Oxford.

Schofield, A. N., & Wroth, C. P. (1968). *Critical state soil mechanics*. London: McGraw Hill.

Scholey, G. K., Frost, J. D., Lo Presti, D. C. F., & Jamiolkowski, M. (1995). A Review of Instrumentation for Measuring Small Strains During Triaxial Testing of Soil Specimens. *Geotechnical Testing Journal*, *18*(2), 137–156.

Schultheiss, P. J. (1981). Simultaneous measurements of P & S wave velocities during conventional laboratory soil testing procedures. *Marine Geotechnology*, *4*(4), 343–366.

Schupp, J. (2009). *Upheaval Buckling and Flotation of Buried Offshore Pipelines*. DPhil Thesis, University of Oxford.

Scott, R. F. (1987). 27th Rankine Lecture: Failure. *Géotechnique*, *37*(4), 423–466.

Scott, R. F. (1989). Constitutive relations for soil: Present and future. In A. S. Saada & G. F. Bianchini (Eds.), *Proceedings of the International Workshop on Constitutive Equations for Granular Non-Cohesive Soils, Cleveland, Ohio, 22-24 July 1987* (pp. 723–725). Cleveland, Ohio: Balkema.

Seed, H. B. (1979). Soil liquefaction and cyclic mobility evaluation for level ground during earthquakes. *Journal of the Geotechnical Engineering Division, ASCE*, *105*(2), 201–255.

Seed, H. B., Idriss, I. M., Makdisi, F., & Banerjee, N. (1975). *Report No. EERC 75-29. Representation of, irregular stress time histories by equivalent uniform stress series in liquefaction analysis*. Earthquake Engineering Research Center.

Seed, H. B., Wong, R. T., Idriss, I. M., & Tokimatsu, K. (1986). Moduli and Damping Factors for Dynamic Analyses of Cohesionless Soils. *Journal of the Soil Mechanics and Foundation Division, ASCE*, *112*(SM11), 1016–1032.

Shajarati, A., Sørensen, K. W., Nielsen, S. D., & Ibsen, L. B. (2012). Behaviour of Cohesionless Soils During Cyclic Loading. *DCE Technical Memorandum No. 14 Aalborg University*, 1–11.

Shuttle, D. A. (2004). Implementation of a viscoplastic algorithm for critical state soil models. In G. N. Pande & S. T. Pietruszczak (Eds.), *Numerical Models in Geomechanics: NUMOG IX; Proceedings of the 9th Symposium on Numerical Models in Geomechanics, 25-27 August 2004, Ottawa, Canada*. Balkema.

Sladen, J. A., D’Hollander, R. D., & Krahn, J. (1985). The liquefaction of sands, a collapse surface approach. *Canadian Geotechnical Journal*, *22*(4), 564–578.

Sladen, J. A., & Handford, G. (1987). A potential systematic error in laboratory testing of very loose sands. *Canadian Geotechnical Journal*, *24*(3), 462–466.

Sloan, S. W. (1987). Substepping schemes for the numerical integration of elastoplastic stress–strain relations. *International Journal for Numerical Methods in Engineering*, *24*(5), 893–911.

Sloan, S. W., Abbo, A. J., & Sheng, D. (2001). Refined explicit integration of elastoplastic models with automatic error control. *Engineering Computations*, *18*(1/2), 121–194.

Sloan, S. W., & Booker, J. R. (1992). Integration of Tresca and Mohr–Coulomb constitutive relations in plane strain elastoplasticity. *International Journal for Numerical Methods in Engineering*, *33*(1), 163–196.

Smith, I. M., & Griffiths, D. V. (2013). *Programming the Finite Element Method* (5th ed.). John Wiley & Sons.

Smith, P. R. (1992). *The behaviour of natural high compressibility clay with special reference to construction on soft ground.* PhD Thesis, Imperial College London.

SoilModels. (2020). SANISAND (Dafalias and Manzari, 2004). Retrieved March 1, 2020, from https://soilmodels.com/sanisand/

Stroud, M. A. (1971). *The behaviour of sand at low stress levels in the simple-shear apparatus*. PhD Thesis, University of Cambridge.

Sture, S., Batiste, S. N., Lankton, M., & Parisi, J. (2004). Properties of sand under low effective stresses. In *Proceedings of the Ninth Biennial Conference on Engineering, Construction, and Operations in Challenging Environments, League City, Houston, Texas, United States March 7-10, 2004* (pp. 78–84). League City, Houston: ASCE.

Sture, S., Costes, N., Batiste, S., Lankton, M., AlShibli, K., Jeremic, B., … Frank, M. (1998). Mechanics of granular materials at low effective stresses. *Journal of Aerospace Engineering*, *11*(3), 67–72.

Sze, H. Y., & Yang, J. (2014). Failure modes of sand in undrained cyclic loading: Impact of sample preparation. *Journal of Geotechnical and Geoenvironmental Engineering*, *140*(1), 152–169.

Taborda, D. M. ., Zdravkovic, L., Kontoe, S., & Potts, D. M. (2014). Computational study on the modification of a bounding surface plasticity model for sands. *Computers and Geotechnics*, *59*, 145–160.

Taborda, D. M. G. (2011). *Development of Constitutive Models for Application in Soil Dynamics*. PhD Thesis, Imperial College London.

Taborda, D. M. G. (2014). MSc Lecture Notes: Behaviour of Sands (Part II). Imperial College London.

Taborda, D. M. G., Potts, D. M., & Zdravković, L. (2016). On the assessment of energy dissipated through hysteresis in finite element analysis. *Computers and Geotechnics*, *71*, 180–194.

Taborda, D. M. G., Zdravković, L., Potts, D. M., Burd, H. J., Byrne, B. W., Gavin, K. G., … McAdam, R. A. (2019). Finite-element modelling of laterally loaded piles in a dense marine sand at Dunkirk. *Géotechnique*, (Ahead of print). https://doi.org/10.1680/jgeot.18.pisa.006

Taiebat, M., & Dafalias, Y. F. (2008). SANISAND: Simple anisotropic sand plasticity model. *International Journal for Numerical and Analytical Methods in Geomechanics*, *32*(8), 915–948.

Tatsuoka, F. (1987). Discussion: "The strength and dilatancy of sands" by Bolton, M.D. *Géotechnique*, *37*(2), 219–226.

Tatsuoka, F. (1988). State-of-the-Art Paper: Some Recent Developments in Triaxial Testing Systems for Cohesionless Soils. In R. T. Donaghe, R. C. Chaney, & M. L. Silver (Eds.), *Advanced Triaxial Testing of Soil and Rock, ASTM STP 977* (pp. 7–67).

Tatsuoka, F., Goto, S., & Sakamoto, M. (1986). Effects of Some Factors on Strength and Deformation Characteristics of Sand At Low Pressures. *Soils and Foundations*, *26*(1), 105–114.

Tatsuoka, F., & Haibara, O. (1985). Shear resistance between sand and smooth or lubricated surfaces. *Soils and Foundations*, *25*(1), 89–98.

Tatsuoka, F., Molenkamp, F., Torii, T., & Hino, T. (1984). Behavior of lubrication layers of platens in element tests. *Soils and Foundations*, *24*(1), 113–128.

Tatsuoka, F., Muramatsu, M., & Sasaki, T. (1982). Cyclic undrained stress-strain behavior of dense sands by torsional simple shear test. *Soils and Foundations*, *22*(2), 55–70.

Tatsuoka, F., Ochi, K., Fujii, S., & Okamoto, M. (1986). Cyclic undrained triaxial and torsional shear strength of sands for different sample preparation methods. *Soils and Foundations*, *26*(3), 23–41.

Tatsuoka, F., Sakamoto, M., Kawamura, T., & Fukushima, S. (1986). Strength and Deformation Characteristics of Sand in Plane Strain Compression at Extremely Low Pressures. *Soils and Foundations*, *26*(1), 65–84.

Tatsuoka, F., Shibuya, S., Goto, S., Sato, T., & Kong, X. J. (1990). Discussion on "The use of hall effect semiconductors in geotechnical instrumentation." *Geotechnical Testing Journal*, *13*(1), 63–67.

Tavenas, F., & La Rochelle, P. (1972). Accuracy of relative density measurements. *Géotechnique*, *22*(4), 549–562.

Taylor, D. W. (1941). *Seventh progress report on shear research to U.S. engineers*. MIT Publication, Masachusetts Institute of Technology, Cambridge, Mass.

Taylor, D. W. (1948). *Fundamentals of Soil Mechanics*. New York: John Wiley & Sons, Ltd.

Thieken, K., Achmus, M., & Schröder, C. (2014). On the behavior of suction buckets in sand under tensile loads. *Computers and Geotechnics*, *60*, 88–100.

Townsend, F. C. (1978). A review of factors affecting cyclic triaxial tests. In M. L. Silver & D. Tiedemann (Eds.), *Dynamic Geotechnical Testing, ASTM STP 654* (pp. 356–383). Baltimore: ASTM.

Truong, P., Lehane, B. M., Zania, V., & Klinkvort, R. T. (2019). Empirical approach based on centrifuge testing for cyclic deformations of laterally loaded piles in sand. *Géotechnique*, *69*(2), 1–13.

United Nations. Paris Agreement - Framework Convention on Climate Change (2015).

Uthayakumar, M., & Vaid, Y. P. (1998). Static liquefaction of sands under multiaxial loading. *Canadian Geotechnical Journal*, *35*(2), 273–283.

Vaid, Y. P., & Chern, J. C. (1983). Effect of Static Shear on Resistance to Liquefaction. *Soils and Foundations*, *23*(1), 47–60.

Vaid, Y. P., & Chern, J. C. (1985). Cyclic and monotonic undrained response of sands. In

Advances in the art of testing soils under cyclic loading conditions, ASCE (pp. 171–176). Reston, VA.

Vaid, Y. P., Chung, E. K. F., & Kuerbis, R. H. (1990). Stress path and steady state. *Canadian Geotechnical Journal*, *27*(1), 1–7.

Vaid, Y. P., & Negussey, D. (1984a). A critical assessment of membrane penetration in the triaxial test. *Geotechnical Testing Journal, ASTM, 7*(2), 70–76.

Vaid, Y. P., & Negussey, D. (1984b). Relative density of pluviated sand samples. *Soils and Foundations*, *24*(2), 101–105.

Vaid, Y. P., & Negussey, D. (1988). Preparation of Reconstituted Sand Specimens. In R. T. Donaghe, R. C. Chaney, & M. L. Silver (Eds.), *Advanced Triaxial Testing of Soil and Rock, ASTM STP 977* (pp. 405–411). Philadelphia, PA: ASTM.

Vaid, Y. P., & Sasitharan, S. (1992). The strength and dilatancy of sands. *Canadian Geotechnical Journal*, *29*, 522–526.

Vaid, Y. P., Sivathayalan, S., & Stedman, D. (1999). Influence of Specimen-Reconstituting Method on the Undrained Response of Sand. *Geotechnical Testing Journal. GTJODJ*, *22*(3), 187–195.

Van Eekelen, H. A. M. (1980). Isotropic yield surfaces in three dimensions for use in soil mechanics. *International Journal for Numerical and Analytical Methods in Geomechanics, 4,* 89–101.

Verdugo, R., & Ishihara, K. (1996). The steady state of sandy soils. *Soils and Foundations*, *36*(2), 81–91.

Vermeer, P. A., & de Borst, R. (1984). Non-Associated Plasticity for Soils, Concrete and Rock. *Heron*, *29*(3), 1–64.

VJ-Tech. (2017). Dynamic Triaxial Test (csDYNA). Version 2.1.

von Wolffersdorff, P. A. (1996). Hypoplastic relation for granular materials with a predefined limit state surface. *Mechanics of Cohesive-Frictional Materials, 1*(3), 251–271.

Vucetic, M. (1994). Cyclic Threshold Shear Strains in Soils. *Journal of Geotechnical Engineering, ASCE, 120*(12), 2208–2228.

Wang, J. (2005). *The Stress-Strain and Strength Characteristics of Portaway Sand*. PhD Thesis, University of Nottingham.

Wang, R., Fu, P., Zhang, J. M., & Dafalias, Y. F. (2017). Evolution of various fabric tensors for granular media toward the critical state. *Journal of Engineering Mechanics, ASCE, 143*(10), 1–9.

Whyte, S. A. (2019). *Development, Implementation, Calibration and use of Practical Constitutive Models in Finite Element Analysis of Offshore Foundations*. DEng Thesis, University of Oxford.

Wichtmann, T. (2005). *Explicit accumulation model for non-cohesive soils under cyclic loading*. PhD Thesis, Ruhr University Bochum.

Wichtmann, T., Fuentes, W., & Triantafyllidis, T. (2019). Inspection of three sophisticated constitutive models based on monotonic and cyclic tests on fine sand: Hypoplasticity vs. Sanisand vs. ISA. *Soil Dynamics and Earthquake Engineering*, *124*, 172–183.

Wichtmann, T., & Triantafyllidis, T. (2004). Influence of a cyclic and dynamic loading history on dynamic properties of dry sand, part I: Cyclic and dynamic torsional prestraining. *Soil Dynamics and Earthquake Engineering*, *24*(2), 127–147.

Wichtmann, T., & Triantafyllidis, T. (2010). On the influence of the grain size distribution curve on P-wave velocity, constrained elastic modulus Mmax and Poisson’s ratio of quartz sands. *Soil Dynamics and Earthquake Engineering, 30*(8), 757–766.

Wichtmann, T., & Triantafyllidis, T. (2016). An experimental database for the development, calibration and verification of constitutive models for sand with focus to cyclic loading: part II—tests with strain cycles and combined loading. *Acta Geotechnica*, *11*(4), 763–774.

Wong, R. T., Chan, C. K., & Seed, H. B. (1975). Cyclic Loading Liquefaction of Gravelly Soils. *Journal of the Geotechnical Engineering Division, ASCE*, *101*(6), 571–583.

Wood, F. M., Yamamuro, J. A., & Lade, P. V. (2008). Effect of depositional method on the undrained response of silty sand. *Canadian Geotechnical Journal*, *2*(4), 211–221.

Wroth, C. P., & Bassett, R. H. (1965). A Stress–Strain Relationship for the Shearing Behaviour of a Sand. *Géotechnique*, *15*(1), 32–56.

Wu, J., Kammerer, A. M., Riemer, M. F., Seed, R. B., & Pestana, J. M. (2004). Laboratory Study of Liquefaction Triggering Criteria. In *13th World Conference on Earthquake Engineering, Vancouver, Canada. August 1-6, 2004*.

Wu, W., & Kolymbas, D. (2000). Hypoplasticity then and now. In D. Kolymbas (Ed.), *Constitutive Modelling of Granular Materials*. Springer-Verlag Berlin Heidelberg.

Yamashita, S., Kawaguchi, T., Nakata, Y., Mikami, T., Fujiwara, T., & Shibuya, S. (2009). Interpretation of international parallel test on the measurement of Gmax using bender elements. *Soils and Foundations*, *49*(4), 631–650.

Yang, J., & Dai, B. B. (2011). Is the quasi-steady state a real behaviour? a micromechanical perspective. *Géotechnique*, *61*(2), 175–183.

Yang, J., & Sze, H. Y. (2011). Cyclic Strength of Sand under Sustained Shear Stress. *Journal of Geotechnical and Geoenvironmental Engineering, ASCE*, *137*(12), 1275–1285.

Yang, Z., & Elgamal, A. (2008). Multi-surface cyclic plasticity sand model with lode angle effect. *Geotechnical and Geological Engineering*, *26*(3), 335–348.

Yoshimi, Y., Richart, F. E., Prakash, S., Balkan, D. D., & Ilyichev, V. A. (1977). Soil dynamics and its application to foundation engineering. State-of-the-art report. In *Proceedings of the 9th International Conference on Soil Mechanics and Foundation Engineering, Tokyo* (Vol. 2, pp. 605–650).

Yoshimine, M., & Ishihara, K. (1998). Flow Potential of Sand During Liquefaction. *Soils and Foundations*, *38*(3), 189–198.

Yu, H.-S. (1998). CASM: a Unified State Parameter Model for Clay and Sand. *Int. J. Numer. Anal. Meth. Geomech*, *22*, 621–653.

Yu, H.-S. (2006). *Plasticity and Geotechnics*. Springer.

Yu, H.-S., & Khong, C. D. (2003). Bounding surface formulation of a unified critical state model for clay and sand. In H. DiBenetto, T. Doanh, & H. Geoffroy (Eds.), *Proceedings of the 3rd International Symposium on Deformation Characteristics of Geomaterials, Sept 2003, Lyon, France* (pp. 1111–1118). Taylor & Francis.

Yu, H.-S., Khong, C. D., Wang, J., & Zhang, G. (2005). Experimental evaluation and extension of a simple critical state model for sand. *Granular Matter*, *7*(4), 213–225.

Yu, H.-S., Khong, C., & Wang, J. (2007). A unified plasticity model for cyclic behaviour of clay and sand. *Mechanics Research Communications*, *34*(2), 97–114.

Zdravković, L., Jardine, R. J., Taborda, D. M. G., Abadias, D., Burd, H. J., Byrne, B. W., … Ushev, E. (2019). Ground characterisation for PISA pile testing and analysis. *Géotechnique*, (Ahead of print). https://doi.org/10.1680/jgeot.18.pisa.001

Zerfa, F. Z., & Loret, B. (2003). Coupled dynamic elastic-plastic analysis of earth structures. *Soil Dynamics and Earthquake Engineering*, *23*(6), 435–454.

Zhang, H., & Garga, V. K. (1997). Quasi-steady state: A real behaviour? Discussion. *Canadian Geotechnical Journal*, *34*(5), 749–761.

Zhang, J. M., Shamoto, Y., & Tokimatsu, K. (1997). Moving Critical and Phase Transformation Stress State Lines of Saturated Sand During Undrained Cyclic Shear. *Soils and Foundations*, *37*(2), 51–59.

Zhao, J., Sheng, D., Rouainia, M., & Sloan, S. W. (2005). Explicit stress integration of complex soil models. *International Journal for Numerical and Analytical Methods in Geomechanics*, *29*(12), 1209–1229.

Zhu, F., Bienen, B., O'Loughlin, C., Morgan, N., & Cassidy, M. J. (2018). The response of suction caissons to multidirectional lateral cyclic loading in sand over clay. *Géotechnique*, *68*(8), 729–741.

Ziegler, H. (1959). A Modification of Prager's Hardening Rule. *Quarterly of Applied Mathematics*, *17*(1), 55–65.

Ziegler, H. (1983). *An introduction to thermomechanics* (2nd ed.). North Holland.

Zytynski, M., Randolph, M. F., & Wroth, C. P. (1978). On Modelling the Unloading-Reloading. *International Journal for Numerical and Analytical Methods in Geomechanics*, *2*, 87–93.

APPENDIX A MODELLING PRELIMINARIES

A.1 STRESS INVARIANTS

Formulation of simple isotropic elastoplastic constitutive models in general stress space requires definition of various stress and strain invariants. The following sections give an overview of these invariants based on the definitions given in (Lade, 2016).

A 3D stress state using Cartesian axes (x, y, z) and assuming a compression-positive sign convention, may be defined by the stress tensor:

$$\hat{\boldsymbol{\sigma}} = \begin{bmatrix} \sigma_{xx} & \tau_{xy} & \tau_{xz} \\ \tau_{yx} & \sigma_{yy} & \tau_{yz} \\ \tau_{zx} & \tau_{zy} & \sigma_{zz} \end{bmatrix} \tag{A-1}$$

Where the bold typeset and $\frown$ notation denote tensorial form. When implementing constitutive models, it is generally more convenient to work with vectors, and expressing the stress tensor in Voigt/vector form gives:

$$\boldsymbol{\sigma} = \left[\sigma_{xx}\ \sigma_{yy}\ \sigma_{zz}\ \tau_{xy}\ \tau_{yz}\ \tau_{zx}\ \right]^T \tag{A-2}$$

Similarly, the effective stress tensor, $\hat{\boldsymbol{\sigma}}'$, may be expressed as:

$$\boldsymbol{\sigma}' = \left[\sigma'_{xx}\ \sigma'_{yy}\ \sigma'_{zz}\ \tau_{xy}\ \tau_{yz}\ \tau_{zx}\ \right]^T \tag{A-3}$$

where:

$$\boldsymbol{\sigma}' = \boldsymbol{\sigma} - u[1\ 1\ 1\ 0\ 0\ 0\ ]^T \tag{A-4}$$

and u is the pore water pressure. For brevity, the prime notation (used to denote effective stresses) is dropped, with all stresses representing their effective stress equivalent. The ‘fundamental’ stress invariants, I_1, I_2, I_3, may be obtained from:

$$I_1 = \sigma_{xx} + \sigma_{yy} + \sigma_{zz} = \text{trace}(\hat{\sigma}) \tag{A-5}$$

$$I_2 = \sigma_{xx}\sigma_{yy} + \sigma_{yy}\sigma_{zz} + \sigma_{zz}\sigma_{xx} + \tau_{xy}^2 + \tau_{yz}^2 + \tau_{zx}^2 \tag{A-6}$$

$$I_3 = \sigma_{xx}\sigma_{yy}\sigma_{zz} - \tau_{xy}^2\sigma_{zz} - \tau_{yz}^2\sigma_{xx} - \tau_{zx}^2\sigma_{yy} + 2\tau_{xy}\tau_{yz}\tau_{zx} = \det(\hat{\sigma}) \tag{A-7}$$

It is also useful to decompose the stress tensor into its hydrostatic and deviatoric components:

$$\begin{bmatrix} \sigma_{xx} & \tau_{xy} & \tau_{xz} \\ \tau_{yx} & \sigma_{yy} & \tau_{yz} \\ \tau_{zx} & \tau_{zy} & \sigma_{zz} \end{bmatrix} = \underbrace{\begin{bmatrix} p & 0 & 0 \\ 0 & p & 0 \\ 0 & 0 & p \end{bmatrix}}_{hydrostatic\ component} + \underbrace{\begin{bmatrix} s_{xx} & s_{xy} & s_{xz} \\ s_{yx} & s_{yy} & s_{yz} \\ s_{zx} & s_{zy} & s_{zz} \end{bmatrix}}_{deviatoric\ component} \tag{A-8}$$

where p is the mean (or hydrostatic) effective stress:

$$p = \frac{1}{3}\left(\sigma_{xx} + \sigma_{yy} + \sigma_{zz}\right) = \frac{1}{3}I_1 \tag{A-9}$$

and $\hat{\boldsymbol{s}}$ is the deviatoric stress tensor, defined as:

$$\hat{s} = \begin{bmatrix} s_{xx} & s_{xy} & s_{xz} \\ s_{yx} & s_{yy} & s_{yz} \\ s_{zx} & s_{zy} & s_{zz} \end{bmatrix} = \begin{bmatrix} \sigma_{xx} - p & \tau_{xy} & \tau_{xz} \\ \tau_{yx} & \sigma_{yy} - p & \tau_{yz} \\ \tau_{zx} & \tau_{zy} & \sigma_{zz} - p \end{bmatrix} \tag{A-10}$$

The invariants of $\hat{\boldsymbol{s}}$ may then be found from:

$$J_1 = s_{xx} + s_{yy} + s_{zz} = \mathrm{trace}(\hat{s}) = 0 \tag{A-11}$$

$$J_2 = -s_{xx}s_{yy} - s_{yy}s_{zz} - s_{zz}s_{xx} + s_{xy}^2 + s_{yz}^2 + s_{zx}^2 = \frac{1}{2}\hat{s} : \hat{s} \tag{A-12}$$

$$J_3 = s_{xx}s_{yy}s_{zz} - s_{xy}^2 s_{zz} - s_{yz}^2 s_{xx} - s_{zx}^2 s_{yy} + 2s_{xy}s_{yz}s_{zx} = \det\left(\hat{s}\right) \tag{A-13}$$

Where the contraction symbol, :, represents the trace of the product of two tensors (i.e. $\hat{\boldsymbol{x}} : \hat{\boldsymbol{y}} = \mathrm{trace}(\hat{\boldsymbol{x}}\hat{\boldsymbol{y}})$. However, it is generally more useful to express J_2 in terms of the components of $\hat{\boldsymbol{\sigma}}$, which after some algebra, yields:

$$J_2 = \frac{1}{6}\left[\left(\sigma_{xx} - \sigma_{yy}\right)^2 + \left(\sigma_{yy} - \sigma_{zz}\right)^2 + (\sigma_{zz} - \sigma_{xx})^2\right] + \tau_{xy}^2 + \tau_{yz}^2 + \tau_{zx}^2 \tag{A-14}$$

There is no simple expression for J_3 in terms of the stress components σ_{ij}. However, both J_2 and J_3 may be calculated directly from the invariants of $\hat{\boldsymbol{\sigma}}$ from:

$$J_2 = \frac{1}{3}I_1^2 - I_2 \tag{A-15}$$

$$J_3 = \frac{2}{27}I_1^3 - \frac{1}{3}I_1 I_2 + I_3 \tag{A-16}$$

Any set of three independent stress invariants can be used to describe a 3D stress state, with different sets being useful in different situations. The set $\{I_1, J_2, \theta\}$ is particularly useful in constitutive modelling, where θ, known as the ‘Lode angle’, represents an angular measure of the location of the stress point on the deviatoric plane in principal stress space (see Figure 11.1b), defined from:

$$\theta = \frac{1}{3}\arcsin\left(-\frac{3\sqrt{3}}{2}\frac{J_3}{(J_2)^{3/2}}\right) \tag{A-17}$$

Various definitions of θ exist (e.g. Jefferies & Been, 2015; Manzari & Dafalias, 1997). The version used here is similar to that proposed by Potts & Zdravkovic (1999) and Yu (2006), and yields $\theta = -30°$, and 30° for triaxial compression and extension conditions, respectively.

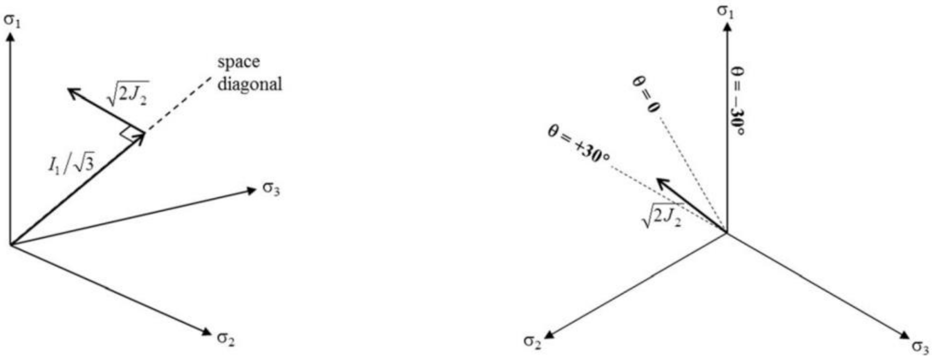

(a) ***(b)***

Figure 11.1: Geometric interpretation of the invariant set {I₁, J₂, θ} in principal stress space

The physical meaning of the invariant set $\{I_1, J_2, \theta\}$ is shown in Figure 11.1. The second invariant of the deviatoric stress tensor, J_2, is often scaled when developing constitutive models. For example, the scaled value $\sqrt{2J_2}$ is sometimes used as this represents the perpendicular distance of the stress point from the space diagonal in principal stress space, as shown in Figure 11.1a. Another advantage of utilising the invariant set $\{I_1, J_2, \theta\}$ is that the principal stresses, $\{\sigma_1, \sigma_2, \sigma_3\}$, may then be easily determined (e.g. for post processing purposes) from:

$$\sigma_1 = \frac{1}{3} I_1 + \frac{2}{\sqrt{3}} \sqrt{J_2} \sin\left(\theta + \frac{2\pi}{3}\right) \tag{A-18}$$

$$\sigma_2 = \frac{1}{3} I_1 + \frac{2}{\sqrt{3}} \sqrt{J_2} \sin(\theta) \tag{A-19}$$

$$\sigma_1 = \frac{1}{3} I_1 + \frac{2}{\sqrt{3}} \sqrt{J_2} \sin\left(\theta - \frac{2\pi}{3}\right) \tag{A-20}$$

The stress invariants I_1 and J_2 are closely related to the 'Cambridge' triaxial stress invariants p' and q, commonly used to interpret triaxial tests and to formulate elastoplastic constitutive models. p' is defined according to Eq. (A-9), while the deviator stress, q, may be obtained from:

$$q = \sqrt{3J_2} = \sqrt{\frac{3}{2} \hat{s} : \hat{s}} \tag{A-21}$$

$$q = \left[\frac{1}{2}\left[\left(\sigma_{xx} - \sigma_{yy}\right)^2 + \left(\sigma_{yy} - \sigma_{zz}\right)^2 + \left(\sigma_{zz} - \sigma_{xx}\right)^2\right] + 3\tau_{xy}^2 + 3\tau_{yz}^2 + 3\tau_{zx}^2\right]^{\frac{1}{2}} \tag{A-22}$$

A.2 FORMULATION OF ELASTOPLASTIC CONSTITUTIVE MODELS

The basic factors of the formulation and implementation of an elastoplastic constitutive model are described in detail by several authors (Britto & Gunn, 1987; Pietruszczak, 2010; Potts & Zdravkovic, 1999; Yu, 2006). The following therefore provides only a brief overview of the fundamental components required to formulate conventional, single surface, elastoplastic constitutive models.

Most conventional elastoplastic constitutive models consist of four components:

- a yield function;
- a plastic potential function;
- a hardening /softening rule; and
- an elastic model.

The yield function defines the region of allowable stress states, and separates elastic from elastoplastic behaviour. It typically takes the form, $f(\boldsymbol{\sigma},\kappa)$, where $\boldsymbol{\sigma}$ is the vector of current stresses, and κ is some hardening parameter. The equation $f(\boldsymbol{\sigma},\kappa)=0$ defines a (usually convex) surface in stress space known as the yield surface. For stress states lying inside the yield surface (i.e. $f(\boldsymbol{\sigma},\kappa)<0$), the material behaviour is purely elastic, and the incremental stiffness is given by the constitutive relation:

$$\delta\boldsymbol{\sigma}=\boldsymbol{D}^{\boldsymbol{e}}\delta\boldsymbol{\varepsilon} \tag{A-23}$$

where $\boldsymbol{D}^{\boldsymbol{e}}$ is the elastic stiffness matrix, $\boldsymbol{\varepsilon}$ is the total strain tensor in Voigt/vector form (Eq. (A-27)), and δ denotes an infinitesimal increment. For a linear isotropic elastic material, $\boldsymbol{D}^{\boldsymbol{e}}$ is given by:

$$\boldsymbol{D}^{\boldsymbol{e}}=\begin{bmatrix} K+4G/3 & K-2G/3 & K-2G/3 & 0 & 0 & 0 \\ K-2G/3 & K+4G/3 & K-2G/3 & 0 & 0 & 0 \\ K-2G/3 & K-2G/3 & K+4G/3 & 0 & 0 & 0 \\ 0 & 0 & 0 & G & 0 & 0 \\ 0 & 0 & 0 & 0 & G & 0 \\ 0 & 0 & 0 & 0 & 0 & G \end{bmatrix} \tag{A-24}$$

where K and G are the elastic shear and bulk moduli, respectively, defined as:

$$K=\frac{E}{3(1-2\mu)}=\frac{2G(1+\mu)}{3(1-2\mu)} \tag{A-25}$$

$$G=\frac{E}{2(1+\mu)}=\frac{3(1-2\mu)K}{2(1+\mu)} \tag{A-26}$$

and E is the Young's modulus (units N/m^2), and μ is the (dimensionless) Poisson's ratio. The total strain tensor, $\boldsymbol{\varepsilon}$, expressed in Voigt/vector form is given by:

$$\boldsymbol{\varepsilon} = \left[\varepsilon_{xx}\ \varepsilon_{yy}\ \varepsilon_{zz}\ \gamma_{xy}\ \gamma_{yz}\ \gamma_{zx}\right]^T \tag{A-27}$$

where $\gamma_{ij} = 2\varepsilon_{ij}$ is the engineering shear strain. For stress states lying on the yield surface (i.e. $f(\boldsymbol{\sigma}, \kappa) = 0$), the behaviour is elastoplastic, resulting in the mobilisation of plastic strains. Given that the condition $f(\boldsymbol{\sigma}, \kappa) > 0$ represents an inadmissible stress state, the stress point must remain on the yield surface during elastoplastic yielding. This leads to the consistency condition:

$$\delta f = \left(\frac{\partial f}{\partial \boldsymbol{\sigma}}\right)^T \delta\boldsymbol{\sigma} + \frac{\partial f}{\partial \kappa}\delta\kappa = \boldsymbol{a}^T\delta\boldsymbol{\sigma} + \frac{\partial f}{\partial \kappa}\delta\kappa = 0 \tag{A-28}$$

Where $\boldsymbol{a}$ is the gradient vector to the yield surface and equal to:

$$\boldsymbol{a} = \frac{\partial f}{\partial \boldsymbol{\sigma}} = \left[\frac{\partial f}{\partial \sigma_{xx}}\ \frac{\partial f}{\partial \sigma_{yy}}\ \frac{\partial f}{\partial \sigma_{zz}}\ \frac{\partial f}{\partial \tau_{xy}}\ \frac{\partial f}{\partial \tau_{yz}}\ \frac{\partial f}{\partial \tau_{zx}}\right]^T \tag{A-29}$$

For elastic-perfectly plastic constitutive models (e.g. Von Mises, Mohr-Coulomb), no hardening occurs, and the shape and position of the yield surface remain fixed in stress space. However, isotropic and kinematic hardening models include a hardening/softening rule which controls the evolution of κ as plastic strains occur. This new value of κ is then used to update the shape and/or position of the yield surface in stress space.

To satisfy the consistency condition requires two assumptions. Firstly, the total strain increment, $\delta\boldsymbol{\varepsilon}$, may be decomposed into the sum of its elastic and plastic components:

$$\delta\boldsymbol{\varepsilon} = \delta\boldsymbol{\varepsilon}^{\boldsymbol{e}} + \delta\boldsymbol{\varepsilon}^{\boldsymbol{p}} \tag{A-30}$$

The second assumption is that the direction of the plastic strain increment, $\delta\boldsymbol{\varepsilon}^{\boldsymbol{p}}$, is normal to a surface known as the plastic potential function. This assumption is conventionally known as the 'flow rule' and is usually expressed as:

$$\delta\boldsymbol{\varepsilon}^{\boldsymbol{p}} = \Lambda\frac{\partial g}{\partial \boldsymbol{\sigma}} = \Lambda\boldsymbol{b} \tag{A-31}$$

therefore:

$$\delta\boldsymbol{\varepsilon}_{\boldsymbol{p}}^{\boldsymbol{p}} = \Lambda\frac{\partial g}{\partial p'}; \delta\boldsymbol{\varepsilon}_{\boldsymbol{q}}^{\boldsymbol{p}} = \Lambda\frac{\partial g}{\partial q} \tag{A-32}$$

where Λ is a non-negative quantity known as the scalar plastic multiplier, g is the plastic potential function, and $\boldsymbol{b}$ is the unit outward normal gradient vector to g, defined as:

$$\boldsymbol{b} = \frac{\partial g}{\partial \sigma} = \left[\frac{\partial g}{\partial \sigma_{xx}} \; \frac{\partial g}{\partial \sigma_{yy}} \; \frac{\partial g}{\partial \sigma_{zz}} \; \frac{\partial g}{\partial \tau_{xy}} \; \frac{\partial g}{\partial \tau_{yz}} \; \frac{\partial g}{\partial \tau_{zx}}\right]^T \tag{A-33}$$

Λ therefore defines the magnitude of the incremental plastic strains, while b defines the direction in stress space, as shown in Figure 11.2.

When the gradients to the yield function and plastic potential functions are coincident, (i.e. $a = b$) incremental plastic flow takes place in a direction which is normal to the yield surface, and the flow rule is said to be associated. For the more general case of $\boldsymbol{a} \neq \boldsymbol{b}$, flow is said to be non-associated.

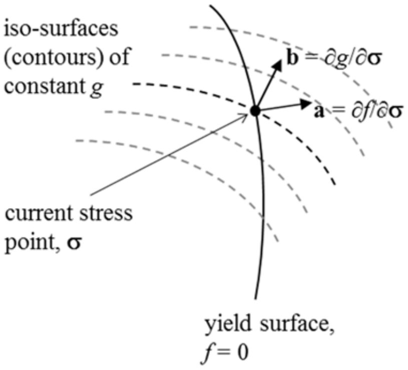

Figure 11.2: Yield surface and plastic potential (Martin & Burd, 2018)

Substituting Eqs. (A-30) and (A-31) into Eq. (A-23) yields:

$$\delta\boldsymbol{\sigma} = \boldsymbol{D^e}(\delta\boldsymbol{\varepsilon} - \delta\boldsymbol{\varepsilon^p}) = \boldsymbol{D^e}\delta\boldsymbol{\varepsilon} - \Lambda\boldsymbol{D^e b} \tag{A-34}$$

Inserting Eq. (A-34) into Eq. (A-28) allows the plastic multiplier, Λ, to be written as:

$$\Lambda = \frac{\boldsymbol{a}^T\boldsymbol{D^e}\delta\boldsymbol{\varepsilon}}{\boldsymbol{a}^T\boldsymbol{D^e b} + A} \tag{A-35}$$

where A is the hardening modulus. The precise from of A depends on the type of the hardening model adopted. For critical state type models, the hardening law is usually defined by a rate relation between $\delta\kappa$ and an increment of plastic (volumetric and/or deviatoric) strain, and is defined as:

$$A = -\frac{1}{\Lambda}\frac{\partial f}{\partial \kappa}\delta\kappa \tag{A-36}$$

It is convenient to link the increment of stresses to increments of strain via a single, elastoplastic stiffness matrix, $\boldsymbol{D^{ep}}$, such that:

$$\delta\boldsymbol{\sigma} = \boldsymbol{D^{ep}}\delta\boldsymbol{\varepsilon} \tag{A-37}$$

$\boldsymbol{D^{ep}}$ may then be obtained by substituting the expression for Λ from Eq. (A-35) into Eq. (A-34):

$$\boldsymbol{D^{ep}} = \boldsymbol{D^e} - \frac{\boldsymbol{D^e b a^T D^e}}{\boldsymbol{a^T D^e b} + A} \tag{A-38}$$

With known initial stress conditions, Eq. (A-37) describes a small system of incremental non-linear equations which may solved by integrating over an enforced increment of strain (or stress) to obtain the unknown stresses (or strains) and hardening parameter.

A.3 STRESS INVARIANT DERIVATIVES

The partial derivatives required to form the $\boldsymbol{D^{ep}}$ matrix may be determined by applying the chain rule to the partial derivatives of the stress invariant set $\{p', q, \theta\}$:

$$\frac{\partial f}{\partial \boldsymbol{\sigma}} = \frac{\partial f}{\partial p'}\frac{\partial p'}{\partial \boldsymbol{\sigma}} + \frac{\partial f}{\partial q}\frac{\partial q}{\partial \boldsymbol{\sigma}} + \frac{\partial f}{\partial \theta}\frac{\partial \theta}{\partial \boldsymbol{\sigma}} \tag{A-39}$$

$$\frac{\partial g}{\partial \boldsymbol{\sigma}} = \frac{\partial g}{\partial p'}\frac{\partial p'}{\partial \boldsymbol{\sigma}} + \frac{\partial g}{\partial q}\frac{\partial q}{\partial \boldsymbol{\sigma}} + \frac{\partial g}{\partial \theta}\frac{\partial \theta}{\partial \boldsymbol{\sigma}} \tag{A-40}$$

The leading terms on the right hand side of equations Eqs. (A-39) and (A-40) are partial derivatives of the yield and plastic potential functions with respect to their defining stress invariants, and are therefore specific to the formulation of the adopted constitutive model. However, the trailing terms are the partial derivatives of the invariants themselves and are therefore standard for any isotropic elastoplastic constitutive model formulated in terms of the stress invariant set $\{p', q, \theta\}$, and are defined as:

$$\frac{\partial p'}{\partial \boldsymbol{\sigma}} = \frac{1}{3}\begin{bmatrix}1 & 1 & 1 & 0 & 0 & 0\end{bmatrix}^T \tag{A-41}$$

$$\frac{\partial q}{\partial \boldsymbol{\sigma}} = \frac{3}{2q}\begin{bmatrix}\sigma_{xx} - p' & \sigma_{yy} - p' & \sigma_{zz} - p' & 2\tau_{xy} & 2\tau_{yz} & 2\tau_{zx}\end{bmatrix}^T \tag{A-42}$$

$$\frac{\partial \theta}{\partial \boldsymbol{\sigma}} = \frac{\sqrt{3}}{2J_2^{3/2}\cos 3\theta}\left(\frac{3}{2}\frac{J_3}{J_2}\frac{\partial J_2}{\partial \boldsymbol{\sigma}} - \frac{\partial J_3}{\partial \boldsymbol{\sigma}}\right) \tag{A-43}$$

$$\frac{\partial J_2}{\partial \boldsymbol{\sigma}} = \begin{bmatrix}\sigma_{xx} - p' & \sigma_{yy} - p' & \sigma_{zz} - p' & 2\tau_{xy} & 2\tau_{yz} & 2\tau_{zx}\end{bmatrix}^T \tag{A-44}$$

$$\frac{\partial J_3}{\partial \boldsymbol{\sigma}} = \begin{bmatrix}\frac{1}{3}\left(\sigma_{xx}s_{xx} + \sigma_{yy}s_{zz} + \sigma_{zz}s_{yy} + \tau_{xy}^2 + \tau_{yz}^2 + \tau_{zx}^2\right) \\ \frac{1}{3}\left(\sigma_{yy}s_{yy} + \sigma_{zz}s_{xx} + \sigma_{xx}s_{zz} + \tau_{yz}^2 + \tau_{zx}^2 + \tau_{xy}^2\right) \\ \frac{1}{3}\left(\sigma_{zz}s_{zz} + \sigma_{xx}s_{yy} + \sigma_{yy}s_{xx} + \tau_{xy}^2 + \tau_{yz}^2 + \tau_{zx}^2\right) \\ -2\tau_{xy}s_{zz} + 2\tau_{yz}\tau_{zx} \\ -2\tau_{yz}s_{xx} + 2\tau_{zx}\tau_{xy} \\ -2\tau_{zx}s_{yy} + 2\tau_{xy}\tau_{yz}\end{bmatrix} \tag{A-45}$$

For models that adopt a circular shape in the deviatoric plane (e.g. Drucker-Prager), the final terms of Eqs. (A-39) and (A-40) may be omitted. However, for models which account for Lode angle effects, $\partial f/\partial\theta$ and $\partial g/\partial\theta$ may be further broken down according to Eq. (A-46), in which the material derivatives depend on the chosen idealisation for M (e.g. Mohr-Coulomb, Matsuoka & Nakai, 1974).

$$\frac{\partial f}{\partial\theta} = \frac{\partial f}{\partial M}\frac{\partial M}{\partial\theta}; \frac{\partial g}{\partial\theta} = \frac{\partial g}{\partial M}\frac{\partial M}{\partial\theta} \tag{A-46}$$

APPENDIX B MONOTONIC UNLOAD-RELOADS

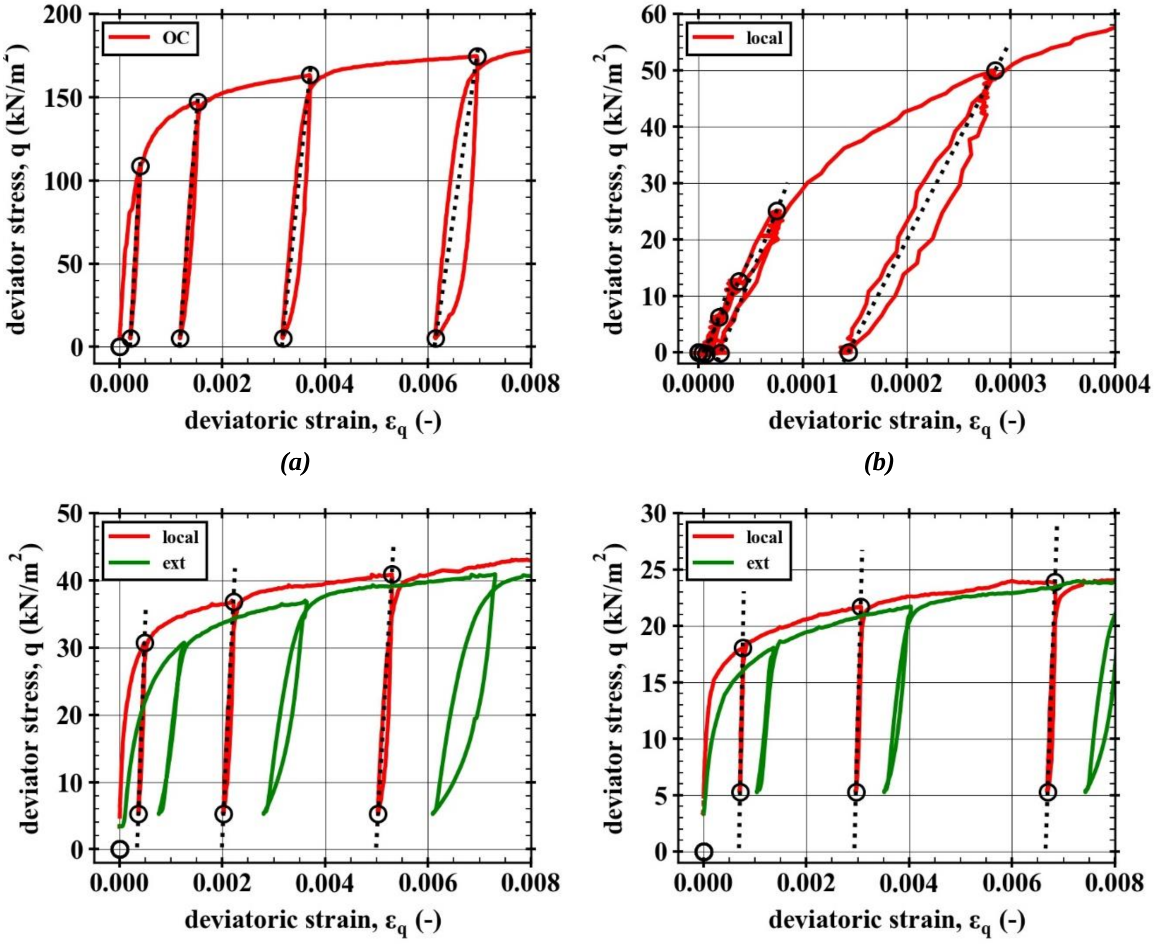

(a) *(b)*

(c) *(d)*

Figure B-1: Plots of q vs ε_q used to estimate the unload-reload modulus, G_{UR}, from CIDc(+v') tests undertaken at initial confining stresses of (a) 50kN/m^2; (b) 25kN/m^2; (c) 12kN/m^2; and (d) 6kN/m^2

Table B-1: Summary of calculated unload-reload shear moduli, G_{UR}, estimated from CIDc(+v') tests

Test ID	p'_0	**UR loop**	ε_q	q_{ur}	η	G_{ur}	$\frac{G_{ur}}{G_{0(BE)}}$
(#)	**(kN/m^2)**	**(#)**	**(-)**	**(kN/m^2)**	**(-)**	**(MN/m^2)**	**(-)**
s01	50						
s02	25.2	1	1.93E-05	6.28	0.23	183.15	1.36
s02	25.2	2	3.85E-05	12.6	0.43	122.03	0.90
s02	25.2	3	7.50E-05	25.05	0.75	155.13	1.15
s02	25.2	4	2.85E-04	49.97	1.20	118.15	0.87
s03	14	1	4.86E-04	30.73	1.31	71.00	0.94
s03	14	2	2.21E-03	36.81	1.46	54.45	0.72
s03	14	3	5.30E-03	40.91	1.53	44.27	0.58
s04	7.2	1	7.62E-04	18.06	1.46	81.76	1.45
s04	7.2	2	3.06E-03	21.72	1.58	58.55	1.04
s04	7.2	3	6.84E-03	23.88	1.66	43.17	0.77
s21	50.6	1	4.01E-04	108.84	1.27	184.98	1.23
s21	50.6	2	1.52E-03	147.13	1.49	138.62	0.92
s21	50.6	3	3.70E-03	163.26	1.57	100.19	0.67
s21	50.6	4	6.95E-03	174.60	1.62	70.54	0.47

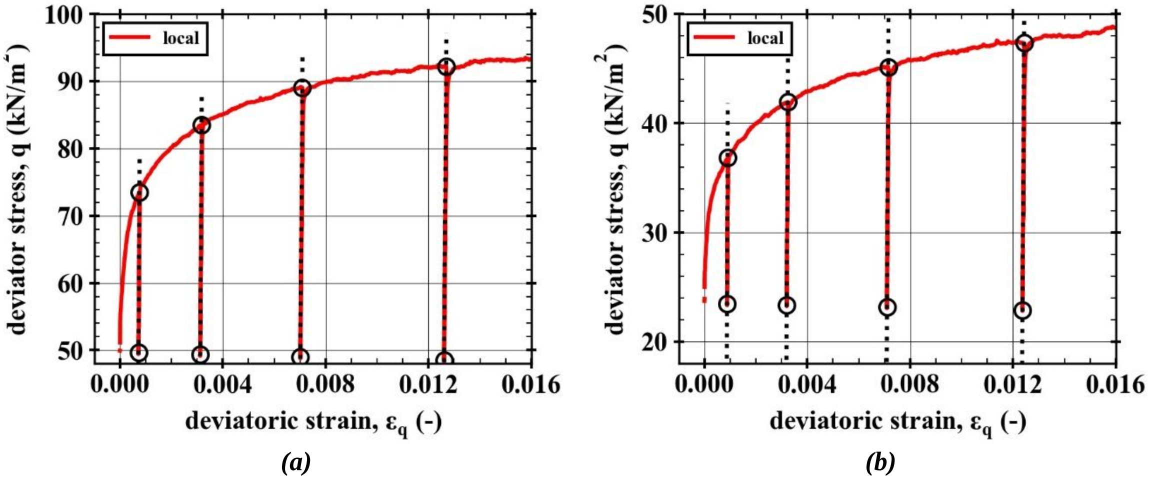

Figure B-2: Plots of q vs ε_q used to estimate the unload-reload modulus, G_{ur}, from CADc(+'v) tests undertaken at initial confining stresses of (a) 40kN/m^2; and (b) 20kN/m^2.

Table B-2: Summary of calculated unload-reload shear moduli, G_{ur}, estimated from CADc(+v') tests

Test ID (#)	p'_0 (kN/m^2)	**UR loop** (#)	ε_q (-)	q_{ur} (kN/m^2)	η (-)	G_{ur} (MN/m^2)	$\frac{G_{ur}}{G_{0(BE)}}$ (-)
s06	42.5	1	7.55E-04	73.5	1.45	203.8	1.41
s06	42.5	2	3.17E-03	83.45	1.55	226.51	1.56
s06	42.5	3	7.09E-03	89.05	1.60	177.61	1.23
s06	42.5	4	1.27E-02	92.18	1.63	180.37	1.24
s07	20.5	1	8.96E-04	36.82	1.47	214.72	1.90
s07	20.5	2	3.24E-03	41.94	1.55	159.14	1.41
s07	20.5	3	7.15E-03	45.12	1.60	147.98	1.31
s07	20.5	4	1.24E-02	47.33	1.64	135.51	1.20

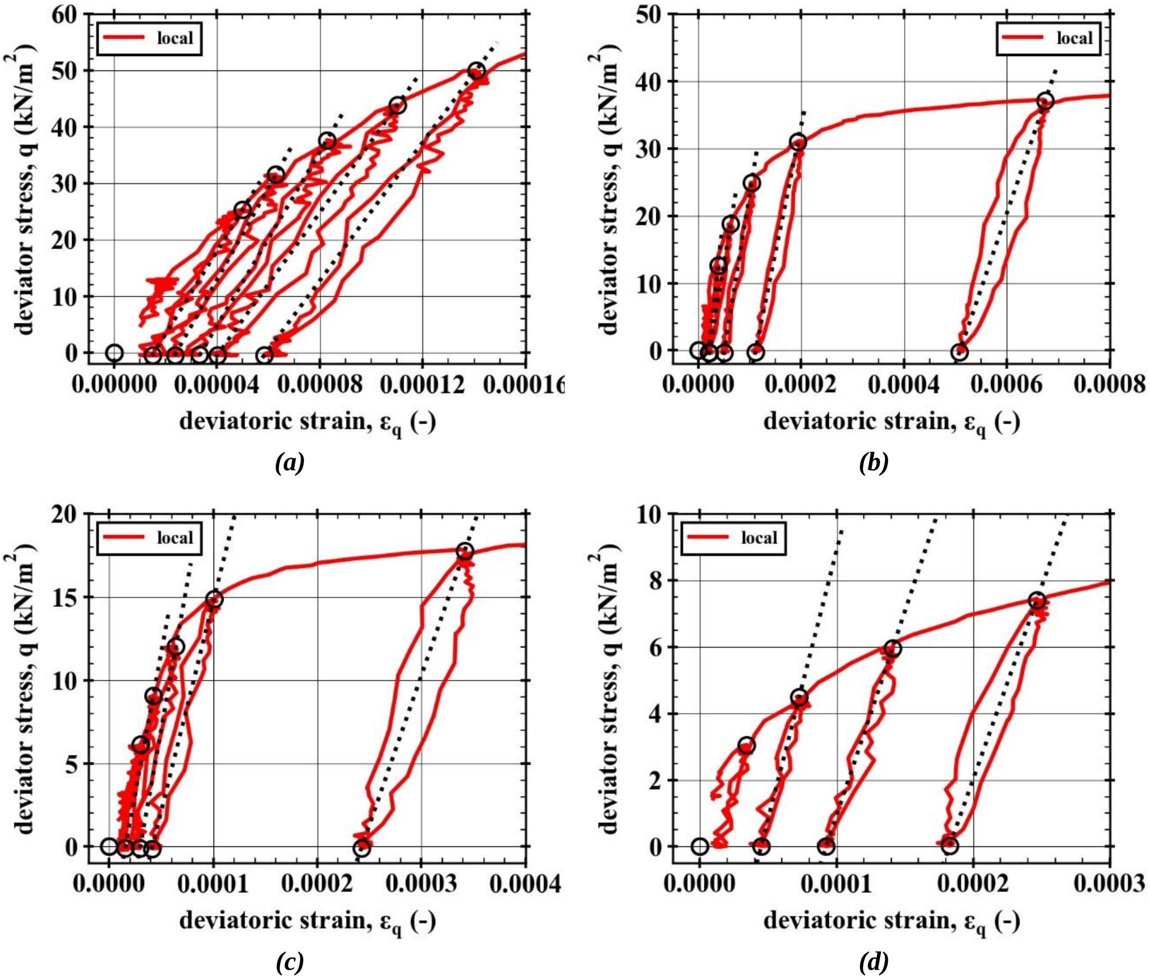

(a) *(b)*

(c) *(d)*

Figure B-3: Plots of q vs ε_q used to estimate the unload-reload modulus, G_{ur}, from CIDc(+q) tests undertaken at initial confining stresses of (a) 50kN/m^2; (b) 25kN/m^2; (c) 12kN/m^2; and (d) 6kN/m^2.

Table B-3: Summary of calculated unload-reload shear moduli, G_{ur}, estimated from CIDc(+q) tests

Test ID (#)	p'_0 (kN/m^2)	**UR loop** (#)	ε_q (-)	q_{ur} (kN/m^2)	η (-)	G_{ur} (MN/m^2)	$\frac{G_{ur}}{G_{0(BE)}}$ (-)
s13a	50.2	1	4.99E-05	25.29	0.5	245.17	1.37
s13a	50.2	2	6.29E-05	31.52	0.62	271.2	1.51
s13a	50.2	3	8.27E-05	37.64	0.75	256.64	1.43
s13a	50.2	4	1.10E-04	43.87	0.87	210.76	1.18
s13a	50.2	5	1.41E-04	49.95	0.99	204.09	1.14
s14	25.3	1	3.85E-05	12.64	0.5	230.96	2.01
s14	25.3	2	6.29E-05	18.84	0.74	154.23	1.35
s14	25.3	3	1.04E-04	24.91	0.98	156.10	1.36
s14	25.3	4	1.94E-04	31.05	1.23	125.29	1.09
s14	25.3	5	6.75E-04	37.11	1.47	74.62	0.65
s15	12.4	1	3.01E-05	6.14	0.49	-	-
s15	12.4	2	4.24E-05	9.08	0.71	112.82	1.47
s15	12.4	3	6.42E-05	12.01	0.93	116.87	1.52
s15	12.4	4	1.01E-04	14.89	1.16	83.95	1.09
s15	12.4	5	3.42E-04	17.76	1.40	59.92	0.78
s16	6.6	1	3.43E-05	3.05	0.46	-	-
s16	6.6	2	7.27E-05	4.50	0.67	53.67	1.24
s16	6.6	3	1.41E-04	5.95	0.89	40.9	0.95
s16	6.6	4	2.47E-04	7.40	1.11	38.53	0.89
s16	6.6	5	6.20E-04	8.87	1.32	22.72	0.53